VSEBINA – CONTENTS

PREGLEDNI ČLANKI – REVIEW ARTICLES

IZVIRNI ZNANSTVENI ČLANKI – ORIGINAL SCIENTIFIC ARTICLES

STROKOVNI ČLANKI – PROFESSIONAL ARTICLES

IN MEMORIAM

ALUMINIUM: THE METAL OF CHOICE

ALUMINIJ: KOVINA IZBIRE

María Josefa Freiría Gándara

Xunta de Galicia, Consellería de Educación e Ordenación Universitaria, 15704 Santiago de Compostela, La Coruña, Spain
josefa.freiria@yahoo.es

This article summarizes the importance of aluminium as the metal of choice for many applications. Aluminium is a lightweight, durable metal. It is silvery in appearance when freshly cut, is a good conductor of heat and electricity, and is easily shaped by moulding and extruding. Aluminium has two main advantages when compared with other metals. Firstly, it has a low density, about one-third that of iron and copper. Secondly, although it reacts rapidly with the oxygen in air, it forms a thin, tough and impervious oxide layer that resists further oxidation. This removes the need for surface-protection coatings such as those required with other metals, in particular with iron.

All the indications are that the growth in the use of aluminium will likely accelerate. It is expected that in the near future the use of aluminium with specifically improved properties will grow in many applications, meeting the increased economic and ecological demands.

Considering the entire life-cycle of an automobile, from the extraction of materials to the final disposal, including recycling and reuse applications, aluminium proves to be a potential alternative to steels in future automotive applications.

Keywords: corrosion resistance, aluminium alloys, aluminium applications, aluminium in vehicles, CO_2 emission, aluminium recycling

Članek povzema pomembnost aluminija kot izbrane kovine z mnogimi možnostmi uporabe. Aluminij je lahka, zdržljiva kovina. Je srebrne barve, ko je sveže odrezan, je dober prevodnik toplote in elektrike in se lahko oblikuje z ulivanjem v kokile in z ekstruzijo. Aluminij ima v primerjavi z drugimi kovinami dve glavni prednosti. Prva je majhna gostota, okrog ene tretjine gostote železa ali bakra. Druga: čeprav hitro reagira s kisikom iz zraka, tvori tanko, trdo in neprepustno oksidno plast, ki preprečuje nadaljnjo oksidacijo. Zato ni potrebe po površinski zaščiti, kot jo zahtevajo druge kovine, še posebno železo.

Kaže, da se bo rast porabe aluminija še nadaljevala. V bližnji prihodnosti se pričakuje, da bo zaradi povečanja ekonomskih in ekoloških zahtev uporaba aluminija s posebnimi, izboljšanimi lastnostmi rastla na mnogih področjih uporabe.

Z upoštevanjem celotnega trajnostnega cikla avtomobila, od pridobivanja materiala do odlaganja, vključno z recikliranjem in možnostjo nadaljnje uporabe, aluminij dokazuje, da je mogoča alternativa jeklom v prihodnji proizvodnji avtomobilov.

Ključne besede: odpornost proti koroziji, aluminijeve zlitine, uporaba aluminija, aluminij v vozilih, emisija CO_2, recikliranje aluminija

1 INTRODUCTION

Aluminium is a light, conductive, corrosion-resistant metal with a strong affinity for oxygen. This combination of properties has made it a widely used material, with applications in the aerospace, architectural construction and marine industries, as well as many domestic uses.

Aluminium is the second most widely used metal in the world today. It is used extensively in aircraft, in building construction, and in consumer durables such as fridges, cooking utensils and air conditioners, as well as in food-processing equipment and cans.

Aluminium is not found in its metallic form in nature. It occurs as bauxite, a mixture of aluminium oxides, iron oxides and clay. Manufacturing aluminium metal from bauxite is a complex process.

Aluminium is one of the most important metals used by modern societies. Aluminium´s combination of physical properties results in its use in a wide variety of products, many of which are indispensable in modern life. Because of its light weight and electrical conductivity, aluminium wire is used for the long-distance transmission of electricity. Aluminium's strength, light weight, and workability have led to increased use in transportation systems, including light vehicles, railcars, and aircraft in efforts to reduce fuel consumption. Aluminium's excellent thermal properties and resistance to corrosion have led to its use in air conditioning, refrigeration, and heat-exchange systems. Finally, its malleability has allowed it to be rolled and formed into very thin sheets used in a variety of packaging.

In 1903, the Wright brothers made aviation history when they achieved the world's first flight powered by a lightweight engine made with aluminium components. Today, aluminium is fundamental to the aviation industry. It was in the 1920s that aluminium shipping applications started to expand due to new alloys becoming available for marine applications. In the 1980s, aluminium emerged as the metal of choice for reducing running costs and improving the acceleration of metros, tramways, intercity and high-speed trains. The average volume of aluminium used in passenger cars was significantly increased in 2000.

The examples given for its success prove the major breakthroughs in automotive applications for aluminium that have been achieved during recent years by developing innovative light-weight and cost-efficient solutions.

Vehicle manufacturers must constantly improve their performance at minimum costs. The choice of a material will therefore depend on its price, its mechanical properties and its impact on vehicle production costs. Due to its low weight, good formability and corrosion resistance, aluminium is the material of choice for many automotive applications, such as the chassis, auto body and many structural components.[1–4]

2 ALUMINIUM PRODUCTION

The major raw materials required for aluminium production are alumina, carbon, power, aluminium fluoride and cryolite. The aluminium industry consumes nearly 90 % of the bauxite mined; the remainder is used in abrasives, cement, ceramics, chemicals, metallurgical flux, refractory products, and miscellaneous products. Virtually all the alumina commercially produced from bauxite is obtained using a process patented by Karl Josef Bayer (Austria) in 1888.

Primary aluminium is produced by the electrolysis of alumina dissolved in molten fluoride salt. The process was independently invented in 1886 by Charles Martin Hall (United States) and Paul Louis Toussaint Héroult (France) and underwent continual improvement over the years. The electrolysis of alumina to produce aluminium involves the use of aluminium fluoride, carbon anodes, and large amounts of electricity.[5–7]

Taking the purity grades of aluminium into account, the aluminium content is usually the main consideration and other elements are considered only as impurities. The common purity grades of aluminium are listed in **Table 1**.[8,9]

3 CORROSION RESISTANCE

Aluminium's well-known corrosion resistance is an obvious advantage in road transport. It contributes to a long service life, especially in vehicles that work in conditions that can cause serious corrosion problems. Usually, no painting or other surface protection is required and it is easy to clean. Maintenance is therefore kept to a minimum.

Corrosion is an electrochemical interaction between a metal and its environment which results in changes to the properties of the metal and which may often lead to impairment of the function of the metal, the environment, or the technical system of which these form a part. Corrosion can occur locally (pitting), or it can extend across a wide area to produce a general deterioration.

A clean aluminium surface is very reactive and will react spontaneously with air or water to form aluminium oxide. This oxide builds a natural protective layer on each aluminium surface with a thickness of around 1–10 nm. The oxide layer is chemically very stable, has a good adhesion to the metal surface, repairs itself and protects the aluminium from further corrosion. The oxide layer can be destroyed in strong acidic or alkaline environments or where aggressive ions are present. Aggressive ions can destroy the layer locally and lead to local corrosion attack (pitting). A typical case for this reaction is the contact between aluminium and chloride ions, which are present in seawater or road salts. Some alloying elements might increase the corrosion resistance of the oxide layer, while others can weaken it. Vehicle manufacturers or fleet operators should contact the aluminium supplier in any case of critical working conditions, like elevated temperatures or aggressive loads.

Some general rules need to be applied to prevent corrosion, in most cases to prevent any kind of water trap or areas where condensation can occur.

Although aluminium can be used without any surface protection and keeps its natural beauty throughout its life, it is most likely to use different surface treatment methods to optimise its attractiveness and optical appearance and to protect it from severe atmospheric conditions.[10]

4 ALUMINIUM ALLOYS

In aluminium alloys other elements are deliberately added to improve the properties in some way. Many alloys have been developed, the aim being to improve the strength while retaining the desirable properties of aluminium, most notably its lightness and corrosion resistance. In general though, while the addition of an alloying element increases the strength, it reduces the resistance to corrosion, making a compromise of the properties necessary. A possible exception to this is magnesium alloys, which have improved corrosion resistance in marine environments. Aluminium-copper alloys have very poor resistance to corrosion, and sheets are often produced in sandwich form with thin layers of pure corrosion-resistant aluminium on the outside. A summary of typical alloys is given in **Table 2**.[6,7,9]

Table 1: Purity grades of aluminium
Tabela 1: Stopnje čistote aluminija

Aluminium content in mass fractions, w/%	Major impurities in mass fractions, w/%		Some typical uses
	Silicon	Iron	
99.95 (high purity)	<0.006	<0.006	Extrusion joinery, electrical conductor, anodic trim, foil
99.80	<0.15	<0.15	Plumbing, reflectors, jewellery
99.50	<0.25	<0.40	Chemical plant, tanks, tubes
99.50	w(Si + Fe) < 1.0 %		Pots, pans, sheet-metal work

Table 2: Aluminium alloys
Tabela 2: Zlitine aluminija

Major alloy element	Content in mass fractions, w/%	Product	Some typical uses
Copper	Up to 4.5	Sheet Extrusions Castings	High-strength aircraft parts
Manganese	1.25	Sheet	Sheet-metal work, pots, pans, etc.
Silicon	Up to 13	Castings	Motor parts, castings of all types
Magnesium and Silicon	0.7 Mg 0.4 Si	Sheet Extrusions	Architectural extrusions
Magnesium	Up to 5	Sheet	Marine uses, boats, fish boxes, beer-can lids, etc.
Zinc, Magnesium and Copper	5.8 Zn 2.5 Mg 1.4 Cu	Sheet Extrusions	High-strength aircraft

Aluminium alloys used in the manufacture of commercial vehicles and their accessories are easy to process. They lend themselves to a variety of shaping and joining techniques. Correctly used, aluminium alloys have been developed to offer optimum corrosion resistance in all environments. Just one example: the widespread use of unpainted aluminium in marine applications.

Aluminium alloys tailored by suitable variations in chemical composition and processing best fit many requirements, like the non-heat-treatable Al-Mg alloys used in chassis optimized for superb resistance against inter-crystalline corrosion and concurrent high strength or the heat-treatable Al-Mg-Si alloys for extrusions and auto-body sheet modified for improved age-hardening response during the automotive paint bake cycle.

Moreover, Al-Mg-Mn alloys show an optimum combination of formability and strength achieved by the mechanism of solid solution and deformation hardening due to their specific high-strain hardening. Further improvements in the properties required for specific applications (e.g., surface appearance, corrosion resistance, thermal stability) have been achieved by small additions of other alloy elements and/or modified processing routes, e.g., stretcher strain free (SSF) sheet, avoiding Lüders-lines. Non-heat-treatable Al-Mg-Mn alloys are often applied for automobile parts in larger quantities as hot- and cold-rolled sheet and hydroformed tubes, due to their good formability, which can always be regained during complex forming operations by inter-annealing, where quenching is needed for age hardening. In chassis parts or wheel applications the benefit is twofold, since the weight reduction in the unsprung mass of moving parts additionally enhances driving comfort and reduces noise levels.[11–19]

5 ALUMINIUM APPLICATIONS: ALUMINIUM IN VEHICLES

Aluminium in its pure form is a very soft metal and hence not suited for structural applications. Thanks to the addition of alloying elements such as copper, manganese, magnesium, zinc, etc., and thanks to adequate production processes, the physical and mechanical properties can be varied over a great range, making it possible to have suitable alloys for literally all applications.

There are challenges with aluminium. Perhaps the biggest challenge is the history of the auto industry. The many years of experience based on steel technology represents a significant barrier for aluminium, especially in the areas of manufacturing, i.e., forming and joining, which are critical to the automotive industry.

In the eighteenth century, aluminium was very expensive, in spite of the fact that aluminium is a very abundant metal in the earth's crust. Since that time the cost of aluminium has been on a continuous and steep decline in price based on technological advancements. This trend will certainly continue since there are a great number of initiatives, which will continue this decline in prices.

Aluminium can be used for the car body structure and there can be a weight advantage of at least 30 % without any loss of performance. In some cases where very high strengths are demanded, 7xxx series alloys can be used to maintain this significant weight advantage. For a large volume, aluminium solutions are the most cost effective. Castings will be applied for areas where a strong part integration is feasible. Extrusions can easily be applied as straight profiles, but also forming of an extruded profile is a competitive process for high volumes, e.g., as bumper beams. Aluminium is the ideal light-weight material as it allows a weight saving of up to 50 % over competing materials in most applications without compromising safety.

Due to the positive experiences and from former successful applications its volume fraction used in cars of all classes and all sizes will grow significantly. Applying full knowledge about the physical processes involved and the microstructure/properties correlation a tuning of properties is possible in order to produce optimum and stable products required for the high demands in automobile applications.

The automotive industry has more than doubled the average amount of aluminium used in passenger cars during recent years and will do even more so in the coming years. The automotive industry, in close co-operation with the aluminium industry, has developed and introduced numerous innovative light-weight solutions based on established and improved aluminium alloys and optimized aluminium-oriented car design. Synergic effects together with a multi-material exploitation can guarantee an optimum design solution. One of

the main advances of aluminium is its availability in a large variety of semi-finished forms, such as shape castings, extrusions and sheet, all suitable for mass production and innovative solutions. Compact and highly integrated parts meet the strong demands for high performance, quality and cost-efficient manufacturability. Challenges involved here are mainly joining and surface treatment issues for which many suitable solutions have been developed. Aluminium semis are applied as castings, extrusions and sheet increases, e.g., in engine blocks and power-train parts, space frames, sheet structures or as closures and hang-on parts and other structural components.

Material-specific processing routes and individual solutions have been developed in close cooperation with partners and suppliers. With a sound knowledge about the specific material properties and effects excellent light-weight solutions for automotive applications have been successfully applied by the automobile industries. Intensive and continuous collaboration of material suppliers and application engineers provided optimum solutions for sometimes contradicting aspects of the specific requirements, e.g., for the specific material selection and optimum combinations of strength and formability. Safety has become a crucial issue for vehicle manufacturers. Aluminium has the advantage of being much stronger than steel on a weight basis, so that with proper design a lighter aluminium vehicle can be expected to protect vehicle passengers as well (or better) than a heavier steel vehicle.

The manufacturing flexibility of aluminium also represents a real advantage for the metal in auto applications. Thus, aluminium is easier to extrude and cast than steel. Other processes, such as semi-solid forming and forging, are finding niches in the automotive business as well. Aluminium sheet applications are increasing at a rapid rate in structural, exterior panels and closure panels.

The auto industry is highly competitive and increasingly global. Automakers are being challenged not only to meet the expectations of shareholders and customers, but also to answer the growing environmental concerns of society. Aluminium is the third most highly used material in vehicles and is rapidly gaining on its rival materials (iron and steel). Aluminium contributes to the reduction of CO_2 emissions from road transport. In recent years the potential problem of global warming has provided additional pressure on automakers worldwide to improve fuel economy. Carbon dioxide is considered to be the biggest anthropogenic contribution to global warming. It results primarily from the combustion of fossil fuels, hence the pressure on autos to burn less fuel. However, when one considers material substitutions, such as aluminium for steel, it is necessary to take account of the entire process of obtaining, processing, using and recycling the material.[20,21]

The automotive industry is known worldwide as being technically advanced and innovative. Based on economic and political pressure to reduce fuel consumption and CO_2 emissions the efforts for light weight in automobile design and constructions have increased significantly and specific solutions based on the intensive use of aluminium as modified or new alloys have been developed in recent decades.

Reducing manufacturing costs and tailpipe emissions by using light-weight materials which can be easily recycled or reused are among the major issues in today's automobile industry. The growing emphasis on total cost and environmental impact has forced the life-cycle cost issue to be the driving factor. Weight savings in the overall car mass is considered to be a major research focus. Aluminium is proven to be among the potential materials capable of achieving weight reduction without sacrificing either vehicle safety or performance. Despite significant technological advantages in aluminium alloys, the use of aluminium alloys to replace traditional materials such as steels has been slow due to the lack of a comprehensive economic analysis of the entire life-cycle of automotive products. In considering the total life-cycle of an automobile covering four stages (pre-manufacturing, manufacturing, use, and post-use), it is apparent that during the operational (use) stage of a vehicle, aluminium is proven to be a reliable alternative for traditional materials currently used in automotive body structures, largely due to its cost-effectiveness and superior performance due to light weight. With gas price variations, the initial cost advantage of using steel in body components gained in pre-manufacturing and manufacturing stages can be overcome during the operational (use) stage of the vehicle, since the lighter alternative provides significant savings in terms of fuel consumption and consequently the generation of airborne gas emissions. Also, the superior recyclability and reusability of aluminium in the post-use stage outweighs that of traditional materials, despite the higher costs involved in producing primary aluminium.

Knowing that the greatest opportunity for weight savings comes from the body structure and exterior closure panels, and that additional weight reduction can be achieved by downsizing the other components such as engine components, it can be considered as achieving a weight reduction by replacing the conventional material used in the vehicle's construction (i.e., steel) with a lighter mass equivalent material (i.e., aluminium), maintaining the same vehicle design and using the same manufacturing processes for the body components.[22–28]

6 ALUMINIUM RECYCLING

Aluminium is easily and economically recycled. Aluminium does not degrade during the recycling process, which means it can be recycled over and over again. Recycling aluminium reduces the need for raw

materials and reduces the use of valuable energy resources. Moreover, recycling reduces the amount of waste in landfill.

Aluminium is a valuable material to recycle due to the large amount of energy and resources used in the initial manufacture. It can be infinitely recycled. Recycled aluminium is made into aircraft, automobiles, bicycles, boats, computers, cookware, gutters, sidings, wires, cans, etc.

7 REFERENCES

[1] M. J. Crooks, R. E. Miner, Journal of Metals, 48 (**1996**) 7, 13–15

[2] Y. Kurihara, Journal of Metals, 45 (**1993**) 11, 32–33

[3] G. P. Syukla, D. B. Goel, P. C. Pandey, All India Seminar on Aluminium, New Delhi, 1978

[4] Report of Investigation on the Technical Trend of Patent Applications in 2004: Automobile Weight reduction Technologies, Japan Patent Office, 2005

[5] J. E. Gould, Projection welding, ASM Handbook, ASM International, Metals Park, Ohio, 6, 1993, 230–237

[6] A. S. Russell, Aluminum, McGraw-Hill Encyclopedia of Science & Technology, McGraw-Hill, New York 1997

[7] D. Altenpohl, Aluminum Viewed from within: An Introduction into the Metallurgy of Aluminum Fabrication, Aluminium-Verlag, Düsseldorf 1982

[8] U. M. J. Boin, M. Bertram, Journal of Metals, 5 (**2005**), 26–33

[9] K. Grjotheim, B. J. Welch, Aluminium Smelter Technology: A Pure and Applied Approach, 2nd ed., Aluminium-Verlag, 1988

[10] G. D. Davis, J. S. Ahearn, J. D. Venables, J. Vac. Sci. Technol., A2 (**1984**), 763–766

[11] I. N. Fridlyander, V. G. Sister, O. V. Grushko, V. V. Berstenev, L. M. Sheveleva, L. A. Ivanova, Metal Science and Heat Treatment, September (**2002**), 3–9

[12] M. P. Meinel, Product Engineering, 23 (**1951**), 163–165

[13] T. R. Gauthier, W. J. Rowe, Mechanical Engineering, 70 (**1948**), 505–514

[14] W. B. F. Mackay, R. L. Dowdell, Metal Progress, 56 (**1949**), 331–336, 404, 406

[15] P. O'Keefe, Materials and Methods, 33 (**1951**), 90–104

[16] T. P. Fisher, British Foundryman, 66 (**1973**), 71–83

[17] R. F. Shyu, C. T. Ho, Journals of Materials Processing Technology, 171 (**2006**) 3, 411–416

[18] H. Xu, Q. Han, T. T. Meek, Materials Science and Engineering: A, 473 (**2008**) 1–2, 96–104

[19] F. Taghari, H. Saghafian, Y. H. K. Kharrazi, Materials & Design, 30 (**2009**) 5, 1604–1611

[20] A. A. Fernandez-Bremauntz, M. R. Ashmore, Atmospheric environment, 29 (**1995**), 525–532

[21] P. G. Flachsbart, Journal of exposure analysis and environmental epidemiology, 5 (**1995**), 473–495

[22] R. V. Vanden Berg, Product Engineering, 22 (**1951**), 179–186

[23] W. D. Stewart, Mechanical Engineering, 75 (**1953**), 450–455

[24] F. H. Froes, Journals of Materials & Design, 10 (**1989**) 3, 110–120

[25] J. Jennings, J. E. Gould, Welding Journal, 87 (**2008**) 10, 26–30

[26] Energy consumption Trend in Transport Sector: 2-2-1. Analysis on private passenger cars' contribution to the total energy consumption. Home page provided by the Energy Conservation Center, Japan, http://www.eccj.or.jp/transportation/2-1-1.html

[27] M. Surappa, Sadhana, 28 (**2003**) 1, 319–334

[28] U.S. Department of Energy (DOE), Aluminum Project Fact Sheet: Dynamic Inert Metal Anodes, 2001 Office of Industrial Technologies, Washington D.C., 2001

NANOTECHNOLOGY FOR BALLISTIC MATERIALS: FROM CONCEPTS TO PRODUCTS

NANOTEHNOLOGIJA ZA BALISTIČNE MATERIALE: OD IZHODIŠČ DO PROIZVODA

Víctor M. Castaño, Rogelio Rodríguez

Centro de Física Aplicada y Tecnología Avanzada, Universidad Nacional Autónoma de México, Boulevard Juriquilla 3001, Santiago de Querétaro, 76230 Querétaro, México
castano@fata.unam.mx

The main trends and materials in protection technologies are briefly reviewed, emphasizing the properties and limitations of p-aramid fibres, widely used in armour systems, particularly in terms of their susceptibility to UV radiation, humidity and chemical attacks. Then, a novel nanotechnology capable of effectively diminishing these effects is described, as well as its application for an actual commercial ballistic vest.

Keywords: nanotechnology, ballistic materials, aramid fibres, bullet-proof materials, nanoparticles, degradation

Podan je pregled glavnih usmeritev in materialov v tehnologijah zaščite s poudarkom na lastnostih in omejitvah p-aramidnih vlaken, ki se uporabljajo v oboroževih sistemih s poudarkom na njihovo občutljivost za UV-sevanje, vlago in kemični napad. Nato so opisane nove nanotehnologije, ki so sposobne zmanjšati te vplive, kot tudi njihova uporaba pri dejanskem komercialnem balističnem telovniku.

Ključne besede: nanotehnologija, balistični materiali, aramidna vlakna, neprebojen material, nanodelci, degradacija

1 INTRODUCTION: THE WORLD OF PROTECTIVE MATERIALS

Protection represents an important industry, both economically and socially speaking, that includes, in the broad sense, industrial, laboratory, home and, of course, military protection, with an enormous variety of products, from simple plastic gloves to sophisticated and confidential military armour. It is considered a "fragmented industry", in spite of the high volumes involved, for literally thousands of manufacturers of raw materials, producers of finished goods, distributors at all scales, consultants, etc., operating worldwide with a steady growth rate of around 3 % annually.[1–10] In particular, the materials that may be used for personal garment have attracted a great deal of attention in the past few decades. In fact, in December (2003), U.S. Attorney General John Ashcroft instructed the National Institute of Justice to implement a new initiative *"to address the reliability of body armour...and to examine the future of bullet-resistant technology and testing..."*[2,11–17]

In the particular area of protective materials, thanks to the technological breakthrough of the 1960s that will be discussed later on, the share of the market for high-performance fibres for garment applications of one single company (Dupont) is 60 %, whereas Honeywell has 30 % and Toyobo, with the most recent technologies, has 5 %.[3–17]

Nanotechnology is already a subject taught not only at universities but also at the industrial level, while the capacities of creating new nanomaterials have been explored only in part.[18–32]

In the sections below we will focus, among all the ballistic conceivable materials, on those intended for personal protection, particularly on the ballistic vests and related gadgets.

2 MODERN TRENDS IN BALLISTIC MATERIALS

Today's generation of body-armour systems can provide protection at various levels designed to defeat most common low- and medium-energy handgun rounds. However, currently the highest-threat-level ballistic needs in the market are fulfilled by special, high-performance ceramics that tend to be very costly, fragile for standard handling, extremely heavy and very difficult to shape to the requirements of an ergonomic design.[3–5] The search for novel polymer-based armour materials dates back to the invention of synthetic macromolecules. Accordingly, some companies have recently publicized some nanofibre-reinforced systems that are expected to provide very attractive weight/protection relationships not only for personal equipment, but also for belly plates for motor vehicles and even aircrafts[5], exposed to the impacts caused by dust, birds and other objects, not necessarily by combat conditions, offering an interesting potential market for novel ballistic materials.

From the military point of view and according to a recent report[3], nanotechnology offers two important

advantages: first, the potential to achieve high degrees of miniaturization, which will be reflected in the weight of the equipment and second, the possibility of finding unexpected effects at the nanoscale, which not only will represent a strategic advantage over the enemy, but will also include a possibility of concealing the technology behind a given effect.

According to this view, a list of potential applications of nanotechnology for equipping the soldiers of the XXIst century is limited only by imagination, at least according to the Massachusetts Institute of Technology's Institute for Soldier Nanotechnologies, which includes 56 specific projects divided into 7 work teams,[3] one of them dedicated to energy-absorbing materials, an area of obvious relevance for the use of nanoparticles and nanostructured composites, in addition to "smart" materials, of course[4].

3 KEVLAR: A TRUE TECHNOLOGICAL REVOLUTION

The modern history of ballistic polymers begins with Stephanie Kwolek's 1966 patent on Kevlar, a para-aramid, invented while working with Dupont.[6] Chemically speaking, the "para" configuration allows the formation of fibres, as opposed to the "cis" one that is sterically hindered due to the large aromatic groups of the structure. Thus, the discovery of the properties of this molecular configuration has led to the development of a whole family of high-performance polymeric materials: the so-called p-aramids. In particular, Kevlar certainly represents a technological revolution not only for armour materials, but for many other important applications, from brake lining to space vehicles, including boats, parachutes, building materials, etc. From the chemistry standpoint, Kevlar is an aromatic polyamide, produced with a condensation reaction of para-phenylenediamine and terephthaloyl chloride, yielding a product with a chemical composition of poly-para-phenylene terephthalamide (PPD-T), having the technical name of Kevlar. It is known that aromatic and amide groups of the type contained in the structure of PPD-T provide a high mechanical and thermal strength. One of the important, and not very well known, facts about Kevlar is that it constitutes a type of liquid crystalline polymer. Indeed, when PPD-T solutions are extruded to produce an actual fibre, the liquid crystalline nanodomains align themselves according to the flow, thus producing a highly anisotropic material, capable of withstanding very high impact energies. For example, the tensile modulus of Kevlar 29, a high-toughness variant used for ballistic vests, is of around 60 GPa, which can be further increased to 130 GPa (Kevlar 49) with thermal treatments under tension, increasing the anisotropy of the crystallites in the material[7]. The aromatic rings in the structure of Kevlar provide a high thermal stability, since the corresponding decomposition temperature is nearly 430 °C.[8] After the success of the original Kevlar formulation, Dupont and a number of other companies have developed a whole family of p-aramids that, along with the other special polymeric materials (e.g., ultra-high-molecular-weight polyethylene –UHMWPE), nowadays constitute the core of the ballistic vest industry.

One very important limitation of Kevlar, however, is its susceptibility to degradation due to UV exposure, environmental humidity and the chemicals contained in perspiration (sweat), the conditions that cannot be avoided during in-field operations. A report by the U.S. Lawrence Livermore Laboratory[9] reveals that Kevlar "is susceptible to photo-degradation from UV light sources". Photo-degradation is a phenomenon, in which the tensile strength of the fibres is reduced as a result of exposure to UV light sources such as sunlight and fluorescent light. Photo-degradation leads to reduced abrasion and tear resistance in aramid fibres such as Kevlar. This problem is so serious that, for example, the User Instruction, Safety and Training Guide provided to the customers by Lion Apparel (Dayton, Ohio, U. S.) gives the following warning:

"Exposure to ultraviolet light (found in the sun's rays and fluorescent light) will severely weaken and damage the fabrics in your protective clothing after only A FEW DAYS. This is especially true for fabrics of the following aramid materials: Hoechst Celanese Pbi, Dupont Kevlar, Dupont Nomex, Dupont Nomex Omega, Dupont Nomex IIIA, Lenzing P84, Southern Mills Advance, and BASF Basofil."

4 NOVEL BALLISTIC FIBRES

One of the most promising recent advances in polymeric materials for protection garments is the Japanese fibre Zylon[10], a poly(p-phenylene benzobisoxazole) (PBO), which has a tensile strength of around twice that of Kevlar and similar commercial p-aramids, such as Twaron (by Teijin Twaron Co.). The amazing properties of Zylon have allowed super light, very comfortable (and very expensive!) vests. However, recent studies[9-12] reveal inherent limitations in terms of its degradation under visible light, heat and, particularly, when exposed to humidity and the chemicals commonly found in sweat, which can lead to a 65 % strength loss over a period of only six months.[10] Sealing the fabric into some thermoplastic does not improve much this effect, even at room temperature, due to the capillarity behaviour of the Zylon fibre.[12] These important limitations, along with the price, have severely limited the use of an otherwise attractive material.
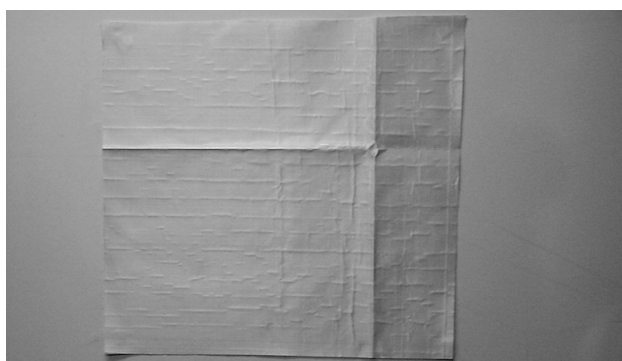
5 STRATUM nanoPROTEC[TM]: NANOTECHNOLOGY IN ACTION

In the above context, armour industry faces an interesting conundrum: the availability of very strong polymeric materials that are highly sensitive to standard

working conditions. A number of solutions have been proposed and tested so far, from protective coatings, to the use of irradiation[13–16] to change the molecular configuration of polymeric materials such as HIPS, Nylon, Kevlar and Zylon and make them less susceptible to the environment, to the humidity coming from both the ambient and, particularly, from the bearer of the vest (i.e., the sweat). The problem is not simple at all, because the treatment or coating must not only preserve the ballistic properties of the system, but also allow a good deal of comfort that can be affected by stiffening the fibres through crosslinking or surface layers of various kinds. The challenge is, thus, too great for the standard technology of ballistic materials, as it can be corroborated by the fact that the leading industries in the field have spent years and enormous amounts of money to produce an environmentally stable garment to no avail.

An opportunity for nanotechnology is then to find a solution using the unique characteristics of nanoscale systems. Indeed, ceramics are known to have a very high resistance to UV degradation, as compared to polymers.[17–30] Their brittleness and specific density, however, prevent their use in a garment. By chemically attaching suitable ceramic nanoparticles to the surface of the fibre, one is able to effectively shield the material against UV without changing any other property. This can be done with a proper reaction between the nanoparticles and the previously modified Kevlar 29 fibre, using an organic coupling agent for the fibre and the particles.[31–34]

The problem of humidity is a more complicated one, since the common paradigm is to offer a *physical* barrier to the water molecules. The obvious difficulty is to ensure, at a molecular level, that the barrier keeps its integrity during the use, enduring bending, shear and all the typical abuses of a military garment. Chemically functionalized nanoparticles linked to organic structures offer a possibility of presenting a *chemical* barrier to water molecules. This has a number of unique advantages: first, no need to have a 100 % continuous coverage of the surface; second, no danger of detachment as with a

Figure 2: Detail of the fibres
Slika 2: Detajl vlaken

coating, and third, no change in the other relevant physical and chemical properties of the fibre.[34]

The above hypothetical scheme has been applied to an actual armour vest, first commercially produced by Parafly, S. A.,[17] under the trade mark of STRATUM nanoPROTEC™, and currently by QUANTICORP.[33] The proprietary technology includes a multicomponent network, which uses, among other materials, Kevlar 29, to which chemically modified nanoparticles were attached during the fabrication process. Photographs of the modified Kevlar 29 fabric can be appreciated in **Figures 1** and **2**.

In the case of STRATUM nanoPROTEC™, the Kevlar fibres were thermally treated to become ribbon-like fibres that changed, after the weaving, into a cloth with a better resistance to bullet penetration. This improvement is essentially due to an increase in the resistance to fibre openings in the fabric as a bullet penetrates the vest. **Figure 3** displays a photograph of a standard

Figure 1: Overview of Kevlar-based STRATUM nanoPROTEC™ fabric
Slika 1: Videz tkanine STRATUM nanoPROTEC™, ki temelji na kevlarju

Figure 3: Detail of a standard Kevlar fabric using threads with a cylindrical shape
Slika 3: Detajl navadnega kevlarskega tkanja z uporabo niti z valjasto obliko

Figure 4: Photograph of a STRATUM nanoPROTEC[TM] ballistic vest
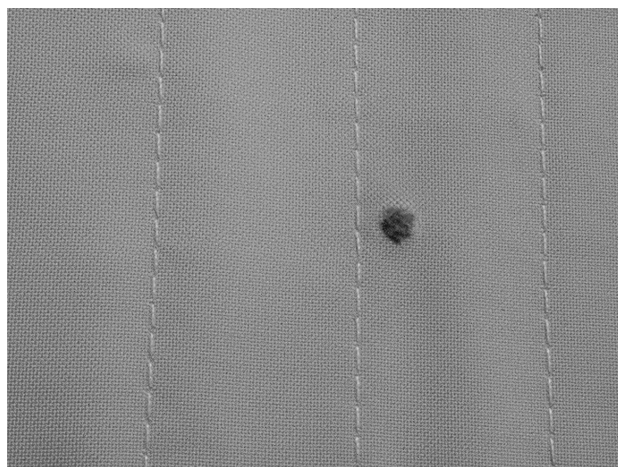**Slika 4:** Posnetek balističnega telovnika STRATUM nanoPROTEC[TM]

Kevlar fabric employing threads with a cylindrical shape, where a clean hole produced by a projectile 9 mm is clearly observed.

STRATUM nanoPROTEC[TM] is then one of the first commercial examples of an effective use of nanotechnology in armour devices. Nanotechnology added very significant UV and chemical resistance to the ballistic performance of the vest, which fulfils the international regulations in the area, being a unique garment. **Figure 4** shows a photograph of a STRATUM nanoPROTEC[TM] vest.

6 CONCLUDING REMARKS

Today, the area of materials for various types of protection represents a unique opportunity for nanotechnology, though perhaps not to develop brand new systems with amazing properties in a short term, but to overcome some of the serious limitations of the current technologies discussed above. Some other desirable features for armour garments can be achieved with current techniques available to many groups working in nanosystems throughout the world. In particular, the development of adequate variations of the nanotechnology products described above, specifically Zylon and other high-performance ballistic fibres,[35] is currently under way and will be reported separately.

Acknowledgements

7 REFERENCES

[1] Market Report, Protective Clothing and Body Armour Industry: Fire, Chemicals and Bullets, Business Communications Co., Inc., 2002

[2] U. S. Department of Justice, National Institute of Justice, Statement regarding body armour safety initiative, December 24, 2003 http://www.ojp.usdoj.gov/ocpa

[3] MIT Institute for Soldier Nanotechnologies, Natick Soldier Centre (http://composite.about.com/gi/dynamic/offsite.htm?site=http://www.iol.co.za/index.php%3Fclick%5Fid=116%26art%5Fid=iol1073473748336F362%26set%5Fid=1)(http://web.mit.edu/isn/research/researchprojects.html)

[4] Ballistic Missile Defence Organization (Department of Defence, U.S.A.) Newsletter, 38, 2001

[5] US Global Nanospace, Inc. (http://www.usgn.com)

[6] http://www1.dupont.com/NASApp/dupontglobal/corp/index.jsp

[7] C. O. Pruneda, W. J. Steele, R. P. Kershaw, R. J. Morgan, Structure-property relations of Kevlar 49 fibers, Department of Energy Report UCRL-85744; CONF-810813-3, 1981

[8] R. J. Morgan, C. O. Pruneda, N. Butler, F. M. Kong, L. Caley, R. L. Moore, Hydrolytic degradation of Kevlar 49 fiber, Department of Energy Report UCRL-89625; CONF-840459-2, 1983

[9] U. S. Nuclear Regulatory Commission Information Notice 2000-12: Potential degradation of fire-fighter primary protective garments, 2002 and references therein

[10] Toyobo PBO Fiber Zylon Technical Information F0461K, 2001

[11] T. Kitagawa, K. Yabukia, R. J. Young, An investigation into the relationship between processing, structure and properties for high-modulus PBO fibers, Part 1. Raman band shifts and broadening in tension and compression, Polymer, 42 (**2001**), 2101

[12] T. Kitagawa, K. Yabuki, An Analysis of Capillary Water Behaviour in Poly-p-Phenylenebenzobisoxazole Fibers, J. Appl. Polym. Sci., 80 (**2001**), 1030

[13] M. Olivares, H. López, G. Vázquez, H. Carrasco, A. Alvarez, E. Oliva, V. M. Castaño, Studies on the effect of γ-radiation on the mechanical properties of nylon 6-12 fibers, Polym. Bull., 36 (**1996**), 629

[14] M. Olivares, A. Mondragón, G. Vázquez, E. Martínez, V. M. Castaño, FT-Raman studies of semi-crystalline nylon 6,12 filaments, Inter. J. Polymer. Mater., 40 (**1998**), 213

[15] C. Menchaca, A. Alvarez, G. Martínez, H. López, H. Carrasco, V. M. Castaño, Mechanisms for the modification of nylon 6,12 by gamma irradiation, Int. J. of Materials & Product Technology, 19 (**2003**), 521

[16] G. Martínez-Barrera, H. López, V. M. Castaño, R. Rodríguez, Studies on the Rubber Phase Stability in Gamma Irradiated Polystyrene-SBR Blends by Using FT-IR and Raman Spectroscopies, Radiation Physics and Chemistry, 69 (**2003**) 2, 155–162

[17] http://parafly.com

[18] X. S. Zekri, L. M. Clayton, A. Kumar, G. Okokbaa, L. Martin-Vega, Long term integration plan of nanotechnology and material science into fourth and fifth grade science curriculum, J. Mater. Ed., 27 (**2005**), 217

[19] A. Otterbein, An approach to K-12 education in the age of networked information, J. Mater. Ed., 20 (**1998**), 167

[20] K. J. Pawlowski, C. P. Barnes, E. D. Boland, G. E. Wnek, G. L. Bowlin, Biomedical nanoscience: Electrospinning basic concepts, applications and classroom demonstration, J. Mater. Ed., 26 (**2004**), 195

[21] D. L. Leslie-Pelecky, G. A. Buck, A. Zabawa, Broadening middle-school student images of science and scientists at the fifth grade level, J. Mater. Ed., 27 (**2005**), 173

[22] K. Cowan, Y. Gogotsi, The Drexel/UPenn IGERT: Creating a new module for graduate education in nanotechnology, J. Mater. Ed., 26 (**2004**), 147

[23] D. Hammer, D. Srikantaiah, Graduate teaching fellows in the classroom: Connecting university research and resources to the K-12 community, J. Mater. Ed., 26 (**2004**), 245

[24] L. C. Klein, Implementing an undergraduate interdisciplinary concentration in nanomaterials science and engineering, J. Mater. Ed., 28 (**2006**), 7

[25] N. Skoulidis, H. M. Polatoglou, Integrated tool for the teaching of structural and optical properties of nanostructures, J. Mater. Ed., 29 (**2007**), 117

[26] D. B. Shieh, C. S. Yeh, W. C. Chang, Y. Tzeng, The integration of biomedical nanotechnology education program in Taiwan, J. Mater. Ed., 29 (**2007**), 107

[27] Y. M. Meyyappan, Nanotechnology education and training, J. Mater. Ed., 26 (**2004**), 313

[28] W. Brostow, W. Chonkaew, T. Datashvili, K. P. Menard, Tribological properties of epoxy + silica hybrid materials, J. Nanosci. & Nanotech., 9 (**2009**), 1916

[29] L. F. Giraldo, W. Brostow, E. Devaux, B. L. Lopez, L. D. Perez, Scratch and wear resistance of Polyamide 6 reinforced with multi-wall carbon nanotubes, J. Nanosci. & Nanotech., 8 (**2008**), 3176

[30] A. Arribas, M. D. Bermudez, W. Brostow, F. J. Carrion-Vilches, O. Olea-Mejia, Scratch resistance of a polycarbonate + organoclay nanohybrid, Express Polymer Letters, 3 (**2009**), 621

[31] M. D. Bermudez, W. Brostow, F. J. Carrion-Vilches, J. Sanes, Scratch resistance of polycarbonate containing ZnO nanoparticles: Effects of sliding direction, J. Nanosci. & Nanotech., 10 (**2010**), 6683

[32] http://www.tradetag.com/c9/c921b4314554145c-company.html

[33] G. Hernandez-Padron, F. Rojas, V. M. Castano, Ordered SiO_2-(phenolic-formaldehyde resin) in-situ nanocomposites, Nanotechnol., 15 (**2003**) 1, 98

[34] A. E. Akinay, W. Brostow, V. M. Castaño, R. Maksimov, P. Olszynski, Time-temperature correspondence prediction of stress relaxation of polymeric materials from a minimum of data, Polymer, 43 (**2002**) 13, 3593

[35] C. González, A. L. Martínez, V. M. Castaño, O. Kharissovaa, R. S. Ruoff, C. Velasco, Polysaccharide nanocomposites reinforced with modified graphene: oxidation and keratin grafting, Ind. & Eng. Chem. Res., 51 (**2012**) 9, 3619–3629

MULTI-FUNCTIONAL K_{Ic}-TEST SPECIMEN FOR THE ASSESSMENT OF DIFFERENT TOOL- AND HIGH-SPEED-STEEL PROPERTIES

VEČFUNKCIJSKI K_{Ic}-PREIZKUŠANEC ZA DOLOČANJE RAZLIČNIH LASTNOSTI ORODNIH IN HITROREZNIH JEKEL

Vojteh Leskovšek, Bojan Podgornik

Institute of Metals and Technology, Lepi pot 11, 1000 Ljubljana, Slovenia
vojteh.leskovsek@imt.si

Depending on the differences in the balanced alloy composition and steel processing technology, the properties of tool and high-speed steel, like temper resistance, hot yield strength, ductility and toughness, thermal fatigue and shock resistance, as well as wear resistance can differ considerably among the same type of steel. A high hot-yield strength, a high temper resistance and a good ductility tend to result in a high resistance to thermal fatigue, while a resistance to mechanical and thermal shocks depends on the ductility and toughness. However, the properties of tool and high-speed steels also depend on the final vacuum-heat-treatment process. Normally, hardness and fracture toughness are used to determine the influence of vacuum-heat-treatment parameters and to optimize them for the specific operating conditions of the tool. However, there are also other tool properties which are equally important and need to be taken into consideration. To determine such a wide range of properties, different test procedures and different test specimens are required since none of the standard tests alone is capable of providing the relevant properties completely. Currently the best overall appraisal of tool and high-speed steel applicability seems to be a combination of fracture toughness, bending or compression testing and in specific cases of impact or small-punch creep tests. The aim of the paper is to show the possibility of using a single K_{Ic}-test specimen for the determination of such a wide range of properties, being important for tool and high-speed steels. Besides that, the usability of K_{Ic}-test specimens for the assessment of technological properties such as nitridability, machinability, wear resistance, etc. was confirmed.

Keywords: tool steel, vacuum heat treatment, characterization, fracture toughness

Odvisno od razlik v sestavi in tehnologije izdelave jekla lahko pri isti vrsti orodnega ali hitroreznega jekla močno variirajo lastnosti, kot so: odpornost proti popuščni krhkosti, natezna trdnost v vročem, duktilnost in žilavost, odpornost proti termičnemu utrujanju in udarcem, kot tudi odpornost proti obrabi. Visoka meja elastičnosti v vročem, velika odpornost proti popuščanju in dobra duktilnost se izražajo v visoki odpornosti proti termičnemu utrujanju, medtem ko sta odpornost proti mehanskim udarcem in termičnim šokom odvisni od duktilnosti in žilavosti. Vendar pa so lastnosti orodnega in hitroreznega jekla odvisne tudi od procesa končne vakuumske toplotne obdelave. Navadno se uporabljata trdota in lomna žilavost za ugotavljanje vpliva parametrov vakuumske toplotne obdelave in za njeno optimiranje pri orodjih, namenjenih specifičnim razmeram pri uporabi. Vendar obstajajo tudi druge lastnosti orodja, ki so enako pomembne in jih je potrebno upoštevati. Za določanje tako širokega področja lastnosti so potrebne različne vrste preizkusov in različni preizkusni vzorci, saj nobena standardna preizkusna metoda ni sposobna ugotavljanja vseh lastnosti. Trenutno najboljše presojanje uporabnosti orodnih in hitroreznih jekel omogoča kombinacija lomne žilavosti, upogibne ali tlačne trdnosti in v posebnih primerih udarni preizkus ali "small-punch" preizkus lezenja. Namen članka je prikazati možnost uporabe K_{Ic}-preizkušanca za določanje različnih lastnosti, pomembnih za orodna in hitrorezna jekla. Poleg tega je bilo potrjeno, da K_{Ic}-preizkusni vzorec omogoča tudi določanje tehnoloških lastnosti, kot so sposobnost za nitriranje, obdelovalnost, obrabna odpornost in druge.

Ključne besede: orodno jeklo, vakuumska toptona obdelava, karakterizacija, lomna žilavost

1 INTRODUCTION

The forming industry is confronted with ever-increasing demands for higher productivity, lower production costs and more complex products, which together with an increased focus on advanced, high-strength, low-weight materials put increased requirements on tools and dies.[1–4] Consequently, this means strengthened property requirements for the tool and high-speed steels, including temper resistance, hot yield strength, ductility and toughness, wear resistance, thermal fatigue and shock resistance.[5,6] Furthermore, with the tool design being pushed to the very limit of the material strength, any unexpected deterioration in the tool material properties will eventually lead to premature and unwanted tool failure. Therefore, tool and high-speed steels are continuously subjected to the development, both in the direction of improved properties as well as better quality with reduced properties' deviation.

Many of the tool- and high-speed-steel grades used today have been developed over a period of several decades. The most significant developments to date are the balanced chemical composition and the introduction of specific, technologically optimised production steps for an optimally annealed condition. Depending on the differences in the balanced alloy composition and the optimised processing route, the material properties can differ considerably among the same type of martensitic tool and high-speed steels. A high hot-yield strength, a high temper resistance and a good ductility tend to result in a high resistance to thermal fatigue. The resistance to mechanical and thermal shocks depends mainly on the

ductility and toughness, but to some extent it is also related to a high yield strength. Finally, the hardness and microstructure will define the friction, the wear and the anti-galling properties of the tool.

All the properties of tool and high-speed steels depend not only on the balanced chemical composition and the processing route, but also greatly on the final vacuum-heat-treatment process, which defines the final microstructure. Real metallic materials, i.e., tool steels, usually have a multi-phase microstructure with carbide precipitates and non-metallic inclusions. When the tools are subjected to loads, local stress concentrations will occur next to these hard, non-deformable, wear-resistant particles, which, if stresses cannot be released through micro-yielding of the matrix, will accelerate tool breakage.[7–9] Traditionally, a trade-off between a tough matrix and hard, wear-resistant carbide precipitates was required. Vacuum heat treatment, on the other hand, allows the optimization of the tool-steel microstructure, which satisfies ever greater demands on the properties of tools and dies, particularly in respect of a greater fracture toughness, while maintaining or even increasing the hardness and wear resistance.[10] In this respect the hardness and fracture toughness, K_{Ic}, were found to be the most suitable parameters when optimizing the final vacuum heat treatment of tool and high-speed steels.[11]

Despite the enormous variety of tooling operations, some basic properties of tool materials are common to almost all applications. These properties are the ductility, toughness and hardness.[8,10,12] Ductility and toughness prevent instantaneous fracture of the tool or tool edges due to local overload, while a high hardness prevents any local plastic deformation. However, ductility, toughness and hardness are more or less mutually exclusive properties, which means the prevention of instantaneous tool failure is often connected with a critical hardness level that must not be exceeded in a specific application. On the other hand, a low hardness may lead to a premature thermal shock, despite the associated high toughness level. Therefore, for a given hardness, the ductility and toughness of the tool should be as high as possible to ensure a good cracking resistance.[10]

Besides hardness, ductility and toughness there are also other tool steel properties that are becoming equally important as we move towards more and more complex tools. These include creep and wear resistance, bending strength, elastic properties under bending as well as compressive properties at room and elevated temperatures. Finally, the time and costs required to produce a tool depend on the technological properties, like high-speed machinability, grindability, nitridability, etc. Although all these properties can be determined using standard test methods, each one requires specific and often quite unique test specimens, which are expensive and not always easy to produce. Furthermore, different geometries of standard specimens mean different heat-treatment conditions, which makes it practically impossi-

ble to directly correlate the properties of tool and high-speed steels after the final heat treatment.

Therefore, the aim of this research work was to determine the applicability of a single K_{Ic}-test specimen for the determination of a very wide range of properties in the final heat-treated condition, which are important for tool and high-speed steels. Furthermore, work is intended to show the potential of K_{Ic}-test specimens for optimizing the final vacuum heat treatment of tool and high-speed steels.

2 RELEVANT TOOL STEEL PROPERTIES

2.1 Ductility, toughness and hardness

Ductility and toughness were found to be the most relevant properties in terms of the resistance to total failure of tool and high-speed steels, being a result of mechanical or thermal overloading.[8,12] However, these are two different material properties, even though both are too often referred to as toughness since the opposite of both is brittleness. Unfortunately, no standardised tests for the determination of toughness or ductility are in common use and although some data are available, the use of different test methods leads to confusion. The importance of ductility and toughness for tool-steel performance depends a lot on the tool geometry.[12] In the case of smooth un-notched surfaces the ductility and the fracture stress are the relevant material properties. However, if sharp notches or cracks are present, which is more critical, the toughness is the most relevant property. From this point of view, tool and high-speed steels should be optimised in terms of ductility for the un-notched regions, and in terms of toughness for the notched regions.

The most reliable measure of toughness is the plain-strain fracture toughness. The same value of fracture toughness should be found for specimens of the same material but with different geometries and with a critical combination of crack size and shape and fracture stress. Within certain limits, this is indeed the case, and information about the fracture toughness can be used to predict the failure for different combinations of stress and crack size and for different geometries.[13] Although standardized methods for a fracture-toughness determination are available,[14,15] their applicability is limited in the case of hard and brittle materials, such as tool and high-speed steels.[10,11,16] Due to the high notch sensitivity, the manufacture of a sharp fatigue crack is difficult and expensive. On the other hand, a method based on a circumferentially notched and fatigue-precracked tensile specimen[17,18] (**Figure 1**) has been found to be the most promising alternative method.[11,17,19] The fatigue crack in the specimen can be obtained without producing any disturbing effect on the fracture toughness of the steel if such a crack is obtained in the soft-annealed condition, i.e., prior to the final heat treatment.[19]

274

The advantage of the K_{Ic}-test specimen over the standardized CT specimen (ASTM E399-90) lies in the radial symmetry, which makes the specimen particularly suitable for studying the influence of the microstructure on the fracture toughness. The advantage relates to the heat transfer, which provides a completely uniform microstructure.[19,20] Furthermore, in the case of K_{Ic}-test specimens the fatigue crack can be created with rotating-bending loading before the final heat treatment.[11,19] And finally, for K_{Ic}-test specimens, plain-strain conditions can be achieved using specimens with smaller dimensions than those of conventional CT test specimens. Shen Wei et al.[21] proved that for circumferentially notched and precracked round-bar tensile specimens, plain-strain conditions are achieved when $D \geq 1.5$ (K_{Ic} /$R_{p0.2}$)^2 and $L \geq 4 \cdot D$ ($R_{p0.2}$ is the yield stress).

In the case of circumferentially notched and fatigue-precracked tensile-test specimens showing linearly elastic behaviour up to fracture, the fracture toughness K_{Ic} can be calculated using equation (1) [22]:

$$K_{Ic} = \frac{P}{\sqrt{D^3}} \left(-1.27 + 1.72 \frac{D}{d} \right) \qquad (1)$$

where P is the load at failure, D is the outside non-notched diameter, and d is the diameter of the instantly fractured area, i.e., the diameter of the ligament next to the crack. Eqn. (1) is valid as long as the condition $0.5 < d/D < 0.8$ is fulfilled. It is known that the fracture toughness of conventionally produced tool steels depends on the specimen orientation.[23] It is the highest for crack propagation perpendicular to the rolling direction and the lowest for a crack propagating along the rolling direction. Therefore, the way how specimens are taken from the master block is very important and to be on the conservative side specimens should be taken in a short transverse direction.

Besides toughness also the hardness of tool and high-speed steels greatly depends on the vacuum-heat-treatment procedure, with both properties being mutually related. The hardening mechanism is different for as-quenched and fully-heat-treated tool steels. In the as-quenched tool steel, mostly the work-hardening and solid-solution hardening affect the steel's hardness. Tempering then leads to the precipitation of carbide particles and a significant decrease of the carbon content in a solid solution of martensite as well as of the density of dislocations. Thus, the hardness of fully-heat-treated tool steels is mainly the result of precipitation hardening and, to a small extent, solid-solution hardening. A high hardness is required to facilitate a high resistance to plastic deformation and wear. However, with a high hardness the toughness is reduced, which can lead to cracking. Therefore, for a given hardness level, the fracture toughness of tool and high-speed steels should be as high as possible to ensure a good cracking resistance.

2.2 Bending strength

The standard bend testing, which is widely used to measure the bending fracture strength of tool and high-speed steels is considered to be the most reliable and to give a great deal of information regarding the toughness and the ductility of the material. According to the ASTM E290-09 standard,[24] bend testing can be performed under 3- or 4-point loading. The bending moment diagrams show that for each mode compression stress is present on the concave side of the specimen, which for the 4-point mode is constant in a central span between the two inner supports, the opposite to the peak concentration under the central support of the 3-point method. Stresses under bending can be calculated using simple conventional theory, but only if the stress throughout the specimen remains below the limit of proportionality. If the limit of proportionality is exceeded than the calculated stress will be higher than the actual stress, which in the extreme case of fully plastic deformation reaches 1.5 times the actual stress value.

Hoyle and Ineson[25] showed that by progressively correcting the calculated stress, taking into account the limit of proportionality, a curve similar to the tensile curves can be obtained. An analysis of such a corrected curve can provide data related to the toughness properties, and more important, the behaviour of tool and high-speed steels. By performing experiments in the elastic region of high-speed steel, it was found that the test can discriminate between the elastic behaviour of good and bad specimens.[25] This can be quantified by using an empirical relationship L/ϕ, the ratio of the actual limit of proportionality L to the fracture stress ϕ, taken at a given hardness. Another parameter obtained from the bending-test curve is the amount of plastic deformation, or more correctly the deformation beyond the limit of proportionality. This parameter is used to determine the energy to fracture. Finally, with bend testing the modulus of elasticity is also obtained.
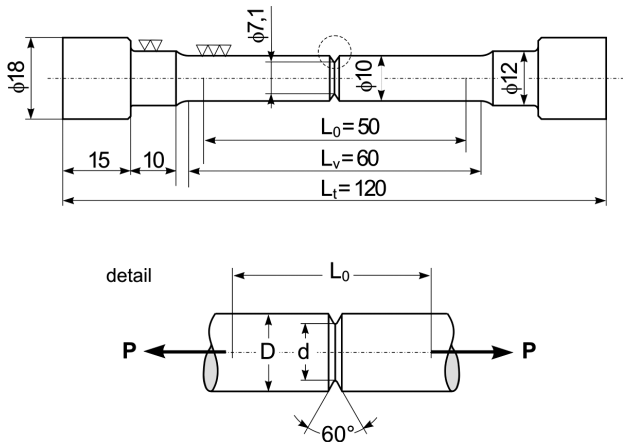
Figure 1: Circumferentially notched and fatigue-precracked K_{Ic}-test specimen (all dimensions are in milimeters)
Slika 1: K_{Ic}-preizkušanec z obodno zarezo in utrujenostno inicialno razpoko (vse dimenzije so v milimetrih)

2.3 Compression properties

For tool and high-speed steels in the hardened and tempered condition the compression properties are considered to be of far greater importance than the tensile properties. Namely, their ductility in the hardened and tempered condition is low and therefore not easily revealed in a tensile test. The compression properties of tool and high-speed steels at room and elevated temperatures can be determined using standard test methods ASTM E9-09 [26] and ASTM E209,[27] respectively. The parameters obtained from the compression test include the compressive strength, the compressive yield strength and the strain-hardening exponent. Compressive strength correlates with the hardness of tool steel, while the strain-hardening exponent describes its ductility.

2.4 High-speed machinability

The trend among toolmakers is to abandon the old strategy of roughing and machining a piece of steel, hardening it, finishing and grinding it, eroding features impossible to cut, and polishing the surfaces. With the introduction of high spindle-speed machines, which can create an excellent surface finish that needs little or no polishing, toolmakers prefer high-speed machining (HSM) in hardened conditions. In the case of HSM complex tool geometries can be machined in a single operation, thus eliminating many time-consuming operations and reducing costs. Since HSM combines the roughing, semi-finishing, and finishing operations of hardened steel, spindles with high speed to allow fine step-overs for finishing and with an adequate amount of torque for roughing are required. Today, the HSM of hardened and tempered tool and high-speed steels with an uninterrupted cut is possible up to a hardness of about 65–67 HRc.[28]

HSM is different from conventional machining and to make it work a completely new philosophy needs to be adopted.[29] The understanding begins with the definition of high-speed machining. Rather than using the conventional definitions based on spindle speed, tool-tip speed, or bearing ratio, it has to be defined in terms of frequency. According to this, HSM occurs as the tooth-pass frequency approaches a substantial fraction of the dominant natural frequency of the machine-tool system.[29] A definition based on tool-pass frequency gives engineers a tool for eliminating chatter and its deteriorating effect on tool wear, surface finish, and machine life. Machinability as well as the HSM of different tool and high-speed steels can vary considerably. Factors largely influencing the machinability of tool steels are the chemical composition, the microstructure, the hardness, non-metallic inclusions and residual stresses. However, the main factor generally regarded as influencing the machinability of a tool steel is its hardness. The harder the material is and the more carbides it has the more difficult it is to machine.

2.5 Grindability

As grinding is an important operation in the final production of many components from tool and high-speed steel, the grindability of the material in the hardened and tempered condition can have important consequences for productivity and economics. Tool and high-speed steels have a high hardness and wear resistance, which makes them difficult to grind, especially when using aluminium-oxide wheels. Furthermore, high temperatures generated during the grinding of tool and high-speed steels lead to thermal damage in the form of surface oxidation, softening, tensile residual stress generation and re-hardening.[30] Therefore, one needs to differentiate between thermal sensitivity, a material's tendency to be damaged at high temperatures, and grindability, the material's effect on the cutting ability of the abrasive grits.[31]

Hardened and tempered tool and high-speed steels are composed of tungsten-molybdenum carbides ($\approx$1400 HV) and vanadium carbides ($\approx$3300 HV) in a matrix of martensitic steel. It was found that the vanadium content and the size of the vanadium carbides are the dominant factors affecting the grindability of high-speed steel.[32] According to König and Messer[33] grindability can be expressed by the G-factor, i.e., the ratio of ground material volume to grinding wheel volume lost. By taking the equivalent carbide content (ECC), based on the stoichiometric sum of the carbide-forming elements in mass fractions w (ECC/% = w(W) + $1.9 \cdot w$(Mo) + $6.3 \cdot w$(V)), it was shown that the G-ratio is decreasing with increased ECC.[33] When comparing conventional and powder metallurgy (P/M) tool steels the G-ratio for latter can be up to 7 times higher, thus indicating better grindability.[34] In this case better grindability is the result of a smaller carbide size found in the P/M steels.[32]

Besides the G-ratio, being an adequate way to measure grindability, the rate of power increase represents a more meaningful measurement. Quantitatively, the machinability and grindability can be determined on the basis of a tribological evaluation as well as by measuring the forces during cutting or grinding.[35] Thus, the instrumented wedge grinding test (WGT),[36] involving the measurement of grinding forces in the tangential and radial directions as well as the contact zone temperature, gives the capability of characterizing the material behaviour resulting from the grinding operation.

3 EXPERIMENTAL

3.1 Material and vacuum heat treatment

To demonstrate the applicability and potential of K_{Ic}-test specimens (**Figure 1**), ESR high-speed steel AISI M2 (delivered in the shape of rolled, soft-annealed and peeled bars ϕ20 mm × 4000 mm) with the following chemical composition (mass fractions): 0.89 % C, 0.20 % Si, 0.26 % Mn, 0.027 % P, 0.001 % S, 3.91 % Cr, 4.74 %

Table 1: Tempering temperatures used in the vacuum furnace
Tabela 1: Temperature popuščanja v vakuumski peči

Tempering temperature (°C)	500	520	540	550	555	560	580	600	630
K_{Ic}-test specimens group A T_A = 1180 °C	A1	A2	A3	A4	–	–	A7	A8	A9
K_{Ic}-test specimens group B T_A = 1230 °C	B1	B2	B3	B4	B5	B6	B7	B8	B9

Mo, 1.74 % V, and 6.10 % W was used. K_{Ic}-test specimens were cut from the delivered bars in the direction of rolling and due to the high notch sensitivity of the hardened high-speed steel, a fatigue pre-crack of about 0.3 mm was created prior to the final heat treatment using a rotating-bending loading. All the K_{Ic}-test specimens were then quenched in a horizontal vacuum furnace, using N_2 at a pressure of 5 bar. After the last preheat the specimens were rapidly heated (25 °C/min) to the austenitizing temperature of 1180 °C or 1230 °C, soaked for 2 min and then gas quenched to a temperature of 80 °C. Finally, high-pressure, gas-quenched K_{Ic}-test specimens were double tempered for 1 h, which was carried out in the same furnace at 9 different tempering temperatures (**Table 1**). For each tempering temperature at least 16 K_{Ic}-test specimens were prepared.

3.2 Material properties evaluation

The fracture-toughness measurement on the K_{Ic}-test specimens was performed at room temperature using an Instron 1255 tensile-test machine and a special specimen fixture, which provided complete axiallity of the tensile load. The cross-head speed was 1.0 mm/min, the speed used for standard tensile-test specimens. During each tensile test the tensile-load/displacement relationship until failure was recorded, which for all K_{Ic}-test specimens investigated showed linearly elastic behaviour, thus confirming the validity of Eqn. (1).

After the tensile test the notch-section diameter d and the radial distance of the crack initiation site from the fatigue crack frontline x were measured for each fractured surface using an optical microscope. The analysis of the fractured surfaces was followed by a Rockwell-C hardness (HRc) measurement, performed on each half of the individual K_{Ic}-test specimen using a Wilson 4JR hardness machine.

One half of the fractured K_{Ic}-test specimen was then used to make a cylindrical 4-point bending-test specimen (ϕ5 mm × 60 mm), with the bending test carried out according to the ASTM E290-09 standard.[24] The 4-point bending-test specimens were prepared by high-speed turning, using Sandvik SNMG 120408 K15 cutting inserts, a feed rate of 0.1 mm/r, a depth of cut of 0.15 mm and a cutting speed of 100 m/min.[28] After high-speed turning, cylindrical specimens were further ground by high-speed, centreless grinding (HSCG, v_g = 63 m/s) in order to obtain the prescribed average surface roughness of 0.2 μm. During the preparation of the 4-point

bending-test specimens, high-speed turning and grinding procedures were also used to evaluate the high-speed machinability and grindability of the investigated high-speed steel. The high-speed machinability was analysed in terms of the evolution of the cutting inserts' flank and the notch wear and appearance of the chips. On the other hand, the effectiveness of the grinding and grindability were assessed on the basis of the final surface roughness, achieved on 4-point bending-test specimens. In spite of the fact that the G-ratio is normally used to measure the effectiveness of the grinding wheel, we rather focused on the quality of the ground surface.

The other half of the fractured K_{Ic}-test specimen was cut 6 mm below the fractured surface in order to prepare a metallographic sample for the fracture and microstructure examination. A further 12.5 mm down compression test specimen (ϕ10 mm × 12.5 mm) was cut from the fractured K_{Ic}-test specimen and tested on an Instron 1255 test machine at room temperature according to the ASTM E9-09 standard.[26] The compression-test results included the compressive yield strength, the compressive strength, the modulus of elasticity and the strain-hardening exponent.

4 RESULTS

4.1 Fractography and metallography

Through an analysis of the fractured surface the main crack-nucleation site can be identified. As shown in **Figure 2a**, the main crack-nucleation site does not coincide with the fatigue crack frontline in the case of high-speed steels.[11] For all the investigated specimens the main crack-nucleation site was found to be slightly away from the fatigue crack, with typical Chevron lines designating the crack initiation and the direction of propagation. Furthermore, no crack re-initiation in the very tip of the existing fatigue crack could be observed. A higher magnification of the crack-nucleation site, denominated also as the weak spot, revealed the site to be composed of large carbide clusters and strings and a region of dimpled ductile fracture (**Figure 2b**).

The presence of the weak spot leads to an over estimation of the fracture toughness. Blunting of the fatigue-crack tip due to its branching out causes a constraint effect and displaces the region of maximum stresses and crack re-initiation from the area close to the surface more into the bulk, ahead of the fatigue-crack frontline.[19] Consequently, the apparent fracture toughness is elevated. In such cases a statistical analysis of the
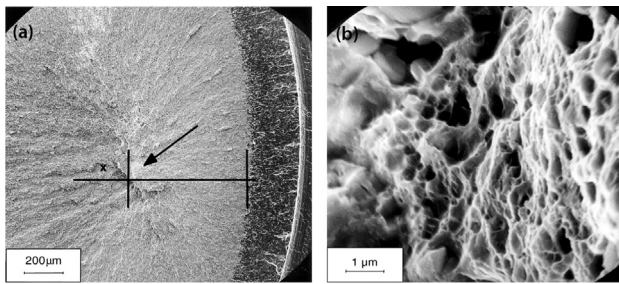
Figure 2: a) Typical fractured surface of a K_{Ic}-test specimen from high-speed steel and b) main crack-nucleation site
Slika 2: a) Značilna površina preloma K_{Ic}-preizkušanca iz hitroreznega jekla in b) mesto nukleacije razpoke

measured fracture toughness vs. the position of the weak spot should be employed. If a linear correlation coefficient R is larger than 0.6 the fracture toughness obtained on a statistically relevant number of specimens (>10) is already the true value. Otherwise, a linear extrapolation to the fatigue-crack frontline (i.e., $x = 0$) should be performed.[19] In the present case, for all specimen groups, the linear correlation coefficient R was between 0.8 and 0.95, thus confirming the validity of the measured fracture-toughness values.

Polishing the fractured surface and the preparation of metallographic specimens reveal the microstructure of the high-speed steel after a particular vacuum heat treatment. Microstructures for K_{IC}-test specimens austenitized from 1230 °C and tempered at temperatures between 500 °C and 600 °C are shown in **Figure 3**. The microstructure of the investigated high-speed steel consists of tempered martensite, fairly well dispersed undissolved eutectic carbides and some stabilised retained austenite in the matrix. The amount of retained austenite is reduced with increased tempering temperature and becomes nearly absent above 580 °C. A lower austenizing temperature of 1180 °C was found to produce a
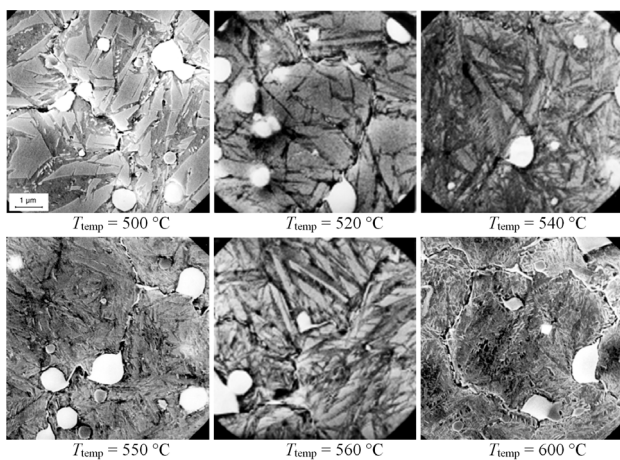
similar microstructure. However, it resulted in a higher volume fraction of undissolved carbide particles, which can be up to three times higher. Quantitative metallography and microscopy, including Scanning Electron Microscopy with Electron Back-Scattered Diffraction (SEM/EBSD), further enable a detailed determination of the eutectic carbide type, size and volume fraction, the cumulative fraction of undissolved eutectic carbides and carbide clusters, and the volume fraction of retained austenite.

4.2 Fracture toughness and hardness

The fracture toughness and hardness values for two austenitizing temperatures are presented in the tempering diagram, shown in **Figure 4**. For both austenitizing temperatures the fracture toughness shows a peak value of more than 15 MPa m$^{1/2}$ at the lowest tempering temperature of 500 °C, which coincides with the relatively high volume fraction of stabilised retained austenite and the low hardness (60–61 HRc). By increasing the tempering temperature the hardness level of the investigated high-speed steel was increasing before reaching a peak value of 64–66 HRc between 560 °C and 570 °C, which was followed by a further decrease in the hardness. However, at about the same hardness, the under-tempered specimens quenched from the same austenitizing temperature, show a higher fracture-toughness value. For example, after vacuum quenching from 1230 °C and double tempering at about 620 °C the investigated high-speed steel achieves a hardness of 63 HRc and a fracture toughness of 8.5 MPa m$^{1/2}$. The same hardness, but with an approximately 30 % higher fracture toughness, can be obtained by using a tempering temperature of ≈510 °C (**Figure 4**). The use of a lower austenitizing temperature results in a reduced hardness and an increased fracture toughness, with the difference becoming more evident at higher tempering temperatures. These results clearly show that the high volume fraction of stabilized retained austenite in under-tempered high-speed steel significantly improves its fracture toughness.
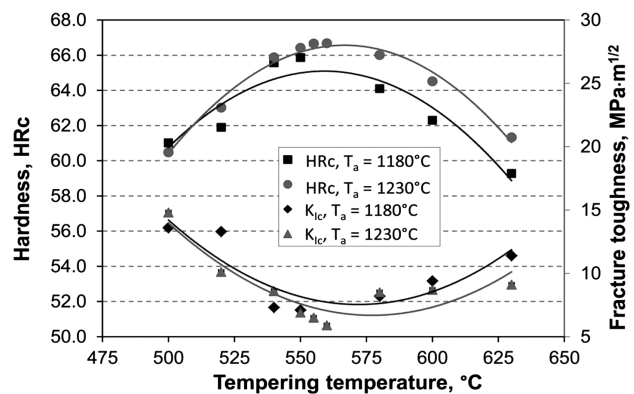

Figure 3: Typical microstructure of group B K_{Ic}-test specimens austenitized from 1230 °C
Slika 3: Značilna mikrostruktura skupine B K_{Ic} preizkušancev, avstenitiziranih iz 1230 °C

Figure 4: Tempering diagram for the investigated AISI M2 high-speed steel
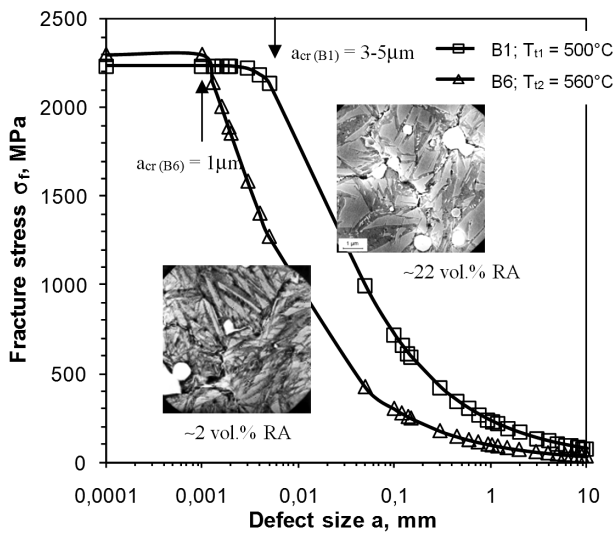**Slika 4:** Diagram popuščanja pri preiskovanem hitroreznem jeklu AISI M2

278

Figure 5: Example of the calculated fracture stress
Slika 5: Primer izračunane napetosti loma

Figure 6: Bending-test results for vacuum heat-treated AISI M2 high-speed steel
Slika 6: Rezultati upogibnega preizkusa za vakuumsko toplotno obdelano hitrorezno jeklo AISI M2

Based on the fracture toughness K_{Ic} and the ultimate tensile stress σ_u, estimated from the Rockwell-C hardness, the fracture stress σ_f can be calculated.[37] A reduction in the fracture stress is observed, when the defect size, represented by carbides and carbide clusters, exceeds a critical value.[10] This gives us a tool to estimate the critical defect size in vacuum heat-treated high-speed steel depending on the austenitizing and tempering temperatures. For example, in the case of an austenitizing temperature of 1230 °C and a tempering temperature of 500 °C the critical defect size is in the range of 3–5 μm, while it is reduced to about 1 μm for a tempering temperature of 560 °C, at the same time showing a faster drop in the fracture stress with the defect size (**Figure 5**).

4.3 Bending and compression strength

The results of the bending and compression tests, performed on 6 groups of specimens (A1, A4, A9, B1, B4 and B9) are shown in **Figures 6** and **7**. The bending strength of the investigated high-speed steel is increasing for both austenitizing temperatures as the tempering temperature gets higher. In the case of an austenitizing temperature of 1180 °C the bending yield strength σ_{yB} and the bending strength σ_B reached maximum values of ≈ 4000 MPa and ≈ 4150 MPa at the highest tempering temperature of 630°C. By increasing the austenitizing temperature to 1230 °C the bending yield strength and the bending strength are reduced by about 15 %, as shown in **Figure 6**.

The compressive strength of the vacuum heat-treated high-speed steel shows the same dependency on the tempering temperature as displayed by the Rockwell-C hardness, with the peak values ($\sigma_{yC} \approx 3000$ MPa, $\sigma_C \approx 3600$ MPa) reached at the intermediate tempering temperature of 550 °C. However, no noticeable difference in the compre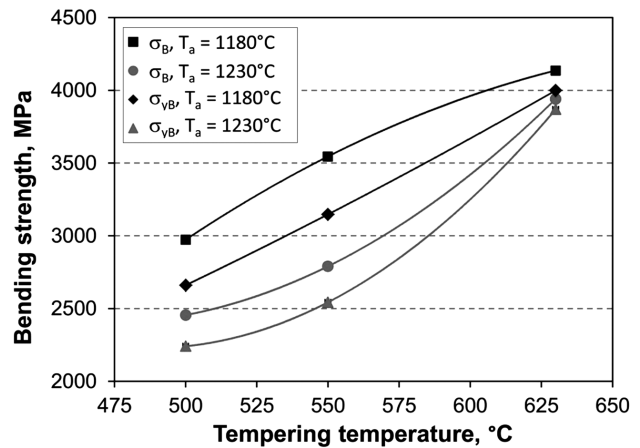ssive strength was observed between the two austenitizing temperatures used (**Figure 7**). On the other hand, the strain-hardening exponent, indicating the ductility of the material, shows a steep decrease with increasing tempering temperature, while an increase in the austenitizing temperature has the opposite effect, as shown in **Figure 7**. The strain hardening exponent of the investigated high-speed steel, austenitized from 1180 °C, was reduced from 0.18 down to 0.04 as the tempering temperature increased from 500 °C to 630 °C. When using a higher austenitizing temperature of 1230 °C the strain-hardening exponent also increased, indicating better ductility. For under-tempered specimens ($T_{temp} = 500$ °C) it increased to 0.31 and for specimens tempered at 630 °C to 0.07 (**Figure 7**).

4.4 High-speed machinability and grindability

In order to evaluate the high-speed machinability behaviour of vacuum heat-treated high-speed steel investigation of cutting inserts was carried out. In the
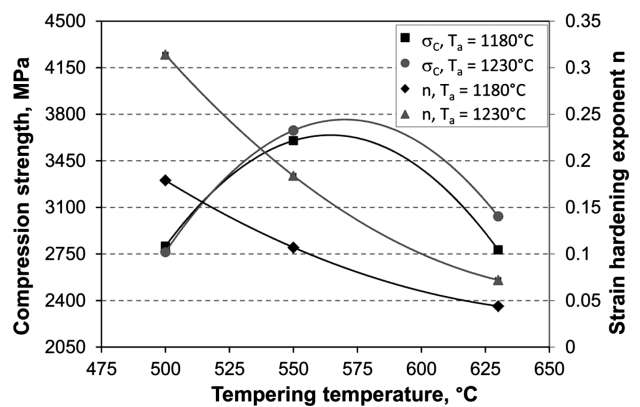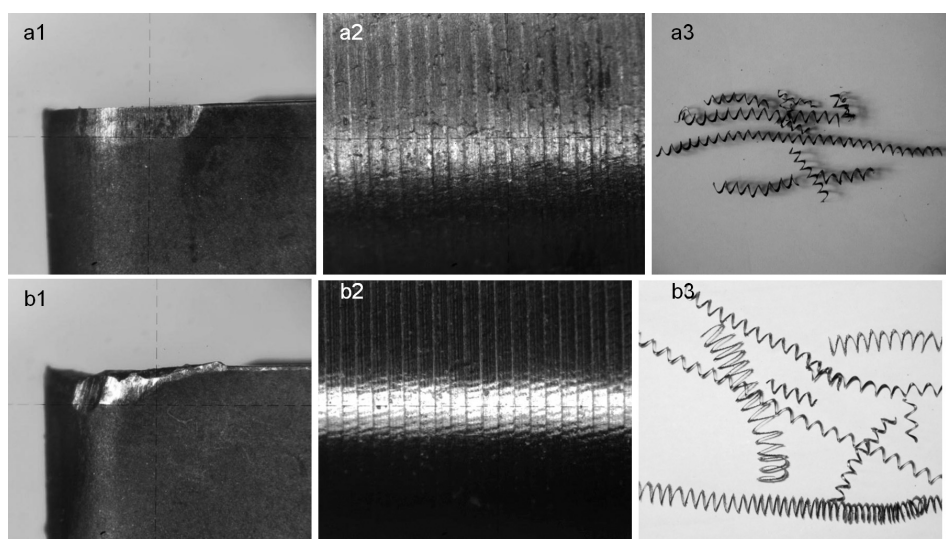

Figure 7: Compression test results for vacuum heat-treated AISI M2 high-speed steel; curves for σ_c are obtained with quadratic regression
Slika 7: Rezultati tlačnih preizkusov vakuumsko toplotno obdelanega hitroreznega jekla AISI M2; krivulje σ_c so dobljene s kvadratno regresijo

Figure 8: High-speed machinability test results for: a) specimen A1 (t = 8.5 mm) and b) specimen A4 (t = 9.2 min); 1) edge of the cutting insert at the end of the test, 2) machined surfaces and 3) associated chips
Slika 8: Rezultati preizkusa obdelovalnosti z veliko hitrostjo za: a) vzorec A1 (t = 8,5 mm) in b) vzorec A4 (t = 9,2 min); 1) rob rezalne ploščice na koncu preizkusa, 2) obdelana površina in 3) pripadajoči ostružki

absence of a systematic observation of the cutting inserts as a function of time the observed difference in the appearance of the cutting inserts at the end of the tool life was used to draw qualitative information. In most cases a stable evolution of the wear along both the rake and flank surface was observed, being a result of one or a combination of the following modes; namely, abrasive wear along with progressive micro-chipping, notching, localized chipping and final destruction of the edge. A comparison of the cutting inserts' worn edge used to machine specimens tempered at 500 °C (A1) and 550 °C (A4), together with the machined surface and the corresponding chips is shown in **Figure 8**. In the case of a worse machinability tendency for notch formation and adhesion of the work material to the cutting insert was evident. However, when the work material adhesion was postponed, as was the case for the specimens tempered at 550 °C (**Figure 8b**), the tool life was sufficiently prolonged ($\approx$10 %). Indirect evidence of better machinability also comes from the appearance of the chips, which for the higher tempering temperature become more continuous, longer and smoother (**Figure 8b**).

From the investigation performed it can be concluded that the high-speed machining of vacuum heat-treated high-speed steel poses no technical problem. However, it was observed that even at a comparable hardness level, the increase in the carbide content observed for the lower austenitizing temperature contributed to a deterioration in the machinability of high-speed steel. At this point it should be pointed out that proper cutting inserts (material and micro-geometry) and cutting conditions have to be selected to achieve the optimal tool life.

In spite of the fact that normally the G-ratio of a grinding wheel is used to measure the grinding efficiency, our focus was on the quality of the ground surface. Therefore, the surface roughness of the 4-point bending-test specimens (A1, A4, A9, B1, B4 and B9) was analysed after grinding. The results are summarized in **Table 2**.

Table 2: Surface roughness after high-speed centreless grinding
Tabela 2: Hrapavost površine po "centreless" brušenju z veliko hitrostjo

Rough-ness	4-point bending test specimen					
	A1	A4	A9	B1	B4	B9
R_a/µm	0.21	0.18	0.19	0.21	0.20	0.18
R_{max}/µm	1.88	1.62	1.82	1.85	1.82	1.81

For the selected high-speed centreless grinding parameters and specimens austenitized from 1180 °C (group A) the smoothest surface with a minimum average roughness of 0.18 µm was reached in the case of specimen A4, tempered at 550 °C. In the case of specimens austenitized from 1230 °C the surface quality was found to improve with an increased tempering temperature, as shown in **Table 2**. In terms of the roughness level, no noticeable difference was observed between the two austenitizing temperatures used. However, SEM microscopy of the surface after high-speed machining and centreless grinding revealed that for a higher austenitizing temperature (group B) the undissolved eutectic carbide particles were pulled out, which was not the case for group A specimens, austenitized from 1180 °C.

5 DISCUSSION

The properties required from the tool and high-speed steels greatly depend on the application and the process the tool will be used for. In some instances the wear resistance is the main concern, requiring a high hardness
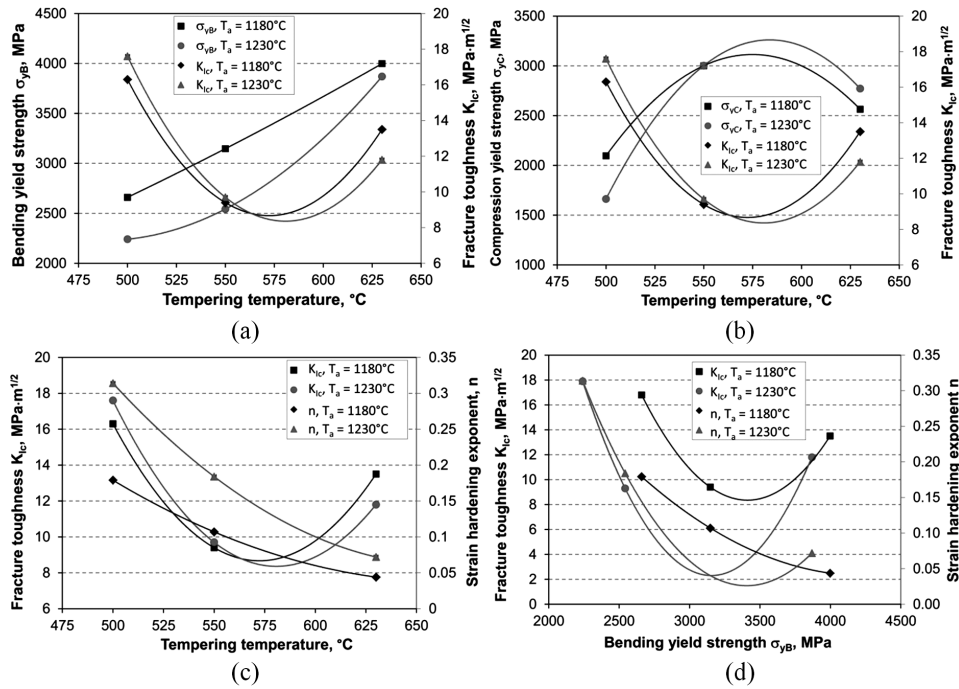
Figure 9: Examples of tempering diagrams combining different properties required from tool material (a–c); a) bending yield strength and fracture toughness, b) compression yield strength and fracture toughness, c) fracture toughness and strain hardening exponent, and d) diagram combining fracture toughness, strain hardening exponent and bending yield strength

Slika 9: Primeri popuščnih diagramov, ki kombinirajo različne lastnosti, zahtevane od materiala orodja (a–c); a) meja tečenja pri upogibu in lomna žilavost, b) meja tečenja pri tlaku in lomna žilavost, c) lomna žilavost in eksponent napetostnega utrjevanja in d) diagram, ki kombinira lomno žilavost, eksponent napetostnega utrjevanja in mejo tečenja pri upogibu

at sufficient fracture toughness, while in others the fatigue properties and the resistance to crack propagation are more important, demanding a high fracture toughness and bending strength. Thus, the combination of different tool properties becomes important and should be optimized for a specific tool through proper vacuum heat-treatment. Besides tempering diagrams displaying the fracture toughness and hardness as a function of the austenitizing and tempering temperatures (**Figure 4**) diagrams combining other tool and high-speed steel properties can also be prepared in order to relate the properties of the material to its performance. For example, when looking for toughness, a properties combination of fracture toughness and bending or compression yield strength should be used (**Figures 9a** and **9b**), and for ductility, a combination of fracture toughness and strain hardening exponent should be used (**Figure 9c**). However, an accurate comparison and correlation of different material properties, as exemplified in **Figure 9d**, combining the fracture toughness, the strain hardening exponent and the bending yield strength is only possible when different specimens are vacuum heat-treated under identical conditions, not only in terms of temperature and time, but more importantly in terms of heat transfer and microstructure uniformity.

As already mentioned, due to the axial symmetry and uniform heat transfer the K_{Ic}-test specimens are particularly suitable for studying the influence of vacuum heat-treatment parameters on the microstructure of metallic materials and consequently on their properties. Since different test specimens can be made from the same K_{Ic}-test specimen, a proper correlation between the different material properties can also be carried out and statistically analysed if using relevant number of K_{Ic}-test specimens.

After measuring the fracture toughness, using the K_{Ic}-test specimen, two halves of the test sample are obtained, as shown in **Figure 10**. Both parts can be used for a Rockwell-C or Vickers hardness measurement. Then, from one of the halves a metallographic specimen (ϕ10 mm × 6 mm) is cut for analysis of the fractured surface and the microstructure just below the fracture.
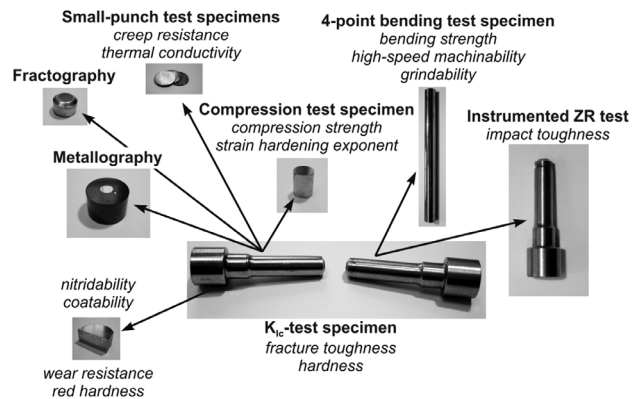
Figure 10: Versatility of K_{Ic}-test specimen
Slika 10: Vsestranskost K_{Ic}-preizkušanca

From the same part of the K_{Ic}-test specimen, also the compression test specimen (ϕ10 mm × 12.5 mm) is cut and used to determine the compressive strength, the compressive yield strength and the strain-hardening exponent, correlating with the ductility of the steels. The remaining can be used for an evaluation of the creep resistance using the small-punch method (ϕ8 mm × 0.5 mm), the thermal conductivity, the wear resistance or for an assessment of technological properties such as nitridability, suitability for hard coating deposition, etc. The other half of the fractured K_{Ic}-test specimen is used to manufacture a 4-point bending test specimen (ϕ5 mm × 60 mm) for an assessment of the bending strength. During the manufacturing the high-speed machinability and grindability in the hardened and tempered conditions can also be evaluated. If bending properties are not required a modified specimen with a circumferential notch ($r = 10$ mm, $z = 1$ mm) for instrumented impact ZR testing[25] can be prepared. An instrumented impact test provides the initial and maximum fracture force, the total fracture time, the time to maximum fracture force, the force-time diagram and the work used. The main advantage of such an impact test lies in the possibility to obtain a single fracture without shattering. This allows further examination of the fractured surface, including X-ray diffraction.

6 CONCLUSIONS

In the present paper the multi-functional K_{Ic}-test specimen is presented. The idea is to minimize the costs for tool and high-speed steel characterization. Due to the fact that none of the standard tests alone is capable of describing all the relevant properties, more than one test is required. Besides this, the test results need to be related to the service behaviour of the tool and high-speed steels.

With the use of a K_{Ic}-test specimen, it is possible to simultaneously assess basic properties such as hardness, fracture toughness, bend and compressive strength etc., which can be directly correlated to the vacuum heat-treatment parameters and microstructure obtained. In this way the heat treatment of the tool and high-speed steels can be optimized for a specific application. The other properties such as wear and creep resistance, machinability, grindability, nitridability, hard-coatings adhesion etc., can be determined and correlated to the microstructure as well as between each other.

As a result of the relatively simple and economical manufacturing of the axially symmetric K_{Ic}-test specimen, a sufficient number of specimens (10–20) for statistical analyses can be produced, allowing an accurate and reliable evaluation of the tool and high-speed steel properties.

7 REFERENCES

[1] R. Ebara, K. Kubota, Failure analysis of hot forging dies for automotive components, Eng. Fail. Anal., 15 (**2008**), 881–893

[2] B. A. Behrens, E. Doege, S. Reinsch, K. Telkamp, H. Daehndel, A. Specker, Precision forging processes for high-duty automotive components, J. Mater. Process. Technol., 185 (**2007**), 139–146

[3] M. Bayramoglu, H. Polat, N. Geren, Cost and performance evaluation of different surface treated dies for hot forging process, J. Mater. Process. Technol., 205 (**2008**), 394–403

[4] L. Lavtar, T. Muhic, G. Kugler, M. Tercelj, Analysis of the main types of damage on a pair of industrial dies for hot forging car steering mechanisms, Eng. Fail. Anal., 18 (**2011**), 1143–1152

[5] R. Seidel, H. Luig, Friction and wear processes in hot die forging, Proceedings of International Conference on Tooling Materials, Interlaken, Switzerland, 1992, 467–480

[6] O. Barrau, C. Boher, C. Vergne, F. Rezai-Aria, Investigations on friction and wear mechanisms of hot forging tool steels, Proceedings of 6th International Tooling Conference, Karlstad, Sweden, 2002, 81–94

[7] K. H. Schwalbe, On the influence of microstructure on crack propagation mechanisms and fracture toughness of metallic materials, Eng. Fract. Mech., 9 (**1977**), 795–832

[8] H. Jesperson, Toughness of tool steels, Proceedings of 5th International Conference on Tooling, Leoben, Austria, 1999, 93–102

[9] U. Krupp, Fatigue Crack Propagation in Metals and Alloys: Microstructural Aspects and Modelling Concepts, John Wiley & Sons, Weinheim 2007

[10] V. Leskovsek, B. Sustarsic, G. Jutrisa, The influence of austenitizing and tempering temperature on the hardness and fracture toughness of hot-worked H11 tool steel, J. Mater. Process. Technol., 178 (**2006**), 328–334

[11] V. Leskovsek, B. Ule, B. Liscic, Relations between fracture toughness, hardness and microstructure of vacuum heat-treated high-speed steel, J. Mater. Process. Technol., 127 (**2002**), 298–308

[12] R. Ebner, H. Leitner, F. Jeglitsch, D. Caliskanoglu, Methods of property oriented tool steel design, Proceedings of 5th International Conference on Tooling, Leoben, Austria, 1999, 3–24

[13] M. Janssen, J. Zuidema, R. J. H. Wanhill, Fracture Mechanics, 2nd ed., Delft University Press, Delft, Netherlands 2002

[14] ASTM E399-90: Standard Test Method for Plane-Strain Fracture Toughness of Metallic Materials, 1997

[15] ASTM E1820-11: Standard Test Method for Measurement of Fracture Toughness, 2011

[16] V. Leskovsek, B. Podgornik, Vacuum heat treatment, deep cryogenic treatment and simultaneous pulse plasma nitriding and tempering of P/M S390MC steel, Mater. Sci. Eng., A 531 (**2012**), 119–129

[17] W. Chang, Applying similarity methods to fracture mechanics measurement of fracture toughness K_{Ic}, KQ values by small-scale single specimen, Eng. Fract. Mech., 31 (**1988**), 807–816

[18] W. Chang, An improvement of applying similarity methods to fracture mechanics-measurement of fracture toughness K_{Ic}, KQ values by smallscale single specimen, Eng. Fract. Mech., 36 (**1990**), 313–320

[19] B. Ule, V. Leskovsek, B. Tuma, Estimation of plain strain fracture toughness of AISI M2 steel from precracked round-bar specimens, Eng. Fract. Mech., 65 (**2000**), 559–572

[20] V. Leskovsek, B. Ule, A. Rodic, Development of a modified method for determining fracture toughness of HSS with non-standard cylindrical round-notched tension specimens, Met. Alloys Technol., 27 (**1993**), 195–204

[21] S. Wei, Z. Tingshi, G. Daxing, L. Dunkang, L. Poliang, Q. Xiaoyun, Fracture toughness measurement by cylindrical specimen with ring-shaped crack, Eng. Fract. Mech., 16 (**1982**), 69–92

[22] H. F. Bueckner, Discussion on "Stress analysis of cracks" by P. C. Paris, G. C. Sih, ASTM-STP, 381 (**1965**), 82

[23] H. F. Fischmeister, L. R. Olson, Cutting Tool Materials, Proceedings of International Conference on Cutting Tool Materials, Ft. Mitchell, Kentucky, USA, 1980, 111–118

[24] ASTM E290-09: Standard Test Methods for Bend Testing of Material for Ductility, 2009

[25] G. Hoyle, High Speed Steels, Butterworths & Co., London 1988

[26] ASTM E9-09: Standard Test Methods of Compression Testing of Metallic Materials at Room Temperature, 2009

[27] ASTM E209-00: Standard Practice for Compression Tests of Metallic Materials at Elevated Temperatures with Conventional or Rapid Heating Rates and Strain Rates, 2010

[28] J. Kopac, V. Leskovsek, Minimizing of machining effect on HSS structure characteristics, Proceedings of 7th international tooling conference – Tooling materials and their applications from research to market, Torino, Italy, 2006, 303–311

[29] J. R. Koelsch, High-speed machining: A strategic weapon, Machine Shop Guide, November 2001

[30] L. P. Tarasov, Some Metallurgical Aspects of Grinding, in: Machining Theory and Practice, American Society for Metals, Metal Park, Ohio, 1950, 409–464

[31] L. P. Tarasov, Grindability of Tool Steels, Trans. Amer. Soc. Metals, 43 (**1951**), 1144–1151

[32] J. Badger, Grindability of Conventionally Produced and Powder-Metallurgy High-Speed Steel, Annals of the CIRP, 56 (**2007**), 353–356

[33] W. König, J. Messer, Influence of the Composition and Structure of Steels on Grinding Process, Annals of the CIRP, 30 (**1981**), 547–552

[34] K. Kishi, Y. Ichida, S. Marumo, Effects of Grain Refining of Carbides on the Grindability of High-Vanadium High-Speed Steels, Proceedings of the 25th Japan Congress of Materials Research, Tokyo, Japan, 1982, 171–176

[35] B. Šuštaršič, Composite high speed steel with solid lubricant, Ph. D. thesis, Ljubljana, 2000

[36] H. Chandrasekaran, H. Izadi, O. Johansson, Temperature and thermal damage during grinding of some tool steels, Proceedings of 5th International conference on tooling, Leoben Austria, 1999, 539–549

[37] S. Karagoz, H. Fischmeister, Microstructure and toughness in high-speed tool steels – the influence of hot reduction and austenitization temperature, Steel research, 58 (**1987**), 353–361

NANOSILICA-REINFORCED POLYMER COMPOSITES

POLIMERNI KOMPOZITI OJAČANI Z NANOSILIKO

Marjetka Conradi

Institute of Metals and Technology, Lepi pot 11, 1000 Ljubljana, Slovenia
marjetka.conradi@imt.si

In the fast growing field of nanotechnology, polymer nanocomposites have become a prominent area of current research and development. Silica/polymer nanocomposites are dominating the polymer and composite literature as well as a variety of applications, many industrial products and other significant areas of current and emerging interest. This review will give a general overview of the leading and most commonly used techniques and strategies for the preparation of both silica fillers and silica/polymer nanocomposites, followed by a discussion of the main characterization methods, mechanical testing, properties and applications. Typical examples of different systems will be reported and referred to the corresponding references for more detailed descriptions.

Keywords: nanosilica, polymers, composites

V sklopu hitro razvijajoče se panoge, imenovane nanotehnologija, so dobili polimerni nanokompoziti pomembno vlogo na področju raziskav in razvoja. Polimerni silicijevi dioksidni nanokompoziti dominirajo tako v literaturi, namenjeni raziskavam polimerov in kompozitov, kot tudi v številnih aplikacijah ter industrijskih produktih. V tem preglednem članku se bomo osredinili na splošni pregled vodilnih in najpogosteje uporabljenih tehnik ter strategij za pripravo tako silicijevih vključkov kot tudi polimernih silicijevih dioksidnih nanokompozitov. Sledila bo razprava o glavnih metodah karakterizacije silika/polimernih nanokompozitov, mehanskih preizkusov, o lastnostih ter njihovih aplikacijah. Predstavljeni bodo primeri različnih polimernih silicijevih dioksidnih kompozitnih sistemov skupaj z ustreznimi referencami za podrobnejši vpogled.

Ključne besede: nano silicijev dioksid, polimeri, kompoziti

1 INTRODUCTION

Polymer (nano)composites have been extensively studied over a long period of time. They are generally organic polymer composites mostly filled with inorganic fillers. Their properties combine the advantages of the inorganic filler material (i. e., rigidity, thermal stability) and of the organic polymer (i. e., flexibility, ductility, processability). However, the main advantage of these composites is characterized by the volume fraction and size of the fillers. If the fillers decrease in size from the micro- to the nanoscopic scale, unique properties of polymer nanocomposites are emphasized as the small size of the fillers leads to a dramatic increase in the interfacial area as compared with the ordinary composites. This interfacial area then creates a significant volume fraction of the interfacial polymer with the properties different from the bulk polymer even at low filler loadings.[1,2]

Reinforcement agents such as glass particles,[3,4] ceramic particles,[5] layered silicates,[6–8] metal particles,[9] rubber plastics[10] and thermoplastics[11,12] have already been successfully used. Several researchers have studied the effects of the particle size and volume fraction on the mechanical response of polymer composites.[13–17] There are a few analytical models based on the crack propagation along the particle surfaces taking the interspacing between the particles into account[18] as well as mathematically considered trapping, pinning and bridging of the crack front on the particles.[19–21] It has been shown that the fracture phenomena of the composites filled with nanometer-sized particles differ from the behaviour of the composites filled with micrometer-sized or larger filler particles.

However, among the numerous polymer composites, silica/polymer nanocomposites are the most commonly reported in the literature and are also employed in a variety of applications, such as electronics, automotive and aerospace industries as well as used in many industrial products due to their good mechanical characteristics[22]. In order to further improve the properties of silica/polymer nanocomposites, their preparation, characterization, mechanical properties and applications have become quickly expanding fields of research in the past few years.

The aim of this review is to give a general overview of the leading and most commonly used techniques and strategies for the preparation of both silica fillers and nanosilica/polymer composites, followed by a short discussion of the main characterization methods, mechanical testing, properties and applications. Typical examples of different systems are reported and referred to the corresponding references for more detailed descriptions.
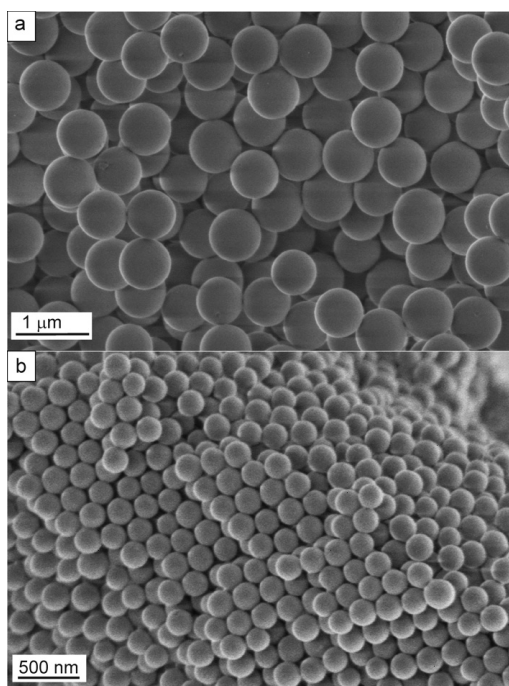
2 PREPARATION OF SILICA FILLERS

Silica particles normally exist in a form of a fine, white amorphous powder or colloid suspension. Its most

important characteristic is an extremely large surface area and a smooth nonporous surface, which can promote a strong physical contact when embedded in a polymer matrix.

Nowadays silica particles are commercially available in all sizes ranging from nanometer to micrometer; however, several researchers still synthetize particles on their own. Two main methods have been developed for silica-particle formation: the sol-gel method and the microemulsion method.[23] In 1968, however, Stöber and Fink[24] introduced a simple synthesis of monodisperse spherical silica particles starting with tetraethyl ortho-silicate (TEOS 98 %), deionized water, ammonia (25 %) and absolute ethanol (99.9 %) as the alkoxide precursor, hydrolyzing agent, catalyst and solvent. In the process, two mother solutions are prepared, one containing ammonia–water, and the other containing TEOS–etha-nol. The two solutions are mixed in a thermostatically controlled water bath (50 ± 1) °C. After 60 min, the resulting spheres are separated from the liquid phase with centrifugation and then ultrasonically dispersed in deionized water. Finally, the particles can be dried in an oven at 50 °C to obtain white powder. Note that using this method, the final particle size critically depends on the reagent concentrations, molar ratio and reaction temperature. As shown in **Figure 1** good monodispersity of silica spheres can be obtained with this method.[25]

The dispersion of silica fillers and, consequently, the compatibility between the polymer and silica have a crucial impact on the mechanical properties of silica/polymer composites. As most of the polymers are hydrophobic in nature, it is important to improve the interfacial interaction between the matrix and silica via silica-surface modification, which can also improve its dispersion in the matrix at the same time. In general, the surface of silica fillers can be successfully modified with either chemical or physical methods.

Modification of silica via a chemical interaction involves a modification of its surface with modifying agents (i. e., silanes) or grafting polymers. The most common way of making silica hydrophobic and polymer compatible, is silanization. We can find a long list of silane coupling agents that generally have hydrolysable and organofunctional ends and can be represented as $RSiX_3$. X stands for hydrolysable groups, typically chloro, methoxy or etoxy gropus, and R stands for the organo group that has to be chosen according to the properties of the polymer. Silanes are attached to the silica surface through the reaction of hydrolysable groups with the hydroxyl groups on the silica surface while the alkyl chains interact with the polymer[26] (**Figure 2**).

Hydrophobicity, on the other hand, can be success-fully increased by grafting the polymer chains to silica particles either with a covalent attachment of end-func-tionalized polymers to the surface or with an in-situ monomer polymerization.

If silica is modified via a physical interaction, the procedure usually involves surfactants or macromole-cules adsorbed onto its surface. In principle, a polar group of surfactants is adsorbed to the surface of silica by an electrostatic interaction. As a consequence, the physical attraction between the silica particles within agglomerates is reduced, making silica particles easy to incorporate into a polymer matrix.[27]

Figure 1: Scanning electron microscopy (SEM) images of SiO_2 particles prepared according to the Stöber procedure, a) 650 nm silica particles, b) 240 nm silica particles[25]
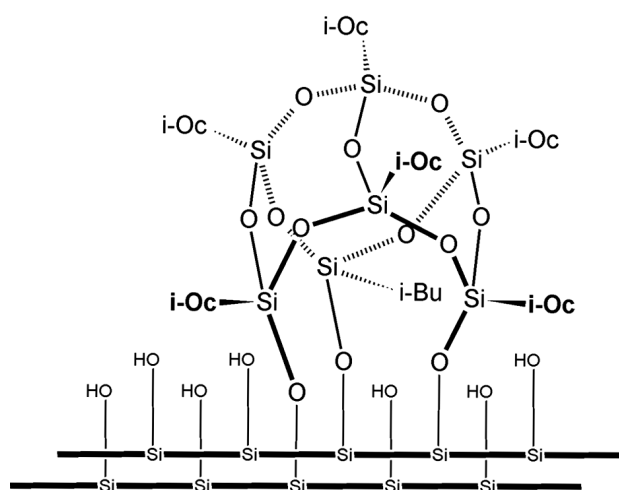**Slika 1:** SEM-slika SiO_2 delcev, sintetiziranih po metodi Stöberja, a) silicijevi delci 650 nm, b) silicijevi delci 240 nm[25]

Figure 2: Schematic presentation of the silica-surface modification by trisilanol heptaisobutyl silesquioxane ($IB_5(SiO_{3/2})_8(OH)_3$) via a cova-lent bonding[26]
Slika 2: Shematski prikaz modifikacije silicijeve površine s trisilanol heptaisobutil sileskvioksanom ($IB_5(SiO_{3/2})_8(OH)_3$) na osnovi kova-lentne vezi[26]

3 COMPOSITE PREPARATION

The main concern in composite preparation is the mixing process and the obtained homogeneous silica dispersion in the polymer matrix. Therefore, prior to the composite preparation, the compatibility between the two components has to be assured to avoid silica agglomeration, using one of the methods described in the previous section.

The simplest method of silica/polymer composite preparation is direct mixing of silica into the polymer matrix, i. e., by melt or solution blending. Besides blending, sol-gel processes and in-situ polymerization are also widely used among the preparation techniques.

3.1 Blending

Melt blending is the most commonly used method in composite preparation due to its efficiency and operability. In the process, the polymer and the inorganic filler (i. e., silica) are sheared in the melt at a temperature equal or greater than the melting point of the polymer. Under suitable conditions the material exfoliates and disperses to the desired extent. This technology is very versatile and can be applied to various polymers.[28–31] It is also possible to add swelling and compatibilizing agents in order to improve the exfoliation and reach a better adhesion between the two major components.

Solution blending, on the other hand, is a liquid-state powder-processing method that allows a good molecular level of mixing. Solution blending can be achieved by either dissolving only the polymer matrix or dissolving both the matrix and the nanoparticles.

3.2 Sol-gel process

The sol-gel process is a synthesis route consisting of the preparation of a sol, the successive gelation and the solvent removal. Within the past decades sol-gel processes have been widely used to synthesize novel organic/inorganic composite materials. In the case of composites, the goal is to carry out the sol-gel reaction in the presence of polymeric molecules (i.e., the organic phase) containing functional groups that improve their bonding to the inorganic phase. This is a very successful reinforcement technique that can generate filler particles within a polymer matrix.

3.3 In-situ polymerization

In-situ polymerization is a very effective and fast way to construct a nanocomposite material. In this method, the fillers are first pretreated with appropriate surface modifiers and then added directly to the liquid monomer during the polymerization stage. Using the solution method, fillers are added to a polymer solution using solvents such as toluene, chloroform and acetonitrile to integrate the polymer and filler molecules.

4 CHARACTERIZATION

A homogeneous distribution of finely dispersed fillers in a silica/polymer composite is a prerequisite for obtaining good mechanical properties of the end material. In a composite, interfacial interaction between the fillers and the polymer matrix plays a crucial role in toughening the composite. In order to achieve a high particle/polymer area and to distribute the mechanical stresses within the composite, the composite has to consist of homogeneously distributed filler particles which are not agglomerated. Therefore, prior to further mechanical testing, the chemical structure, morphology and microstructure of the composites must be analysed.

## 4.1 Infrared and Raman spectroscopy

Infrared and Raman spectroscopy are normally used to confirm the surface modification of the silica fillers implemented in a polymer matrix. Building up a modifier layer around the silica particles can be followed by inspecting the spectra of the filler[32,33] or the vibrational bands of the surface modifier, the intensities of which depend on the number of the filler surface sites occupied by the modifier.

In **Figure 3**, typical IR transmission spectra of the silica-surface modifier trisilanol (IO_7) POSS, polymer polyvinyl chloride (PVC), 30 nm silica/PVC and 130 nm silica/PVC composites are presented.[34] The silanol groups of open-cage POSS do not spontaneously lead to condensation, as silanols of other simple alkoxysilanes, but preferentially interact with the active sites on the surface of the filler.[35] Normally, the bands attributed to trisilanol POSS are weak because the Si-O-Si bands are covered by the same band of silica spheres. However, a closer inspection of the peak intensity of the band at 2907 and 2953 cm^{-1} indicates a progressive occupation of the accessible sites on the silica surface. A comparison of the infrared spectra in the C-H region of trisilanol POSS (**Figure 3** zoom), modified silica/PVC
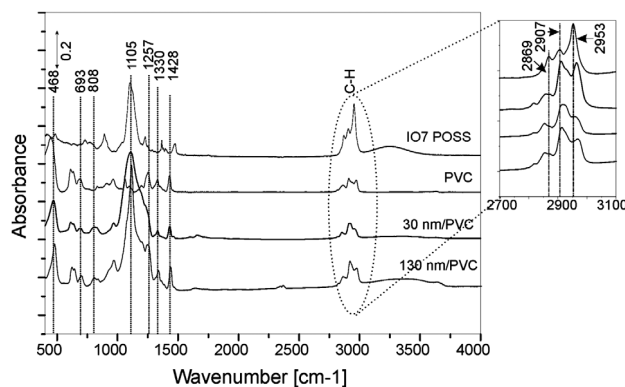
Figure 3: IR transmission spectra of trisilanol (IO_7) POSS, PVC, 30 nm silica/PVC and 130 nm silica/PVC composites[34]
**Slika 3:** IR-transmisijski spektri trisilanola (IO_7) POSS, PVC-ja, kompozitov silicijev dioksid-PVC 30 nm in silicijev dioksid-PVC 130 nm[34]
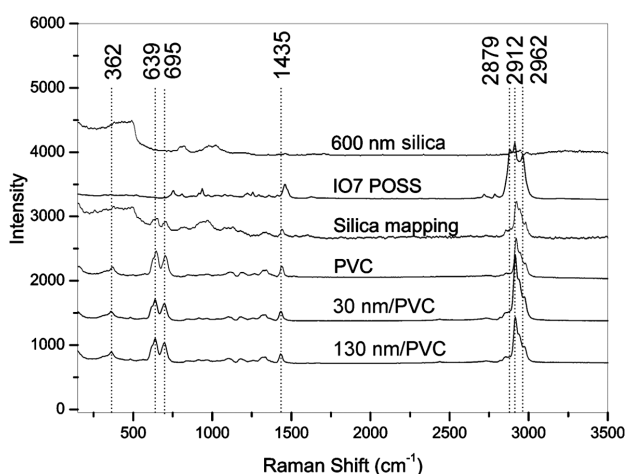
Figure 4: Raman spectra of pure 600 nm silica spheres, trisilanol (IO7) POSS, the average spectrum of silica mapping, pure PVC, 130 nm silica/PVC and 30 nm silica/PVC composites[34]
Slika 4: Ramanski spektri neobdelanih 600 nm silicijevih delcev, trisilanola (IO7) POSS, povprečnega spektra silicijevega mapiranja čistega PVCja ter 130 nm silika/PVC in 30 nm silika/PVC kompozitov[34]

composite and bulk PVC revealed the presence of trisilanol POSS on the silica surface. The C-H band at 2953 cm^{-1} was also present in the spectrum of the bulk PVC and could be seen in the spectrum of the PVC composite as well. Surprisingly, the C-H band at 2907 cm^{-1} surpasses the band at 2953 cm^{-1} because of the presence of isooctyl groups on the surface.
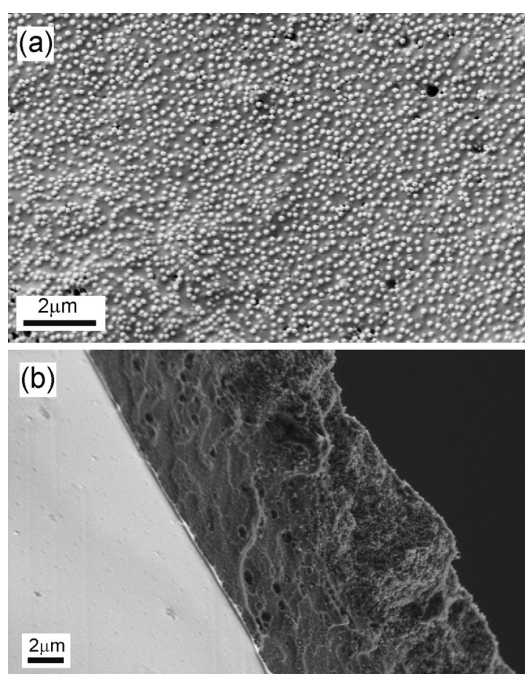
Figure 5: a) Top-view and b) side-view SEM micrographs of a silica/PVC composite composed of volume fraction 30 % of POSS-silanated, 130 nm silica fillers[34]
Slika 5: SEM-pogled: a) z vrha in b) pogled s strani kompozitov silicijev dioksid-PVC, sestavljenih iz volumenskega deleža 30 % POSS-silaniziranih silicijevih dioksidnih vključkov 130 nm[34]

In **Figure 4** typical Raman spectra of composite silica/PVC recorded as a function of the size of silica spheres is presented. In the Raman spectrum of PVC, polarized lines are observed at 639, 695, and 1435 cm^{-1}. The band at 1435 cm^{-1} is assigned to the CH$_2$ scissors vibration and a broad doublet-like band envelope in the region of 600-700 cm^{-1} was attributed to C-Cl stretching vibrations.[36] For comparison, we recorded the Raman spectrum of pure, bulk, 600 nm silica spheres, which have a very weak response in the fingerprint range (i.e., 500–2000 cm^{-1}) and also in the CH region. Inside the composites under investigation, we, therefore, used the mapping of silica spheres. The average spectrum of silica mapping in **Figure 4** indicates a modification of the silica spheres as the spectrum includes the bands of pure silica and the bands of trisilanol IO$_7$ POSS. In addition, PVC has a similar response in the CH region. A successful modification of 30 nm silica/PVC and 130 nm silica/PVC composites was further identified with an elevated band at 2912 cm^{-1}. This band reveals the isooctyl structure of POSS mostly because the other bands are not so strong in the Raman spectra.

4.2 Scanning electron microscopy and transmission electron microscopy

Scanning electron microscopy (SEM) and transmission electron microscopy (TEM) are the most common methods used in the morphology evaluation.

In **Figure 5** we see typical SEM micrographs of POSS-silanated, 130 nm silica/PVC composites. We can see that a 130 nm silica/PVC composite consisted of 3D-ordered silica particles. SEM micrographs also revealed (**Figure 5b**) that the 3D silica-particle structure was ousted towards the film surface, frequently encountered with polymers consisting of two phases with a poor mutual compatibility due to their different chemical compositions. Typical examples are polymers with a low surface energy obtained with an addition of fluoropolymers or fluorosilanes.[37]

Another example of SEM imaging in composite-morphology characterization is an analysis of the fracture surface of a composite filled with a very low amount of silica fillers, i.e., less than volume fraction 1 %. Due to the small amount of silica fillers it is not possible to observe isolated particles or an arrangement of particles as shown previously in **Figure 5**; however, the information on the particle inclusion can be revealed with an analysis of the properties of fracture surfaces.

In **Figure 6** typical fracture surfaces of the neat epoxy and diglycidyl ether of bisphenol A surface-treated, 30-nm and 130-nm silica/epoxy composites are presented.[38] Prior to the SEM imaging the samples were frozen in liquid nitrogen and broken by hand in order to observe the natural crack propagation in the composite. The inclusion of silica fillers in the epoxy matrix is confirmed by an increased roughness of the composite's
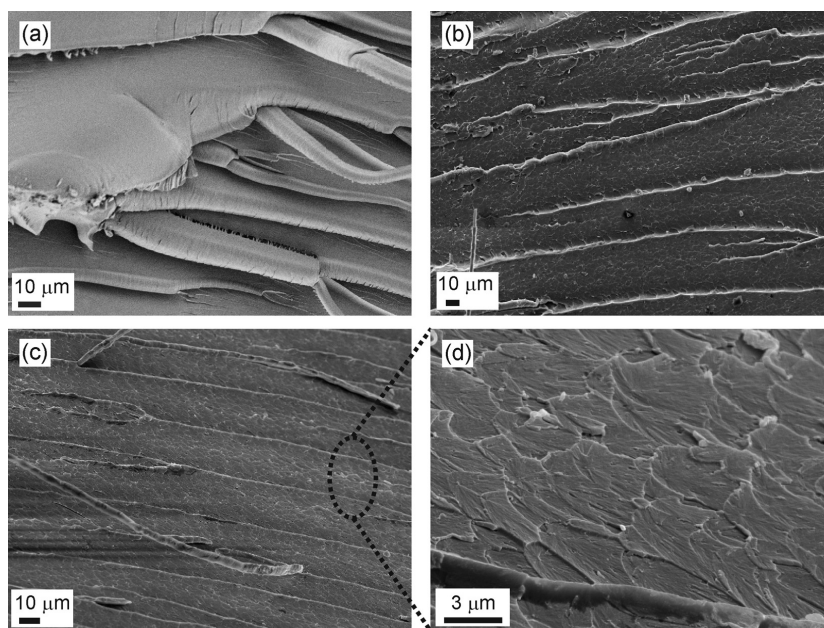
Figure 6: a) Hand broken fracture surfaces of pure epoxy, b) composite with the volume fraction 0.5 % diglycidyl ether of bisphenol A surface-treated, 30-nm silica fillers, c) composite with 0.5 % diglycidyl ether of bisphenol A surface-treated, 130-nm silica fillers and d) a fracture surface detail – a fish-skin-like microstructure – of the 130-nm silica/epoxy composite[38]
Slika 6: a) Lomna površina vzorcev čistega epoxyja, b) kompozita, obogatenega z volumenskim deležem 0,5 % z diglicidil etrom bisfenola A površinsko obdelanih 30-nm silicijevih vključkov, c) kompozita, obogatenega z volumenskim deležem 0,5 % z diglicidil etrom bisfenola A površinsko obdelanih silicijevih dioksidnih vključkov 130 nm in d) detajl lomne površine – mikrostruktura ribje kože v kompozitu silicijev dioksid-epoksi 130 nm[38]

fracture surface as compared to the smooth surface of the pure epoxy. Both silica and epoxy composites break in sharp fracture lines and characteristic steps decorated with a fish-skin-like microstructure (**Figure 6d**) that also indicates an increased brittleness compared to the pure epoxy. The roughness of the fracture surface, however, slightly decreased with the decreasing particle size.

Transmission electron microscopy can serve as a very useful tool for determining the exact size and distribution of the embedded nanoparticles. In **Figure 7** a typical micrograph of the metal nanoparticles embedded in a polymer matrix is presented.
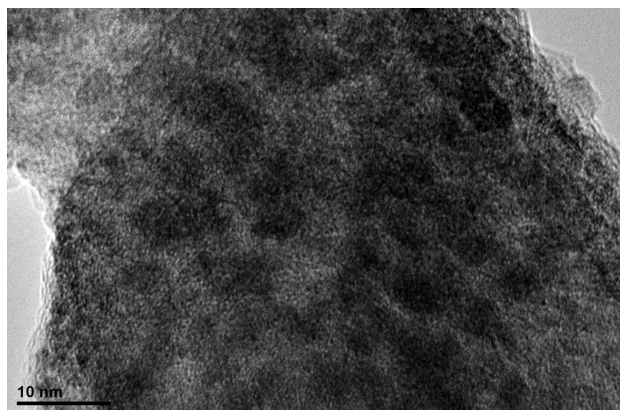
Figure 7: TEM micrograph of the Fe_2O_3 nanoparticles embedded in the polypropylene (PP) matrix
Slika 7: TEM-slika Fe_2O_3 nanodelcev v mreži polipropilena (PP)

5 MECHANICAL PROPERTIES

One of the primary reasons for adding inorganic fillers to polymers is to improve their mechanical performance through optimization of the balance between the strength/stiffness and the toughness of a composite. The mechanical response of composites strongly depends also on the silica content and size and is generally characterized with respect to different properties, such as the tensile strength, flexural strength, hardness, impact strength, fracture toughness, etc.

5.1 Tensile-strength test

With the tensile test we analyse stress σ and strain ε that are determined from the measured load and deflection using the original specimen cross-sectional area S_0 and length l_0 as follows:

$$\sigma = F/S_0, \ \varepsilon = \mathrm{d}l/l_0$$

Typical stress-strain curves of pure PVC and POSS-silanated silica/PVC composites with two types of silica fillers, 130 nm and 30 nm in diameter, are summarized in **Figure 8**. For silica/PVC composites, the trend reported in **Figure 8** can be divided into four stages before the material breaks: the initial linear elasticity, nonlinear transition to global yield, region of necking and strain softening. However, the stress-strain behaviour of pure PVC is different, typically with a broad constant stress regime for increasing the strain without a pro-
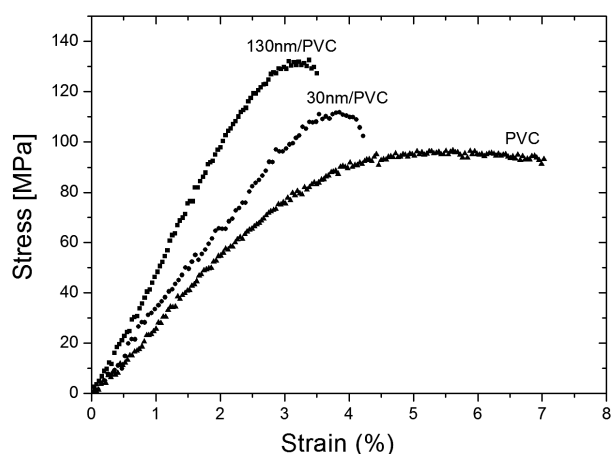
Figure 8: Typical stress-strain diagram for pure PVC and silica/PVC composites with POSS-silanated, 130 nm and 30 nm silica fillers as obtained with the tensile-strength test[34]
Slika 8: Z nateznim preizkusom dobljen značilen diagram napetost-deformacija čistega PVCja in kompozitov silicijev dioksid-PVC, obogatenih s POSS-silaniziranimi 130 nm in 30 nm silicijevimi dioksidnimi vključki[34]

nounced necking or strain softening before the sample breaking.

In the low strain portion of the curves all the investigated samples followed Hooke's law giving us the information on the composite modulus of elasticity E. As shown in **Table 1**, we observed a 30–40 % increase in E, making 30 nm and 130 nm silica/PVC composites stiffer. This large increase in elastic modulus is due to a large amount of silica particles. Another material proportion that we can obtain from the stress-strain diagram is the maximum tensile strength (UTS). A significant strengthening is observed in both 30 nm and 130 nm silica/PVC composites, 20–30 %, respectively (**Table 1**). An opposite response is, however, observed for the elongation at break depending on the silica size in the PVC matrix (**Table 1**). In contrast to the increased stiffness of 30 nm and 130 nm silica/PVC composites, their elongation at break that is lower than for pure PVC (15–30 %) indicates an embrittlement effect upon an addition of silica fillers.

5.2 Three-point bending test

The three-point bending test (3PB) covers the determination of flexural properties of a material by measuring the deflection of a sample under applied load. **Figure 9** shows a typical stress-strain curve for the samples under investigation, diglycidyl ether of bisphenol A surface-treated silica composites and the neat epoxy. **Table 2** lists the corresponding material proportions obtained with the 3PB test: elastic modulus (E), maximum tensile strength (UTS) and elongation at break.

We observed an approximately 10–20 % increase in E and UTS for both composites compared to the pure epoxy. The experimental scattering of both the Young's
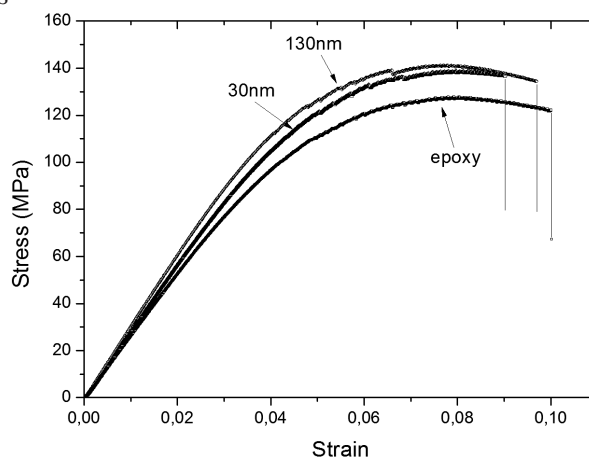
Figure 9: Typical stress-strain curves of diglycidyl ether of bisphenol A surface-treated silica/epoxy composites and the neat epoxy as obtained with the 3PB test[38]
Slika 9: Z upogibnim preizkusom (3PB) dobljen značilen diagram napetost – deformacija z diglicidil etrom bisfenola A silaniziranih kompozitov silicijevega dioksida-epoksi in čistega epoksija[38]

Table 1: Elastic modulus (E), tensile strength (UTS) and elongation at break of POSS-silanated silica/PVC composites and pure PVC evaluated with the tensile test[34]
Tabela 1: Z nateznim preizkusom dobljen elastični modul (E), maksimalna natezna trdnost (UTS) in raztezek pri pretrgu POSS-silaniziranih kompozitov silicijev dioksid-PVC in čistega PVC[34]

Sample	E/GPa	UTS/MPa	elongation at break (%)
PVC	1.7	89.9	7.0
PVC + 60 % vol. fractions of SiO$_2$ 30 nm	2.4	112.1	6.0
PVC + 60 % vol. fractions of SiO$_2$ 130 nm	3.0	122.2	4.9

Table 2: Elastic modulus (E), tensile strength (UTS) and elongation at break of diglycidyl ether of bisphenol A surface-treated silica/epoxy composites and the neat epoxy evaluated with the 3PB test[38]
Tabela 2: Z upogibnim preizkusom (3PB) dobljen elastični modul (E), maksimalna natezna trdnost (UTS) in raztezek pri pretrgu z diglicidil etrom bisfenola A silaniziranih kompozitov silicijev dioksid-epoksi in čistega epoksija[38]

Sample	E/GPa	UTS/MPa	elongation at break (%)
Epoxy	2.6	127	10.0
Epoxy + 0,5 % vol. fractions of SiO$_2$ 130 nm	3.0	141	9.6
Epoxy + 0,5 % vol. fractions of SiO$_2$ 30 nm	2.8	138	9.0

modulus and the UTS was less than 10 %. The incorporation of silica fillers, on the other hand, caused a decrease in the elongation at break, which implies an increase in the composite brittleness.

5.3 Fracture toughness

The fracture-toughness test is designed to characterize the toughness of a material in terms of the critical-stress-intensity factor, $K_{IC,}$ and the energy per unit area of a crack surface or the critical strain energy

release rate, G_{IC}, at the fracture initiation. In the experiment, the load-deflection curves are measured as shown in **Figure 10**. The fracture toughness, K_{IC}, is then calculated by using linear elastic fracture mechanics:[39]

$$K_{IC} = \frac{SP_c}{BW^{3/2}} f(\xi)$$

where

$$f(\xi) = \frac{3\xi^{1/2}\left\{1.99 - \xi(1-\xi)(215 - 3.93\xi + 2.7\xi^{2)})\right\}}{2(1+2\xi)(1-\xi)^{3/2}}$$

$$\xi = \frac{a_0}{W}$$

S and P_c are the span length and the maximum load; B, W and a_0 are the thickness, the width and the pre-crack length of the specimen.

In **Figure 10** diglycidyl ether of bisphenol A surface-treated silica composites and the neat epoxy show a linear response until the brittle fracture occurs. The extracted experimental results for the fracture toughness, K_{IC}, for the composites and the neat epoxy are listed in **Table 3**, showing a fracture toughness increase by 25–30 % with the addition of silica fillers.
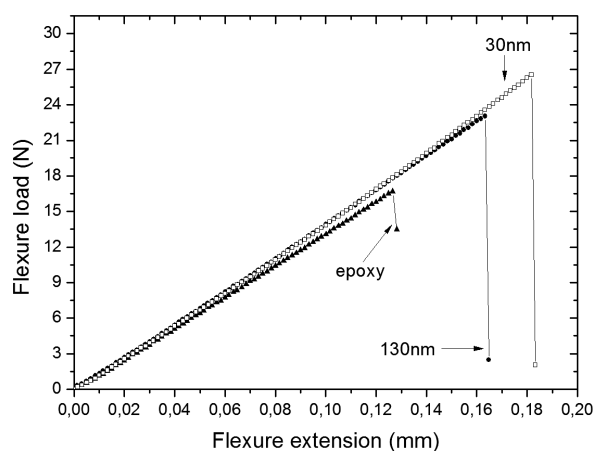
Table 3: Fracture toughness of diglycidyl ether of bisphenol A surface-treated silica composites and the neat epoxy[38]
Tabela 3: Lomna žilavost z diglicidil etrom bisfenola A silaniziranih kompozitov silicijev dioksid-epoksi in čistega epoksija[38]

Sample	K_{IC}/(MPa m$^{1/2}$)
Epoxy	0.66 ± 0.05
Epoxy + 0.5 % vol. fractions of SiO$_2$ 130 nm	0.91 ± 0.06
Epoxy + 0.5 % vol. fractions of SiO$_2$ 30 nm	0.93 ± 0.06

5.4 Charpy impact strength test

The Charpy test is used to evaluate the amount of absorbed energy by a material during a fracture, there-

fore giving us information on the impact toughness of the material. An example of the Charpy impact strength test results is in **Table 4**, presenting the impact energy and the impact resistance for diglycidyl ether of bisphenol A surface-treated silica composites and the neat epoxy.

Table 4: Impact energy and impact resistance of diglycidyl ether of bisphenol A surface-treated silica composites and the neat epoxy[38]
Tabela 4: Energija pri prelomu in odpornost proti prelomu z diglicidil etrom bisfenola A silaniziranih kompozitov silicijevega dioksida-epoksi in čistega epoksija[38]

Sample	Impact energy E_{imp}/J	Impact resistance R_{imp}/(kJ/m^2)
Epoxy	0.19 ± 0.02	6.4 ± 0.7
Epoxy + 0.5 % vol. fractions of SiO$_2$ 130 nm	0.26 ± 0.02	8.9 ± 0.6
Epoxy + 0.5 % vol. fractions of SiO$_2$ 30 nm	0.33 ± 0.03	10.8 ± 0.7

The addition of silica particles increases the impact resistance as well as the impact energy up to 60 %. Surprisingly, the results of the Charpy impact test are also strongly influenced by a particle diameter.

6 APPLICATIONS

As shown earlier, nanosilica-reinforced polymer composites significantly improve the mechanical pro-

Figure 10: Load-deflection curves of diglycidyl ether of bisphenol A surface-treated silica composites and the neat epoxy[38]
Slika 10: Diagram sila – deformacija z diglicidil etrom bisfenola A silaniziranih kompozitov silicijev dioksid-epoksi in čistega epoksija[38]
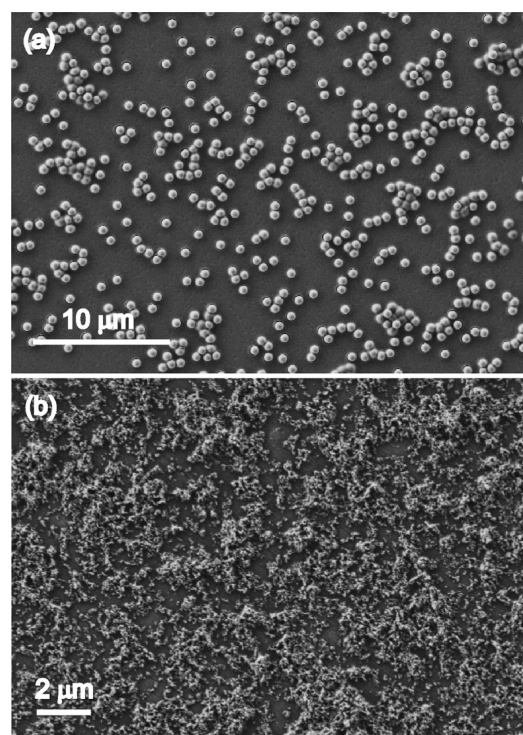
Figure 11: SEM micrographs of POSS-silanated, a) 600 nm and b) 30 nm silica/PVC composite coatings on the AISI 316L surface[45]
Slika 11: SEM-slike POSS-silaniziranih kompozitnih prevlek silicijevega dioksida-PVC a) 600 nm in b) 30 nm na površini AISI 316L jekla[45]
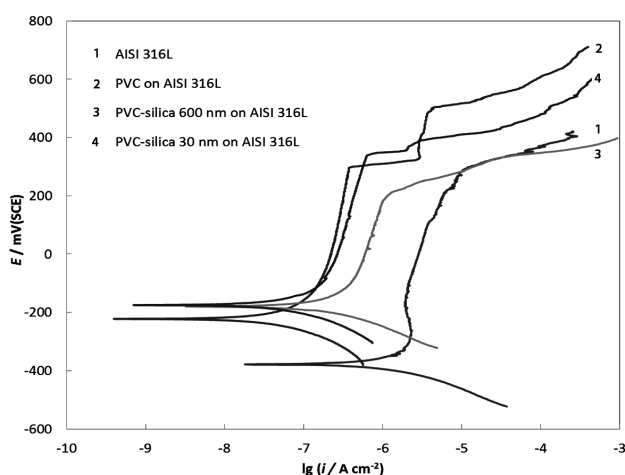
Figure 12: Potentiodynamic curves for AISI 316L, AISI 316L + PVC, AISI 316L + 600 nm/PVC and AISI 316L + 30 nm/PVC in 3.5 % NaCl[45]

Slika 12: Potenciodinamske krivulje vzorcev AISI 316L, AISI 316L + PVC, AISI 316L + 600 nm/PVC in AISI 316L + 30 nm/PVC v 3,5-odstotni NaCl[45]

perties of the end material and exhibit some unique properties allowing many potential applications. Silica/polymer nanocomposites have been reported to be used in coatings,[40,41] optical devices,[42] electronics,[43] photoresist materials,[44] etc.

In most cases silica/polymer nanocomposites are used as protective coatings, either to improve the mechanical characteristics of the substrate material (i. e., wear, scratch, abrasion resistance) or to insure the corrosion resistance in various environments. Corrosion-protection nanosilica/polymer coatings on metallic substrates, for example, provide an effective physical barrier between the metal and its environment containing aggressive species, such as enhanced chloride-ion concentration, O_2 or H^+. A uniform dispersion of nanoparticles (i.e., SiO_2) in a chosen polymer matrix with desirable characteristics (i. e., epoxy) is shown to increase the surface hydrophobicity (i.e., the self-cleaning effect) and to improve the adhesion between the composite coating and the metallic surface.[26,45–47]

In **Figures 11a** and **b** we can see an example of a POSS-silanated silica/PVC coating adsorbed on a steel substrate of type AISI 316L. **Figure 12** further presents potentiodynamic measurements of these coatings in a 3.5 % NaCl solution at room temperature indicating an improved anticorrosion behaviour in a chloride-ion-rich environment as compared to the clean AISI 316L surface. Potentiodynamic curves reflect the decreased corrosion-current densities and corrosion potentials for the silica/PVC-coated AISI 316L substrates.

7 SUMMARY AND OUTLOOK

A modification of a polymer matrix with silica fillers allows significant increases in the modulus and strength

contributions of the matrix to the overall composite properties. Obtaining the optimum properties for the nanocomposites, however, requires an excellent homogeneous dispersion of the fillers, as the tendency of the silica particles to agglomerate can seriously affect the achievable properties. Therefore, to provide a strong interfacial interaction between the inorganic particles and the polymer matrix, silica fillers must have suitably modified surfaces. The end result is a composite with unique and significantly improved mechanical properties having a high ability to transfer the stresses from the polymer matrix to the embedded particles. This allows the silica/polymer nanocomposites to be used in a variety of applications and industrial products successfully replacing the classical materials. Although much work has already been done on the silica/polymer nanocomposites, more research is needed to further understand the complex filler-matrix relationship that would allow a step forward and even enable a synthesis of the nanocomposites with controllable properties through tailoring the interfacial interaction between silica and a polymer matrix.

8 REFERENCES

[1] A. C. Balazs, T. Emrick, T. P. Russell, Nanoparticle polymer composites: Where two small worlds meet, Science, 314 (**2006**), 1107–1110

[2] R. Krishnamoorti, R. A. Vaia, Polymer nanocomposites, Journal of Polymer Science Part B-Polymer Physics, 45 (**2007**), 3252–3256

[3] J. Spanoudakis, R. J. Young, Crack-propagation in a glass particle-filled epoxy-resin. 2. Effect of particle matrix adhesion, Journal of Materials Science, 19 (**1984**), 487–496

[4] A. C. Moloney, H. H. Kausch, T. Kaiser, H. R. Beer, Parameters determining the strength and toughness of particulate filled epoxide-resins, Journal of Materials Science, 22 (**1987**), 381–393

[5] M. Hussain, Y. Oku, A. Nakahira, K. Niihara, Effects of wet ball-milling on particle dispersion and mechanical properties of particulate epoxy composites, Materials Letters, 26 (**1996**), 177–184

[6] E. P. Giannelis, Polymer-layered silicate nanocomposites: Synthesis, properties and applications, Applied Organometallic Chemistry, 12 (**1998**), 675–680

[7] T. Lan, T. J. Pinnavaia, Clay-reinforced epoxy nanocomposites, Chemistry of Materials, 6 (**1994**), 2216–2219

[8] A. S. Zerda, A. J. Lesser, Intercalated clay nanocomposites: Morphology, mechanics, and fracture behavior, Journal of Polymer Science Part B-Polymer Physics, 39 (**2001**), 1137–1146

[9] R. P. Singh, M. Zhang, D. Chan, Toughening of a brittle thermosetting polymer: Effects of reinforcement particle size and volume fraction, Journal of Materials Science, 37 (**2002**), 781–788

[10] R. A. Pearson, A. F. Yee, Influence of particle-size and particle-size distribution on toughening mechanisms in rubber-modified epoxies, Journal of Materials Science, 26 (**1991**), 3828–3844

[11] C. B. Bucknall, G. Maistros, C. M. Gomez, I. K. Partridge, Elastomers and thermoplastics as modifiers for thermosetting resins, Makromolekulare Chemie-Macromolecular Symposia, 70-1 (**1993**), 255–264

[12] R. A. Pearson, Toughening epoxies using rigid thermoplastic particles – a review, Advances in Chemistry, vol. 233, American Chemical Society, 1993, 405–425

[13] A. C. Moloney, H. H. Kausch, H. R. Stieger, The fracture of particulate filled epoxide-resins, Journal of Materials Science, 19 (**1984**), 1125–1130

[14] M. Frounchi, T. A. Westgate, R. P. Chaplin, R. P. Burford, Fracture of polymer networks based on diethylene glycol bis(allyl carbonate), Polymer, 35 (**1994**), 5041–5045

[15] F. Stricker, Y. Thomann, R. Mulhaupt, Influence of rubber particle size on mechanical properties of polypropylene-SEBS blends, Journal of Applied Polymer Science, 68 (**1998**), 1891–1901

[16] R. T. Quazi, S. N. Bhattacharya, E. Kosior, The effect of dispersed paint particles on the mechanical properties of rubber toughened polypropylene composites, Journal of Materials Science, 34 (**1999**), 607–614

[17] A. Boonyapookana, K. Nagata, Y. Mutoh, Fatigue crack growth behavior of silica particulate reinforced epoxy resin composite, Composites Science and Technology, 71 (**2011**), 1124–1131

[18] S. V. Kamat, J. P. Hirth, R. Mehrabian, Mechanical-properties of particulate-reinforced aluminium matrix composites, Acta Metallurgica, 37 (**1989**), 2395–2402

[19] F. F. Lange, K. C. Radford, Fracture energy of an epoxy composite system, Journal of Materials Science, 6 (**1971**), 1197–1205

[20] A. G. Evans, Strength of brittle materials containing second phase dispersions, Philosophical Magazine, 26 (**1972**), 1327–1333

[21] A. F. Bower, M. Ortiz, An analysis of crack trapping by residual-stresses in brittle solids, Journal of Applied Mechanics-Transactions of the Asme, 60 (**1993**), 175–182

[22] A. Moisala, Q. Li, I. A. Kinloch, A. H. Windle, Thermal and electrical conductivity of single- and multi-walled carbon nanotube-epoxy composites, Composites Science and Technology, 66 (**2006**), 1285–1288

[23] M. Darbandi, R. Thomann, T. Nann, Hollow silica nanospheres: In situ, semi-in situ, and two-step synthesis, Chemistry of Materials, 19 (**2007**), 1700–1703

[24] W. Stober, A. Fink, E. Bohn, Controlled growth of monodisperse silica spheres in micron size range, Journal of Colloid and Interface Science, 26 (**1968**), 62–71

[25] M. Zorko, S. Novak, M. Gaberscek, Fast fabrication of mesoporous SiC with high and highly ordered porosity from ordered silica templates, Journal of Ceramic Processing Research, 12 (**2011**), 654–659

[26] I. Jerman, M. Kozelj, B. Orel, The effect of polyhedral oligomeric silsesquioxane dispersant and low surface energy additives on spectrally selective paint coatings with self-cleaning properties, Solar Energy Materials and Solar Cells, 94 (**2010**), 232–245

[27] Y. H. Lai, M. C. Kuo, J. C. Huang, M. Chen, On the PEEK composites reinforced by surface-modified nano-silica, Materials Science and Engineering A, 458 (**2007**), 158–169

[28] E. Moncada, R. Quijada, J. Retuert, Nanoparticles prepared by the sol-gel method and their use in the formation of nanocomposites with polypropylene, Nanotechnology, 18 (**2007**) 33, 335606

[29] F. Yang, G. L. Nelson, Polymer/silica nanocomposites prepared via extrusion, Polymers for Advanced Technologies, 17 (**2006**), 320–326

[30] M. Tanahashi, M. Hirose, Y. Watanabe, J. C. Lee, K. Takeda, Silica/perfluoropolymer nanocomposites fabricated by direct melt-compounding: A novel method without surface modification on nanosilica, Journal of Nanoscience and Nanotechnology, 7 (**2007**), 2433–2442

[31] M. Avella, F. Bondioli, V. Cannillo, M. E. Errico, A. M. Ferrari, B. Focher, M. Malinconico, T. Manfredini, M. Montorsi, Preparation, characterisation and computational study of poly(epsilon-caprolactone) based nanocomposites, Materials Science and Technology, 20 (**2004**), 1340–1344

[32] M. Iijima, M. Tsukada, H. Kamiya, Effect of surface interaction of silica nanoparticles modified by silane coupling agents on viscosity of methylethylketone suspension, Journal of Colloid and Interface Science, 305 (**2007**), 315–323

[33] M. Marrone, T. Montanari, G. Busca, L. Conzatti, G. Costa, M. Castellano, A. Turturro, A Fourier transform infrared (FTIR) study of the reaction of triethoxysilane (TES) and bis 3-triethoxysilyl-propyl tetrasulfane (TESPT) with the surface of amorphous silica, Journal of Physical Chemistry B, 108 (**2004**), 3563–3572

[34] M. Conradi, M. Zorko, I. Jerman, B. Orel, I. Verpoest, Mechanical properties of high density packed silica/poly(vinyl chloride) composites, Polymer Engineering & Science, (**2012**), DOI: 10.1002/pen.23412

[35] I. Jerman, M. Mihelcic, D. Verhovsek, J. Kovac, B. Orel, Polyhedral oligomeric silsesquioxane trisilanols as pigment surface modifiers for fluoropolymer based Thickness Sensitive Spectrally Selective (TSSS) paint coatings, Solar Energy Materials and Solar Cells, 95 (**2011**), 423–431

[36] L. Huber, B. V. Jose, Handbook of plastics analysis, Marcel Dekker, New York 2003

[37] X. Y. Ling, I. Y. Phang, G. J. Vancso, J. Huskens, D. N. Reinhoudt, Stable and Transparent Superhydrophobic Nanoparticle Films, Langmuir 25 (**2009**), 3260–3263

[38] M. Conradi, M. Zorko, A. Kocijan, I. Verpoest, Mechanical properties of epoxy composites reinforced with a low volume fraction of nanosilica fillers, Materials Chemistry and Physics, 137 (**2013**), 910–915

[39] J. P. Benthem, W. T. Koiter, Asymptotic approximations to crack problems, Ed., G. C. Sih, Methods of Analysis and Solutions of Crack Problems, Noordhoff International Publishing, Leyden 1973

[40] X. H. Li, G. M. Chen, Y. M. Ma, L. Feng, H. Z. Zhao, L. Jiang, F. S. Wang, Preparation of a super-hydrophobic poly(vinyl chloride) surface via solvent-nonsolvent coating, Polymer, 47 (**2006**), 506–509

[41] T. Tamai, Y. Matsuura, M. Watanabe, K. Matsukawa, Acrylic polymer/silica hybrid for electron-beam resists, Journal of Polymer Science, Part A: Polymer Chemistry, 44 (**2006**), 2107–2116

[42] Y. Y. Yu, C. Y. Chen, W. C. Chen, Synthesis and characterization of organic – inorganic hybrid thin films from poly(acrylic) and mono-dispersed colloidal silica, Polymer, 44 (**2003**), 593–601

[43] Y. Y. Sun, Z. Q. Zhang, K. S. Moon, C. P. Wong, Glass transition and relaxation behavior of epoxy nanocomposites, Journal of Polymer Science Part B-Polymer Physics, 42 (**2004**), 3849–3858

[44] J. D. Cho, H. T. Ju, Y. S. Park, J. W. Hong, Kinetics of cationic photopolymerizations of UV-curable epoxy-based SU8-negative photoresists with and without silica nanoparticles, Macromolecular Materials and Engineering, 291 (**2006**), 1155–1163

[45] M. Conradi, A. Kocijan, M. Zorko, I. Jerman, Effect of silica/PVC composite coatings on steel-substrate corrosion protection, Progress in Organic Coatings, 75 (**2012**), 392-397

[46] J. Mardel, S. J. Garcia, P. A. Corrigan, T. Markley, A. E. Hughes, T. H. Muster, D. Lau, T. G. Harvey, A. M. Glenn, P. A. White, S. G. Hardin, C. Luo, X. Zhou, G. E. Thompson, J. M. C. Mol, The characterisation and performance of Ce(dbp)(3)-inhibited epoxy coatings, Progress in Organic Coatings ,70 (**2011**), 91–101

[47] I. Marabotti, A. Morelli, L. M. Orsini, E. Martinelli, G. Galli, E. Chiellini, E. M. Lien, M. E. Pettitt, M. E. Callow, J. A. Callow, S. L. Conlan, R. J. Mutton, A. S. Clare, A. Kocijan, C. Donik, M. Jenko, Fluorinated/siloxane copolymer blends for fouling release: chemical characterisation and biological evaluation with algae and barnacles, Biofouling, 25 (**2009**), 481–493

THE FATIGUE BEHAVIOUR OF ALUMINIUM FOAM

VEDENJE ALUMINIJEVIH PEN PRI PREIZKUSU UTRUJENOSTI

Martin Nosko, František Simančík, Roman Florek

Institute of Materials and Machine Mechanics, Slovak Academy of Sciences, Račianska 75, 831 02 Bratislava, Slovakia
ummsnoso@savba.sk

The aim of this work was to study the fatigue behaviour of aluminium foam during compression-compression cyclic loading under an applied load. The reason was to estimate the amount of load for a fatigue life of 10^5 cycles with or without a small amount of permanent plastic deformation determined to be less than 1 mm. The samples were subjected to cyclic loading under various forces (proportion of level force estimated from a uni-axial compression test) in one given direction due to the elimination of the foam anisotropy. Moreover, the fatigue behaviour of the aluminium foam under compression-compression cyclic loading is described macroscopically. It was revealed that 50 % of the applied load estimated from the uni-axial compression test is sufficiently low for a fatigue life 10^5 cycles in the case of a foam density of 0.211 ± 0.007 g cm^{-3}.

Keywords: aluminium foam, fatigue life, level force, endurance limit

Cilj tega dela je bilo preučevanje vedenja aluminijevih pen pri preizkusu utrujenosti s tlačno-ciklično tlačnim obremenjevanjem v odvisnosti od uporabljene obremenitve. Razlog je bil ugotoviti obremenitev za zdržljivost za utrujenost do 10^5 ciklov brez majhne plastične deformacije, manj kot 1 mm ter z njo. Vzorci so bili ciklično obremenjeni z različnimi silami (proporcionalno ravnotežni sili, ugotovljeni pri enoosnem tlačnem preizkusu) v eni smeri, da bi izločili vpliv anizotropije pene. Poleg tega je makroskopsko predstavljeno vedenje aluminijeve pene pri preizkusu utrujenosti s tlačno-ciklično tlačnim obremenjevanjem. Ugotovljeno je, da je 50 % obremenitve, dobljene pri enoosnem tlačnem preizkusu, dovolj, da pena z gostoto $0,211 \pm 0,007$ g cm^{-3} pri utrujenostnem preizkusu zdrži 10^5 ciklov.

Ključne besede: pena iz aluminija, zdržljivost za utrujenost, stopnja sile, maksimalna obremenitev

1 INTRODUCTION

Aluminium foam is known in industry as a good candidate material for the cores of sandwich panels due to its good stiffness-to-weight ratio.[1–4] The effect of composition, manufacturing parameters, sound-absorption properties and electrical behaviour on the foams' properties was already studied for example in[3,5–8]. The deformation mechanism of aluminium foam during uni-axial compression and during uni-axial compression-compression cyclic loading was studied in[5,9–15] macroscopically and by using X-ray computed tomography and surface strain mapping. These studies were focused on determining the deformation modes and revealing the structural character responsible for ore-mature yielding. Our study is focused on contributing to an estimate of the force at which the aluminium foam can be used for 10^5 compression-compression cyclic loadings.

2 EXPERIMENTAL

2.1 Material

Alporas® aluminium foamed block of composition Al + 1.5 % Ca + 1.6–3 % TiH$_2$ [2,8] was used for the study. Since the aluminium foam block is anisotropic,[8,16,17] the middle area of the block, which is characterized by the presence of the largest amount of non-uniformities within the structure (the presence of the elongated pores, pore agglomerates, fractured pore faces, microstructural

in-homogeneities, etc.) was chosen for an estimation of the level force. The density of the represented area is 0.211 ± 0.007 g cm^{-3}. Uni-axial compression-compression cyclic loadings were performed on a material testing system device (MTS 810) using cubic samples of dimension $a = 45$ mm. The deformation mechanism on the macro-scale was revealed using a digital camera set on an MTS device
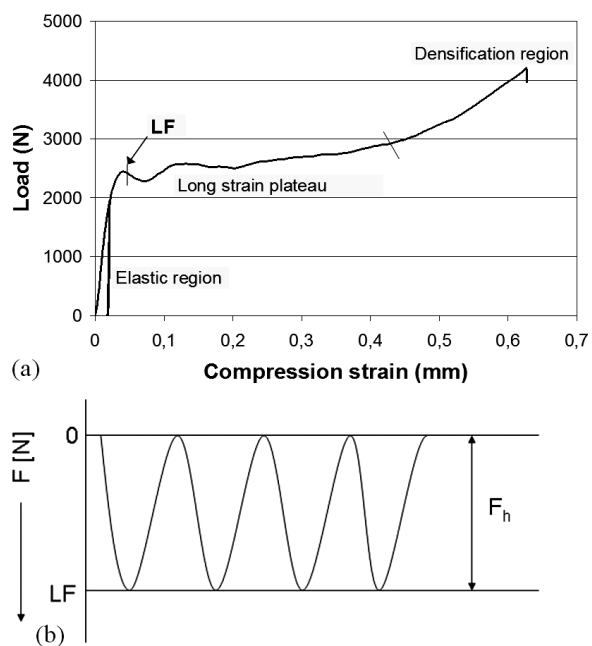
2.2 Estimation of the level force

The uni-axial load-stress behaviour of the aluminium foam has been studied elsewhere[5–7] and is shown in **Figure 1a**. It covers three regions: the elastic region at low loads (includes the hardening region) ended by peak stress, the long load-strain plateau wherein localized plastic collapse propagates from one cell band to another. After all bands collapse densification region of rapid rise of load starts.

The level force (responsible for the plastic collapse of the first cell band within the sample[5–7]) was estimated as an average from 25 uni-axial compression tests according to the DIN norm[18] to 2200 N. It should be noted that 10 of the 25 samples showed a load peak well below (1000 N and 1800 N, respectively) due to the occurrence of large, elongated pores within the structure of the represented area.

2.3 Compression-compression fatigue behaviour

To find out the relation between the ultimate proportions of the level force (LF) and the fatigue behaviour

Figure 1: a) Typical uni-axial compression load-strain curve with definition of the level force (LF), b) description of the applied load during the compression-compression cyclic loading
Slika 1: a) Značilna krivulja sila – raztezek z opredeljeno stopnjo sile (LF), b) videz uporabljene obremenitve med tlačno-cíklično tlačnim obremenjevanjem

the samples were loaded by forces increases from 50 % to 90 % LF with a step of approximately 5 % and 10 %. The samples were subjected to compression-compression cyclic loading according to **Figure 1b** during the period over 10^5 cycles. The fatigue life is defined as the number of cycles corresponding to the onset of an abrupt strain jump.

3 RESULTS AND DISCUSSION

3.1 Deformation mechanism

As presented in **Figure 2a**, the compression-compression S-N curves during the cyclic loading are comparable for applied fraction of LF, but the onset of the yielding starts after different number of cycles. While in the case of 90 % LF, it is achieved immediately after the cyclic loading, in case of 69 % LF it starts after 30000 cycles and is characterized by changes in the strain-rates. In the case of 63 % LF, it is achieved after approximately 97000 cycles, which is almost the defined endurance limit (10^5 cycles) – see detail in **Figure 2b**. It suggests that the fatigue life (in case of a rigid material – rapid coalescence and growth of cracks, in the case of foamed material – evolution and subsequent collapse of weak pore bands) is mainly affected by the proportion of the loading force and the mechanism of fatigue damage is delayed with a decrease of the fraction (%) LF.
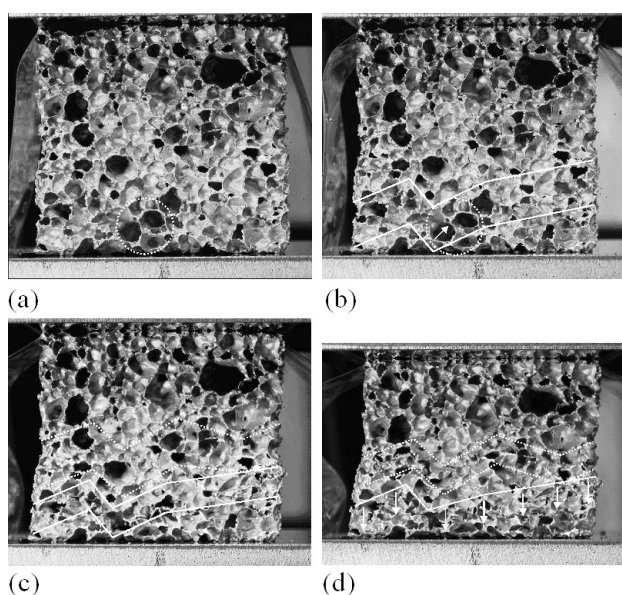
The deformation mechanism during compression-compression cyclic loading can be described through S-N curves and is revealed macroscopically in **Figure 3**.
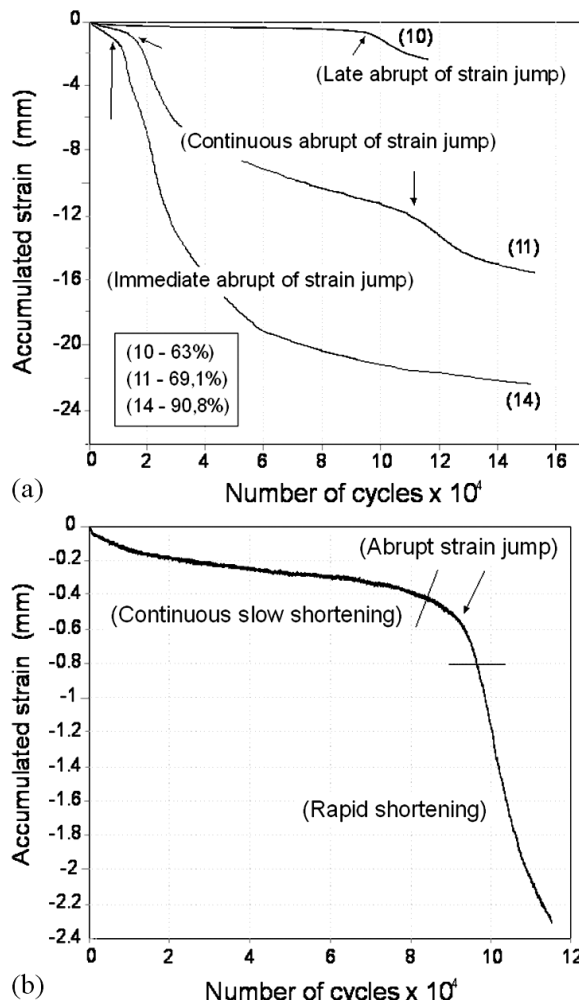
Figure 2: Compression-compression S-N curves; a) representation of the different fatigue life with respect to the proportion of LF, b) detail of the S-N curve
Slika 2: Tlačno-tlačne S-N-krivulje; a) predstavitev različne zdržljivosti pri utrujenostnem preizkusu v odvisnosti od LF, b) detajl S-N-krivulje

The principle of evolution of the plastic deformation and its spreading within the sample during uni-axial compression and cyclic loading is similar.[9–12] Immediately after loading in the elastic region, the uniform evolution of the plastic hinges within the whole samples was observed. The buckling and bending of the pore walls (**Figure 3a**, **b**) together with the continuous evolution of the plastic hinges follows as the deformation continues into the "hardening region" and through the hardening region.[12] These features are responsible for the loss of stiffness associated with a continuous shortening before the abrupt strain jump presented in **Figure 2b**. The abrupt strain jump is related to a macroscopically viewed plastic collapse of a group of pores within the deformation bands (**Figure 3b**, **c**) and causes changes in the strain rate due to the softening effect after the collapse.[12] Subsequently, in the vicinity of the already plastically deformed group of pores the whole deformation band

Figure 3: Deformation mechanism during compression-compression cyclic loading in a macroscopic view; a) un-deformed sample, b) buckling of the pore faces within the pore band, c) plastic collapse of the pore band and the creation of another one and d) continuous shortening

Slika 3: Deformacijski mehanizem med tlačno-ciklično tlačnim obremenjevanjem v makroskopskem pogledu; a) nedeformiran vzorec, b) uklanjanje por v pasu por, c) plastično posedanje pasu por in nastajanje drugih por, d) neprekinjeno skrajšanje

closes up and the process is repeated within the other region of the foamed sample (**Figure 3c**, **d**), also accompanied by changes in the strain rate (**Figure 2a**, No.11). However, the changes in the strain rates are omitted if the loading is performed with a high proportion of LF, as presented in **Figure 2a** No.14. Vice-versa, no permanent deformation occurs if the

Figure 4: S-N curves for compression-compression cyclic loading for various LF proportion; a) 50 %, b) 63 %, c) 70 % and d) 90 %

Slika 4: S-N-krivulje za tlačno-ciklično tlačno obremenjevanje pri različnih LF-razmerjih; a) 50 %, b) 63 %, c) 70 % in d) 90 %

loading is performed by a small proportion of LF to overcome the load of the plastic collapse of the pore band, as seen in **Figure 2a** No.10.

3.2 Estimation of LF

As seen in **Figure 4**, the fatigue behaviour of the foam is very sensitive to the proportion of $LF = 2200$ N. While during loading at 50 % LF (**Figure 4a**), all the samples achieved the endurance limit, the increment of LF causes a decreased number of samples and is responsible for the premature shortening of the samples accompanied by changes in the strain rate, as presented in **Figures 4b** to **d**. In case of 63 % LF, two of the six samples achieved the endurance limit without premature shortening; if 70 % of LF is applied, only one from three samples reaches the limit, as presented in **Figure 4c**. During cycling at 90 % LF (**Figure 4d**), all the samples collapsed immediately after loading without changes in the strain rate.

4 CONCLUSION

It was revealed that a 50 % of level force is sufficient for uni-axial compression-compression cyclic loading to achieve an endurance limit of 10^5 cycles with no significant deformation, estimated to be less than 1mm. In the elastic region, only the creation of plastic hinges during the loading occurs, but in the region of hardening the buckling and bending of the cell walls start, which overcomes the reversible elastic deformation. The tests were performed on samples chosen from an area with the presence of the largest amount of non-uniformities within the structure at 50 % LF. This suggests that 50 % LF is the force that prevents the buckling and bending of cell faces responsible for the plastic collapse of pore bands. A force above 50 % LF causes continuous damage to the foam before the endurance limit is achieved.

5 REFERENCES

[1] M. F. Ashby, A. G. Evans, L. J. Gibson, J. W. Hutchinson, H. N. G. Wadley, Metal Foam: A Design Guide, Butterworth-Heinemann, Woburn 2000

[2] J. Banhart, Prog. Mater. Sci., 46 (**2001**), 559–632

[3] F. Simancik, J. Jerz, J. Kovacik, P. Minar, Metall. Mater., 35 (**1997**), 265–277

[4] A. M. Harte, N. A. Fleck, M. F. Ashby, Inter. J. Fatigue, 23 (**2001**), 499–507
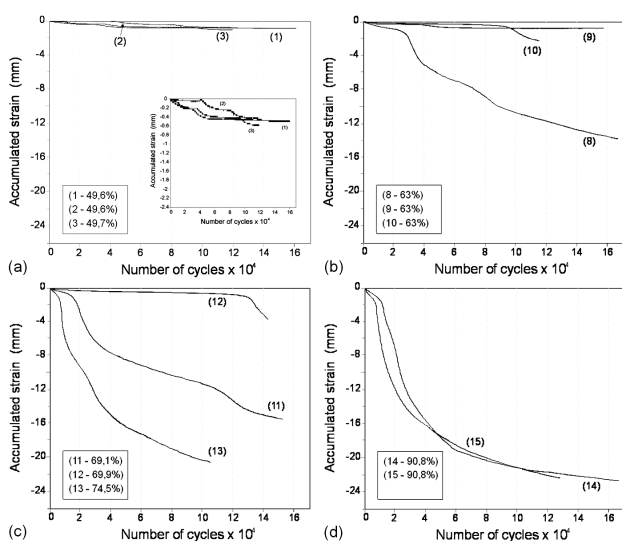
[5] U. Ramamurty, A. Paul, Acta Mater., 52 (**2004**), 869–876

[6] E. Koza, M. Leonowicza, S. Wojciechowskia, F. Simancik, Mater. Lett., 58 (**2003**), 132–135

[7] M. Nosko, F. Simancik, R. Florek, Mater. Sci. and Eng. A., 527 (**2010**), 5900–5908

[8] M. Nosko, Reproducibility of aluminium foam properties, Ph.D. Thesis, Institute of materials and machine mechanics SAS, 2009

[9] H. Bart-Smith, A. F. Bastawros, D. R. Mumm, A. G. Evans, D. J. Sypeck, H. N. G. Wadley, Acta Mater., 46 (**1998**), 3583–3592

[10] A. F. Bastawros, H. Bart-Smith, A. G. J. Evans, Mech. Physical Solids, 48 (**2000**), 301–322

[11] H. Bart-Smith, A. F. Bastawros, D. R. Mumm, A. G. Evans, D. J. Sypeck, H. N. G. Wadley, Acta Mater., 46 (**1998**), 3583–3592

[12] A. F. Bastawros, A. G. Evans, Adv. Eng. Mat., 2 (**2000**), 210–214

[13] M. Kolluri, M. Mukherjee, F. Garcia-Moreno, J. Banhart, U. Ramamurty, Acta Mater., 56 (**2008**), 1114–1125

[14] E. Amsterdam, J. Th. M. De Hosson, P. R. Onck, Acta Mater., 54 (**2006**), 4465–4472

[15] A. M. Harte, N. A. Fleck, M. F. Ashby, Acta Mater., 47 (**1999**), 2511–2524

[16] M. Nosko, F. Simancik, K. Izdinsky, P. Svec, R. Florek, Mat. Lett., 65 (**2011**), 1378–1380

[17] M. Nosko, F. Simancik, R. Florek, In: G. Stephani, B. Kieback, editors, Cellular metals for structural and functional applications, Fraunhofer IFAM, Dresden 2009, 246–25

[18] DIN 50134, Testing of metallic materials – Compression test of metallic cellular materials, 2008

ADDITION OF STRONTIUM TO AN Mg-3Sn ALLOY AND AN INVESTIGATION OF ITS PROPERTIES

DODATEK STRONCIJA ZLITINI Mg-3Sn IN PREISKAVA NJENIH LASTNOSTI

Mediha Öbekcan[1], Aysun Ayday[1], Hüseyin Şevık[2], Süleyman Can Kurnaz[1]

[1]Sakarya University, Engineering Faculty, Department of Metallurgical and Materials Engineering, Sakarya, Turkey
[2]Mersin University, Engineering Faculty, Department of Metallurgical and Materials Engineering, Mersin, Turkey
ckurnaz@sakarya.edu.tr

The effect of strontium additions in mass fractions of (0.05, 0.1, 0.2, 0.5 and 1) % to a magnesium alloy (Mg-3Sn) was investigated in this work. The alloys were gravity cast under a controlled atmosphere. The mechanical properties and the microstructures of the above alloys were examined and recorded. The results revealed that an addition of strontium to the above alloy had significantly affected its microstructure. The X-ray diffraction results showed that in all of the obtained alloys the main phases were α-Mg and Mg_2Sn, and that the strontium-based intermetallics were not detected. The hardness values increased with the increasing strontium content. The highest yield strength, tensile strength and elongation were exhibited by the Mg-%3Sn-%0.1Sr alloy.

Keywords: Mg-Sn alloy, Sr addition, mechanical properties

V tem delu je bil preiskovan učinek dodatka masnih deležev stroncija (0,05; 0,1; 0,2; 0,5 in 1) % magnezijevi zlitini (Mg-3Sn). Zlitine so bile gravitacijsko lite v kontrolirani atmosferi. Preiskane in ugotovljene so bile mehanske lastnosti in mikrostrukture navedenih zlitin. Rezultati so pokazali, da dodatek stroncija pri tej zlitini močno vpliva na mikrostrukturo. Rezultati rentgenske difrakcije so pokazali, da so glavne faze α-Mg, Mg_2Sn v preiskovanih zlitinah, niso pa bile odkrite intermetalne faze na osnovi stroncija. Vrednosti trdote so naraščale z naraščajočo vsebnostjo stroncija. Najvišja meja plastičnosti, najvišja trdnost in največji raztezek se je pokazal pri zlitini Mg-%3Sn-%0,1Sr.

Ključne besede: zlitina Mg-Sn, dodatek Sr, mehanske lastnosti

1 INTRODUCTION

There have been various investigations to identify the properties of magnesium and its alloys with regard to their use in industrial applications due to their low density in comparison with the other commercial, low-density alloys such as aluminium.[1–5] Generally, magnesium alloys are based on the Mg–Al system. For example, aluminium-containing magnesium alloys will have an $Mg_{17}Al_{12}$ compound, which adversely influences the mechanical properties at high temperatures.[6,7] It is therefore important to add another alloying element to reverse such an effect. Such elements are strontium (Sr), calcium (Ca) and tin (Sn).[8,9] In this work aluminium-free magnesium alloys were used (Mg-3Sn).

2 EXPERIMENTAL WORK

The alloys were melted in a stainless-steel crucible using an electric-resistance furnace facilitated with a CO_2-0.2SF_6 atmosphere. Commercially pure magnesium, tin and Mg-%20Sr were used in this case as shown in **Table 1**. The melt was held at 760 °C for 10 min, then stirred to ensure a homogeneous distribution of all the alloying elements. The melts was then poured into a preheated steel die at 270 °C. Cross-sections were taken from similar areas of all the castings and ground down to

1200 grit using silicon carbide papers. The cross-sections were then polished down to 1 μm samples using abrasive diamond wheels. The specimens were chemically etched using an acetic picric acid compound (5 ml of acetic acid, 6 g of picric acid, 10 ml of distilled water, 100 ml of ethanol), then examined using a JOEL scanning electron microscope (SEM). The second lot of cross-sections were taken from similar areas of all the castings. The sections were ground using silicon carbide papers before examining them with an X-ray diffraction [(XRD) Rigaku D-Max 1000 X-ray diffractometer with Cu Kα radiation] machine to identify their compounds and phases.

Table 1: Chemical compositions of the investigated alloys (mass fraction, *w*/%)
Tabela 1: Kemijska sestava preiskovanih zlitin (masni deleži, *w*/%)

Alloys	Composition	Mg	Sn	Sr
1	Mg-3Sn	96.8	2.97	–
2	Mg-3Sn-0.05Sr	96.5	2.92	0.046
3	Mg-3Sn-0.1Sr	96.1	2.94	0.09
4	Mg-3Sn-0.2Sr	95.9	2.97	0.183
5	Mg-3Sn-0.5Sr	95.9	2.94	0.45
6	Mg-3Sn-1Sr	95.7	2.89	0.92

Brinell hardness tests were performed on all the cross-sections using a diameter ball 2.5 mm with an
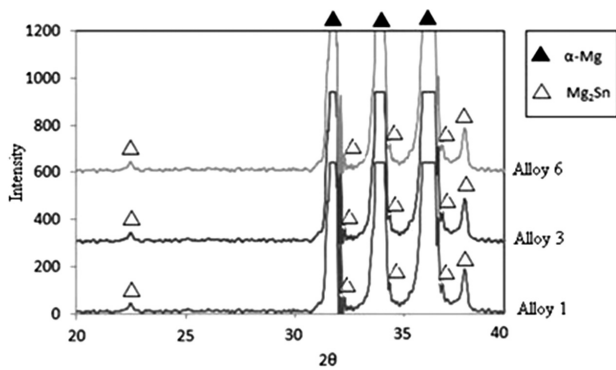
Figure 1: XRD spectrums of selected alloys
**Slika 1:** XRD-spektri izbranih zlitin

applied load of 31.25 kg. Tensile tests were carried out using an Instron 3367 universal testing machine with a fixed ram speed of 0.2 mm/s at ambient temperature.

3 RESULTS AND DISCUSSION

The XRD results shown in **Figure 1** revealed that the main phases were α-Mg and Mg_2Sn. The XRD results, on the other hand, failed to show any Mg-Sr- and Sn-Sr-based intermetallics in any of the tested castings. Here the results are in agreement with the study made by Hongmei Liu.[9]

The SEM images shown in **Figure 2** revealed that the microstructures of these alloys mainly consisted of the primary α-Mg surrounded by the boundary of the Mg_2Sn phase. It is very clear that the primary α-Mg in the strontium-free alloy 1 is much bigger than those seen in alloys 2, 3, 4, 5 and 6. The intermetallics (Mg_2Sn), on the other hand, appear to be smaller and more nodular than those of 2, 3, 4, 5 and 6. The increase in the strontium content influenced the formation of a large Mg_2Sn phase, which also influenced the mechanical properties. **Figure 3** shows the results of the energy-dispersive spectrometer (EDS) obtained for alloy 6. The figure shows that strontium was completely dissolved in the Mg_2Sn intermetallic, which influenced its final shape.

The hardness increased and was directly proportional to the increase in the strontium content as shown in
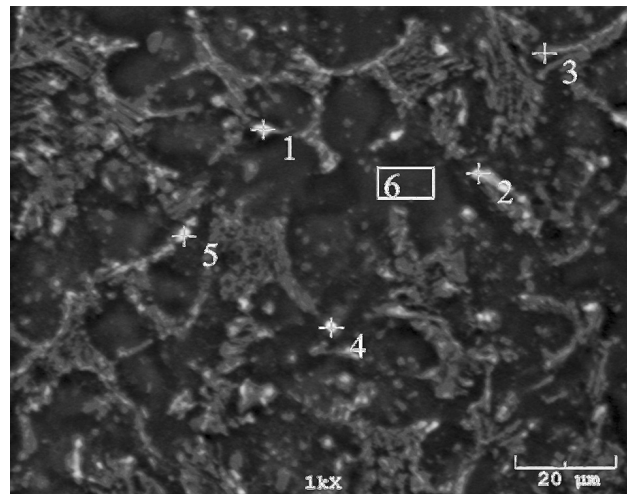
	Mg	Sn	Sr	O
1	79.266	9.935	0.961	9.837
2	80.628	8.260	0.699	10,412
3	84.764	4.952	2.634	7.649
4	75.648	11.145	0.438	12.770
5	71.894	11.235	2.091	14.780
6	98.733	1.267	–	–

Figure 3: EDS analysis of alloy 6
Slika 3: EDS-analiza zlitine 6

Figure 4. The tensile and the yield strengths increased only up to alloy 3, then they decreased for alloys 4, 5 and 6. The elongation results showed a similar manner as seen in the cases of the tensile and yield strengths. It is clear from **Figure 4** that the yield and tensile strengths reached their maximum of about 78 MPa and 157 MPa when 0.1 % Sr was used. The hardness, on the other hand, reached a maximum of 40 BH when 1 % Sr was used.

The reason for the increase in the tensile and yield properties in the case of alloy 3 can be clearly attributed to its microstructure. It is very clear from the microstructure that the longitudinal shape of the Mg_2Sn intermetallic has influenced the increase in its tensile and yield strengths.
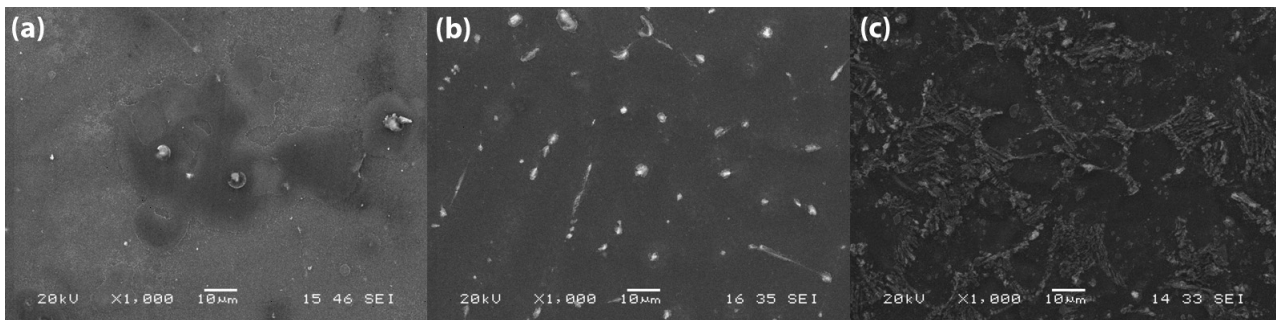

Figure 2: SEM micrographs showing microstructures of: a) alloy 1, b) alloy 3 and c) alloy 6
Slika 2: SEM-posnetki mikrostrukture: a) zlitina 1, b) zlitina 3 in c) zlitina 6
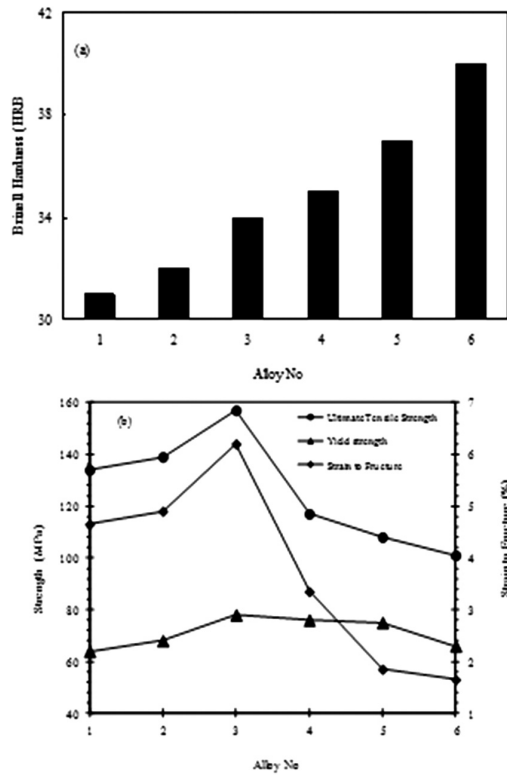
Figure 4: Mechanical test results for the alloys: a) hardness and b) strength and strain
Slika 4: Rezultati mehanskih preizkusov zlitin: a) trdota in b) trdnost in deformacija

4 CONCLUSIONS

1. The microstructures of all the above alloys consisted of the α-Mg and Mg$_2$Sn phases.
2. The strontium addition modified the microstructural shapes of the intermetallics.
3. The addition of Sr affected the UTS, yield and elongation only to a certain extent.
4. The hardness increase was directly proportional to the increase in strontium.

5 REFERENCES

[1] A. Yu, S. Wang, N. Li, H. Hu, Journal of Materials Processing Technology, 191 (**2007**), 247–250
[2] H. Hu, Journal of Materials Science, 33 (**1998**), 1579–1589
[3] H. Q. Sun, Y. N. Shi, M. X. Zhang, Surface and Coating Technology, 202 (**2008**), 2859–2864
[4] W. Huang, B. Hou, Y. Pang, Z. Zhou, Wear, 260 (**2006**), 1173–1178
[5] T. A. Leil, N. Hort, W. Dietzel, C. Blawert, Y. Huang, K. U. Kainer, K. P. Rao, Transactions of Nonferrous Metals Society of China, 19 (**2009**), 40–44
[6] S. Kleiner, O. Beffort, A. Wahlen, P. J. Uggowitzer, Journal of Light Metals, 2 (**2002**), 277–280
[7] H. Liu, Y. Chen, H. Zhao, S. Wei, W. Gao, Journal of Alloys and Compounds, 504 (**2010**), 345–350
[8] S. Li, B. Tang, D. Zeng, Journal of Alloys and Compounds, 437 (**2007**), 317–332
[9] H. Liu, Y. Chena, Y. Tang, S. Wei, G. Niu, Journal of Alloys and Compounds, 440 (**2007**), 122–126

THE EFFECT OF BINDER ON CHEMICALLY PRECIPITATED HYDROXYAPATITE DURING SPRAY DRYING

VPLIV VEZIVA NA KEMIJSKO IZLOČENI HIDROKSIAPATIT MED ATOMIZACIJO

Fatih Erdem Baştan, Ezgi Demiralp, Yıldız Yaralı Özbek, Fatih Üstel

Sakarya University, Engineering Faculty, Department of Metallurgical and Materials Engineering, Esentepe Campus, 54187 Sakarya, Turkey
yyarali@sakarya.edu.tr

The synthesis of appropriate calcium phosphate powders for thermal-spraying applications is a fundamental, crucial stage in the production of bioceramical coatings coupled with the desired characteristics. The performance, lifespan and quality of the resulting biological coating in-vivo is largely dependent on the coating morphology, phase composition, particle size and the crystallites of the spray powders. In order to achieve very reliable coatings from thermal-spray processes, spherical powders of a specified size distribution are recommended. The aim of this work was to produce hydroxyapatite powder with a chemical precipitation method and to reshape it in a spray dryer and investigate the effect of binder on the powder structure to provide an insight into the preparation and characterization aspect of HA powders using the spray-drying process. Ethanol, pure water and polyvinilalcohol (PVA) + ethanol were used as the binder. Different temperatures were applied in the spray dryer. Then, the precipitated, spray-dried powders were examined for morphology. Scanning electron microscopy (SEM), X-ray diffraction (XRD), (EDX) and ICP were used to characterize the specimen powders.

Keywords: hydroxyapatite, chemical precipitation, spray dryer, ICP (Inductively Coupled Plasma)

Sinteza primernega prahu kalcijevega sulfata za termično naprševanje, povezana z želenimi lastnostmi, je osnovna in ključna faza pri izdelavi biokeramičnih prevlek. Uspešnost, zdržljivost in kvaliteta biološke prevleke v živo je močno odvisna od morfologije prevleke, fazne sestave, velikosti delcev in kristalnih zrn naprševanega prahu. Za zagotovitev zelo zanesljivega premaza se priporoča uporaba prahu z okroglimi delci določene porazdelitve velikosti zrn. Cilj tega dela je izdelati prah hidroksiapatita (HA) z metodo kemijskega izločanja, s preoblikovanjem z atomizacijo in preiskati učinek veziva na strukturo prahu, da bi dobili vpogled v načine priprave in karakterizacijo HA-prahov z atomizacijo. Kot veziva so bili uporabljeni etanol, čista voda in polivinil alkohol, (PVA) + etanol. Pri atomizaciji so bile uporabljene različne temperature. Nato je bila pregledana morfologija atomiziranega prahu. Karakterizacija vzorcev prahov je bila izvršena z vrstično elektronsko mikroskopijo (SEM), rentgensko difrakcijo (XRD), energijsko disperzijsko rentgensko spektroskopijo (EDX) in induktivno sklopljeno plazmo (ICP).

Ključne besede: hidroksiapatit, kemijsko izločanje, atomizacija, induktivno sklopljena plazma ICP

1 INTRODUCTION

Bone is formed by collagen fibres and hydroxyapatite natural bone tissue can be considered as a composite consisting of a mineralized collagen matrix.[1] Hydroxyapatite (HAp) $Ca_{10}(PO_4)6(OH)_2$ and other related calcium phosphate minerals have been evaluated as implant materials for many years due to their good biocompatibility and bioactivity as well as their similarity with the inorganic components of the hard tissues in natural bones. Their Ca/P ratio of 1.5–2.0 makes them an excellent choice for most dental and orthopedic applications in the form of bioceramic coatings. Moreover, HA has been used as a biological chromatography support in protein purification and DNA isolation. Also, HA is currently used for the fraction and purification of a wide variety of biological molecules, such as subclasses of enzymes, antibodies fragments and nucleic acids.[2–6]

Several methods, such as precipitation, solid-state synthesis, hydrolysis, wet chemical, hydrothermal and sol-gel methods have been used to prepare synthetic HAp. The synthetic HAp is used for coating in medical applications.

The HAp coating produced by plasma-spraying technology combines the mechanical advantages of a metal substrate with the excellent biological properties of HAp. Some important factors are the particle size, particle size distribution and particle morphology, which affect the lifetime and quality of the resulting biological coating.[7,8]

These important factors determine the flow characteristics in the powder-feeding systems and the melting behavior in the plasma jet.[2,3]

The hydroxyapatite powder size is very important for a thermal-spray coating system. Therefore, we have to increase the size of the powder for a good flow rate. The spray-dryer system was used to adjust the particle size. The spray-drying method is a kind of granule production technique. The advantages of this method are very simple and the particle size can be controlled quite easily. The process parameters are the slurry concentration, the compressed-air flow rate and the liquid flow rate, which are affected by the specific surface area and size distribution of the final products.[4] The morphology of the powders is generally spherical, the other morphologies are, for example, mushroom-like,[9] doughnut-like,[9] hollow structures[10] etc.

In this study we fabricated HAp powders with the chemical precipitation method and the produced powders were granulated as spherical powders using the spray-drying method by controlling the process parameters. Different binders (pure water, PVA (polyvinyl alcohol) and ethanol) were used for the slurry. The resultant spherical powders were investigated to see the effect of binders on the powder properties (morphology and particle size distribution). The final spherical powders were prepared as bulk materials and sintered. Scanning electron microscopy (SEM), X-ray diffraction (XRD) and inductively coupled plasma (ICP) were used to characterize the powders and the bulk materials.

2 MATERIALS AND METHOD

HAp particles were synthesized by a chemical precipitation method, with calcium nitrate tetrahydrate $(Ca(NO_3)2 \cdot 4H_2O)$ as the calcium source, phosphoric acid (H_3PO_4) as the phosphorous source, and ammonium hydroxide (NH_4OH) as the pH regulator. $(Ca(NO_3)_2 \cdot 4H_2O)$ and (H_3PO_4) were separately dissolved in distilled water continuously for 30 min. The dissolved solutions were mixed together and added (NH_4OH) to obtain the initial pH values of the reaction solutions as 11.00. The mixture was stirred at a speed of 250 r/min. The resulting suspension was aged for 24 h at room temperature and then filtered. The product was washed with water to remove the residual impurities. The precipitated powders were dried at 105 °C to remove the undesired impurities. The dried powders were mixed with pure water, and PVA and ethanol were used as a binder to obtain a slurry for

the spray dryer. Inlet temperatures of 175 °C, 190 °C and 200 °C and a 1.5 bar pressure were chosen for the spray drying. The final product was shaped as a bulk material and sintered at 1050 °C for 1 h.

3 RESULTS AND DISCUSSION

The XRD result of the hydroxyapatite after the sintering process is shown in **Figure 1**. The peaks are sharp and match with the reference hydroxyapatite peaks. The powder has a crystalline structure. These results revealed that hydroxyapatite with a chemical precipitation method could be produced. Also, the composition of the powder was given in **Table 1** (i.e., the results of the ICP). It was shown that the powder not only has Ca and P elements, but also has Fe, Mg and Zn.

Figue 2a shows that the powders had an irregular, and an angular shape distribution, and also range widely.

The SEM micrographs of the powder in **Figures 2b** and **2c** revealed that the powders produced by spray drying had a less spherical and porous microstructure. The high degree of porosity could be due to the elimination of the binder that was used in the binding and agglomeration of the spray-dried powder. Moisture and gases were also released and eliminated as a result of spray drying at an elevated temperature of 200 °C.[11]

Also, these porosities appear as a small surface depression (**Figures 2c** and **2d**), which may be minimized and the material restored to a denser structure through calcination or sintering. Visible colour changes were seen in powder. The colour changes were due to the presence of manganese ions or other transition-metal elements located in the crystal lattice structure. Although they may not have any significant effect on the biocom-
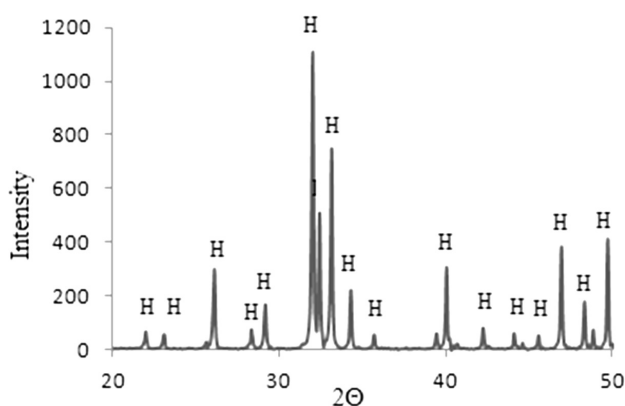
Figure 1: XRD peaks after sintering
Slika 1: XRD-spekter po sintranju

Table 1: ICP analysis result
Tabela 1: Rezultati ICP-analize

Composition	Amount in mass fractions, $w/\%$
PO_4	61.05
Ca	38.50
Fe	0.0030
Mg	0.12
Zn	0.0068
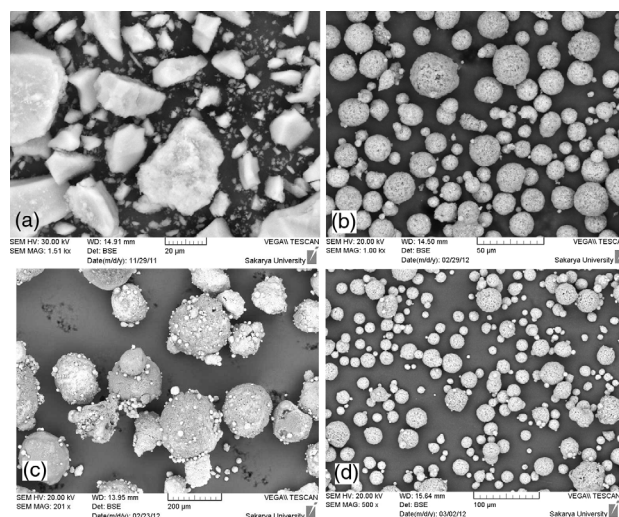
Figure 2: a) Hydroxyapatite microstructure before spray drying, b) after spray drying (175 °C, 1.5 bar, ethanol), c) (200 °C, 1.5 bar, ethanol), d) (175 °C, 1.5 bar, ethanol + PVA)
Slika 2: a) Mikrostruktura hidroksiapatita pred atomizacijo, b) po atomizaciji (175 °C, 1,5 bar, etanol), c) (200 °C, 1,5 bar, etanol), d) 175 °C, 1,5 bar, etanol + PVA)
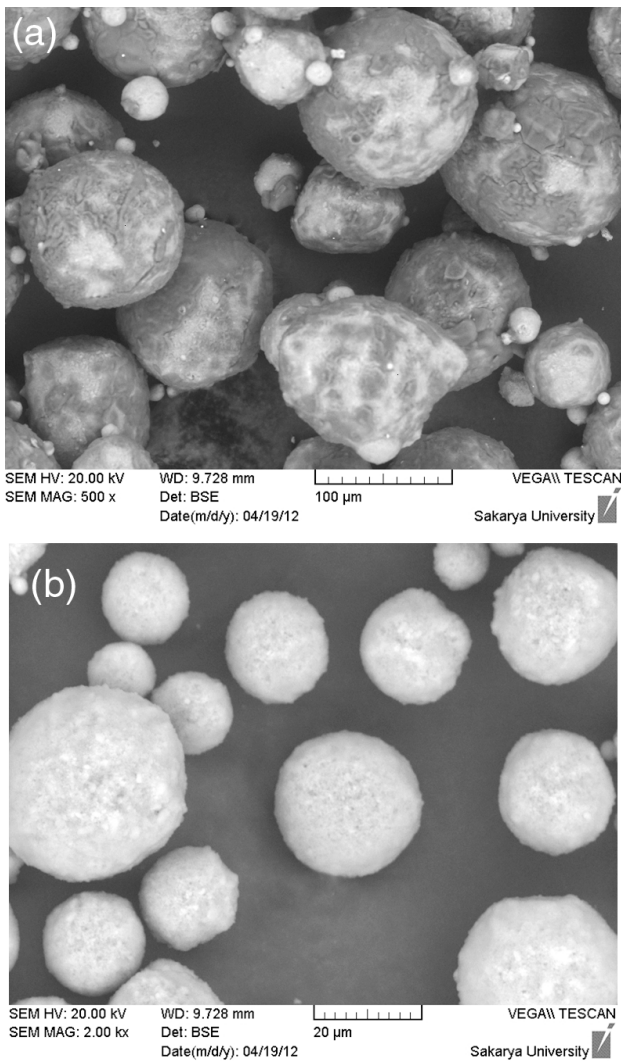
Figure 3: a) After spray drying (175 °C, 1.5 bar, pure water), b) (190 °C, 1.5 bar, pure water)
Slika 3: a) Po atomizaciji (175 °C, 1,5 bar, čista voda), b) (190 °C, 1,5 bar, čista voda)

patibility of HA, the consumer acceptance should be duly considered.[12]

When the binder is ethanol for drying, the optimal parameters are 175 °C inlet temperature and 1.5 bar pressure, for pure water the optimal parameters are 175 °C inlet temperature and 1.5 bar pressure.[13] Spherical particles are seen in **Figure 2b**. The powders have a porous structure because of the early evaporation of the ethanol. A porous and hollow structure with the slow diffusion of solute and a quick solvent evaporation were obtained.[14] Irregular particles are seen in **Figure 2c**. Increasing the inlet temperature results in quick evaporation of the moisture, but a high temperature may cause chemical/physical distortion.[15] The spherical and porous particles are seen in **Figure 3**. Ethanol + PVA were chosen as binders. The results are same as those obtained from the ethanol-added samples. The PVA affected only the particle size. After the particle size analysis, it was

seen that the particle size increases with increasing PVA addition for a good binding. The average particle sizes were 27 μm and 41 μm for the ethanol and ethanol + PVA, respectively.

It was shown in **Figures 3a** and **3b** that spherical particles were obtained at both 175 °C and 190 °C, but it seems that particles have moisture because of the insufficient inlet temperature for drying in **Figure 3a**. Increasing the temperature made the particles dry. Particles have less porosity when using pure water for the binding. Because the pure water's evaporation temperature is higher than the ethanol's, the binder holds together all particles during the process.[15]

4 CONCLUSIONS

Hydroxyapatite powders could be produced by a chemical precipitation method and reshaped with a spray dryer. The change in the binder impacted on the spray-drying parameters. The optimal inlet temperatures are 175 °C for ethanol and 190 °C for pure water. The type of binder was affected by the particle structure. A volatile binder resulted in a lower particle density and the particles had more porosity. The binder holds together all the particles, and increasing the amount of the binder (like PVA) increases the particle size.

Spray-dried powder with the correct particle size is converted to flame spheroidized powder so as to improve the microstructural characteristics and the stability of the powder. A spherical geometry is very desirable for enhanced flowability and deposition consistency, which would eventually give rise to high-quality bioceramic coatings.

5 REFERENCES

[1] F. Chen, Z. C. Wang, C. J. Lin, Materials Letters, 57 (**2002**), 858–861

[2] O. Kikuo, A. I. Mikrajuddin, L. Wuled, I. Ferry, Preparation of functional nanostructured particles by spray drying, Advanced Powder Technol., 17 (**2006**) 6, 587–611

[3] S. W. K. Kweh, K. A. Khor, P. Cheang, An in vitro investigation of plasma sprayed hydroxyapatite (HA) coatings produced with flame-spheroidized feedstock, Biomaterials, 23 (**2002**) 3, 775–785

[4] E. S. Thian, K. A. Khor, N. H Loh, S. B. To, Processing of HA-coated Ti–6Al–4V by a ceramic slurry approach: an in vitro study, Biomaterials, 22 (**2001**) 11, 1225–1232

[5] A. Afshar, M. Ghorbani, N. Ehsani, M. R. Saeri, C. C. Sorrell, Some important factors in the wet precipitation process of hydroxyapatite, Materials & Design, 24 (**2003**) 3, 197–202

[6] E. Lugscheider, M. Knepper, K. A. Gross, J. Thermal Spray Tech., 1 (**1992**) 3, 215–222

[7] S. W. K. Kweh, K. A. Khor, P. Cheang, Journal of Materials Processing Technology, 89–90 (**1999**), 373–377

[8] A. J. Wang, Y. P. Lu, R. F. Zhu, S. T. Li, X. L. Ma, Powder Technology, 191 (**2009**), 1–6

[9] H. Liang, K. Shinohara, H. Minoshima, K. Matsushima, Analysis of constant rate period of spray drying of slurry, Chem. Eng. Sci., 56 (**2001**), 2205–2213

[10] R. Sun, Y. Lu, K. Chen, Materials Science and Engineering C, 29 (**2009**), 1088–1092

[11] F. E. Bastan, Kimyasal Çöktürme Yöntemiyle Gümüş İlaveli Hidroksiapatit Üretimi ve Spray Dryer ile Şekillendirilmesi, Master thesis, Sakarya university, 2012

[12] S. W. K. Kweh, K. A. Khor, P. Cheang, The production and characterization of hydroxyapatite (HA) powders, Journal of Materials Processing Technology, 89–90 (**1999**), 373–377

[13] T. Başargan, Püskürtmeli Kurutucuda Hidroksiapatit-Polimer Malzemelerin Hazırlanması, 2010

[14] K. Mehsana, Spray Drying Technology, An Overview, 2009

[15] R. Chumnanklang, T. Panyathanmaporn, K. Sitthiseripratip, J. Suwanprateeb, Freeform Fabrication of Hydroxyapatite via Three Dimensional Printing, Materials Science and Engineering, 27 (**2007**) 4, 914–921

PLASMA ELECTROLYTIC SATURATION OF 316 L STAINLESS STEEL IN AN AQUEOUS ELECTROLYTE CONTAINING UREA AND AMMONIUM NITRATE

PLAZEMSKO ELEKTROLITSKO NASIČENJE NERJAVNEGA JEKLA 316 L V VODNEM ELEKTROLITU S SEČNINO IN AMONIJEVIM NITRATOM

Levent Cenk Kumruoglu, Ahmet Özel

University of Sakarya, Engineering Faculty, Metallurgy and Materials Department, Esentepe-Sakarya, Turkey
lkumruoglu@sakarya.edu.tr

Plasma electrolytic saturation (PES) is an environmentally friendly electrochemical process that allows altering the surface chemistry and grain size of metallic substrates, negatively biased in an aqueous electrolyte containing ionic species such as N, O and C. Wear- and corrosion-resistive nanocrystalline layers consisting of carbides, nitro carbides, borides and nitro-carbon oxides could be fabricated with PES in short treatment durations. In this study, PES was performed on 316 L stainless steel in an electrolyte containing urea and ammonium nitrate with several treatment durations from 5 s to 30 min. The surface morphology, topography and microstructure were investigated with X-Ray diffraction, optical microscopy, scanning electron microscopy with energy dispersive spectroscopy, a surface profilometer and microhardness testing. The wear and friction properties were evaluated using a ball-on-plate, linear, reciprocating wear test at 1 N to 3 N applied loads with an alumina ball against both the treated and untreated substrates. It was found that PES can increase the wear resistance and mechanical properties of 316 L stainless steel.

Keywords: plasma electrolysis, saturation – diffusion, nitriding, wear, 316 L

Plazemsko elektrolitsko nasičenje (PES) je okolju prijazen elektrokemijski postopek, ki omogoča spreminjanje površinske kemije in velikost zrn v kovinski podlagi, ki je neustrezna v vodnem elektrolitu, ki vsebuje ione N, O in C. V kratkem času je mogoče s PES izdelati obrabno in korozijsko obstojne nanokristalne plasti iz karbidov, nitrokarbidov, botidov in nitro-karbo-oksidov. V tej študiji je bil PES uporabljen pri nerjavnem jeklu 316 L v elektrolitu, ki je vseboval sečnino in amonijev nitrat in so bili časi obdelave od 5 s do 30 min. Preiskovana je bila morfologija površine, topografija in mikrostruktura z rentgensko difrakcijo, svetlobno mikroskopijo, vrstično elektronsko mikroskopijo, energijsko disperzijsko spektroskopijo, s površinskim profilometrom in meritvijo trdote. Obraba in torne lastnosti so bile ocenjene z metodo kroglica na plošči z linearnim izmeničnim obrabnim preizkusom pri obtežbi od 1 N do 3 N s kroglico iz Al$_2$O$_3$ na obdelani in neobdelani površini. Ugotovljeno je bilo, da PES lahko poveča odpornost proti obrabi in izboljša mehanske lastnosti nerjavnega jekla 316 L.

Ključne besede: plazemska elektroliza, nasičenje – difuzija, nitriranje, obraba, 316 L

1 INTRODUCTION

To improve and alter the surface properties of metallic substrates with a plasma-electrolytic-saturation process,[1–7] interstitial atoms like C, N, O and species are diffused into the surface of a biased substrate from an aqueous medium containing interstitial atoms under the appropriate plasma conditions like specific temperature, potential, duration.[1–5] Plasma electrolysis is a special thermo-chemical-mechanical process employing electrolysis in an aqueous solution under particular conditions, for instance specific potential, current, electrolyte and durations.[1–7] Plasma electrolysis is a complex process, which couples physical metallurgy and electrochemical events, such as heating a work piece in a cathodic regime[2,4] (gas liberation, spark ignition, continuous plasma envelope, and arcing regime), where phase transformations and deformations occur simultaneously.

For the PES process, the selection of an electrolyte is relatively simple; for example, for the nitrocarbusing the electrolyte is composed of C/N-containing organic compounds in a conductive solution, e.g., KCl or Na$_2$CO$_3$. In contrast to conventional pack and liquid-based treatments using cyanide, various ecologically friendly organic compounds can be used to provide, with plasma thermal decomposition, desirable carbon/nitrogen ions and/or atoms for the treatment. PES can have a considerable strengthening effect on steel substrates. Even though a wide range of materials has been treated using a plasma-electrolytic-saturation technique,[2] very few studies exist in the literature that report on the wear resistance of oxy-nitrided or oxy-carbon-nitrided 316 L stainless steel. To evaluate the saturation phenomena and wear behaviour of the oxy-nitrided layer, different electrolytes, process durations and dry, reciprocating. sliding tests have been conducted. The modified phases on the surface were investigated with XRD (Rigaku) applying the standard 2θ-scan from 20 to 90 degrees and cross-sections of saturated layers were revealed with optical microscopy (Nikon) and scanning electron microscopy (JEOL 6600) with energy dispersive spectroscopy. The

surface roughness and microhardness of the samples were measured using a surface profilometer (Tencor P6) and a microhardness tester (Shimadzu HMV).

2 EXPERIMENTAL STUDIES

The testing coupons (10 mm × 20 mm × 1.5 mm) made from 316 L stainless steel were used as the substrate materials. The nominal composition of a substrate in mass fractions was Cr 18 %, Mn 1.6 %, Ni 10 %, C 0.02 %, Mo 2.1 %, N < 0.02 %, Fe balance. Prior to PES, the substrates were polished to $R_a \approx 0.05$ μm from 240 to 1200 grit with the emery paper and then with the alumina solution. The PES was carried out by using 24 kW DC power supply and in a specially designed instrumented rig shown in **Figure 1**. Two types of electrolyte at 25 °C were chosen as given in the following formulas, $m(E1) = 4$ kg urea, 40 g KOH and 4 l di-water (cond. 8 mS) and $m(E2) = 4$ kg ammonium nitrate, 4 l di-water, 20 g KOH (cond. 180 mS). The substrates were biased negatively and treated for 5 s and (1, 15 and 30) min at the potentials varying from 100 V (for E2) to 300 V (for E1). The breaking potentials were 550 V for E1 and 350 V for E2. The electrolyte was pumped from the container to the bottom surface of the samples and then the potential was increased manually to fix the plasma envelope. The treated surfaces were tested using the following parameters: the normal loads of 1 N and 3 N, the track length of 10 mm, the frequency of 5 Hz, the sliding speed of 0.1 m s^{-1} and the sliding distances of 100 m and 1200 m. The average value of the friction coefficient was measured in both reciprocating directions of the bearing ball. The CSM tribometer was used for the wear tests. Before and after each test, both the sample and the alumina ball (10 mm) were cleaned ultrasonically in acetone and dried with hot air.
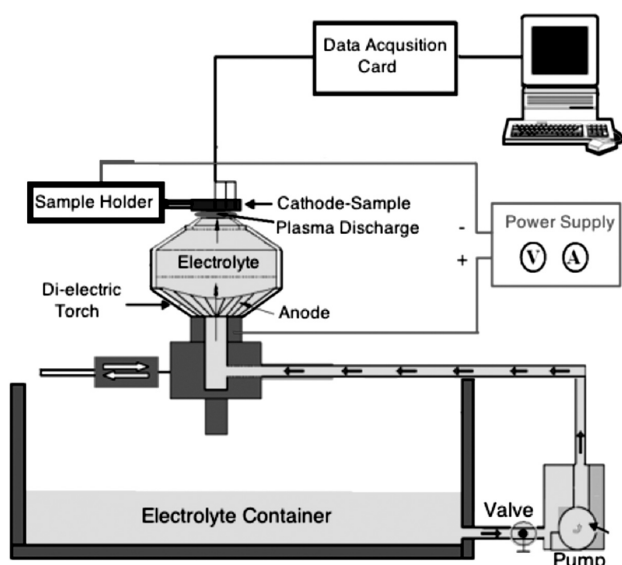

Figure 1: Schematic drawing and picture of the PES setup
**Slika 1:** Shematski prikaz PES-sestava

3 RESULTS AND DISCUSSION

Recent studies have revealed that plasma saturation can produce compound nitrides and oxide phases, e.g., $(Fe,Cr)_2O_4$, Fe_3O_4+FeN, CrN, $\gamma_{(N)}$.[3–6] The XRD patterns of the samples treated with E1 and E2 are given in **Figures 2a** and **b**. SEM and OM studies revealed that the surfaces consist of Fe, Cr_2O_4, Fe_3O_4, $FeN_{0.076}$ and a γ_N saturated layer that is 3 μm to 40 μm thick. In addition to the mixture phases, Fe_2O_3 was detected in the sample saturated in urea for 5 s. According to the Fe-O binary system and the phase-stability diagram, Fe_2O_3 and Fe_3O_4 can be formed at 400 °C, depending on the oxygen concentration, and FeO is not stable below 570 °C. In the Fe-O system, a larger amount of oxygen causes a formation of hematite at high temperatures. However, in the H_2 atmosphere, Fe_2O_3 may be reduced to Fe_3O_4.[8] In plasma electrolysis hydrogen can be produced at the cathode.[3] Hence, longer plasma durations may cause the formation of larger and thicker amounts of Fe_3O_4 and a broadening of the XRD lines. SEM-EDS analyses proved the nitrogen, oxygen and carbon diffusions for both plasma processes (**Figure 3**). The microhardness testing was performed on the saturated layers. The maximum value of 535 HV was observed for the PES using the urea electrolyte for 30 min. However, the hardness testing
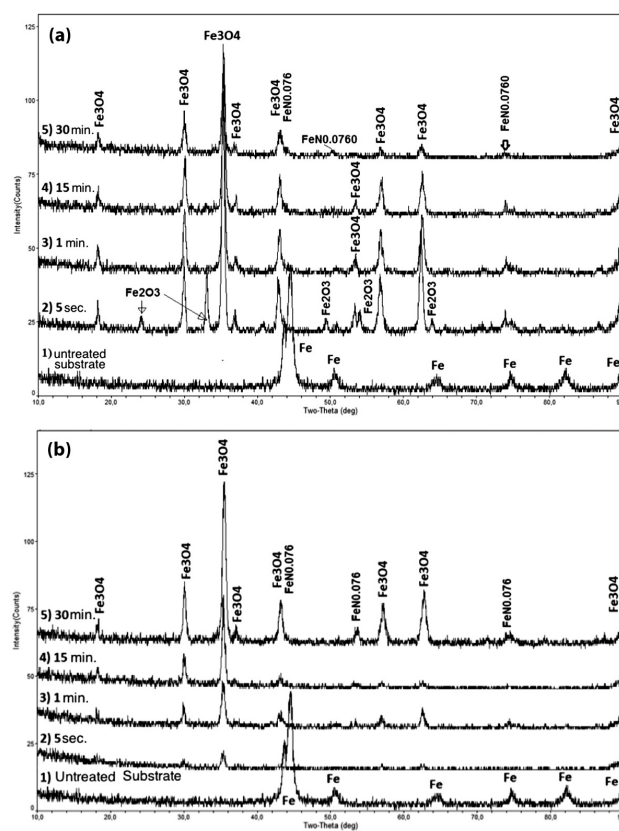
Figure 2: XRD of substrates saturated with electrolytic plasma with: a) urea and b) with ammonium nitrate
Slika 2: XRD podlage, nasičene z elektrolitsko plazmo: a) s sečnino in b) z amonijevim nitratom
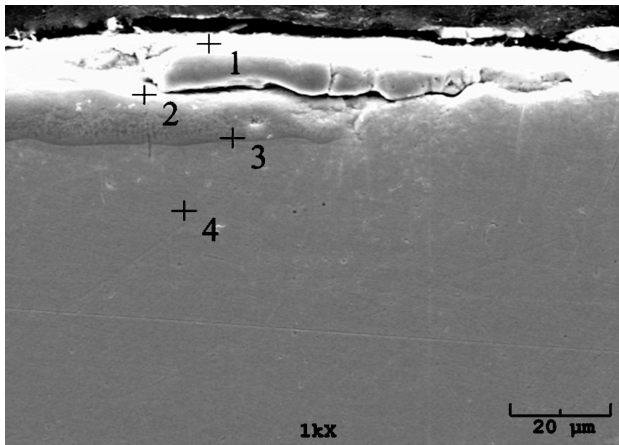
1	w/%	2	w/%	3	w/%	4	w/%
C	21.41	C	1.007	C	3.120	C	3.385
N	0.000	N	0.678	N	0.498	N	0.000
O	41.10	O	38.96	O	19.400	O	2.017
Fe	35.06	Cr	9.472	Cr	22.418	Cr	18.07
Ni	1.898	Fe	47.94	Fe	44.217	Fe	68.78
Mo	0.519	Ni	1.579	Ni	9.984	Ni	7.540
	100.0	Mo	0.354	Mo	0.363	Mo	0.199
			100.0		100.0		100.0

Figure 3: Cross-section SEM view and EDS analysis of a saturation layer (1 min with E1)
Slika 3: Prerez (SEM) in EDS-analiza nasičene plasti (1 min z E1)

cannot be performed on the PES substrates using an ammonium nitrate electrolyte because of the rough and thin hardened layer. On the other hand, the surface hardness was measured as 550 HV using light indentation loads such as 10 g (**Figure 4**). Recently, the post-oxidation treatment was studied on nitrided layers.[9] The studies suggest that a thin Fe_3O_4 layer improves the wear resistance of a nitrided layer.[9] PES may be described as a single-step compound diffusion process that enables both nitriding and post oxidation. Nitriding can be performed in a relatively low temperature range of 400–600 °C.[2,3] In PES, the surface of the substrate may reach this temperature in a few seconds.[3] It is possible to heat a substrate
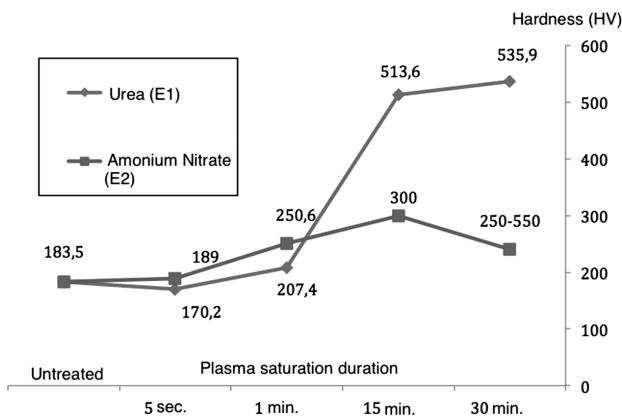

Figure 4: Cross-sectional microhardness profile of saturated samples
Slika 4: Mikrotrdota na prečnem prerezu nasičenih vzorcev

above the nitriding temperatures; if the temperatures increase the oxidation may occur on the nitrided layer because of the oxygen atoms in the electrolyte. The wear behavior and the friction coefficient of the saturated layers sliding against the alumina ball 10 mm under a load of 3 N is shown in **Figures 5a** and **b**, respectively. It can be seen that the wear resistance of the substrate saturated for (1, 15 and 30) min in the E2 electrolyte is much greater than that of the untreated substrate. The untreated sample was marked with the symbol "0". Also, there are a small drop for the PES 1 min and sharp drops for the PESs 15 min and 30 min in the friction coefficient over the sliding distance 1200 m. The Fe_3O_4 layer on the saturated steel may cause this kind of friction behavior.[9] The wear resistance of the substrate treated with the urea electrolyte was improved after the PES 15 min. On the other hand, a good result was observed for the PES 3 min. This may be related to both an increase in the surface hardness and the thickness of the oxynitrided layer. The thin layers (treated for 5 s) were probably delaminated at the onset of the wear test because there was no significant change in the friction coefficients of both electrolyte groups. Below the sliding distance 100 m the wear resistance of the PES layers treated for 5 s in the ammonium nitrate electrolyte was 2.5 times better than that of the untreated substrate, while for the sample treated for 30 min the wear resistance was 10 times higher than that of the untreated one and the worn track was very thin and hardly
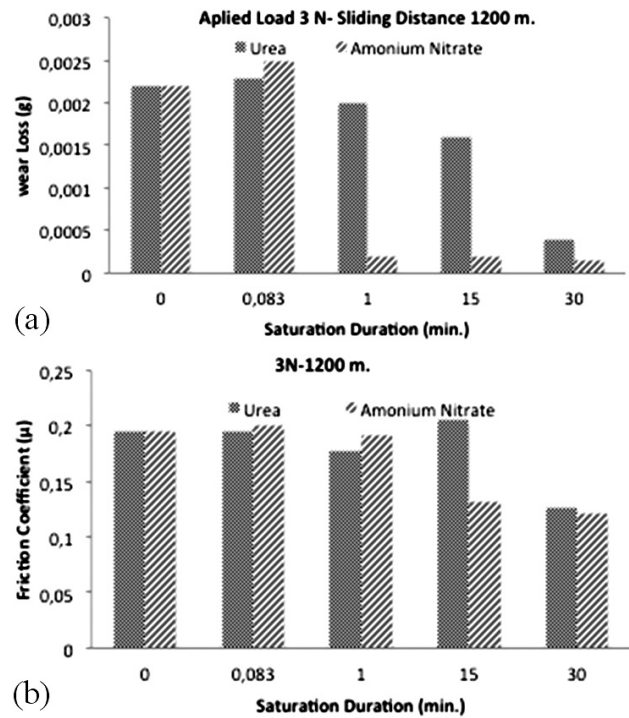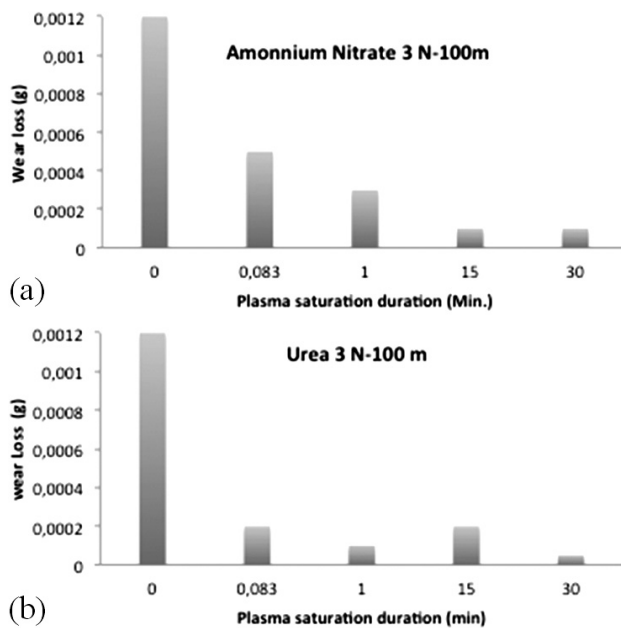

(a)

(b)

Figure 5: a) Wear properties of PES layer for 3 N and 1200 m sliding distance and b) the friction coefficient
Slika 5: a) Obrabne lastnosti PES-plasti pri 3 N in 1200 m drsne poti in b) torni koeficienti

(a)

(b)

Figure 6: Wear properties of PES layer for 3 N and 100 m sliding distance for both electrolytes
Slika 6: Obrabne lastnosti PES-plasti pri 3 N in 100 m drsne poti za oba elektrolita

observed (**Figure 6a**). On the other hand, the wear-test results for the samples treated with the urea solution were slightly better than the results for the ammonium nitrate electrolyte (**Figure 6b**).

4 CONCLUSIONS

The electrolytes containing urea and ammonium nitrate can be used for the surface saturation of 316 L stainless steel. The PES layers consist predominantly of the $FeCr_2O_4$, FeN and Fe_3O_4 phases. In short PES dura-

tions, Fe_2O_3 was observed with the other phases because of the low substrate temperature. At the beginning of PES, the expanded austenite can be formed with an atomic diffusion; however, an increase in the temperature of the substrate gives rise to a formation of metal (nitro) oxides. The H_2 gas at the cathode causes a reduction of hematite; so a stable mix of the $FeCr_2O_4$, $FeN_{0,076}$ and Fe_3O_4 phases can be formed on the surface. These phases increase the hardness and reduce the friction coefficient, thus increasing the wear resistance. There was no scaling or delaminating of the oxide layers under the all-mechanical tests.

The value of the breaking potential depended on the conductivity of the electrolyte. The breaking potentials of the electrolyte were 550–600 V for the conductivity of 8 mS (E1) and 300–350 V for the conductivity of 180 mS (E2).

The layer thickness increases with the treatment time, resulting in an associated increase in the surface hardness.

5 REFERENCES

[1] M. Aliofkhazrae, A. S. Rouhaghdam, T. Shahrabi, Journal of Alloys and Compounds, 460 (**2008**), 614–618
[2] A. L. Yerokhin et al., Surface and Coatings Technology, 122 (**1999**) 2–3, 73–93
[3] C. Cionea, PhD thesis, The University of Texas At Arlington, 2010
[4] T. Paulmier, J. M. Bell, P. M. Fredericks, Thin Solid Films, 515 (**2007**), 2926–2934
[5] P. Taheri, C. Dehghanian, Transaction B: Mechanical Engineering, 16 (**2009**) 1, 87–91
[6] L. C. Kumruoğlu, A. Özel, Materials and Manufacturing Processes, 25 (**2010**) 9, 923–931
[7] L. C. Kumruoglu, D. A. Becerik, A. Ozel, A. Mimaroglu, Materials and Manufacturing Processes, 24 (**2009**), 781
[8] Lin et. al., Thermochimica Acta, 400 (**2003**), 61–67
[9] M. L. Fares, K. Chaoui, J. Le Coze, Surf. Interface Analysis, 41 (**2009**), 4549–4559

MINIMIZATION OF SURFACE DEFECTS BY INCREASING THE SURFACE TEMPERATURE DURING THE STRAIGHTENING OF A CONTINUOUSLY CAST SLAB

ZMANJŠEVANJE POVRŠINSKIH NAPAK Z ZVIŠANJEM TEMPERATURE POVRŠINE KONTINUIRNO ULITEGA SLABA MED RAVNANJEM

Josef Stetina, Tomáš Mauder, Lubomir Klimes, Frantisek Kavicka

Brno University of Technology, Technicka 2, 616 69 Brno, Czech Republic
stetina@fme.vutbr.cz

Surface temperatures of cast slabs on small-radius segments as well as on the unbent areas belong to the parameters that affect the surface quality of continuously cast slabs. Older machines for continuous casting were designed with regard to the quantity (the amount of cast slabs) rather than the quality of the production. Therefore, an adaptation of the secondary cooling is required in order to obtain the desired surface temperatures. The modification consists of a dynamic control of the secondary cooling, surface-temperature monitoring by means of a numerical model of the temperature field as well as a prospective replacement of the cooling nozzles. In order to optimize and control the secondary cooling, characteristics of the nozzles, especially the influences of the water-flow rate, air pressure, casting speed, surface temperatures and heat-transfer coefficient under the nozzles have to be known. Moreover, the heat-transfer coefficient can also be influenced by the age of the nozzles. The paper deals with the relationships between these influences and their impacts on the temperature field of a cast slab. The results are presented for the 1530 mm × 250 mm slabs that are cast in Evraz Vítkovice Steel where the main author's dynamic, 3D solidification model is used, in its off-line version, to control the production interface. The results can be used for the preparation of a real casting process.

Keywords: optimization of the temperature field, surface temperature of a slab, characteristics of nozzles, continuous casting

Temperatura površine ulitega slaba pri segmentih z majhnim radiusom, kot tudi na neukrivljeni površini, spada k parametrom, ki vplivajo na kvaliteto površine kontinuirno ulitega slaba. Starejše naprave za kontinuirno ulivanje slabov so bile pripravljene bolj za večjo zmogljivost kot pa za kvaliteto. Zato je potrebna prilagoditev sekundarnega ohlajanja, da se zagotovi doseganje želene temperature površine. Prilagoditev sestoji iz dinamične kontrole sekundarnega hlajenja, kontrole temperature površine z numeričnim modelom temperaturnega polja, kot tudi morebitna zamenjava hladilnih šob. Optimiranje in kontrola sekundarnega hlajenja je mogoča s poznanjem značilnosti šob in še posebno vpliva hitrosti pretoka vode, tlaka zraka, hitrosti ulivanja, temperature površine in koeficienta prenosa toplote pod šobami. Poleg tega na koeficient prenosa toplote lahko vpliva tudi starost šob. Ta članek obravnava odnos med naštetimi vplivi in njihov učinek na temperaturno polje ulitega slaba. Predstavljeni so rezultati za ulit slab 1530 mm × 250 mm. Avtorjev dinamični 3D-model strjevanja se uporablja za kontrolo vmesnika pri proizvodnji in teče v off-line-verziji. Rezultati se lahko uporabijo kot pripravljalno orodje za realni postopek ulivanja.

Ključne besede: optimiranje temperaturnega polja, temperatura površine slaba, značilnosti šob, kontinuirno ulivanje

1 INTRODUCTION

The presented in-house model of the transient-temperature field of the blank from a slab caster (**Figure 1**) is unique as, in addition to being entirely 3D, it can work in real time. The numerical model covers the temperature field of the complete length of the blank (i.e., from the meniscus inside the mould all the way down to the cutting torch) with up to one million nodes.[1]

The concasting machine (caster) for the casting of slabs (**Figure 1**) has the secondary-cooling zone sub-divided into thirteen sections due to the convection of a greater amount of heat from the voluminous slab casting. The first section engages the water nozzles from all sides of a slab. The remaining twelve sections engage air-mist cooling nozzles, positioned only on the upper and lower sides of the concasting. It is therefore very important to determine the correct boundary conditions for a numeri-
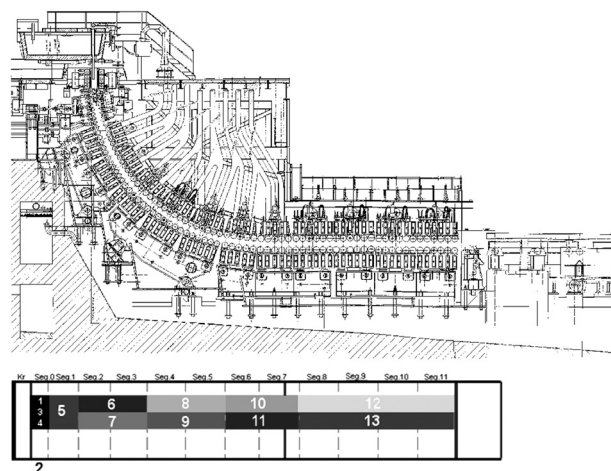
Figure 1: Radial caster and positions of the nozzles along the slab caster in 13 individual zones
Slika 1: Livni stroj z radijem in pozicija šob vzdolž naprave za ulivanje slabov v 13 posameznih področjih

cal model of the temperature field[2] taking into account a real caster that has many types of nozzles with various settings positioned inside a closed cage. A real caster contains a total of 8 nozzle types and geometrical layouts. The aim is to modify the secondary cooling zones 6, 8, and 10 so as to increase the surface temperature of a slab in a small radius at the point of the straightening. Currently, the Lechler 100.638.30.24 air-mist nozzles are installed in the cooling zones 6, 8, and 10 (**Figure 2**).
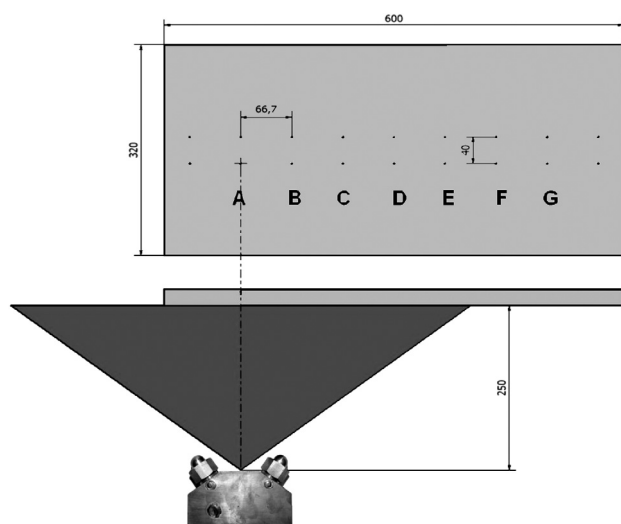
2 MODEL OF THE TEMPERATURE FIELD OF A SLAB

The presented in-house model of the transient-temperature field of the blank from a slab caster (**Figure 1**) is unique as, in addition to being entirely 3D, it can work in real time. It is possible to adapt its universal code and apply it to any slab caster. The numerical model covers the temperature field of the complete length of the blank (i.e., from the meniscus inside the mould all the way down to the cutting torch) with up to one million nodes.

The temperature field of the slab passing through a radial caster with a large radius can be simplified with the Fourier-Kirchhoff equation, where only the v_z component of the velocity is considered.

$$\rho \cdot c \frac{\partial T}{\partial \tau} = \frac{\partial}{\partial x}\left(k\frac{\partial T}{\partial x}\right) + \frac{\partial}{\partial y}\left(k\frac{\partial T}{\partial y}\right) + \frac{\partial}{\partial z}\left(k\frac{\partial T}{\partial z}\right) + $$
$$+ \rho \cdot c \cdot v_z \frac{\partial T}{\partial z} + \dot{Q}_{source} \quad (1)$$

Equation (1) must cover the temperature field of the blank in all three stages: above the liquidus temperature (i.e., the melt), the interval between the liquidus and solidus temperatures (i.e, the so-called mushy zone) and beneath the solidus temperature (i.e., the solid phase). It is therefore convenient to introduce the thermodynamic function of specific volume enthalpy $H_v = c\rho T$, which is dependent on the temperature and also includes the phase and structural heats (**Figure 3**).

Heat conductivity k, specific heat capacity c and density ρ are thermophysical properties that are also the functions of temperature. Equation (1) therefore takes the following form:

$$\frac{\partial H_v}{\partial \tau} = \frac{\partial}{\partial x}\left(k\frac{\partial T}{\partial x}\right) + \frac{\partial}{\partial y}\left(k\frac{\partial T}{\partial y}\right) + \frac{\partial}{\partial z}\left(k\frac{\partial T}{\partial z}\right) + v_z\frac{\partial H_v}{\partial z} \quad (2)$$
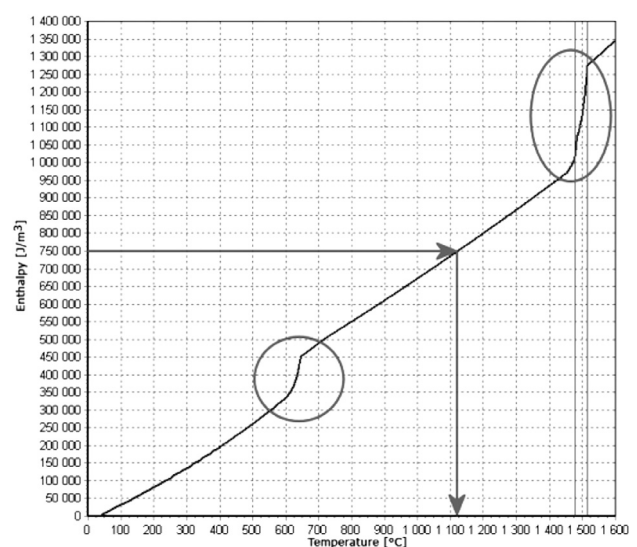
The unknown enthalpy of the general node of the blank in the following instant $(\tau + \Delta\tau)$ is given by the explicit formula:

$$H_{vi,j,k}^{(\tau+\Delta\tau)} = H_{vi,j,k}^{(\tau)} + (QZ1_{i,j} + QZ_{i,j} + QY1_{i,j} + QY_{i,j} + $$
$$+ QX1 + QX) \cdot \frac{\Delta\tau}{\Delta x \cdot \Delta y \cdot \Delta z} \quad (3)$$

Figure 3 indicates how the temperature model for the calculated enthalpy in equation (3) determines the unknown temperature[3]. All the thermodynamic properties of cast steel, dependent on its chemical composition and the cooling rate, enter the calculation as the functions of temperature.[3] This is therefore a significantly non-linear task because, even with the boundary conditions, their dependence on the surface temperature of the blank is considered here.

The boundary conditions are, therefore, as follows:

1. $T = T_{cast}$ the level of steel $\quad$ (4a)

2. $-k\frac{\partial T}{\partial n} = 0$ the plane of symmetry $\quad$ (4b)

3. $-k\frac{\partial T}{\partial n} = htc \cdot (T_{surface} - T_{mould})$ inside the mould $\quad$ (4c)

Figure 2: Diagram of the measurement configuration of the cooling effects of a nozzle
Slika 2: Prikaz konfiguracije meritve hladilnih učinkov šobe

Figure 3: Enthalpy function for steel showing the phase and structural changes
Slika 3: Krivulja entalpije jekla, ki prikazuje fazne premene in spremembe v mikrostrukturi

4. $-k \dfrac{\partial T}{\partial n} = htc \cdot (T_{surface} - T_{amb}) + \sigma\varepsilon(T_{surface}^{4} - T_{amb}^{4})$

within the secondary and tertiary zones   (4d)

5. $-k \dfrac{\partial T}{\partial z} = \dot{q}$ beneath the rollers   (4e)

The boundary conditions are divided into the area of the mould, the area of the secondary cooling and the area of the tertiary cooling.

The initial condition for the investigation is the setting of the temperature in individual points of the mesh. A suitable temperature is the highest possible temperature, i.e., the pouring temperature. The explicit difference method is used for solving this problem. The characteristic of this method is that the stability of the calculation is dependent on the magnitude of the time step. The model uses a method for adapting the time step, i.e., the time step entered by an operator is merely a recommendation and the software is modifying it throughout the calculation.[4]

3 HEAT-TRANSFER COEFFICIENT OF THE NOZZLE

The cooling by the air-mist water nozzles has the main influence and it is, therefore, necessary to establish the relevant heat-transfer coefficient of the forced convection. Commercially sold models of the temperature field describe the heat-transfer coefficient beneath the nozzles as a function of the incident quantity of water per unit area. They are based on various empirical relationships. However, this procedure is undesirable. The model discussed in this paper obtains its heat-transfer coefficients from the measurements of the spraying characteristics of all the nozzles used by the caster on the so-called hot plate in an experimental laboratory and for a sufficient range of operational pressures of water and a sufficient range of casting speeds of a slab. This
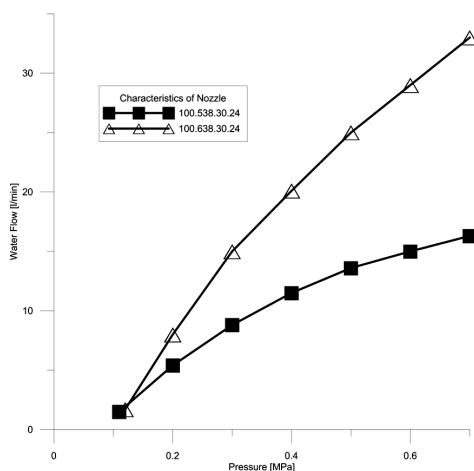
approach represents a unique combination of an experimental measurement in a laboratory and a numerical model for the calculation of the non-linear boundary conditions beneath the cooling nozzle.

A laboratory device enables separate measurements of individual nozzles. It includes a steel plate mounted with 18 thermocouples, heated by an external electric source. The steel plate is heated to the testing temperature, than it is cooled by a cooling nozzle. On the return move the nozzle is covered with a deflector, which enables the movement of the nozzle without cooling the surface. This device measures the temperatures beneath the surface of the slab – again by means of thermocouples.[5]

The laboratory device allows the setting of:
- the nozzle type,
- the flow of water,
- the air pressure,
- the distance between the nozzle and the investigated surface,
- the surface temperature,
- the shift rate.

Since the cooling nozzle 100.638.30.24 for the minimum water flow appeared to be too intense, the measurements were made for the smaller nozzle 100.528.30.24 (**Figure 4**).

Based on the temperatures measured in dependence of the time, the heat-transfer coefficients (*htc*) are calculated with an inverse task. They are then processed further using an expanded numerical and identification model and converted to the coefficients of function *htc*(*T,y,z*) (**Figure 5**), which express *htc* in dependence of the surface temperature and also the position of the concasting with respect to the nozzle. The Lechler air-mist nozzles show a low dependence of the heat-transfer coefficient on the slab surface temperature. The value of *htc* on the surface of a slab, as it enters the secondary-cooling zone, significantly affects the process simulation with respect to the temperature field, the metallurgical length and also the other technological properties. It, therefore, affects the prediction of the quality of a slab.

Figure 4: Characteristics of the Lechler nozzles 100.638.30.24 and 100.528.30.24
Slika 4: Značilnosti šobe Lechler 100.638.30.24 in 100.528.30.24
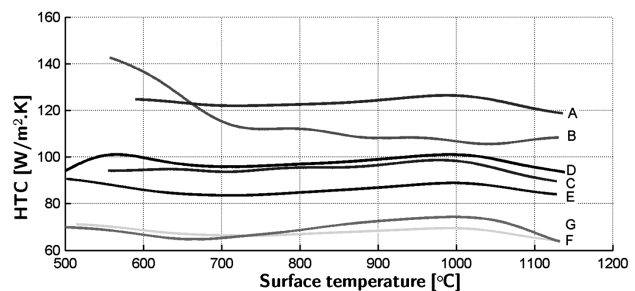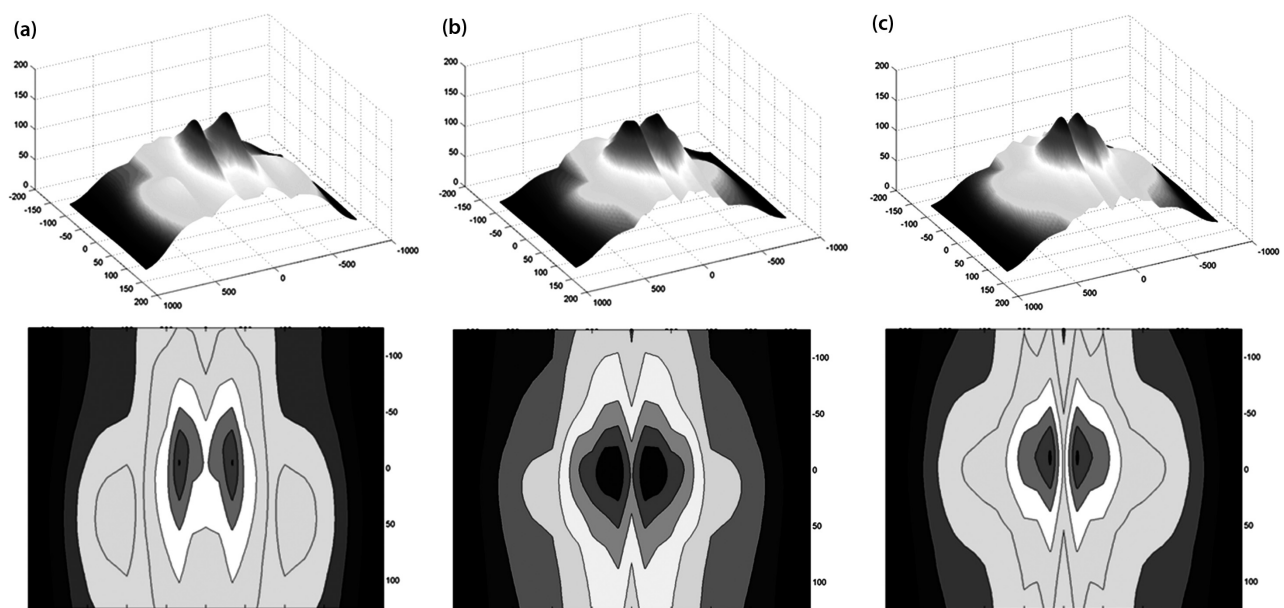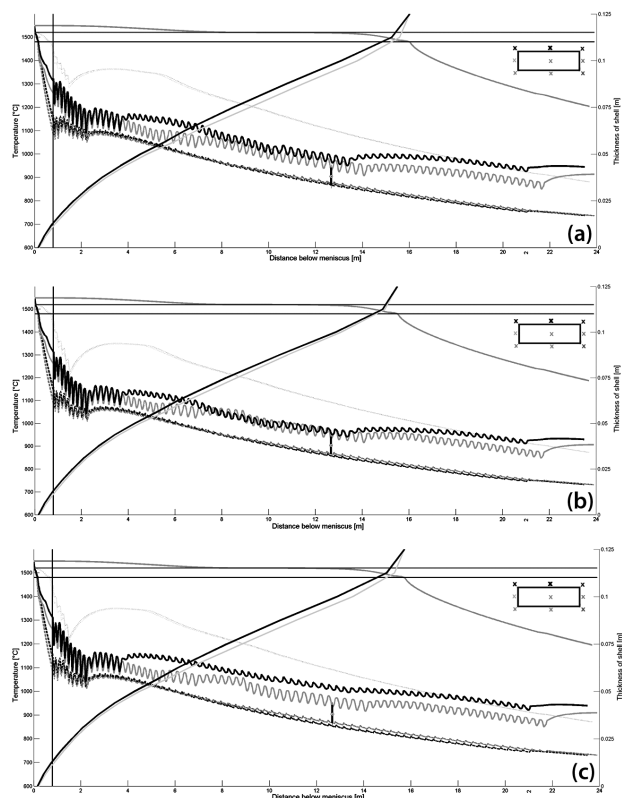

Figure 5: Heat-transfer coefficient as a function of the surface temperature
Slika 5: Koeficient prenosa toplote v odvisnosti od temperature površine

(a)

(b)

(c)

Figure 6: Heat-transfer coefficient for the Lechler air-mist nozzle: a) nozzle 100.638.30.24 with the water flow of 2.2 L/min and air pressure of 0.2 MPa, b) nozzle 100.528.30.24 with the water flow of 2.2 L/min and air pressure of 0.2 MPa, c) nozzle 100.528.30.24 with the water flow of 1.5 L/min and air pressure of 0.2 MPa

Slika 6: Koeficient prenosa toplote pri Lechler šobi za ustvarjanje zračne megle: a) šoba 100.638.30.24, pretok vode 2,2 L/min, zračni tlak 0,2 MPa, b) šoba 100.528.30.24, pretok vode 2,2 L/min, zračni tlak 0,2 MPa, c) šoba 100.528.30.24, pretok vode 1,5 L/min, zračni tlak 0,2 MPa
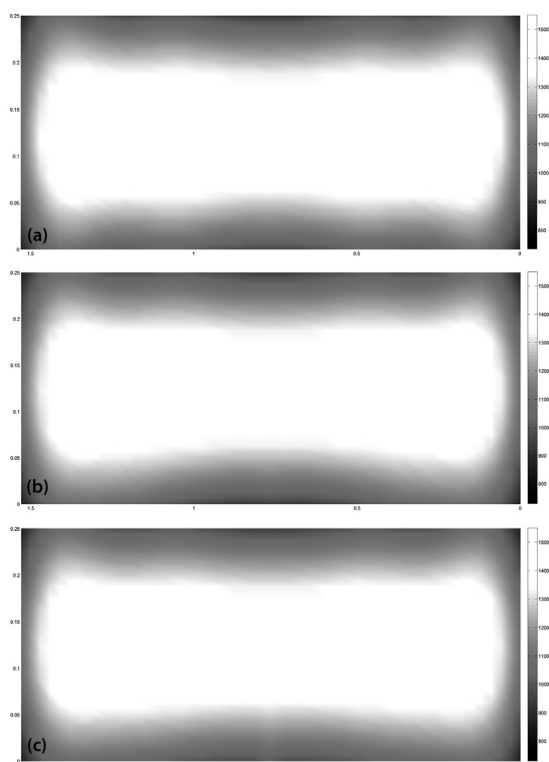

In order to be able to simulate this boundary condition within the numerical model as accurately as possible, it is necessary to conduct an experimental measurement on each nozzle in the secondary-cooling zone.

Each of the eight nozzles was measured separately with the hot model, on which the hot surface of the slab, cooled by a moving nozzle, can be modelled. The temperatures measured on the surface of the model can be entered into an inverse task to calculate the intensity of spraying, which, in turn, can determine *htc* with a special mathematical method.

Figure 5 presents the measured values of the heat-transfer coefficients processed by the temperature model software. For the nozzle configuration, there is a graph of the 3D graph (**Figure 6**) of the heat-transfer coefficient beneath the nozzle. These graphs are plotted for surface temperatures from 800 °C to 1000 °C.

4 TEMPERATURE FIELD

The setting of the secondary cooling and its optimization is a very complicated problem. The graph in **Figure 7** shows the resultant temperature fields for individual cooling curves. This basic set of graphs serves the user making it possible to assess which of the cooling

Figure 7: Temperature history along the caster for different configurations of secondary cooling in zones 6, 8 and 10:
a) nozzle 100.638.30.24 with the water flow of 2.2 L/min per nozzle, b) nozzle 100.528.30.24 with the water flow of 2.2 L/min per nozzle, c) nozzle 100.528.30.24 with the water flow of 1.5 L/min and air pressure of 0.2 MPa

Slika 7: Zgodovina temperature vzdolž livne naprave za različno izvedbo sekundarnega hlajenja v conah 6, 8 in 10:
a) šoba 100.638.30.24, pretok vode skozi šobo 2,2 L/min, b) šoba 100.528.30.24, pretok vode skozi šobo 2,2 L/min, c) šoba 100.528.30.24, pretok vode 1,5 L/min, zračni tlak 0,2 MPa

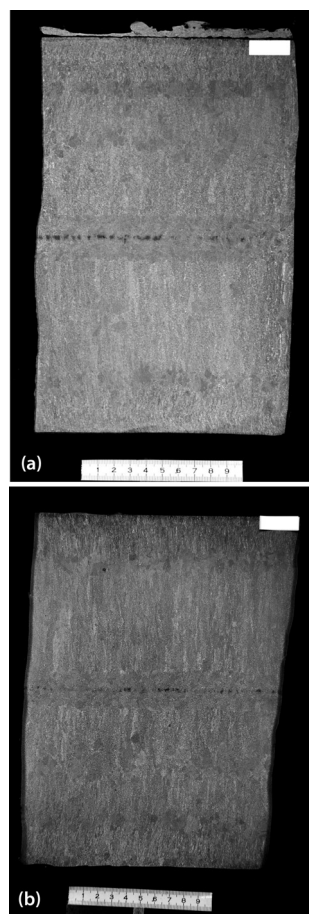**Figure 8:** Temperature field at the cross-section of the slab at the straightening point:
a) nozzle 100.638.30.24 with the water flow of 2.2 L/min per nozzle,
b) nozzle 100.528.30.24 with the water flow of 2.2 L/min,
c) nozzle 100.528.30.24 with the water flow of 1.5 L/min
Slika 8: Temperaturno polje na prerezu slaba v točki ravnanja:
a) šoba 100.638.30.24, pretok vode skozi šobo 2,2 L/min,
b) šoba 100.528.30.24, pretok vode skozi šobo 2,2 L/min,
c) šoba 100.528.30.24, pretok vode skozi šobo 1,5 L/min

Figure 9: Macrostructure of the slab before and after the adjustment of the secondary cooling of steel S 275:
a) nozzle 100.638.30.24 with the water flow of 2.2 L/min per nozzle,
b) nozzle 100.528.30.24 with the water flow of 1.5 L/min per nozzle
Slika 9: Makrostruktura plošče pred prilagoditvijo sekundarnega hlajenja jekla S 275 in po njej:
a) šoba 100.638.30.24, pretok vode skozi šobo 2,2 L/min,
b) šoba 100.528.30.24, pretok vode skozi šobo 1,5 L/min

curves is optimal for the given cast steel[3]. **Figure 7a** shows the surface temperature of the slab in the caster using nozzle 100.638.30.24 with the secondary-cooling flow of 2.2 L/min per nozzle. **Figure 7b** shows the temperature for the same conditions, but only for zones 6, 8, and 10 using nozzle 100.528.30.24. **Figure 7c** shows the surface temperature for the water flow of 1.5 L/min for nozzle 100.528.30.24 in zones 6, 8, and 10. These calculations show that the new nozzles increase the surface temperature at the straightening point of a small radius by about 100 °C, while with the higher water-flow rates a new nozzle can cool as intensely as the original nozzle. **Figure 8** shows the temperature field in the cross-section at the straightening point using the same parameters as for **Figure 7**.

The increase in the surface temperature in the straightening point on the small-radius surface has definitely helped to reduce the surface defects of cast slabs. This conclusion is also confirmed by the macrostructure figures that were made for two slabs of 1530 mm × 250 mm and a steel grade S275. **Figure 9a** shows the macrostructure of the steel that was cast with the previous setup of the cooling (the Lechler nozzle 100.638.30.24 with the flow rate of 2.2 L/min) and

Figure 9b presents the macrostructure obtained with the use of the new setup of the cooling (the Lechler nozzle 100.528.30.24 with the flow rate of 1.5 L/min). The new setup of the cooling has been used on the caster since July 2012, and therefore the statistical evaluation of the surface defects from the operational data is not yet available.

5 CONCLUSIONS

It has been proved that the value of the heat-transfer coefficient on the surface of the slab and the heat withdrawal in the secondary-cooling zone significantly affect the process simulation from the viewpoint of the temperature field, the metallurgical length and also the other technological properties. Moreover, these parameters also influence the surface quality of cast slabs and therefore they enable us to predict the quality of the slabs. In order to simulate the boundary condition of the numerical model as accurately as possible, it is necessary

to conduct experimental measurements for each nozzle in the secondary cooling zone. For this purpose, all the used nozzles were measured separately with the hot model, with which the hot surface of the slab, cooled by a moving nozzle, can be modelled.

The original 3D numerical model of the temperature field was used for optimizing the surface temperatures of cast slabs[6]. The results are presented for the 1530 mm × 250 mm slabs that are cast in Evraz Vitkovice Steel, Czech Republic. The performed optimization proved that a proper replacement of the cooling nozzles in the secondary cooling zone and a reduction of the flow rate through the nozzles can help to increase the surface temperature of a cast slab in the straightening point so that the surface defects can be reduced. Besides, it was also shown, for a particular pair of the Lechler nozzles, that although a nozzle is replaced with a smaller one, in the cases of higher flow rates, it can have the same cooling intensity as a larger nozzle.

Acknowledgments

Nomenclature

c	specific heat capacity	J/kg K
htc	heat transfer coefficient	W/(m² K)
H_v	volume enthalpy	J/m³
k	heat conductivity	W/(m K)
T	temperature	K
T_{amb}	ambient temperature	K
T_{cast}	melt temperature	K
$T_{surface}$	temperature in unbending part	K
$\dot{q}$	specific heat flow	W/m²
QX, QY, QZ	heat flows	W
$\dot{Q}_{source}$	internal heat source	W/m³
x, y, z	axes in given direction	m
v_z	casting speed in given direction	m/s
ρ	density	kg/m³
σ	Stefan-Bolzmann constant	W/m² K⁴
ε	emissivity	−
τ	time	s

6 REFERENCES

[1] J. P. Birat, The Making, Shaping and Treating of Steel, Casting Volume, 11th edition, Alan W. Cramb (ed.), The AISE Steeel Foundation, Pittsburgh, PA, USA, 2003

[2] T. Mauder, J. Stetina, C. Sandera, F. Kavicka, M. Masarik, An optimal relationship between casting speed and heat transfer coefficients for continuous casting process, In Metal 2011, Conference proceedings, Metal. Ostrava, Tanger, 2011, 22–27

[3] P. Charvat, T. Mauder, M. Ostry, Simulation of latent-heat thermal storage integrated with room structures, Mater. Tehnol., 46 (2012) 3, 239–242

[4] R. Pyszko, M. Prihoda, P. Fojtik, M. Kovac, Determination of heat flux layout in the mould of continuous casting of steel, Metalurgija (Metallurgy), 51 (2012) 2, 149–152

[5] T. Luks, J. Ondrouskova, J. Horsky, Nozzle cooling of hot surfaces with various orientations, In Experimental fluid Mechanics 2011, Proceedings of the International conference, Jicín, 2011, 337–346

[6] L. Klimes, P. Popela, An Implementation of Progressive Hedging Algorithm for Engineering Problems, In Mendel 2010 – 16th International Conference on Soft Computing, Brno, BUT, 2010, 459–464

INFLUENCE OF PROCESS PARAMETERS ON THE CORROSION RESISTANCE OF CORRUGATED AUSTENITIC AND DUPLEX STAINLESS STEELS

VPLIV PROCESNIH PARAMETROV NA KOROZIJSKO ODPORNOST REBRASTIH AVSTENITNIH IN DUPLEKSNIH NERJAVNIH JEKEL

Sandra M. Alvarez, Asunción Bautista, Francisco Velasco

Universidad Carlos III de Madrid, Materials Sci. and Eng. Dept – IAAB, Avda. Universidad 30, Leganés, Madrid, Spain
asuncion.bautista@uc3m.es

The main objective of this work is to study the influence of the forming process on two corrugated, lean, duplex stainless steels (DSSs): UNS S32001 and UNS S32304. Both grades have been recently proposed as alternative materials to the austenitic UNS S30403 grade for manufacturing reinforcement bars to be embedded in concrete structures, exposed to corrosive environments. Hot-worked (HW) corrugated bars of both DSSs are analyzed and their corrosion behaviour is compared with that of the HW and cold-worked (CW) corrugated bars of S30403.

The corrosion performance is characterized through cyclic polarization curves in 8 different solutions that simulate those contained inside the pores of concrete in different circumstances.

The obtained results justify a great interest in the studied lean DSS grades with respect to their use as reinforcements. Moreover, it is proved that the corrugated surface of a bar is clearly less corrosion resistant than the centre of the bar. The processing method of producing reinforcements influences not only the pitting susceptibility but also the pitting morphology.

Keywords: corrosion, stainless steel, reinforcements, processing, lean duplex

Glavni cilj tega dela je študija vpliva postopka izdelave na dve rebrasti dupleksni nerjavni jekli brez molibdena (DSS): UNS S32001 in UNS S32304. Obe vrsti jekla sta bili predloženi kot nadomestni material za avstenitno jeklo UNS S30403 za izdelavo palic za ojačanje, ki se vgradijo v strukture iz betona, ki so izpostavljene korozivnemu okolju. Vroče izdelane (HW) rebraste palice obeh DSS so bile analizirane in njihovo korozijsko vedenje je primerjano z vroče (HW) in hladno izdelanimi (CW) rebrastimi palicami iz jekla S30403.

Korozijsko vedenje je ocenjeno z uporabo krivulj pri ciklični polarizaciji v 8 različnih raztopinah, ki simulirajo tekočine, ki so v porah betona v različnih okoliščinah.

Dobljeni rezultati potrjujejo veliko zanimanje za uporabo preučevanih jekel DSS z nizko vsebnostjo molibdena za ojačitev betona. Še več, dokazano je, da je rebrasta površina palic nedvomno bolj korozijsko odporna kot sredina palice. Metoda izdelave ojačitvenih palic vpliva poleg občutljivosti na jamičasto korozijo tudi na morfologijo korozijskih jamic.

Ključne besede: korozija, nerjavno jeklo, ojačitve, izdelava dupleksnega jekla z malo Mo

1 INTRODUCTION

The use of stainless-steel corrugated bars instead of carbon steel bars in those parts of reinforced concrete structures that are more exposed to corrosion is one of the most reliable strategies for assuring the durability of a structure.[1] Initially, austenitic grades were used with this objective.[2]

Duplex stainless steels (DSSs) have shown a good corrosion resistance in many media. With respect to the reinforced concrete exposed to aggressive environments, corrosion studies have shown advantages of the traditional UNS S32205 DSS reinforcements in comparison with the most common austenitic grades[3,4] and they started to be used for corrugated bars about ten years ago. Recently, two more economical DSSs have been proposed for their use in concrete,[5] not for replacing the S32205 reinforcements used in extremely aggressive conditions, but as an alternative to the corrugated bars of the austenitic UNS S30403 grade.

UNS S32304 DSS, considered in the present study, has a low Mo-content and it has been known for years. Since 2003 its use has been growing in desalinization industries, marine applications or production processes, replacing the austenitic UNS S31603 steel. UNS S32001 is the other DSS evaluated in this study. It is a very novel DSS grade, lower alloyed than S32304, with smaller Ni and Cr contents, i.e., cheaper.

There are scarce references about the corrosion behaviour of these lean DSS grades and most of the studies consider the environments very different form concrete. Special chemical characteristics of the solution inside concrete pores introduce factors that modify the protective ability of the passive layers on stainless steels. These characteristics are different from the ones shown by the materials that are exposed to the atmosphere or to other environments.[6] Most authors also agree that a higher alkalinity in a pore solution has a positive impact on the corrosion behaviour of stainless steel,[4–8] though the issue remains controversial.[9]

Moreover, to be used as reinforcements in concrete structures, the stainless steels must be hardened during the processing[10] and their surface must be formed into corrugations to assure a good adherence with the concrete. There are factors that many of the previous corrosion studies on stainless steels in simulated pore solutions have not considered, as they were carried out in stainless steels that were not formed as corrugated bars.[11–14] However, recent studies suggest that the forming process of corrugated bars can dramatically affect the corrosion behaviour of austenitic stainless steels in alkaline solutions with chlorides.[15]

2 EXPERIMENTAL WORK

Four different stainless-steel grades were considered in the study, two corrugated, lean, duplex stainless steels (DSSs): the UNS 32001 and UNS S32304 hot-worked (HW) corrugated bars and two austenitic UNS S30403, HW and cold-worked (CW) corrugated bars. The products were manufactured by Roldán S. A. (Acerinox Group, Spain). The diameters of the corrugated bars considered in the study as well as their chemical compositions can be seen in **Table 1**. The chemical compositions of the bars were experimentally determined with X-ray fluorescence (XRF), using a Spectre XEPOS equipment.

The corrosion behaviour of different places (core and surface) of the corrugated stainless steels was characterized with cyclic polarizations curves, using an EG&G 263A galvanostat- potentiostat from Princeton Applied Research. Electrochemical measurements were carried out in the solutions that simulate those contained in the concrete pores in different conditions. Saturated $Ca(OH)_2$ solutions (pH $\approx$ 13), simulating non-carbonated concrete, with four different NaCl contents in mass fractions were used: (0, 0.5, 1 and 5) %. The saturated $Ca(OH)_2$ solutions, whose pH values decreased to about 9 due to CO_2-bubbling, were used to simulate the behaviour in carbonated concrete. Chloride contents of (0, 0.5, 1 and 5) % were also considered for carbonated solutions.

The testing procedure was based on the ASTM G61 Standard. Cyclic polarization curves were carried out using a three-electrode cell. A saturated calomel electrode (SCE) was used as the reference electrode and a stainless-steel mesh as the counter-electrode. Samples of the corrugated stainless-steel bars acted as working electrodes. The measurements were carried out after a 48-h

exposure of the stainless-steel samples to the testing solution to assure the correct stabilization of the corrosion potential (E_{corr}). The sweeping rate was 0.17 mV/s. The potential was reversed when the current densities reached a value of 10^{-4} A/cm^2.

To study the corrosion behaviour of a corrugated surface, samples 2 cm of the real surfaces of the bars were exposed to the corresponding testing media. The corrosion behaviour of the non-corrugated materials was analyzed exposing the samples from the centres of the bars to the testing solutions. For the samples from the centres of the bars, an Avesta cell was used to assure the absence of crevices that could interfere with the measurements.

An analysis of the morphology of the attack after the polarization curves was carried out with scanning electronic microscopy (SEM) using a Philips XL30 equipment.

3 RESULTS AND DISCUSSION

The polarization curves of the corrugated surfaces and the centres of the stainless-steel bars clearly exhibit different shapes, as can be seen in **Figure 1**, where the curves corresponding to the non-carbonated solutions with 5 % NaCl are shown. For the samples without corrugations (**Figure 1a**), the pitting potential (E_{pit}) is well defined and corresponds with very sharp current increases. On the other hand, in the tests carried out on the real surfaces of the bars (**Figure 1b**), the current increase after E_{pit} is less pronounced. It must be pointed out that on certain materials exposed to particular testing conditions, no corrosion occurred during the test. This is the case, for example, of the centre of the HW S32304 bar in a non-carbonated solution with 5 % NaCl (**Figure 1a**), where the current increase does not correspond to any corrosion phenomenon but it is due to the water decomposition through reaction 1:

$$4OH^- \rightarrow 2H_2O + O_2 + 4e^- \qquad (1)$$
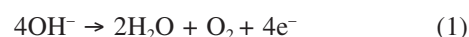
In the case of a sudden current increase and the absence of hysteresis during the reverse cycle, the potential value confirms that no corrosion has taken place during the test.

The $E_{pit} - E_{corr}$ distance is widely considered to be a reliable way of measuring the resistance to localized corrosion. The E_{corr} values of all the systems considered in this study are very similar. The E_{pit} values plotted in

Table 1: Diameters of corrugated bars and experimentally determined chemical compositions of the studied stainless steels
Tabela 1: Premer rebrastih palic in eksperimentalno določena kemijska sestava preiskovanih nerjavnih jekel

| Stainless steel	Diameter d/mm	Main alloying elements, w/%								
		S	Si	Mn	Cr	Ni	Mo	N	C	Fe
CW S30403	10	0.001 0	0.361	1.45	18.30	8.68	0.27	0.050	0.023	Bal.
HW S30403	16	0.001 2	0.298	1.42	18.37	8.74	0.27	0.055	0.026	Bal.
HW S32001	16	0.001 0	0.681	4.14	19.98	1.78	0.24	0.124	0.025	Bal.
HW S32304	16	0.002 0	0.651	1.54	22.70	4.47	0.26	0.153	0.017	Bal.
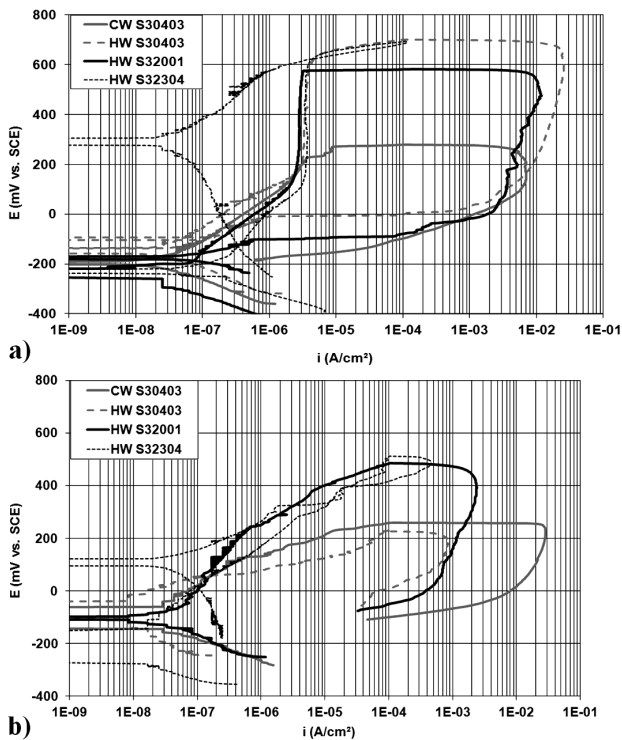
Figure 1: Polarization curves in non-carbonated Ca(OH)$_2$ solutions with 5 % NaCl: a) centres of the bars, b) corrugated surfaces

Slika 1: Polarizacijske krivulje v negazirani raztopini Ca(OH)$_2$ s 5 % NaCl: a) sredina palice, b) rebrasta površina

Figures 2 and **3** can be an adequate tool for comparing the corrosion behaviours of stainless steels in different conditions.

It is very interesting to find a significant decrease in the corrosion resistance of the bars due to the changes to the corrugations taking place during the forming process. **Figure 2** shows the difference between the E_{pit} values of the studied stainless steels in carbonated solutions, with the measurements carried out on the corrugated surfaces
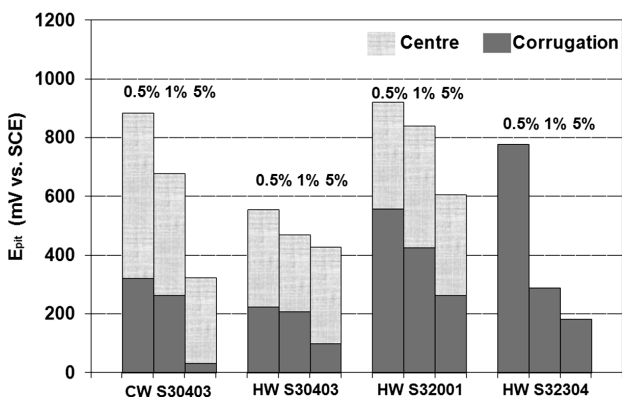
Figure 2: Differences between the E_{pit} measured in the centres of stainless-steel bars and on corrugated surfaces in carbonated Ca(OH)$_2$ solutions with different chloride contents

Slika 2: Razlika med izmerjenim E_{pit} v sredini palice iz nerjavnega jekla in na rebrasti površini v gazirani raztopini Ca(OH)$_2$ z različno vsebnostjo kloridov
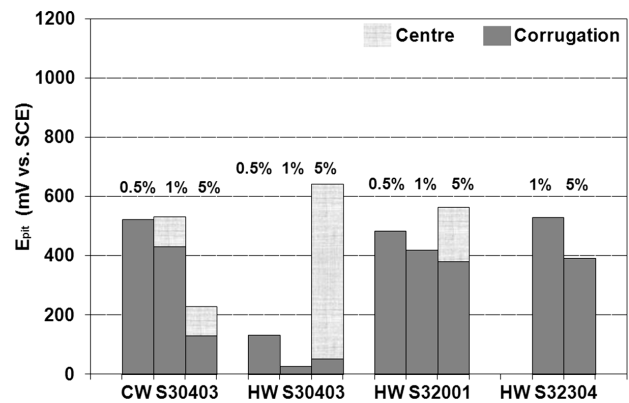
Figure 3: Differences between the E_{pit} measured for the centres of stainless-steel bars and for the corrugated surfaces in non-carbonated Ca(OH)$_2$ solutions with different chloride contents. Conditions without the plotted E_{pit} values correspond to tests where no corrosion takes place.

**Slika 3:** Razlika med izmerjeno E_{pit} za sredino nerjavne palice in za rebrasto površino v negazirani raztopini Ca(OH)$_2$ z različno vsebnostjo kloridov. Primeri brez prikazane E_{pit} ustrezajo preizkusom, kjer se korozija ni pojavila.

or in the centres of the bars. As in some cases the definition of E_{pit} is not easy, the potential, at which the anodic current reaches the value of 10^{-4} A/cm^2, has been chosen as the criterion for determining this parameter.

The marked difference between the E_{pit} values, corresponding to the corrugated surface and to the other regions of a bar, emphasises the effect of the process parameters. It would be risky to extrapolate the results of the stainless steels processed in the way different from that of the corrugated bars to the performance in concrete, though it has been often done in literature. These data confirm the trend observed in the recently published work on more traditional austenitic stainless steels.[15] The minor corrosion resistance of a corrugated surface of stainless steel has been explained with a more deformed microstructure and a higher stress concentration in the corrugation than found in the centre of the bar.[15] Different grain sizes and grain morphologies of the corrugations and of the centres of the bar were studied previously for the reinforced bars considered in our earlier work,[16] and the obtained results proved that the corrugations exhibit a highly deformed microstructure with a reduced grain size.

In the carbonated solutions without chlorides, no corrosion was detected for any of the studied stainless steels. Moreover, the centres of the HW S32304 bars proved to be immune to corrosion during the polarization tests carried out independently of the chloride content of the carbonated solution. However, during the polarization of the corrugated surfaces of HW S32304 in the presence of chlorides, current increases corresponding to a corrosive attack were detected, even with 0.5 % NaCl.

For the other three studied stainless-steel grades, a localized corrosion always occurred during the polarization tests in the carbonated solutions with chlorides.
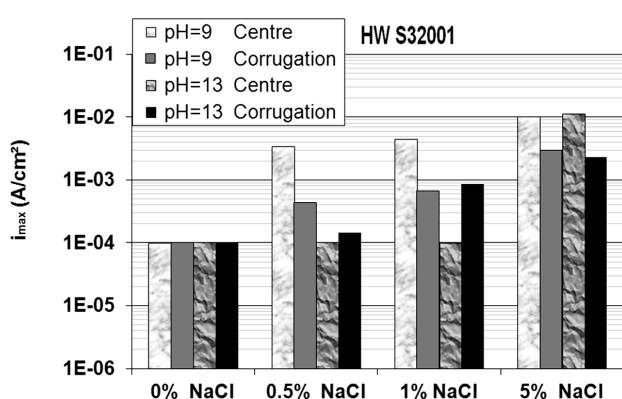
Figure 4: Differences between the i_{max} values obtained with the polarization curves for the centres and the corrugated surfaces of duplex HW S32001 bars in carbonated and non-carbonated $Ca(OH)_2$ solutions with different chloride contents

Slika 4: Razlike med vrednostmi i_{max}, dobljene iz polarizacijskih krivulj iz sredine in iz rebraste površine dupleksnih palic HW S32001 v gazirani in negazirani raztopini $Ca(OH)_2$ z različno vsebnostjo kloridov

For all the materials the E_{pit} of the corrugated surface is much lower than the E_{pit} of the centre of a bar.

As expected, in all the cases an increase in the chloride content of the solution causes a decrease in the resistance to localized corrosion, i.e., a decrease in E_{pit}.

In **Figure 3**, the E_{pit} values detected in non-carbonated solutions are plotted. It can be seen that, at a higher pH, it is more difficult to cause corrosion during the test. In the solutions without chlorides, no corrosion occurs in any of the cases and the centre of HW S32304 is immune to the attacks in the testing media with chlorides, as reported for pH $\approx$ 9. Besides, no corrosion occurs during the polarization in the solutions with 0.5 % NaCl on the centres of the other studied bars. In the case of the 1 % NaCl testing solution, no corrosion was found on the centres of HW S30403 or HW S32001.

The corrugated surfaces of the bars prove again to be much more prone to corrosion. For this type of samples, the only condition where no pitting is detected is HW S32304 with 0.5 % NaCl. The important influence of the microstructural changes occurring in the surfaces of the corrugated bars during the forming process is again clearly proved.

If the results from **Figures 2** and **3** are used to compare the corrosion behaviours of different grades, it is demonstrated that HW S32304 is clearly more corrosion resistant than any of the studied austenitic grades. Despite the volatility of the prices in the market, it can be considered that a S32304 grade can cost about 9 % less than a S30403 grade. This result justifies the great interest in this DSS grade that is seen as an alternative for the traditional austenitic grade used in these applications, as S32304 has a better performance and it is somewhat more economical. The DSS S32001 grade can be estimated to be about 15 % cheaper than the austenitic S30403. The results of the corrosion tests
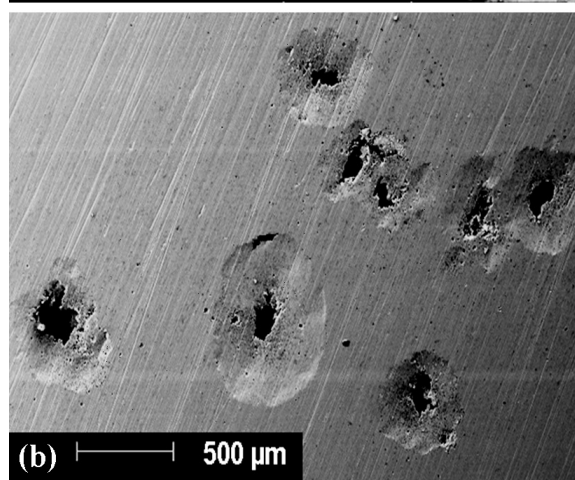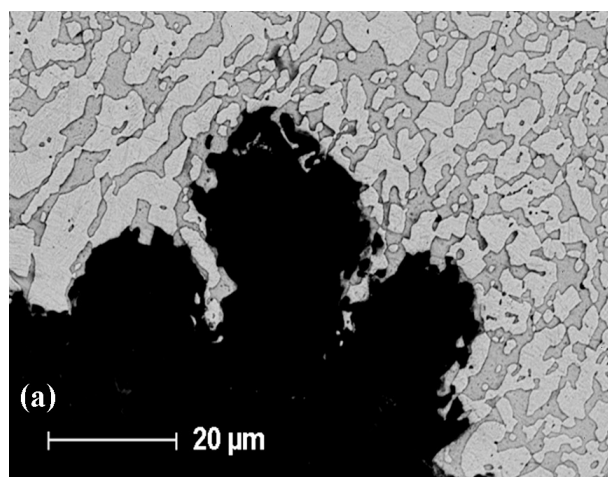
Figure 5: Images of different morphologies of the attacks that appear on the centre of a bar and on the corrugated surface. The pits after the polarization of HW S32001 in non-carbonated $Ca(OH)_2$ solutions with 5 % NaCl: a) corrugated surface, b) center of the bar.

Slika 5: Posnetki različnih morfologij napada, ki se pojavi v sredini palice in na rebrasti površini. Jamice po polarizaciji HW S32001 v negazirani raztopini $Ca(OH)_2$ s 5 % NaCl: a) rebrasta površina, b) sredina palice.

carried out indicate that the corrosion resistance of both grades are quite similar, or that the corrosion resistance of the cheap, new DSS grade is even better.

In addition to E_{pit}, another interesting parameter, which can be obtained from the polarization curves, is the maximum intensity (i_{max}) reached during the measurements. All the curves are programmed to reverse the potential sweep when a current intensity of 10^{-4} A/cm^2 is reached. When no corrosion occurs, i_{max} is 10^{-4} A/cm^2, as the current quickly decreases when the applied potentials decrease. When pits are formed during the anodic polarization, the current still increases as the potentials start to decrease due to the important autocatalytic effect of the localized corrosion. The higher the i_{max}, the more dangerous is the pitting morphology. As an example, the values of this parameter for sixteen tested conditions of HW S32001 were plotted in **Figure 4**. If the conditions, under which no corrosion takes

place, are not considered (0 % NaCl and the centre of the bar for 0.5 and 1 % NaCl at pH $\approx$ 13), it can be seen that the samples from the centre of the bar, though less susceptible to corrosion than the corrugated surfaces, suffer from a more aggressive attack than when it occurs on the surface. The same conclusion is reached if the results for the other four studied materials are analyzed. It can also be seen in **Figure 4** that chlorides have an important influence on the increase of i_{max}.

An observation of the morphology of the pits after the polarization curves confirms the idea deduced from the i_{max} values. As it can be seen in **Figure 5**, the polarization causes small, shallow pits widely distributed on the most deformed regions of the surface of the corrugation. In the centre of the bar, polarizations cause scarce, but much bigger pits that can be much more dangerous.

4 CONCLUSIONS

The susceptibility to pitting corrosion on the corrugated surface of corrugated stainless steel is always much higher than in the centre of the bars of the same material. The forming process clearly decreases the corrosion resistance of stainless steel used as a reinforcement material in concrete structures.

The attack that appears on the corrugated surfaces of stainless steels during an anodic polarization is less localized and less dangerous than the attack that appears in the centres of the bars.

The new lean DSSs for reinforcing bars are very interesting options for substituting the traditional austenitic S30403 bars. S32304 clearly exhibits a better corrosion behaviour being also somewhat cheaper. S32001 is highly interesting from an economic point of view and its corrosion results are similar, even slightly better, than those of S30403.

5 REFERENCES

[1] U. Nürberger (Ed.), Stainless steel in concrete, State of the art report, Publication n° 18, Institute of Materials, London, 1996

[2] L. Bertolini, P. Pedeferri, Corrosion Reviews, 20 (**2002**), 129–152

[3] A. Bautista, G. Blanco, F. Velasco, A. Gutiérrez, S. Palacín, L. Soriano, H. Takenouti, Materiales de Construcción, 57 (**2007**), 17–32

[4] A. Bautista, G. Blanco, F. Velasco, Cement and Concrete Research, 36 (**2006**), 1922–1930

[5] S. M. Alvarez, A. Bautista, F. Velasco, Corrosion Science, 53 (**2011**), 1748–1755

[6] A. Bautista, G. Blanco, F. Velasco, A. Gutiérrez, L. Soriano, F. J. Palomares, H. Takenouti, Corrosion Science, 51 (**2009**), 85–792

[7] M. Kouril, P. Novak, M. Bojko, Cement Concrete Research, 40 (**2010**), 431–436

[8] L. Bertolini, F. Bolzoni, T. Pastore, P. Pedeferri, British Corrosion Journal, 31 (**1996**), 218–222

[9] L. Freire, M. J. Carmezim, M. G. S. Ferreira, M. F. Montemor, Electrochimica Acta, 55 (**2010**), 6174–6181

[10] Guidance on the use of stainless steel reinforcement, Technical report N° 51, The Concrete Society, London, 1998

[11] M. Kouril, P. Novak, M. Bojko, Cement Concrete Composites, 28 (**2006**), 220–225

[12] L. Veleva, M. A. Alpuche-Avilés, M. K. Graves-Brook, D. O. Wipf, Journal of Electroanalytical Chemistry, 578 (**2005**), 45–53

[13] B. Elsener, D. Addari, S. Coray, A. Rossi, Electrochimica Acta, 45 (**2011**), 4489–4497

[14] S. Fajardo, D. M. Bastidas, M. Criado, M. Romero, J. M. Bastidas, Construction and Building Materials, 25 (**2011**), 4190–4196

[15] E. C. Paredes, A. Bautista, S. M. Alvarez, F. Velasco, Corrosion Science, 58 (**2012**), 52–61

[16] S. M. Alvarez, A. Bautista, F. Velasco, S. Guzman, Proceedings of the 7th European Stainless Steel Conference, Como, Italy, 2011

CONCENTRATION AND PATH-LENGTH DEPENDENCE ON THE FARADAY ROTATION OF MAGNETIC FLUIDS BASED ON HIGHLY WATER-SOLUBLE Fe₃O₄/PAA NANOPARTICLES SYNTHESIZED BY A HIGH-TEMPERATURE HYDROLYSIS METHOD

ODVISNOST KONCENTRACIJE IN DOLŽINE POTI OD FARADAYEVEGA VRTENJA MAGNETNIH TEKOČIN NA OSNOVI VISOKOVODOTOPNIH NANODELCEV Fe₃O₄/PAA, SINTETIZIRANIH Z METODO VISOKOTEMPERATURNE HIDROLIZE

Serhat Küçükdermenci[1,5], Deniz Kutluay[2], Erdal Çelik[3,4], Ömer Mermer[1], İbrahim Avgın[1]

[1]Department of Electrical and Electronics Engineering, Ege University, Bornova 35100, Izmir, Turkey
[2]Department of Electronics and Communications Engineering, Izmir University, Uckuyular 35290, Izmir, Turkey
[3]Center for Fabrication and Applications of Electronic Materials (EMUM), Dokuz Eylul University, Tınaztepe Campus, 35160, Izmir, Turkey
[4]Department of Metallurgical and Materials Engineering, Dokuz Eylul University, Tınaztepe Campus, 35160, Izmir, Turkey
[5]Department of Electrical and Electronics Engineering, Balikesir University, Campus of Cagis 10145, Balikesir, Turkey
serhat.kucukdermenci@ege.edu.tr

In this study, highly water-soluble Fe₃O₄/PAA (polyacrylic acid) nanoparticles (NPs) were synthesized by a high-temperature hydrolysis method. We report the first demonstration of the concentration and path-length dependence on the Faraday rotation (FR) for a magnetic fluid (MF) synthesized by this novel method. Experiments were performed in the DC regime ($0–6 \times 10^{-2}$ T) at room temperature. Measurements were carried out with 5–3.33 mg/ml and 1.18 mg/ml samples in cells (2, 5, 7 and 10) mm. The maximum rotation was recorded as $0.96°$ cm^{-1} for the 3.33 mg/ml concentration in the cell 10 mm. It was found that the magnetic fluid behaves with a distinctive phenomenon in different sized cells although its concentration was the same. The role of the different parameters on the FR was discussed via spatial limitations imposed by the cells and a premature saturation term. This work provides a new insight for FR investigations of MFs including highly water-soluble magnetic NPs.

Keywords: magnetic fluids, water soluble Fe₃O₄/PAA-nanoparticles, Faraday rotation

V tej študiji so bili sintetizirani visokovodotopni Fe₃O₄/PAA (poliakrilna kislina)-nanodelci (NPs) z metodo visokotemperaturne hidrolize. Poročamo o prvih predstavitvah odvisnosti koncentracije in dolžine poti od Faradayevega vrtenja (FR) za magnetno tekočino (MF), sintetizirano po tej novi metodi. Preizkusi so bili izvedeni v DC-režimu ($0–6 \times 10^{-2}$ T) pri sobni temperaturi. Meritve so bile izvršene z vzorci 5–3,33 mg/ml in 1,18 mg/ml v celicah (2, 5, 7 in 10) mm. Maksimum vrtenja je bil ugotovljen kot 0,96° cm^{-1} pri koncentraciji 3,33 mg/ml v celici 10 mm. Ugotovljeno je bilo, da magnetna tekočina izkazuje značilne pojave v celicah različne velikosti, čeprav je bila njena koncentracija enaka. Vloga različnih parametrov na FR je bila razložena s prostorskimi omejitvami, ki jo povzročijo celice in z uvajanjem izraza za prezgodnjo prenasičenost. To delo zagotavlja nov vpogled v preiskave Faradayevega vrtenja (FR) magnetnih tekočin (MFs), vključno z visokovodotopnimi magnetnimi nanodelci (NPs).

Ključne besede: magnetne tekočine, vodotopni Fe₃O₄/PAA-nanodelci, Faradayevo vrtenje

1 INTRODUCTION

Magneto-optic (MO) effects occur in gases, liquids, and solids. In general, solids exhibit the strongest MO effects, liquids exhibit weaker effects, and gases exhibit the weakest effects.[1] FR in MFs has been demonstrated in the visible,[2] near-infrared,[3,4] and mid-infrared[5] regimes. The wavelength dependence of FR and Faraday ellipticity was investigated by N. A. Yusuf and co-workers.[6] MO experiments were performed on size-sorted iron oxide (γ-Fe₂O₃) MFs.[7] Water-based MF samples were synthesized by the coprecipitation method followed by a size-sorting process. Davies and Llewellyn[8] have reported measurements on FR in highly diluted samples of Fe₃O₄ and CO particle MFs. From their results they concluded that FR is governed by magnetization. Yusuf et al.[9] have reported measurements on FR in a relatively concentrated sample.

The MO response of MFs depends on various parameters including particle size, the concentration of the particles, the externall applied magnetic field, temperature, and the kinds of particles, surfactants, and carrier fluids.[10] Due to the large variety of MFs, measurements of the MO effects of MFs have still not been reported so widely for novel ones and each new sample should be carefully analyzed.

In 2007, the Yin group synthesized novel superparamagnetic magnetite colloidal NPs which can self-assem-

ble into one-dimensional (1D) particle chains and exhibit excellent tunable photonic properties.[11,12] Since then, there has been a widespread interest in these NPs and their applications. Despite their tremendous potential in various applications, interesting fundamental questions which refer to their colloidal crystallization with and without a magnetic field remain unanswered. Therefore, in this paper we report the first demonstration of the concentration and path-length dependence on FR for MF based on these NPs. Here we report the results of an investigation of long-term stable MFs including highly water-soluble NPs showing FR in the DC regime (0–6 × 10^{-2} T) at room temperature. Water-based MF samples were synthesized by a novel high-temperature hydrolysis method.

The different relationships between the chain length and the concentration obtained by different workers may be attributed to the dependence of the chain length on other parameters such as the field, temperature and spatial limitations imposed by the cells used in containing the sample under investigation.[13–15] In our previous work[16] we measured the FR for 14 different concentrations from 1.8 mg/ml to 5 mg/ml in a cell 10 mm. It was observed that the FR increases for higher concentrations (from 1.18 mg/ml to 3.33 mg/ml). The maximum rotation was recorded as 0.96 °/cm for 3.33 mg/ml and this was named the critical concentration ($C_{CRITICAL}$). It was found that rotation tends to decrease when the concentration is higher than $C_{CRITICAL}$ (for 4 mg/ml and 5 mg/ml). We chose three samples and repeated the measurements for 2–5 mm and 7 mm cells additionally for observing the path-length dependence on the FR and investigating the spatial limitation factor on MO effects.

2 EXPERIMENTAL DETAILS

The synthesis of Fe_3O_4 NPs was explained in detail in our previous report[16] and is summarized here. For the synthesis, diethylene glycol (DEG, 99.9 %), anhydrous ferric chloride ($FeCl_3$, 97 %), sodium hydroxide (NaOH, 96%), and polyacrylic acid (PAA, M_w = 1800) were obtained from Sigma-Aldrich. Distilled water was used in all the experiments. All the chemicals were used as received without an further treatment and/or purification. For the synthesis of the Fe_3O_4 NPs a NaOH/DEG solution was prepared by dissolving 100 mmol of NaOH in 40 m of DEG at 120 °C under nitrogen for 1 h. Then, the light-yellow solution was cooled to 70 °C (stock solution A). Using a 100 ml three-necked flask equipped with a nitrogen inlet, a stirrer and a condenser, 10 mmol of $FeCl_3$ and 20 mmol of PAA were dissolved in 41 ml of DEG under vigorous stirring. In this method, DEG is not only a reducing agent but also a solvent in the reaction. The solution was purged with bubbling nitrogen for 1 h and then heated to 220 °C for 50 min (stock solution B). Subsequently, 20 ml of NaOH/DEG solution was injected rapidly into the above solution. The reaction was allowed to proceed for 2 h. The black color of the solution confirmed the formation of magnetite nanoclusters. The resultant black product was repeadedly washed with a mixture of ethanol and water and collected with the help of a magnet. The cycle of washing and magnetic separation was performed five times. A one-pot synthesis was conducted for the Fe_3O_4/PAA nanoparticles, and thus no extra separate process was needed for the surface modification. The polyol method is based on the theory that NPs will be yielded upon heating precursors in a high-boiling-point alcohol at elevated temperature. DEG is chosen here as the solvent inasmuch as it can easily dissolve a variety of polar inorganic materials due to its high permittivity (ε = 32) and high boiling point (246 °C). PAA is used as the capping agent, on which the carboxylate groups show strong coordination with Fe^{3+} on the Fe_3O_4 surface and the uncoordinated carboxylate groups extend into the water solution, rendering particles with a high water dispersibility.

Powder X-ray diffraction (XRD) analysis of the Fe_3O_4 NPs was performed on a Phillips EXPERT 1830 diffractometer with Cu K_α radiation. The XRD data were collected over the range of 10–80° (2θ) with a step interval of 0.02° and a preset time of 1.6 s per step at room temperature. Particle size distributions of the NPs were measured using a Zetasizer 4 Nano S dynamic light scattering (DSL, Malvern, Worcestershire, UK). The light-scattering measurements were carried out with a laser of wavelength 633 nm at a 90° scattering angle.

The magnetic measurements were carried out using a LakeShore 7400 (Lakeshore Cryotronics) vibrating-sample magnetometer (VSM) at 300 K. For the FR experiments we used a Thorlabs model HGR20 2.0 mW, 543 nm laser source, a GMW Electromagnet Systems model 5403 electromagnet, a Kepco power supply model BOP 20-5M, a LakeShore Model 455 DSP Gaussmeter, a Stanford Research Systems Model SR830 DSP lock-in amplifier, a New focus model 2051 photo detector, a ILX Lightwave model OMM – 6810B optical multimeter and a model OMH – 6703B silicon power head.

3 RESULTS

Figure 1 shows the XRD pattern of PAA-coated Fe_3O_4 NPs synthesized by the high-temperature hydrolysis method. Note that the (220), (311), (400), (422), (511), and (440) diffraction peaks observed for the curves can be indexed to the cubic spinel structure, and all the peaks were in good agreement with the Fe_3O_4 phase (JCPDS card 19-0629). It is clear from **Figure 2** that the average diameter of the Fe_3O_4/PAA NPs obtained from the DLS analysis is approximately 10 nm. The magnetic properties of the NPs were measured at 300 K using the VSM. As given in **Figure 3**, the saturation magnetization was determined as 38.8 emu/g. Worth nothing here is that the NPs showed no remanence
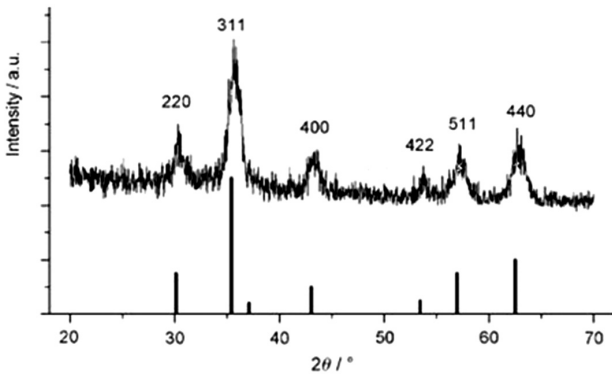
Figure 1: XRD pattern of PAA-coated Fe_3O_4 NPs synthesized by high-temperature hydrolysis
Slika 1: Rentgenska difrakcija (XRD) s PAA, prekritega z Fe_3O_4 nanodelci, sintetiziranimi z metodo visokotemperaturne hidrolize
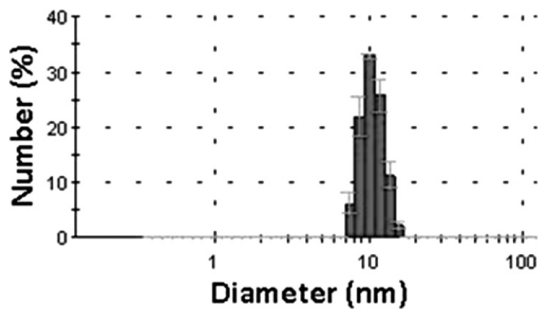

Figure 2: Particle size distribution of Fe_3O_4 NPs synthesized by high-temperature hydrolysis
Slika 2: Razporeditev velikosti nanodelcev Fe_3O_4, sintetiziranih z metodo visokotemperaturne hidrolize

or coercivity at 300 K, i.e., they exhibited superparamagnetic behavior.

The particle content is 20 mg for various concentrations with the addition of distilled water from 4 ml to 17 ml. The NPs kept dispersing well after the MF had been standing for more than 4 weeks and no sedimentation was observed for all the samples. Maintaining long-
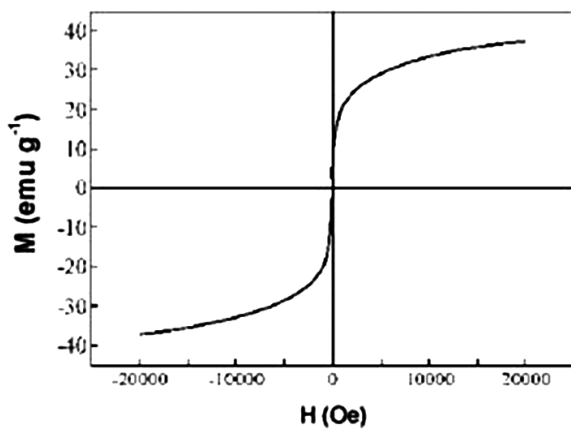

Figure 3: Hysteresis loops of superparamagnetic nanoparticles at room temperature
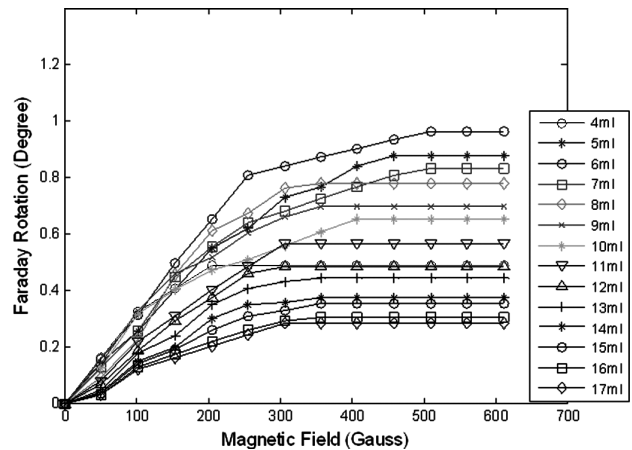**Slika 3:** Histerezna zanka super paramagnetnih nanodelcev pri sobni temperaturi

Figure 4: FR concentration dependence for 10-mm cell
Slika 4: Odvisnost FR od koncentracije pri celici 10 mm

term stability can make these kinds of MFs ideal candidates for optical devices.

The FR measurements for 14 different concentrations from 1.8 mg/ml to 5 mg/ml in a 10 mm cell were shown graphically in **Figure 4**. The maximum FR of these measurements was shown in **Figure 5**. We chose three concentrations for investigating the effect of cell size on the FR measurements. The chosen concentrations were: 3.33 mg/ml $C_{CRITICAL}$, for which we measured the maximum FR; 1.18 mg/ml, for which we measured the weakest FR before $C_{CRITICAL}$; and 5 mg/ml, for which we measured the lowest FR after $C_{CRITICAL}$. The measurements were repeated for 2–5 mm and 7 mm cells for these concentrations.

For sample 14 (**Table 1**) the FR was found to be less than 0.1 degree in the 2 mm thick cell. For the samples that have same concentration but in different cell sizes, the magnetization must be the same at a particular field since all have an equal magnetic dipole moment per unit volume. Therefore, if the FR is only governed by magnetization, it would be the same value for these samples. In order to explain the results, we can introduce terms to the
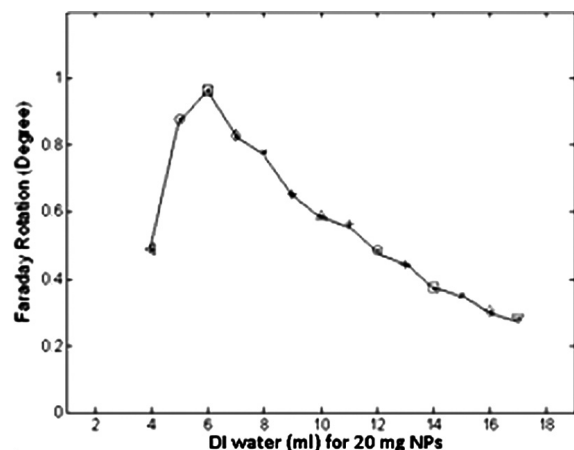

Figure 5: Maximum FR graph of samples for 10-mm cell
Slika 5: Predstavitev FR maksimumov vzorcev pri celici 10 mm

Table 1: Maximum FR of three different concentrated MF in four different cells
Tabela 1: Maksimum za FR pri treh različnih koncentracijah MF v 4 različnih celicah

Sample number	Concentration (mg/ml)	FR maximum degree (°/cm)			
		Cell size (mm)			
		2	5	7	10
1	5.00	0.3	0.36	0.43	0.49
2	4.00				0.87
3	3.33 (C_{CRITICAL})	0.15	0.37	0.6	0.96
4	2.86				0.83
5	2.50				0.78
6	2.22				0.70
7	2.00				0.65
8	1.82				0.56
9	1.67				0.48
10	1.54				0.44
11	1.43				0.37
12	1.33				0.35
13	1.25				0.30
14	1.18	<0.1	0.13	0.22	0.28

Faraday rotation which is due to the chain formation and is given by:

$$\phi_C(B) = VBl(B) \tag{1}$$

where $\phi_C(B)$ is the Faraday rotation due to the chain formation, B is the local field, $l(B)$ is the chain length at field B and V is the Verdet constant.

For a homogeneous colloidal system of single-domain fine ferromagnetic particles, the Faraday rotation is given by:

$$\phi_M(B) = C\,\frac{M(B)}{M_S} \tag{2}$$

in which $\phi_M(B)$ is the Faraday rotation at magnetic field B, $M(B)$ is the magnetization of the sample at magnetic field B, M_S is the saturation magnetization of the sample and C is a constant. Both the magnetization of the sample and the chain formation FR for the MFs can be expressed as shown below:

$$\phi(B) = C\,\frac{M(B)}{M_S} + VBl(B) = \phi_M(B) + \phi_C(B) \tag{3}$$

Here, C is a constant that can be found the at high field assuming that saturated chain length has no change.[14] This artificial saturation can be referred to as "premature saturation" and utilized to explain the different behavior of the same sample but in a different cell thicknesses.

Since samples 1 and 14 were less imposed effect of chain formation, their initial slopes in various cell thickness do not diverge too much in the $0–2 \times 10^{-2}$ T. Nevertheless, at the optimum concentration, sample 3 which has the maximum effect of chain formation, despite the same amount of NPs, the initial slope in different thickness cells is quite different.
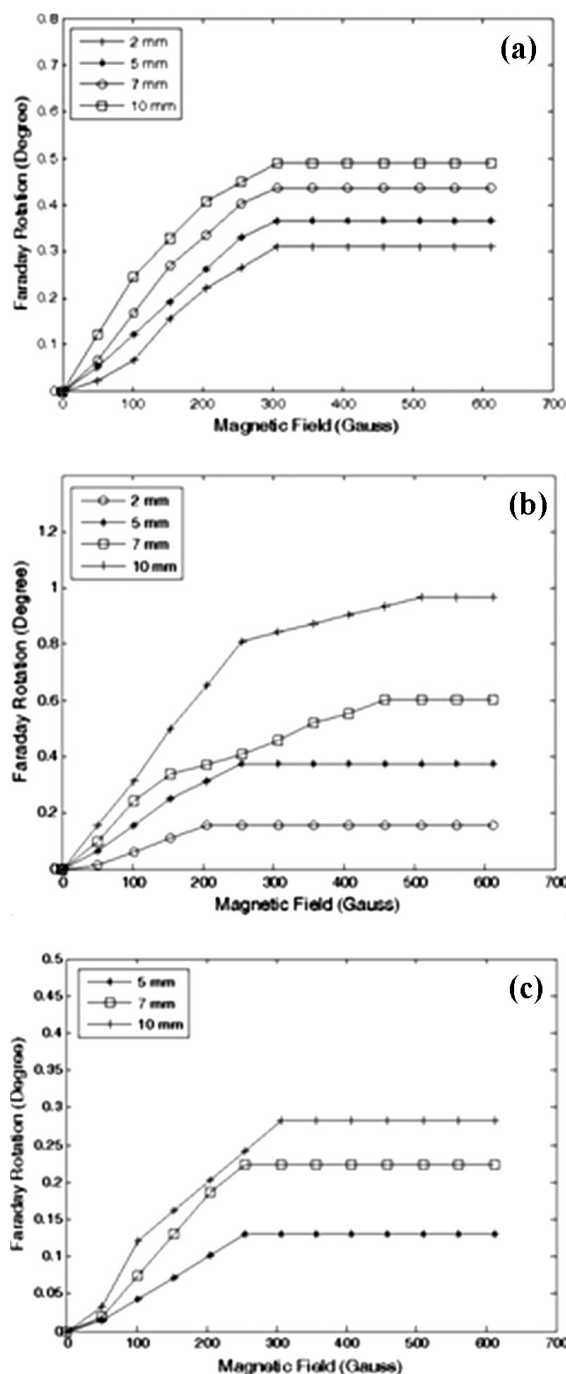
Figure 6: FR of three different concentrated MF in different size cells including: a) sample 1 (concentration: 20 mg/(4 ml)), b) sample 3 (concentration: 20 mg/(6 ml)) and c) sample 14 (concentration: 20 mg/(17 ml)). The dimensions of the cells are indicated on the figures.
Slika 6: FR treh magnetnih raztopin (MF) z različno koncentracijo pri celicah z različno velikostjo: a) vzorec 1 (koncentracija: 20 mg/(4 ml)), b) vzorec 3 (koncentracija: 20 mg/(6 ml)) in c) vzorec 14 (koncentracija: 20 mg/(17 ml)). Velikosti celic so označene na slikah.

We also observed that the FR of the same concentration fluids reached saturation at higher fields for a longer path length (**Figure 6**). This effect might be the result of premature saturation phenomena of the mean chain length in fluids. Notably, for samples 3 and 14, changing

of saturation values on FR with different cell size indicates premature saturation of the chain length.

4 DISCUSSION

The dipole-dipole interactions can be described as $F = 3\mu^2 (1 - 3 \cos^2 \alpha)/l^4$, where μ is the induced magnetic moment, α is the angle between the dipole and the line connecting the dipoles, and l is the center-center distance between two particles. When two dipoles are aligned head-to-end, the dipole interaction is an attraction $F_{ma} = -6(\mu^2/l^4)$. While they are aligned side by side, the interaction becomes a net repulsion $F_{mr} = 3(\mu^2/l^4)$. Along the magnetic field, the particles attract each other and form chains due to the head-to-end alignment of dipoles.[17]

The formed chain length varies with applied magnetic field and the concentration of the MF. The FR is not only governed by the magnetization of the fluid but also by the chain formation. The dimension of the cell in the field direction plays an important role in the length and number of chains formed in the sample. For short path length, a "spatial limitation" on the chain length is imposed, resulting in a "premature saturation" of the length. Jones and Niedoba[18] had a drop of undiluted fluid sandwiched between two parallel glass cover slips and placed normal to the optical axis of a microscope. The magnetic field was applied parallel to the axis of the microscope, i.e., perpendicular to the plane of the thin-film sample. In this experimental arrangement Jones and Niedoba observed the number of chains per unit volume, n, and found it increased rapidly with the applied field. The experimental set up used by Jones and Niedoba put a severe limitation on the length of the formed chains and led to premature saturation in the chain lengths, as was suggested by Fang et al.[19] It is worth mentioning that for thin samples, the chain length approaches the thickness of the sample at very low fields and saturates prematurely. Consequently, the chain length is not expected to increase any further with the field but rather an increase in the number of chains is observed.

If the Faraday rotation is only governed by the magnetization of the sample, then the saturation will take place at practically the same applied field for the same sample, regardless of the thickness of the sample. The difference in the saturation field is attributed to the chain formation in the sample. As was mentioned above, this chain formation may prematurely saturate in thin samples due to the physical limitation imposed on the sample.

5 CONCLUSIONS

In summary, high-quality Fe₃O₄/PAA NPs for MF formation were successfully synthesized. We report the first demonstration of the concentration and path-length dependence on the FR for MF synthesized using this novel method. We have demonstrated the FR of highly water-soluble MF measured in the $0–6 \times 10^{-2}$ in the DC regime. The effects of both spatial limitations imposed by the cells and the chain concentration were observed on the FR. We observed that the chain length is also determined by the physical dimensions of the sample. Four different cells were used for the path-length experiments. The FR of the same concentration fluids with shorter path lengths reached saturation at lower fields as a result of the premature saturation of an average chain length. The experimental results shed some light on the role of agglomeration and chain formation in the FR. Magneto-optical effects in the magnetic fluids have a promising potential for technological and industrial applications as well as their academic importance. These measurements can help to understand the MO behavior of the MFs, including highly water-soluble magnetic NPs.

6 REFERENCES

[1] M. J. Weber, CRC Handbook of Laser Science and Technology, vol. V. Part 3, no. CRC Press, Boca Raton 1995

[2] X. Chen, S. Pu, X. Hu, Y. Xia, Z. Di, Appl. Phys. Lett., 211106 (**2006**), 89

[3] C. W. Du, X. D. Liu, Z. G. Li, R. Birngruber, Y. T. Pan, J. Appl. Phys., 73 (**1993**), 6142

[4] Y. Xuan, Q. Li, X. Fang, Nanoscale Res. Lett., 237 (**2011**), 6

[5] M. M. Maiorov, J. Magnetism and Magnetic materials, 252 (**2002**), 111–113

[6] N. A. Yusuf, Japn. J. Appl. Phys., 819 (**1989**), 28

[7] D. Jamon, J. J. Rousseau, V. Cabuil, D. Zins, H. Roux, C. Bovier, F. Royer, Eur. Phys. J., AP22 (**2003**), 83–87

[8] H. W. Davies, J. P. Llewellyn, J. Phys. D, 13 (**1980**), 2327

[9] A. A. Rousan, H. M. El-Ghanem, N. A. Yusuf, J. Appl. Phys, 2781 (**1988**), 64

[10] R. E. Rosensweig, Ferrohydrodynamics, Cambridge University Press, 1985

[11] S. Gao, T. Ohta, H. Kondoh, Y. Hou, Eur. J. Inorg. Chem, 6 (**2004**), 1169–1173

[12] Y. Hu, M. Biasini, W. P. Beyermann, Y. Yin, J. Ge, Angew. Chem., Int. Ed., 23 (**2007**) 46, 4342–4345

[13] E. Elfimova, J. Magn. Magn. Mater., 203 (**2006**), 300

[14] I. Abu-Aljarayesh, H. M. El-Ghanem, N. A. Yusuf, A. A. Rousan, IEEE Trans. Magn., 26 (**1990**), 2852

[15] N. Yusuf, A. Rousan, H. El-Ghanem, IEEE Trans. Magn., 25 (**1989**), 3121

[16] S. Kucukdermenci, D. Kutluay, I. Avgin, Mater. Tehnol., 47 (**2013**) 1, 71–78

[17] Y. Kraftmakher, Eur. J. Phys, 409 (**2007**), 28

[18] H. Niedoba, G. A. Jones, J. Magn. Magn. Mater., 33 (**1988**), 73

[19] W. X. He, Z. H. Xu, X. Q. Mao, Z. Q. Shen, H. Fang, EPL, 68004 (**2007**), 77

THE POSSIBILITY OF COPPER CORROSION PROTECTION IN ACIDIC MEDIA USING A THIAZOLE DERIVATIVE

MOŽNOST PROTIKOROZIJSKE ZAŠČITE BAKRA V KISLEM MEDIJU Z UPORABO DERIVATOV TIAZOLA

Đenđi Vaštag[1], Suzana Apostolov[1], Miodrag Hadžistević[2], Milenko Sekulić[2]

[1]University of Novi Sad, Faculty of Sciences, Trg D. Obradovića 3, 21000 Novi Sad, Serbia
[2]University of Novi Sad, Faculty of Technical Sciences, Trg D. Obradovića 6, 21000 Novi Sad, Serbia
miodrags@uns.ac.rs

Assessing financial losses on an annual scale, it was determined that the world economy loses about 2.2 trillion US dollars as a result of the corrosion of materials. The most significant losses are caused by the corrosion of metals. Against corrosion, metals can be protected in several ways: by cathodic protection or anodic protection, by the use of inhibitors, or by using various protective coatings that can be metallic, non-metallic, organic or inorganic. In this paper, the possibility of the corrosion protection of copper was investigated in acidic media using inhibitors. The inhibitor properties of 5-(4'-dimetylamino-benzylidene)-2,4-dioxotetrahydro-1,3-thiazole, (DABDT) were tested on copper corrosion in an acidic sulphate-containing solution (0.1 mol dm^{-3} Na$_2$SO$_4$, pH = 3). Using potentiostatic polarization measurements, the inhibitor efficiency of DABDT as a function of concentration was determined and the mechanism of its adsorption on the copper surface was defined. It was found that the DABDT thiazole derivative acts as mixed inhibitor on copper corrosion in acidic media. In the investigation range, increasing the concentration results in a better inhibition efficiency of the DABDT.

Keywords: copper, corrosion, thiazole derivatives, polarization measurements

Ocena finančnih izgub na letnem nivoju je pokazala, da svetovna ekonomija izgubi okoli 2,2 milijardi ameriških dolarjev kot posledico korozije materialov. Najpomembnejše izgube so povzročene s korozijo kovin. Proti koroziji lahko kovine zaščitimo na več načinov: s katodno oziroma anodno zaščito, z uporabo inhibitorjev ali različnih zaščitnih prevlek, ki so lahko kovinske, nekovinske, organskega oziroma anorganskega izvora. V tem prispevku je bila raziskana možnost protikorozijske zaščite bakra v kislem mediju z uporabo inhibitorjev. Lastnosti inhibitorja iz 5-(4'-dimetilaminobenziliden)-2,4-dioksotetrahidro-1,3-tiazol, (DABDT), so bile preizkušene pri koroziji bakra v kislem mediju, ki je vseboval raztopino (0,1 mol dm^{-3} Na$_2$SO$_4$, pH = 3). S potenciostatičnimi meritvami polarizacije je bila določena učinkovitost DABDT kot funkcija koncentracije in mehanizem njegove adsorpcije na površino bakra. Odkrili smo, da se DABDT-derivati tiazola vedejo kot mešani inhibitorji pri koroziji bakra v kislem mediju. V raziskanem območju se je z naraščanjem koncentracije DABDT izboljšala učinkovitost zadrževanja korozije.

Ključne besede: baker, korozija, derivati tiazola, meritve polarizacije

1 INTRODUCTION

In accordance with recent estimates it has been calculated that the effect of corrosion on the US economy in 2012 exceeds 1 trillion dollars per year for the first time.[1] Taking into account this fact, it is clear that corrosion is the cause of significant losses in the economy of each country and therefore falls within one of the important factors of the global financial and energy crisis. It is understandable, therefore, that the great interest and tendency to reduce losses as a result of the corrosion of construction materials is to be kept to a minimum.

Copper and its alloys have good characteristics and a wide range of industrial applications. They have the largest number of applications as conductors of electricity and heat. Copper shows excellent performance as a structural material, because among other things, it is resistant to corrosion over a wide range of pH values. However, it is known that in aggressive media, copper is susceptible to corrosion, due to the lack of a protective passive layer in the acidic environment[2]. Copper as a structural material is often exposed to acidic conditions, e.g., during its purification, electro polishing or during the removal of corrosion products from the heat trans-missions. The most commonly used acid in these pro-cesses is sulphuric acid. The protection of copper in these processes in an acidic environment is usually accomplished with corrosion inhibitors.[3–5]

Organic compounds that contain hetero-atoms such as nitrogen, sulphur and oxygen, or conjugated double bonds have shown good inhibition properties against copper corrosion.[6–8] This kind of organic molecules can be adsorbed at the metal-solution interface, which will reduce the corrosive attack on the metal in acidic media.[9,10]

The degree of corrosion protection of these molecu-les depends on the strength of the interaction between the organic molecule and the metal surface atoms.

The thiazole derivatives are an interesting group of nitrogen- and sulphur-containing organic compounds

that act as inhibitors against the dissolution of copper in acidic electrolytes.

The aim of this study is to investigate and interpret how the thiazole derivative 5-(4'-dimetylaminobenzylidene)-2,4-dioxotetrahydro-1,3-thiazole, (DABDT), inhibits the copper corrosion in aerated 0.1-M Na_2SO_4 at pH = 3.

2 EXPERIMENTAL

Reagent-grade chemicals (Merck) and double-distilled water were used to prepare the electrolyte of 0.1-M Na_2SO_4 at pH = 3; the pH was adjusted to 3.0 using diluted sulphuric acid.

The investigated thiazole derivative was 5-(4'-dimetylaminobenzylidene)-2,4-dioxotetrahydro-1,3-thiazole (DABDT) (**Figure 1**).
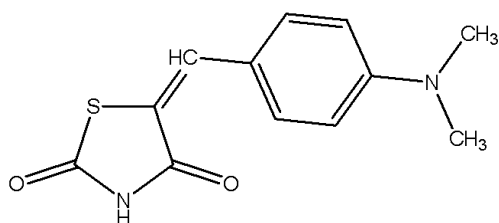
Figure 1: Structure of the investigated thiazoles
Slika 1: Struktura raziskanih tiazolov

All the experiments were conducted in the open atmosphere and at room temperature. Due to the low solubility of the tested thiazole derivative, the inhibitor was first dissolved in 20 ml of ethanol.

Weight-loss measurements were carried out on copper coupons (6 cm × 1.5 cm × 0.2 cm) in 0.1 mol dm^{-3} Na_2SO_4 at pH = 3 for different inhibitor concentrations (0.001 mmol dm^{-3}–0.01 mmol dm^{-3}). The coupons immersed in the test solutions were allowed to stand for one week in an air atmosphere.

For the electrochemical measurements a three-electrode cell was used. High-purity copper rods (99.99 % Cu) with an exposed area of 0.7 cm^2 were used as the working electrode, a saturated calomel electrode (SCE) was used as the reference electrode and platinum was used as the counter electrode. Before using, the working electrode was wet-polished with SiC papers (grit sizes of 800 and 1200), rinsed with acetone and double-distilled water. All the measurements were made at room temperature.

The polarization measurements were performed at five different inhibitor concentrations in the concentration range 0.001–0.01 mmol dm^{-3}. The measurements were carried out when the open-circuit potential (OCP) was stabilized at 5 mV/5 min. The potential was scanned between the OCP and 300 mV/SCE in both the cathodic and anodic directions at a scan rate of 10 mV min.$^{-1}$ A PC-controlled potentiostat (VoltaLab PGZ 301) was applied.

3 RESULTS AND DISCUSSION

3.1 Weight-loss measurements

A weight-loss measurement for monitoring a metal's corrosion rate is a very usefully technique because of its simplicity and reliability.[11] The weight losses of the copper electrodes were determined after 7 d of immersion in the blank (0.1 mol dm^{-3} Na_2SO_4, pH = 3) and the inhibitor-containing solutions. Table 1 shows the weight loss of copper and the protection efficiency of the investigated thiazole derivative.

The protective efficiency, η/%, of the DABDT molecules was calculated using the following equation:[12]

$$\eta(\%) = \frac{W_0 - W}{W_0} \cdot 100$$

where W_0 and W are the weight losses of the copper coupons in the blank and inhibitor-contains solutions.

Table 1: Results of weight-loss measurements
Tabela 1: Rezultati meritev zmanjšanja mase

| c /mmol dm^{-3}	W/mg cm^{-2}	η/%
0	1.54	–
0.001	0.80	48
0.003	0.54	65
0.005	0.25	84
0.007	0.20	87
0.01	0.14	91

It is clear from **Table 1** that the corrosion rates were reduced in the presence of the DABDT derivate. The inhibition efficiency, as given in **Table 1**, is found to increase with the increase in the concentration of the inhibitors.

3.2 Potentiostatic measurements

Potentiostatic polarization measurements were performed to determine the optimal concentration of DABDT and its inhibition efficiency on copper corrosion in acidic media (pH = 3). The polarization measurements were in the range of the concentration 0.001 mmol dm^{-3} to 0.01 mmol dm^{-3} at the room temperature.

Figure 2 shows the anodic and cathodic polarization plots of the copper electrode in the blank and inhibitor-containing solution (c = 0.05 mmol dm^{-3}).

The obtained polarization curve in the blank and the inhibitor-containing solution are typical for copper in an acidic solution. The cathodic part of the polarization curves related to the oxygen reduction reaction:

$$O_2 + 4H^+ + 4e^- \Leftrightarrow 2H_2O$$
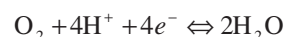
and the anodic part related to the copper dissolution:

$$Cu \Leftrightarrow Cu^+ + e^-$$

$$Cu^+ \Leftrightarrow Cu^{2+} + e^-$$
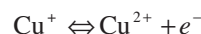
In the blank solution, at low over potentials, the cathodic polarization curves are linear but after approxi-
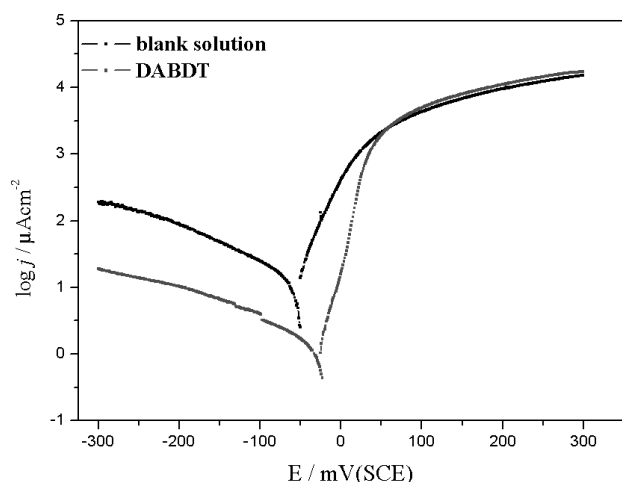
Figure 2: Polarization curves for copper electrodes with and without the thiazole derivatives (c = 0.005 mmol dm^{-3})
Slika 2: Polarizacijske krivulje za bakrove elektrode brez derivatov tiazola in z njimi (c = 0,005 mmol dm^{-3})

Table 2: Electrochemical parameters of copper corrosion in the presence of different concentrations of DABDT
Tabela 2: Elektrokemijski parameteri korozije bakra v različnih koncentracijah DABDT

| c/mmol dm^{-3}	E_{corr}/mV	j_{corr}/μA cm^{-2}	I/%
0	−58	14.16	–
0.001	−18	7.71	46
0.003	−11	4.87	66
0.005	−20	2.74	81
0.007	−12	1.61	89
0.01	−26	1.54	90

Table 3: Copper surface coverage in a different inhibitor concentration
Tabela 3: Obseg prekritja površine bakra pri različnih koncentracijah inhibitorja

c/mmol dm^{-3}	θ
0.001	0.455
0.003	0.656
0.005	0.807
0.007	0.886
0.01	0.898

mately –300 mV/SCE the dependence begins to deviate from linear due to diffusion phenomena, and in these fields the measurements were not made. In the anodic part of the curve a significant dissolution of copper is evident. As **Figure 2** shows, the presence of the DABDT thiazole derivative induced a significant decrease in the cathodic current density and at low over-potentials there is an insignificantly small reduction of the anodic current density. It can be concluded that the investigated thiazole acts primarily as a cathodic inhibitor against copper corrosion, hindering the oxygen reduction reaction in acidic media. The inhibitor's presence in the corrosion solution does not cause a large shift of the corrosion potential.

In **Table 2** are the electrochemical parameters, such as the corrosion potential (E_{corr}) and the corrosion current density (j_{corr}), which were obtained by Tafel extrapolating the anodic and cathodic parts of the polarization curves and the inhibitor efficiency of the DABDT molecule.

The inhibitor efficiency of the DABDT molecule was calculated using the following equation:

$$\eta(\%) = \frac{j_0 - j}{j_0} \cdot 100$$

where, j_0 and j are the corrosion-current density measured on the copper electrode in the blank and inhibitor-containing solutions.

The obtained results are comparable with those calculated from the weight loss measurement (**Table 1**). A small difference can be observed with several authors.[13–15] This difference can be attributed to the fact that a gravimetric measurement gives an average corrosion rate, whereas instantaneous corrosion rates were obtained using polarization methods.

As can be seen from **Table 2** the corrosion rate in the presence of DABDT molecules depended on the concentration of the thiazole. The inhibitor efficiency

increased with the increase in the concentration of thiazole. In the investigated concentration range, the maximum concentration of 0.01 mmol dm^{-3} produced the best inhibitor efficiency. A higher concentration of inhibitor could not be tested because of the low solubility of the DABDT. The increasing inhibitor efficiency with the concentration indicates that DABDT molecules protecting the copper from corrosion via the adsorption onto the metal surface.

During the adsorption onto the metal surface the inhibitor molecules are replacing the water molecules that are pre-adsorbed at the metal surface. According to Bockris,[16] the adsorption of an organic molecule at the metal/solution interface may be written according to the following displacement reaction:

$$inh_{(sol)} + nH_2O_{(ads)} \Leftrightarrow inh_{(ads)} + nH_2O_{(sol)}$$
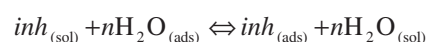
where n is the number of water molecules removed from the metal surface for each molecule of adsorbed inhibitor. The interactions of the organic molecules at the electrical double layer change its properties and structure. Changes in the structure of the electric double layer occur due to the fact that the inhibitor molecules are larger than the water molecules. Organic molecules also have a lower value of the dielectric constant than the water molecules, which reflects in the properties of the double layer as the reduction of its conductivity. Adsorption isotherms provide information about the interaction among the adsorbed molecules themselves and their interactions with the electrode surface.[17] The values of the degree of surface coverage, θ, (**Table 3**) calculated from the following equation[18]:

$$\theta = 1 - \frac{j}{j_0}$$
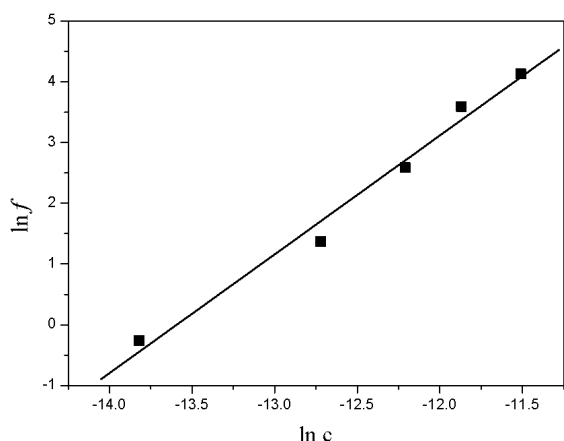
Figure 3: Bockris-Swinkels isotherms
Slika 3: Bockris-Swinkelsove izoterme

were used to determine the isotherm that best describes the adsorption process.

The best correlation between the experimental results and the isotherms described above was obtained using Bockris-Swinkels isotherm:[16,4]

$$\frac{\left[\dfrac{\theta}{(1-\theta)^n}\right]^{[\theta+n(1-\theta)^{n-1}]}}{n^n} = Kc$$

where θ is the surface coverage, n is the number of water molecules substituted, c is the inhibitor concentration and K is the constant of the adsorption process.

Figure 3 shows the Bockris-Swinkels isotherms obtained from copper in the presence of different concentrations of thiazole, where f is equal to the left part of the Bockris-Swinkels isotherms,

Knowing the value of K provides the possibility of calculating the basic thermodynamic parameter, the standard free energy of the adsorption is ΔG_{ads}. The constant of adsorption, K, is related to the standard free energy of adsorption, ΔG_{ads}, with the following equation:[19]

Table 4 reports the data from Bockris-Swinkels isotherm and the value of ΔG_{ads} for the adsorption process of the investigated thiazole derivative.

Table 4: Value of the adsorption constant, K, the number of replacement water molecules, n, the regression coefficient, R, and the standard free energy of adsorption, ΔG_{ads}, for the DABDT molecule
Table 4: Vrednosti adsorpcijske konstante K, število nadomeščenih molekul vode n, regresijski koeficient R in standardna prosta energija adsorpcije ΔG_{ads} za molekulo DABDT

ln K	n	ΔG_{ads}/kJ mol^{-1}	R
13.55	1	−43.5	0.981

The high value of the adsorption constant, K, indicates that the adsorption process of the DABDT molecules takes place relatively quickly on the copper surface. The results in **Table 4** show that the DABDT molecule is adsorbed on the copper surface, replacing one molecule of water. The number of water molecules

that is replaced can be seen as an indicator of the position of the inhibitor molecules on the surface of the copper. The small number of water molecules suggests that the thiazole molecules are vertically oriented in relation to the copper surface.

The negative values of ΔG_{ads} ensure the spontaneity of the adsorption process and the stability of the adsorbed layer on the copper surface. Generally, the values of ΔG_{ads} are used to determine the type of interaction between the organic molecules and the metal surface atoms. It is well known that the values of ΔG_{ads} of the order of –20 kJ mol^{-1} or lower indicate physisorption; those of order of –40 kJ mol^{-1} or higher involve charge sharing or a coordinate type of bond between metals and organic molecules.[20,21] In case of DABDT molecules the calculated values of ΔG_{ads} are slightly more negative than –40 kJ mol^{-1}, and therefore indicate that the adsorption mechanism of this thiazole derivative on copper in acidic sulphur-containing media was typically chemisorption.

The ability to form a chemical bond with copper and the good inhibition efficiency of the DABDT molecules (90 %) can be explained by the characteristics of dimetyl-amino groups, which are present in the molecule at position 5. In the DABDT molecule the dimethyl-amino group has a great influence on the distribution of the electron density around the active site of the thiazole molecule and therefore its inhibitor activity. The dimetyl-amino group has a positive inductive and resonance effect. These effects are powerful electron-donating effects, providing an increase of the electron density of the active centre of the thiazole molecules (sulphur atom). According to this the unshared pair of electrons in the sulphur atom can strongly interact with the copper uncompleted d-orbitals to provide a protective chemisorption film and better copper protection in the acidic media.

4 CONCLUSION

In this paper the possibility of the corrosion protection of copper in acidic media using a DABDT derivative was investigated in an acidic sulphate-containing solution (0.1 mol dm^{-3} Na$_2$SO$_4$, pH = 3) using potentiostatic polarization measurements.

From the obtained results, it can be concluded:
1. The investigated derivative, DABDT, shows a good inhibition efficiency (90 %) towards the copper corrosion in the acidic sulphate-containing solution.
2. DABDT acts as a mixed copper corrosion inhibitor. Compared to the blank solution in the presence of these molecules there is a slowdown in the cathodic reaction as well as the anodic process of the metal dissolution.
3. The best inhibition efficiency was obtained for the concentration 0.01 mmol dm^{-3}.

4. DABDT protects the copper surface from corrosion by adsorption.

5. The adsorption of these molecules on the copper surface happens as a fast and spontaneous process, following the Bockris-Swinkels isotherms by replacing one water molecule on the copper surface.

6. Adsorption leads to the formation of a chemical bond between the thiazole derivative DABDT and the copper atoms.

7. There is a good inhibition efficiency of the tested compound achieved due to the presence of strong electron-donating $N(CH_3)_2$ groups.

Acknowledgments

5 REFERENCES

[1] http://www.g2mtlabs.com/cost-of-corrosion/ 17. 2. 2012

[2] C. Fiad, 8 SEIC, Ferrara, 10 (**1995**), 929–949

[3] R. Fuchs-Godec, V. Doleček, Colloids and Surfaces A Physicochemical and Engineering Aspects, 244 (**2004**), 73–76

[4] G. Moretti, F. Guidi, Corrosion Science, 44 (**2002**), 1995–2011

[5] R. F. V. Villamil, P. Corio, J. C. Rubim, S. M. L. Agostinho, Journal of Electroanalytical Chemistry, 472 (**1999**), 112–119

[6] E. S. M. Sherif, S. M. Park, Electrochim. Acta, 51 (**2006**), 4665–4673

[7] F. Zucchi, G. Trabanelli, M. Fonsati, Corros. Sci., 38 (**1996**), 2019–2029

[8] M. M. Antonijevic, M. B. Petrovic, Int. J. of Electrochem. Sci., 3 (**2008**), 1–28

[9] Gy. Vastag, E. Szőcs, A. Shaban, I. Bertóti, K. Popov-Pergal, E. Kálmán, Solid State Ionics, 141 (**2001**), 87–91

[10] Gy. Vastag, E. Szőcs, A. Shaban, E. Kálmán, Pure Appl. Chem., 73 (**2001**), 1861–1869

[11] I. B. Obot, N. O. Obi-Egbedi, S. A. Umoren, Corros. Sci., 51 (**2009**), 276–282

[12] L. Tang, X. Li, L. Li, G. Mu, G. Liu, Surf. Coat. Technol., 201 (**2006**), 384–388

[13] S. Muralidiharan, M. A. Quraishi, S. V. K. Lyer, Corros. Sci., 37 (**1995**), 1739–1750

[14] E. E. Foad El Sherbini, Mater. Chem. Phys., 60 (**1999**), 286–290

[15] F. Bentiss, M. Lebrini, M. Lagrenee, Corros. Sci., 47 (**2005**), 2915–2931

[16] J. O. M. Bockris, D. A. J. Swinkels, J. Electrochem.Soc., 111 (**1964**), 736

[17] E. A. Noor, A. H. Al-Moubaraki, Mater. Chem. Phys., 110 (**2008**), 145–154

[18] Lj. M. Vačar, D. M. Dražić, Corros. Sci., 44 (**2002**), 1669–1680

[19] J. Flis, T. Zakroczymski, J. Electrochem. Soc., 143 (**1996**), 2458–2464

[20] S. M. A. Hosseini, M. Salari, M. Ghasemi, M. Abaszadeh, Z. Phys. Chem., 223 (**2009**), 769–779

[21] R. Solmaza, G. Kardas, M. Culha, B. Yazici, M. Erbil, Electrochim. Acta, 53 (**2008**), 5941–5952

ENERGY- AND TIME-SAVING LOW-TEMPERATURE THERMOMECHANICAL TREATMENT OF LOW-CARBON PLAIN STEEL

PRIHRANKI ENERGIJE IN ČASA PRI NIZKOTEMPERATURNI TERMOMEHANSKI OBDELAVI MALOOGLJIČNEGA PLOŠČATEGA JEKLA

Hana Jirkova[1], Daniela Hauserova[2], Ludmila Kucerova[1], Bohuslav Masek[1]

[1]University of West Bohemia, The Research Centre of Forming Technology – FORTECH, Univerzitni 22, 306 14 Pilsen, Czech Republic
[2]COMTES FHT, a.s., Prumyslova 995, 334 41 Dobrany, Czech Republic
h.jirkova@email.cz

Reduction of energy is one way of cutting the cost of finished steel products. In this context heat treatment is a costly stage of the production. This paper presents a method of reducing soft-annealing times. The method termed as ASR (accelerated spheroidization and refinement) was employed for improving the cold formability of the ferrite-pearlite steel).
In this study, plain low-carbon RSt-32 steel was used as the experimental material. The influence of deformation below the A_{c1} temperature on grain refinement and carbide spheroidization, as well the influence of the temperature cycling around the A_{c1} temperature within the temperature intervals of various widths were explored. In addition, attention was paid to the effects of the holding time between deformation steps and to the amount of deformation heat.
The initial lamellar pearlite was converted into a recrystallized structure with fine ferrite grains of about 3 μm and fine spheroidized cementite. The final hardness was about 150 HV10. This is by about 25 % lower than the hardness of the initial ferrite-lamellar pearlite structure. Significant time and energy savings can be reached as the treatment shortens the thermomechanical exposure from several hours to several minutes.

Keywords: pearlite morphology, soft annealing, incremental deformation

Zmanjševanje porabe energije je ena od poti za zmanjšanje stroškov končnih jeklenih proizvodov. V tem kontekstu je toplotna obdelava draga faza proizvodnje. Članek predstavlja metodo za zmanjšanje časa mehkega žarjenja. Metoda, označena z ASR (pospešena sferoidizacija in zmanjšanje zrn) je bila uporabljena za izboljšanje hladne preoblikovalnosti feritno-perlitnega jekla.
Za eksperimentalni material v tej študiji je bilo uporabljeno maloogljično jeklo RSt-32. Preiskan je bil vpliv deformacije pod temperaturo A_{c1} na zmanjšanje velikosti zrn in na sferoidizacijo karbida, kot tudi vpliv nihanja temperature okrog A_{c1} v različno širokih temperaturnih intervalih. Dodatna pozornost je bila posvečena še učinku časa zadržanja med posameznimi deformacijami in na delež deformacijske toplote. Začetni lamelarni perlit se je pretvoril v rekristalizirano strukturo z drobnimi zrni ferita, velikosti okrog 3 μm in drobno sferoidiziranim cementitom.
Končna trdota je bila okrog 150 HV10. To je okrog 25 % nižje od trdote začetne strukture s feritom in lamelarnim perlitom. Mogoče je doseči pomembne prihranke v času in energiji, saj termomehanska obdelava skrajša potreben čas od nekaj ur na nekaj minut.

Ključne besede: morfologija perlita, mehko žarjenje, prirastek deformacije

1 INTRODUCTION

Reducing soft-annealing times is one of today's efforts in cutting down the production costs of cold-formed parts. Initial microstructures of the materials suitable for cold forming have a high formability. Such microstructures can be obtained through spheroidization of the cementite shape in pearlite.

Cementite can be spheroidized using several standard heat-treatment procedures. These include the following: a) isothermal annealing at a temperature slightly below A_{c1}, b) soaking at a temperature just above A_{c1} with slow cooling in the furnace, or with a hold just below A_{c1}, c) thermal cycling in the vicinity of A_{c1} [1]. In this context, the new ASR (accelerated spheroidization and refinement) procedure is highly effective[2,3] (**Figure 1**). It is an energy-saving thermomechanical-treatment procedure based on incremental deformation.

2 EXPERIMENTAL WORK

2.1 Experimental Material

The experimental material was cold-drawn, plain, structural steel RSt37 (S232 JRC) (**Table 1**). The as-received microstructure consisted of ferrite and lamellar pearlite. The ultimate strength, yield strength, elongation and hardness of the as-received material were 516 MPa, 450 MPa, 20 % and 200 HV10, respectively. The pearlite fraction found with an image analysis was 9 %. The ferrite-grain size was approximately 30 μm. The A_{c1} temperature found by dilatometric testing was 777 °C.
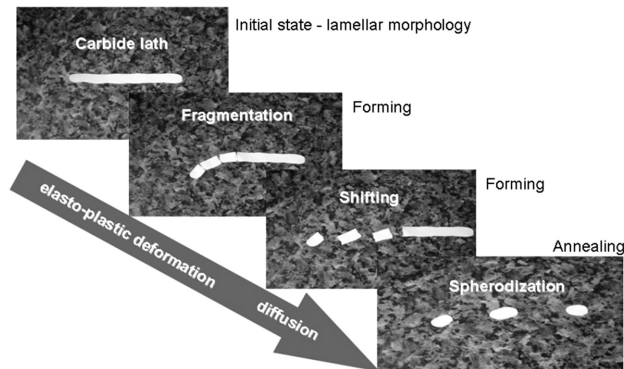
2.2 ASR Trial

To obtain the resulting microstructure of a very fine ferrite with spheroidized cementite, a number of processing parameters had to be optimised: the strain magni-

Table 1: Chemical composition of the RSt37-2 (S232 JRC) steel in mass fractions (%)
Tabela 1: Kemijska sestava jekla RSt37-2 (S232 JRC) v masnih deležih (%)

C	P	S	Mn	Si	N
0.08	0.022	0.023	0.65	0.16	0.004

Figure 1: Scheme of the newly developed ASR process
Slika 1: Shematski prikaz novo razvitega postopka

tude, the deformation temperature and the holding time upon deformation. The effects of deformation heat and thermal cycling in the vicinity of A_{c1} were explored as well. The processing was performed in a thermomechanical simulator.[4]

With the aim to reduce spheroidization times as much as possible, pearlitic cementite lamellae must be not only fractured but also shifted further apart (**Figure 1**). This is why the schedules with two deformation steps were used for the initial experiment (**Table 2**). The first step was the tensile deformation with a strain magnitude of $\varphi =$

Table 2: Thermomechanical-treatment parameters used for exploring the effect of magnitude of compressive strain and the impact of the hold
Tabela 2: Parametri termomehanske obdelave, ki je bila uporabljena za iskanje velikosti tlačnih napetosti in vpliv časa zadrževanja

T_A/°C	φ Tension+ compression	Hold upon def. (s)	HV10	R_m/ MPa	A_{5mm}/%
	0.3 + 1.7	–	166	465	8
740	0.3 + 1.7	300	121	421	20
	0.3 + 0.8	300	143	–	–
	0.3 + 0.3	300	141	–	–

Table 3: Effect of thermal cycling on microstructure evolution
Tabela 3: Vpliv toplotnega nihanja na razvoj mikrostrukture

T_A/°C	φ Tension + compression	Temp. range (°C)	HV10	R_m/ MPa	A_{5mm}/%
740	0.3 + 1.7	740–780	146	426	22
740	–	740–780	145	479	37
700	–	700–780	149	/	/

Table 4: Impact of deformation heat on microstructure evolution during a repeated deformation
Tabela 4: Učinek deformacijske toplote na razvoj mikrostrukture med ponavljanjem deformacij

T_A/°C	No. of def. steps	Time between def. steps (s)	HV10	R_m/ MPa	A_{5mm}/%
700	9	30	150	352	22
	9	10	155	–	–
	9	5	197	260	14
	5	30	140	–	–
	9	30 water	189	502	22

Table 5: Impact of non-isothermal deformation on microstructure evolution
Tabela 5: Vpliv neizotermne deformacije na razvoj mikrostrukture

T_A/°C	No. of cycles	Hold time between def. (s)	HV10
700	9	1	225
700	9	0	192

0.3, whereas the second step included intensive compressive deformation. The strain magnitude φ varied from 1.7 to 0.3 (**Table 2**). The effects of a 300 s hold following the deformation upon recrystallization were mapped. The soaking temperature and the time were 740 °C and 10 s, respectively. The heating rate was 30 °C/s. The schedules were followed by air cooling.

The effect of the thermal cycling between 740 °C and 780 °C, i.e., around A_{c1}, for 50 s (**Table 3**) was investigated. Two schedules were designed: one included deformation prior to the thermal cycling and the other was without deformation. An additional schedule included soaking at a reduced temperature of 700 °C and a thermal cycling within the range of 700–780 °C for 50 s.

The effect of deformation heat on the specimen temperature and carbide spheroidising was explored in the subsequent schedules (**Table 4**). At 700 °C, the tensile and compressive deformations with the magnitudes of 0.3 and 0.4 were applied with varied holding times between the deformation steps. The holding times were between 5–30 s and 5–9 deformation cycles were used. Finally, the specimens were water quenched for the mapping of the microstructure evolution.

While the initial schedules included deformation at a constant temperature, the additional schedules were used to explore the effects of the non-isothermal deformation, during which the specimen was cooled in air (**Table 5**). The increase in the specimen temperature due to deformation heat, the microstructure evolution and its morphology, the refinement and, in particular, the spheroidization processes were examined. A soaking temperature of 700 °C was used in both schedules of this stage.
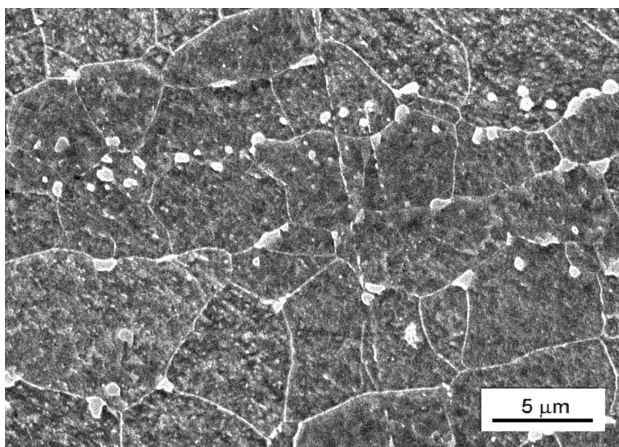
3 RESULTS AND DISCUSSION

3.1 Effects of Strain Magnitude and Holding Time

Using the ASR schedule with the soaking temperature of 740 °C and the tensile and compressive deformations ($\varphi = 0.3 + 1.7$), we broke up the cementite lamellae into the particles (**Figure 1**) of about 1 μm and refined the ferrite grains. The obtained microstructure showed a notable banding. The observation made with a scanning electron microscope revealed that the cementite spheroidization was extensive. The material's hardness, the ultimate strength and the A_{5mm} elongation were 166 HV10, 465 MPa and 8 %, respectively (**Table 2**). The elongation was rather low.

Then, an additional 300 s hold was incorporated, following the tensile-compressive deformation, to promote the recrystallization and to improve the carbide-spheroidising conditions. This hold caused a ferrite coarsening, a local carbide spheroidization and a more uniform distribution of carbides in the ferrite matrix (**Figure 2**). These microstructure changes were reflected in a low hardness of 121 HV10 and a low strength of 421 MPa. Recrystallization led to a higher elongation of 20 % (**Table 2**).

However, the amount of the strain used is too large for some technical applications. At the edges of the test specimen, where the nominal strain was somewhat lower, the ASR process appeared to be less intense. Based on this finding, two schedules were proposed, where the amount of strain in the second deformation step was decreased from $\varphi = 1.7$ to 0.8 and 0.3 (**Table 2**). The total strain levels in these schedules were $\varphi = 1.1$ and $\varphi = 0.6$. The reduction in the total amount of strain was reflected in the reduced hardness values of 143 and 141 HV10. The specimens treated with both schedules contained large lamellar-pearlite colonies.
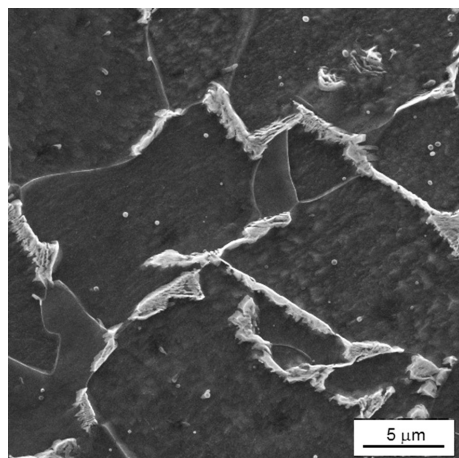
3.2 Effects of Thermal Cycling on Microstructure Evolution

This stage of the study was aimed at verifying the theory that the thermal cycling with the upper limit above A_{c1} accelerates cementite spheroidization through a repeated dissolution of cementite and a formation of new nuclei (**Table 3**). Using the schedule with the thermal-cycling range of 740–780 °C, i.e., in the vicinity of A_{c1}, the specimen microstructure consisted of the ferrite with the grain size of above 20 μm and the pearlite colonies along the grain boundaries with the hardness of 145 HV10 (**Table 3**, **Figure 3**). When a lower heating temperature of 700 °C and a cycling within a wider temperature range were used, the resulting microstructure was coarser but showed the same hardness. The incorporation of a two-step tensile-and-compressive deformation cycle ($\varphi = 0.3 + 1.7$) at 740 °C, prior to the thermal cycling in the range of 740–80 °C led to a finer
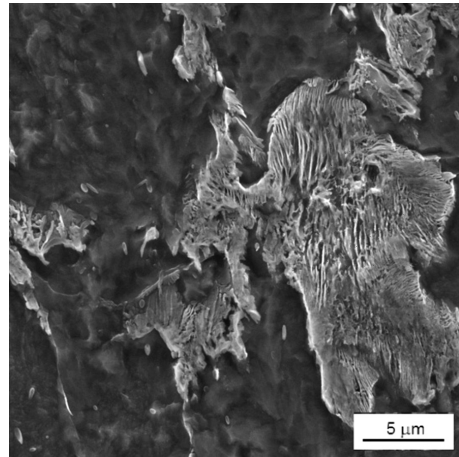
Figure 3: Effects of thermal cycling in the temperature range of 740–780 °C without deformation
Slika 3: Učinek toplotnih ciklov v temperaturnem področju 740–780 °C brez deformacije

Figure 2: 740 °C/10 s – 2-times deformation step: tension + compression ($\varphi = 2.1$) with a hold of 300 s
Slika 2: 740 °C/10s – 2-krat stopnja deformacije: nateg + stiskanje ($\varphi = 2.1$) z zadrževanjem 300 s

Figure 4: Effects of thermal cycling in the temperature range of 740–780 °C with deformation
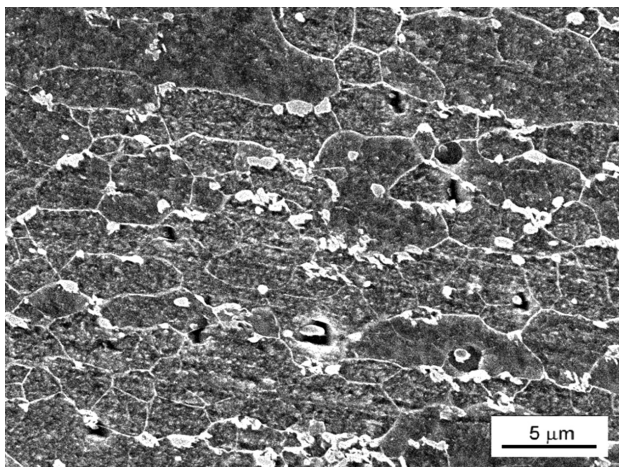**Slika 4:** Učinek toplotnih ciklov z deformacijo v temperaturnem področju 740–780 °C

microstructure with a similar hardness value (**Table 3**, **Figure 4**). The grains were fully recrystallized and had a size of approximately 10 μm. In none of these cases the cementite precipitation within the ferrite grains occurred and the pearlite morphology was mainly lamellar.

3.3 Effects of Deformation Heat on Microstructure Evolution
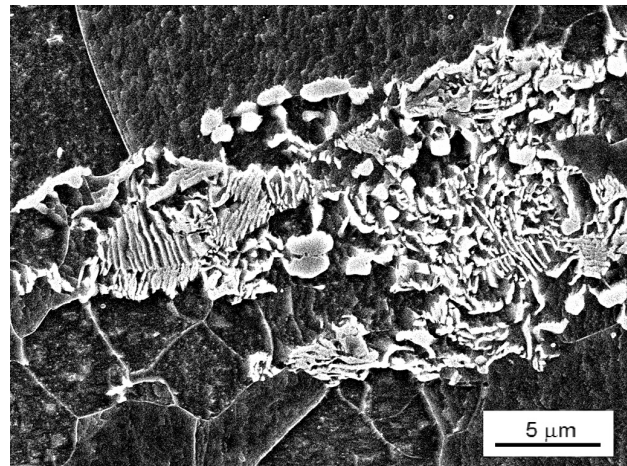
At this stage of the study, the feasibility of the cementite spheroidization and microstructure refinement by applying deformation heat alone was explored. This deformation heat was to be generated by means of a two-step deformation at 700 °C, combined with the pauses of varying lengths (**Table 4**).

The schedule with 9 deformation cycles and 30 s pauses led to an increase in the specimen temperature to 720 °C over the first 5 deformation cycles. The fine, elongated ferrite microstructure with disintegrated pearlite islands and a hardness of 150 HV10 was obtained (**Figure 5**). Cementite was predominantly found along the ferrite-grain boundaries. However, there were some particles within the ferrite grains as well. The microstructure was substantially refined by the forming process. The ferrite-grain size was approximately 5 μm and most of the cementite particles were globular. The steel in this condition had a strength of 352 MPa and an elongation of 22 % (**Table 4**). Where 10 s pauses between deformation cycles were used instead of the 30 s ones, the resulting extent of recrystallization was lower. The final microstructure showed a strong banding and disintegrated, globular pearlite islands indicating the flow direction. The fact that the pauses were shorter by 20 s had no significant impact on the hardness. However, reducing the pauses further to 5 s led to a large increase in the hardness amounting to 197 HV10. The microstructure was similar to that obtained in the previous case. Where the number of deformation cycles was

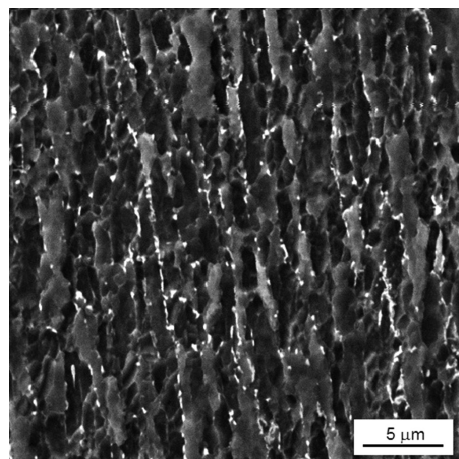**Figure 6:** 700 °C/10 s – 5-times tension + compression ($\varphi = 4$), 0 s pause between deformation cycles
Slika 6: 700 °C/10s – 5-krat nateg + tlak ($\varphi = 4$), 0 s premora med cikli

reduced from 9 to 5, the coarser ferrite was recrystallized (**Figure 6**). Its hardness was 140 HV10 (**Table 4**). The pearlite colonies disintegrated partially, remaining lamellar in character and situated on the ferrite-grain boundaries.

3.4 Impact of Non-Isothermal Deformation on Microstructure Evolution

The last series of optimisation schedules was aimed at exploring the deformation schedules similar to the previous ones, except that the specimen was not kept at the heating temperature during either the deformations or the deformation pauses (**Table 5**). As the specimen was cooled in still air, the pause between deformation steps was either 1 s or zero.

The schedule with 1 s pauses between deformations led to a specimen failure in the 6th cycle at 520 °C. The deformation heat was not sufficient to compensate for the heat losses, which is why the specimen temperature

Figure 5: 700 °C/10 s – 9-times tension + compression ($\varphi = 7.2$), 30 s pause between deformation cycles
Slika 5: 700 °C/10 s – 9-krat nateg + tlak ($\varphi = 7.2$), 30 s premor med cikli deformacije

Figure 7: Effects of non-isothermal deformation without pauses
Slika 7: Učinek neizotermne deformacije brez premora

could not exceed 700 °C. The continuous deformation without pauses generated a deformation heat that increased the specimen temperature to 724 °C. The temperature decreased below 700 °C no sooner than during the 4th deformation cycle. In this case the specimen failed during the 7th cycle at 680 °C. Both schedules resulted in highly distorted microstructures with the fine, ferrite-grain and banded, elongated areas with globular cementite (**Figure 7**). Large strains led to the hardness values of 225 and 192 HV10.

4 CONCLUSION

The experimental programme consisted of a gradual optimisation of the low-temperature thermomechanical treatment of the RSt37-2 structural steel.

It was found that the processes of carbide spheroidization, grain refinement and cementite redistribution from the bands formed upon deformation are governed by the pause between deformation steps. Other important preconditions for a successful ASR process include the presence of strain components of sufficient intensity capable of breaking up and separating fragmented cementite particles through a plastic deformation. The spheroidization process can be accelerated substantially under these conditions. The optimum results of the experimental ASR process were achieved using the schedule with the soaking temperature of 740 °C and two-step tensile-compressive deformation with the following 300 s pause. This procedure led to a microstructure with fine, ferrite-grain and globular carbides. The yield strength of the resulting material was approximately 200 MPa, its ultimate strength was 421 MPa and the elongation was 20 %.

5 REFERENCES

[1] A. Kamyabi-Gol, M. Sheikh-Amiri, Spheroidizing Kinetics and Optimization of Heat Treatment Parameters in CK60 Steel Using Taguchi Robust Design, Journal of Iron and Steel Research International, 17 (**2010**) 4, 45–52

[2] B. Masek, H. Jirkova, L. Kucerova, Rapid Spheroidization and Grain Refinement Caused by Thermomechanical Treatment for Plain Structural Steel, Materials Science Forum, 706–709 (**2012**), 2770–2775

[3] D. Hauserova, J. Dlouhy, Z. Novy, J. Zrnik, M. Duchek, Forming of C45 Steel at Critical Temperature, Procedia Engineering, 10 (**2011**), 2955–2960

[4] B. Mašek et al., Physical modelling of microstructure development during technological processes with intensive incremental deformation, The Mechanical Behaviour of Materials X, 345–346 (**2007**), 943–946

ELECTROCHEMICAL CHARACTERIZATION OF THE NANO Py/DDS/SiO₂ FILM ON A COPPER ELECTRODE

ELEKTROKEMIJSKA KARAKTERIZACIJA NANOPLASTI Py/DDS/SiO2 NA BAKRENI ELEKTRODI

Meysam Sharifirad[1], Farhoush Kiani[2], Fardad Koohyar[2]

[1]Department of Chemistry, Teacher Research Bojnord, Iran
[2]Department of Chemistry, Faculty of Science, Ayatollah Amoli Branch, Islamic Azad University, Amol, Iran
fardadkoohyar@yahoo.com

The electroactive copolymer of pyrrole (Py) and 4.4'-diaminodiphenyl sulfone (DDS) was synthesized electrochemically in 4 M H_2SO_4 and ethanol medium. Both electrochemical synthesis and characterization of the copolymer deposited on a copper electrode were carried out using cyclic voltammetry. The voltammograms exhibited different patterns of behavior with different feed concentrations of Py. Equimolar concentrations of Py and DDS demonstrated a very efficient growth of the copolymer film on the surface of the copper. The scan rate exerted little effect on this copper copolymer film, revealing the film excellent electroactive adherent properties. The effect of pH on the copolymer film showed that the polymer was electrochemically active up to pH 7.0. A spectroelectrochemical analysis of the copolymer film, carried out on an indium tin oxide (ITO) plate, showed multicolor electrochromic behavior when the applied potential was changed. The polymer was characterized with the UV-Vis and FTIR spectral studies. The formation of the polymer through the N-H group was understood from the single N-H stretching vibrational frequency at 3050 cm^{-1}. The surface morphology was studied using a SEM analysis and the grain size of the copolymer was measured using XRD studies and was found to be 50 nm. The electrical conductivity of the copolymer was 5.98×10^{-2} S cm^{-1}, as determined using a four-probe conductivity meter.

Keywords: 4.4'-diaminodiphenyl sulfone, cyclic voltammetry, SEM, nanosize, copper electrode

Električno aktiven kopolimer pirola (Py) in 4,4'-diaminodifenil sulfona (DDS) je bil sintetiziran elektrokemijsko v mediju 4 M H_2SO_4 in etanola. S ciklično voltametrijo je bila narejena elektrokemijska sinteza in karakterizacija kopolimera, nanesenega na bakreno elektrodo. Voltamogrami prikazujejo različne spektralne vzorce pri različnih koncentracijah dodanega Py. Ekvimolarna koncentracija Py in DDS izkazujeta učinkovito rast kopolimerne plasti na površini bakra. Hitrost skeniranja ima majhen učinek na bakrovo kopolimerno plast, razkrije pa odlične elektroaktivne lastnosti. Učinek pH na kopolimerno plast je pokazal, da je plast elektrokemično aktivna do pH 7,0. Spektroelektrokemična analiza kopolimerne tanke plasti na plošči iz indij-kositrovega oksida (ITO) je pokazala večbarvno elektrokromno vedenje, če se je uporabljeni potencial spremenil. Polimer je bil ocenjen z UV-Vis- in FTIR- študijami spektra. Nastanek polimera preko N-H-skupine je razumeti kot N-H razteznostna vibracijska frekvenca pri 3050 cm^{-1}. Morfologija površine je bila preučevana s SEM-analizo, velikost zrn kopolimera je bila izmerjena z XRD in ugotovljeno je bilo, da je velikosti 50 nm. Električna prevodnost kopolimera, izmerjena z merilnikom prevodnosti s štirimi sondami, je bila $5,98 \times 10^{-2}$ S cm^{-1}.

Ključne besede: 4,4'-diamino difenil sulfon, ciklična voltametrija, SEM, nanovelikost, bakrena alektroda

1 INTRODUCTION

Progressive research in the field of conducting polymers has led to the development of the materials with a great potential for commercial applications, including lightweight batteries, light-emitting diodes,[1] capacitors,[2] electrochromic devices,[3,4] optical and electronic devices.[5] Conducting-polymer films have shown promising applications in the field of biosensors and bioelectrochemistry by providing an active matrix with controlled morphology for immobilization of biological materials as well as transduction of electrical signals.[6,7] If an electrode surface is modified with a conducting-polymer film, then the modified electrode can be used as a sensor.[8–10] Polyaniline is among the most important organic conducting polymers having a high conductivity but poor processability.[11] In order to increase its processability and utility, researchers studied the derivatives of polyaniline prepared with different methods. Homopolymerization of aniline derivatives has been effective in the preparation of substituted polyanilines. Increased torsional angles and the presence of a substituent result in a decreased orbital overlap of electrons and nitrogen lone pairs; however, substituted polyanilines exhibit conjugations and conductivities that are significantly lower than those of polyaniline.[12] Several researchers have employed different post treatments after the synthesis of polymer films; however, there are no systematic studies on this aspect. On the other hand, when a polyaniline layer was deposited first and the electropolymerization was continued in a solution of 4.4'-diaminodiphenyl sulfone (DDS), a progressive transformation of the electrochemical behavior of the original polyaniline film was observed. The polyaniline promotes the polymerization by providing electrocatalytic sites and nucleation centers. Thus, the conducting polyaniline surface is protected well and leads to a better modification. Chemical polymerization of DDS also leads to newer polymers. Interestingly, both newly formed polymers are found to have a nanostructure. The preparation

of nanostructured conducting materials has become an important branch of materials research.[13] Many research groups have reported various kinds of polymer nanocomposites, like polyaniline, PEDOT, and polypyrrole.[14–16] Hence, it seemed interesting to study the formation and properties of the new nanostructured polymeric material produced with a reaction of polyaniline and DDS during redox cycling. DDS, an important pharmaceutical compound, is used as an antileprotic drug.[17–19] Utilization of the materials of biointerest for the preparation of newer nanopolymeric materials assumes their importance in the present environment. They are also used in the sorption and transport of carbon dioxide[20–22] and cured in epoxy networks.[23] Here we present the results obtained from a formation of a nanosized electroactive polymer through an electrochemical and chemical polymerization of 4.4'-diaminodiphenyl sulfone (DDS) and the characterizations of the new polymer. The electrical conductivity of the copolymers increased greatly, from 6.00×10^{-4} S cm^{-1} to 2.55×10^{-1} S cm^{-1}, with the increasing aniline content. The UV-Vis spectroelectrochemical studies performed on these copolymer films revealed their electrochromic sites corresponding to individual units. In another study an electroactive conducting polymer, poly(pyrrole-co-4.4'-diaminodiphenyl sulfone), was prepared from pyrrole and 4.4'-diaminodiphenyl sulfone (DDS) using cyclic voltammetry on a copper electrode surface.[24,25] The present study reports an electrochemical synthesis of a new nanosized poly(Py-co-DDS) and its characterization with the SEM, XRD, and FTIR techniques. Furthermore, the solubility in different solvents, conductivity and electrochromic behavior of the copolymer were evaluated and reported.

2 EXPERIMENTAL WORK

Pyrrole (Merck; 99 %) was distilled before use and all the test solutions were freshly prepared. DDS and methanol were purchased from Merck. Nano SiO₂ (Allderich, Germany, 40 nm diameter particles) and a phosphate buffer solution (PBS) with a pH of 7.0 as the electrolyte were prepared with 0.1 M NaH₂PO₄–Na₂HPO₄, while the pH was adjusted with 0.1 M HCl and 0.1 M NaOH. Cyclic voltammetry (CV) was carried out using a Potentiostat/Galvanostat EG&G Model 263 A, USA, with a PC and an electrochemical set up controlled with the M 270 software. A Pt grid was utilized as a counter-electrode and the reference electrode was Ag/AgCl (KCl: 3 M). The working electrode was either a copper (99.99 % purity) disk or a rectangular sheet (an area of 0.2 cm²). The electrodes were mechanically polished with abrasive paper (2400 grade) and rinsed with distilled water and finally dried under an argon flow before each electrochemical experiment. After the deposition the working electrode was removed from the electrolyte and rinsed with double distilled water and then dried in air. The FTIR transmission spectrum of the

polypyrrole coating was recorded in the horizontally attenuated, total reflectance mode in the spectral range of 400–500 cm^{-1} using a Bruker spectrometer, Vector Series 22, Germany. Spectroelectrochemical studies were performed in a quartz cuvette with a path length of 1 cm utilizing an optically transparent working electrode, an indium tin oxide (ITO) plate (10 Ω cm^{-2}), a Pt counter electrode, an Ag/Ag⁺ reference electrode and a computer-controlled JASCO V-530, UV-Vis spectrophotometer. Scanning electron microscopy (SEM) images were taken using a VEGA HV (high potential) 1 500 V at various magnifications. A conducting poly(aniline-*co*-diaminodiphenyl sulfone) was synthesized and characterized and it was shown that the reactivity of 4.4'-diaminodiphenyl sulfone was greater than that of aniline.[26] Our electrochemically synthesized copolymer of aniline and 4.4'-diaminodiphenyl sulfone exhibited novel electrochromic properties.[26] In this paper, the electrochemical copolymerization of pyrrole (Py) with 4.4'-diaminodiphenyl sulfone (DDS) and nanoparticles of SiO₂ is presented. The solubility of copolymers was studied with various organic solvents.

3 RESULTS AND DISCUSSION

3.1 Electrochemical copolymerization of pyrrole, 4.4'-diaminodiphenyl sulfone and nanoparticle SiO₂

Figure 1 shows the cyclic voltammogram of 0.01 M DDS in 4 M H₂SO₄, 0.1 M SiO₂ and the ethanol mixture obtained between –1 V and 1.5 V at a scan rate of 100 mV s^{-1} on a copper electrode. The voltammogram exhibits one broad oxidation peak at 0.2 V in the first cycle. The anodic peak is caused by an oxidation of the amino group in the phenyl ring of DDS in 4 M H₂SO₄, 0.1 M SiO₂ and ethanol medium. After the completion of the
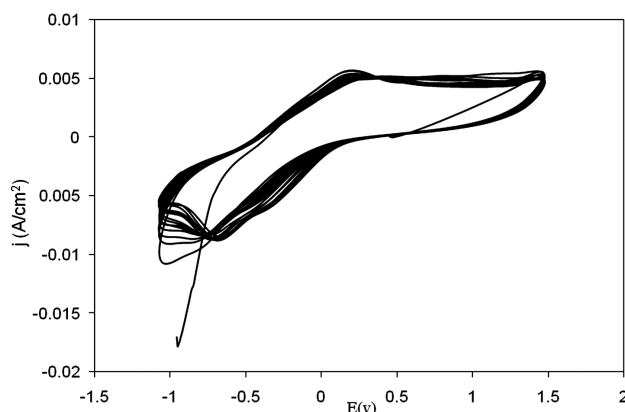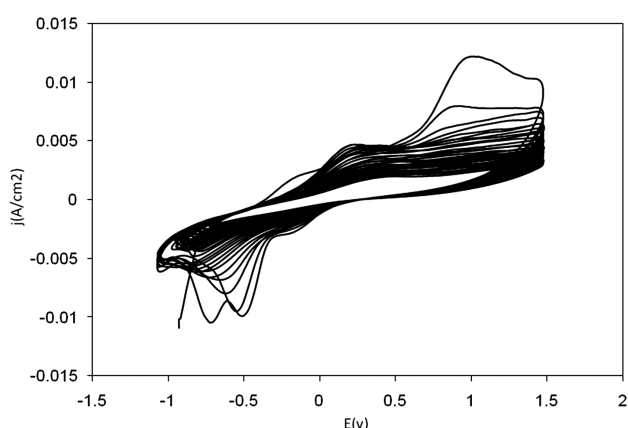

Figure 1: Cyclic voltammetric behavior of 0.01 M DDS and SiO₂ in 4 M H₂SO₄ and ethanol at a scan rate of 100 mV s^{-1} using a copper working electrode
Slika 1: Vedenje pri ciklični voltametriji 0,01 M DDS in SiO₂ v 4 M H₂SO₄ in etanolu pri hitrosti skeniranja 100 mV s^{-1} z uporabo bakrene delovne elektrode
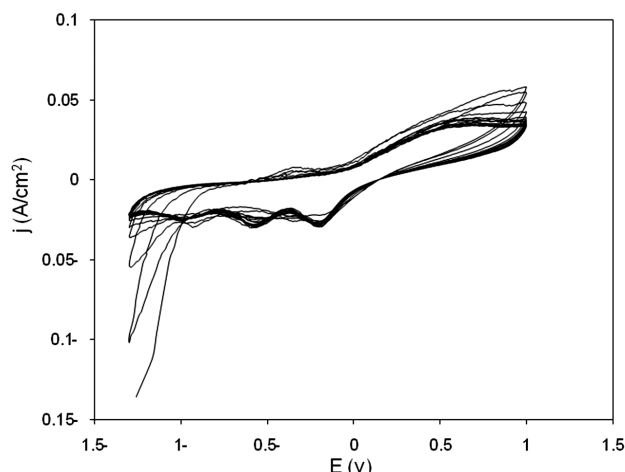
Figure 2: Cyclic voltammetric behavior of 0.01 M Py and 0.1 M SiO$_2$ in 4 M H$_2$SO$_4$ and ethanol at a scan rate of 100 mV s^{-1} using a copper working electrode
Slika 2: Vedenje pri ciklični voltametriji 0,01 M Py in 0,1 M SiO$_2$ v 4 M H$_2$SO$_4$ in etanolu pri hitrosti skeniranja 100 mV s^{-1} z uporabo bakrene delovne elektrode

Figure 3: Cyclic voltammetric behavior of 0.01 M DDS, 0.01 M Py and SiO$_2$ in 4 M H$_2$SO$_4$ and ethanol at a scan rate of 100 mV s^{-1} using a copper working electrode
Slika 3: Vedenje pri ciklični voltametriji 0,01 M DDS, 0,01 M Py in SiO$_2$ v 4 M H$_2$SO$_4$ in etanolu pri hitrosti skeniranja 100 mV s^{-1} z uporabo bakrene delovne elektrode

tenth cycle, the working electrode was washed with ultrapure water and a light brown film was seen on the surface of the copper electrode. The film was thin and further growth was inhibited due to its low conductivity.

Figure 2 represents the cyclic voltammograms of the growth of PPy on a stationary copper electrode in 4 M H$_2$SO$_4$, 0.1 M SiO$_2$ and ethanol medium with a potential range of –1 V to 1.5 V and a scan rate of 100 mV s^{-1}. In the first anodic scan, a peak corresponds to the oxidation of PPy to produce a Py cation radical (PyR) that was observed at 0.2 V. Another peak observed in this first cycle at 1.03 V was due to the oxidation of ethanol.[27] The CVs of the second and subsequent cycles during the electrochemical polymerization of Py show two anodic peaks at 0.3 and 0.8 V. The progressive increases in the current of the peak at 0.3 V suggest a continuous formation of PPy films on the surface of the copper electrode.

The cyclic voltammogram of 0.01M DDS, 0.1 M SiO$_2$ and 0.01 M PPy in the 4 M sulfuric acid and ethanol is presented in **Figure 3**. The potential range applied and the scan rate selected here are the same as in the previous cases. The CVs show two oxidation peaks at –0.5 V and 1 V in the first cycle representing the formation of a pyrrole cation radical (PyR) and a 4.4'-diaminodiphenylsulfone cation radical (DDSCR), respectively. These peaks were assigned to the reduction of polymer products formed with a reaction between the intermediate species PyCR and DDSCR, respectively. According to the CVs recorded during the further cycles, i.e., the second to the tenth cycles, one oxidation and one reduction peak at 0.8 V and 0.3 V, respectively, appeared and they were both intensifying during these cycles. Thus, the CVs recorded during the copolymerization of 0.01 M DDS, 0.1 M SiO$_2$ and 0.01 M Py in the 4 M sulfuric acid and ethanol clearly differ from the CVs recorded during the homopolymerization of either Py or DDS alone. The

twin redox characteristics[28] noticed for the polymerization of Py were virtually merged into a single redox process in the cases of the copolymerization of Py and DDS. The above mentioned oxidation and reduction waves disappeared and one anodic and one cathodic peak appeared at 0.8 V and 0.3 V, respectively. These redox peaks show an effective increase of the current from the second cycle onwards. At the end of the tenth cycle, a dark-green copolymer film was observed on the surface of the copper electrode.

Copolymers were prepared from different molar feed ratios of Py and the copolymer formation was influenced by the Py concentration. The concentration of a Py monomer was plotted against the total charge of the formation of electroactive, oxidative, conducting copolymer
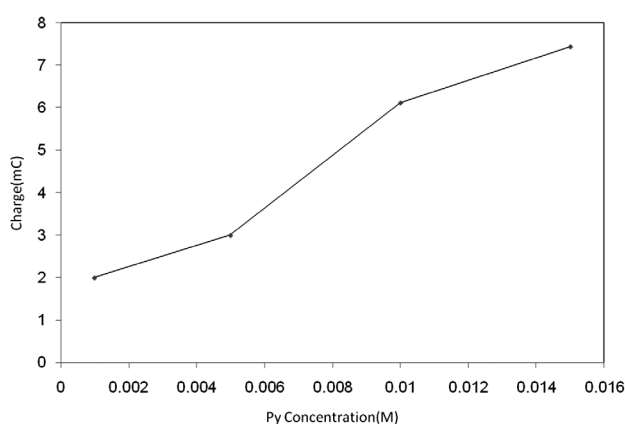
Figure 4: Plot of the charge vs. Py concentration (obtained from the CVs of copolymerization for varying concentrations of Py from 0.002 to 0.016 and 0.01 M of DDS in the 4 M H$_2$SO$_4$, 0.1 M SiO$_2$ and ethanol mixture)
Slika 4: Odvisnost naboja od koncentracija Py (dobljeno iz CV pri kopolimerizaciji za različne koncentracije Py od 0,002 do 0,016 in 0,01 M DDS v mešanici 4 M H$_2$SO$_4$, 0,1 M SiO$_2$ in etanola)
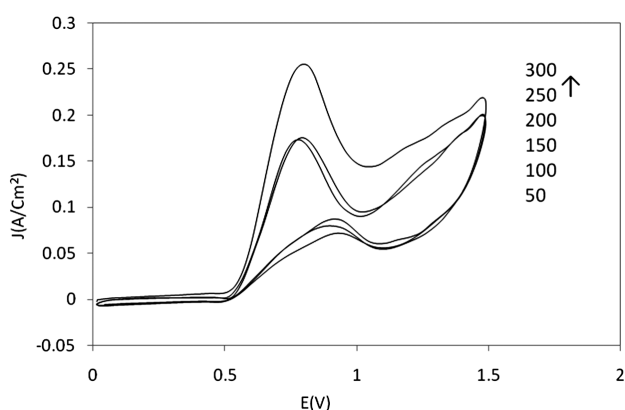
Figure 5: Effect of the scan-rate variation on the cyclic voltammetry of the poly(Py-co-DDS/SiO₂)-film-coated copper electrode from 50 mV s^{-1} to 300 mV s^{-1} in the 4 M H₂SO₄ medium
Slika 5: Vpliv spreminjanja hitrosti skeniranja od 50 mV s^{-1} do 300 mV s^{-1} v mediju 4 M H₂SO₄ na ciklično voltametrijo poli (Py-co-DDS/SiO₂) plasti, ki pokriva bakreno elektrodo

films (**Figure 4**). **Figure 4** shows that the total charge is on a rapid increase due to the increase in the Py concentration until Py reaches 0.01 M, when the increase in the charge slows down depending on the Py concentration. These observations indicate an increasing number of Py units in the copolymer formation.
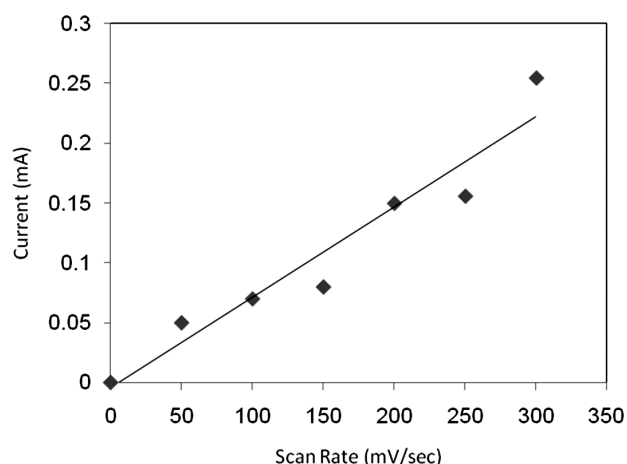
3.2 Effect of the scan rate

The copolymer film of poly(pyrrole-co-4.4'-diaminodiphenyl sulfone-SiO₂) was washed with ultrapure water and a monomer-free background solution and then the film was scanned in the solution in the range of 0 mV to 1.5 mV. The cyclic voltammogram presented in **Figure 5** resembles that of the electroactive polymer obtained during the copolymerization of Py and DDS. The main oxidation-peak current increased linearly (**Figures 5** and **6**) as the scan rate increased from 50 mV s^{-1} to 300 mV s^{-1} indicating the presence of the electroactive copolymer film.

3.3 Effect of pH

The copolymer film formed on the surface of the copper electrode was washed with ultrapure water and a monomer-free solution. Then the film was scanned in the monomer-free solution and the pH range between 4 and 9 was considered. The voltammetry range between 0 V and 1.5 V was considered. The CV (**Figure 7**) resembles that of the electroactive polymer obtained earlier. The maximum current was observed for pH 7 and the minimum for pH 4.

The peak voltammetric current decreased with the increasing pH (**Figure 7**), indicating an involvement of H$^+$ ions. The film was also first cycled at a high pH of 7.0 (**Figure 7**). Thus, when the copolymer film was scanned at pH 4 the increase in the current was due to the change in the dopant. The effect of pH was studied


Figure 6: Effect of the scan-rate variation on the poly(Py-co-DDS/SiO₂)-film-coated copper electrode from 50 mV s^{-1} to 300 mV s^{-1} in the 4 M H₂SO₄ medium
Slika 6: Vpliv spreminjanja hitrosti skeniranja od 50 mV s^{-1} do 300 mV s^{-1} v 4 M H₂SO₄ na poly (Py-co-DDS/SiO₂) plast, ki prekriva bakreno elektrodo

on the copolymer films of Py, SiO₂ and DDS at various monomer concentrations and similar results were observed.

3.4 UV-Vis spectra and conductivity of copolymers

In-situ UV-Vis spectroelectrochemistry provides a useful tool for studying the electropolymerization and intermediate products analysis.[29] To study the spectro-electrochemical properties of the copolymer, the copolymer film was electrochemically deposited on an ITO glass plate at a constant potential of 1.2 V vs Ag/Ag$^+$. To ensure a consistent content of the electroactive polymer on the electrode surface between poly-
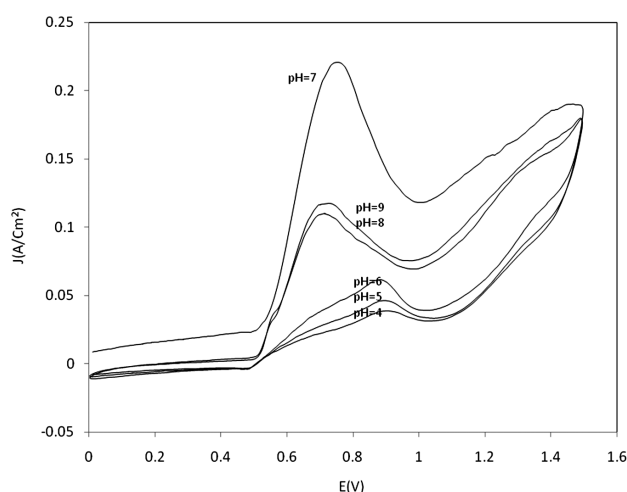
Figure 7: Effect of the pH variation from 4 to 9 on the poly(Py-co-DDS/SiO₂)-film-coated copper electrode in the acidic, neutral and basic media
Slika 7: Vpliv spreminjanja pH od 4 do 9 na poly (Py-co-DDS/SiO₂) plast, ki prekriva bakreno elektrodo, v kislem, nevtralnem in alkalnem mediju
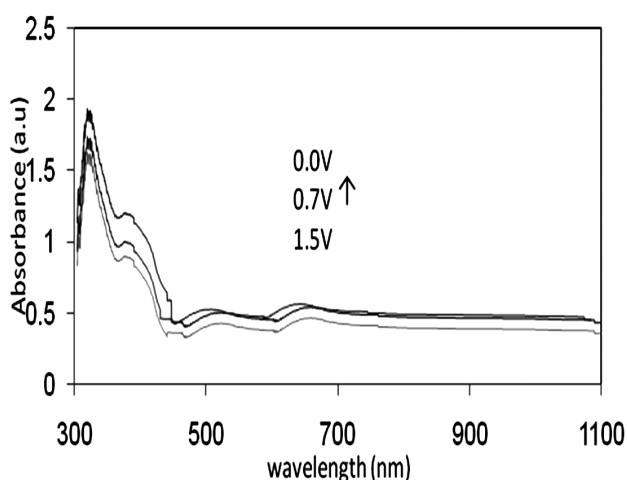
Figure 8: Spectroelectrochemical behavior of 0.3 M pyrrole, 0.1 M DDS and 0.1 M SiO₂ deposited on an ITO plate in the 0.1 M H₂SO₄ medium with various applied potentials
Slika 8: Spektroelektrokemično vedenje 0,3 M pirola, 0,1 M DDS in 0,1 M SiO₂, nanesenih na ITO-plošči v mediju 0,1 M H₂SO₄ pri različnih uporabljenih potencialih
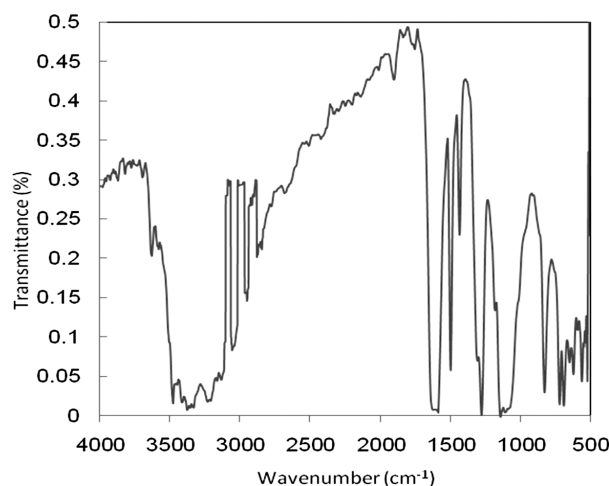

Figure 9: FTIR spectral behavior of poly(Py-co-DDS/SiO₂)
Slika 9: FTIR-spekter poly (Py-co-DDS/SiO₂)

merizations, the same amount of charge was passed during copolymerization. After deposition, the blue, oxidized ITO-adhered films were washed with the monomer-free electrolyte solution before recording the spectra at various applied potentials in the 0.1 M H₂SO₄ medium. Since all of the copolymer films are blue in their oxidized state, each film was subsequently reduced to determine whether there was a direct correlation between the monomer compositions and electrochromic response. As an illustration, the spectra of the copolymer films obtained from 0.3 M pyrrole, 0.1 M SiO₂ and 0.1 M DDS at various applied potentials are presented in **Figure 8**. When the applied potentials changed from 0 V to 1.5 V, the spectra exhibited absorption bands at 320 nm and 390 nm; the former one may be due to a π-π* transition and the latter one may be a benzenoid band. As the applied potential expanded to the oxidation side, the film color changed from yellow to blue. Apart from these bands, an additional broad band was observed in the visible region. The wavelength maxima of this band depended on the applied potentials. When an applied potential changed from 0.0 V to 0.8 V, an absorption band was obtained between 320 nm and 390 nm, exhibiting neutral yellow due to the formation of cation radicals (polaronic forms). As the potential varied from 0.0 V to 0.8 V, the absorption band shifted to the lower-energy side, i.e., a bath chromic shift was observed. The non-conducting blue film may be formed because of the fully oxidized copolymer. The feed ratio of the DDS monomer increased to 0.5 M and the film was coated as previously. After the deposition, the oxidation film was dark blue, indicating a higher amount of DDS in the copolymer. Here the π-π* transition and benzenoid bands were also observed.

The conductivity of this copolymer film was measured with a four-probe conductivity meter. At room temperature the conductivity of the copolymer, poly(Py-co-DDS/SiO₂), was determined to be 5.98×10^{-2} S cm⁻¹. Thus, the conductivity of the copolymer is lower than that of Py/SiO₂ (6.68×10^{-2} S cm⁻¹) and higher than that of polyDDS/SiO₂ (6.01×10^{-3} S cm⁻¹).

3.5 FTIR spectral behavior of copolymers

The IR spectrum, **Figure 9**, reveals the presence of different species involved in the fabrication of the composite polymer. The bands at (3470, 3350, and 3215) cm⁻¹ correspond to the N-H stretching vibration, whereas the bands at (3050, 2970, and 2850) cm⁻¹ result from the aromatic C-H stretching vibration. The peak at 1600 cm⁻¹ is due to the stretching deformation of the quinone ring. The 1280 cm⁻¹ band is assigned to the C-N stretching in the secondary aromatic amine, whereas the peaks at 1080 cm⁻¹ and 1150 cm⁻¹ represent the aromatic C-H in-plane bending modes. The out-of-plane deformation of C-H in the 1.4-disubstituted benzene ring is located at 835 cm⁻¹. The bands at 1302 cm⁻¹ and 555 cm⁻¹ correspond to the S=O stretching and S=O bending mode, respectively, of the sulfone group of the PDDS shift of their frequency and intensity in poly(Py-co-DDS/SiO₂) to 1308 cm⁻¹ and 576 cm⁻¹, respectively.

3.6 SEM and XRD

Chemically copolymerized materials were characterized with a SEM analysis. A SEM photograph (**Figure 10a**) of the copolymer formed from 0.3 M Py/SiO₂ and 0.02 M DDS showed a leave-like structure. This irregular structure confirmed the formation of the copolymer. The grain size of the material is 60 nm. When the concentration of DDS increased to 0.03 M, the formed copolymer exhibited only small changes in the structure (**Figure 10b**). When the incorporation of DDS increased
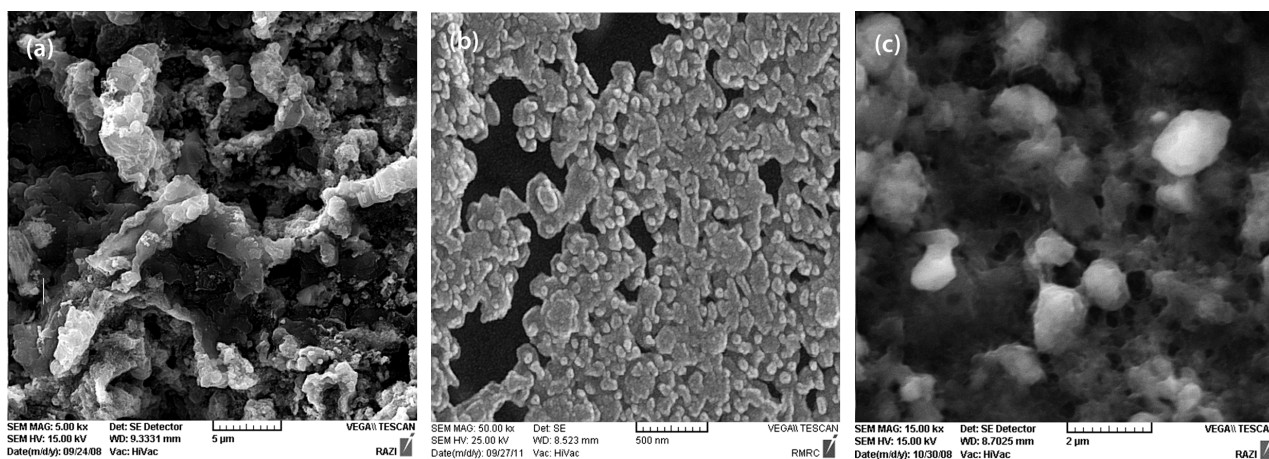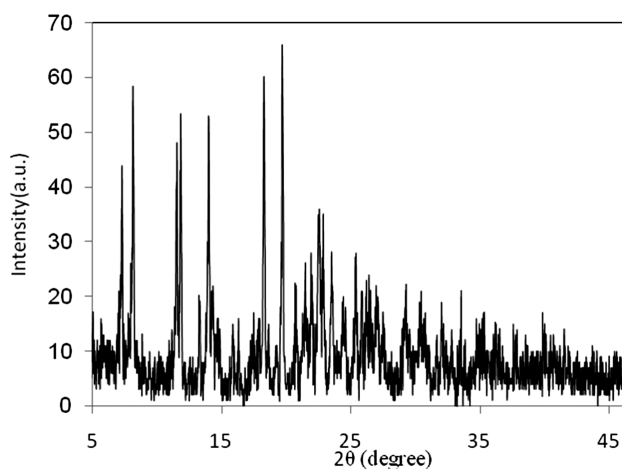
Figure 10: SEM photographs of the copolymer (Py-co-DDS/SiO$_2$): a) 0.3 M Py, 0.1 M SiO$_2$ and 0.02 M DDS surface; b) 0.3 M Py, 0.1 M SiO$_2$ and 0.03 M DDS surface; c) 0.3 M Py, 0.1 M SiO$_2$ and 0.02 M DDS surface
Slika 10: SEM-posnetki kopolimera (Py-co-DDS/SiO$_2$): a) površina 0,3 M Py, 0,1 M SiO$_2$ in 0,02 M DDS, b) površina 0,3 M Py, 0,1 M SiO$_2$ in 0,03 M DDS, c) površina 0,3 M Py, 0,1 M SiO$_2$ in 0,02 M DDS

to 0.1 M, the SEM photograph (**Figure 10c**) exhibited different, irregular, broken nanostructures.

The crystalline regions in the copolymers are characterized by the presence of relatively sharp peaks. The amorphous regions are visible due to broad, low intensity peaks. The X-ray diffraction profile (**Figure 11**) of the copolymer indicates a substantial degree of crystalinity in the doped forms. The base form of the copolymer with low DDS/SiO$_2$ exhibited less crystallinity than the highly doped form. The use of the Scherrer equation is the primary technique for determining the size or thickness of the polymer crystallites. The crystallite size of the copolymer was determined by employing the XRD results and the Scherrer equation (1):

$$L = \frac{K\lambda}{\beta(2\theta)\cos\theta} \qquad (1)$$

Here K is the shape factor of the average crystallite (the expected shape factor is 0.9), λ is the wavelength (usually 0.154056 nm), θ is the peak position and FW is the full width at half maximum. By employing the above method, the crystallite size of the copolymer was determined as 50 nm confirming the presence of nanostructured copolymers. This is the first report on the crystallite size of a copolymer of pyrrole/SiO$_2$ and 4.4'-diaminodiphenyl sulfone. However, earlier findings showed a similar result for poly 4.4'-diaminodiphenyl sulfone.[24]

4 CONCLUSION

The copolymer of pyrrole and 4.4'-diaminodiphenyl sulfone was prepared electrochemically using the continuous-cycling method in a solution of 4 M H$_2$SO$_4$, SiO$_2$ and ethanol, with different concentrations of both pyrrole and 4.4'-DDS. The copolymer formation was more significant with the feed concentrations of 0.01 M Py and 0.01 M 4.4'-DDS and exhibited a varying, cyclic voltammetric behavior. The synthesized poly(Py-co-DDS/SiO$_2$) films demonstrated a good adherence in acidic and neutral solvents and were found to be electroactive. The copolymer films were responsive up to pH 7.0 in the acid and neutral media. The formation of the copolymer, poly(Py-co-DDS/SiO$_2$), was further ascertained from the FTIR and SEM data. The XRD results revealed the formation of a nanosized copolymer. These results indicate that the copolymers herein can be used in the development of dynamic electrochromic devices and their conducting films can be used to modify the electrodes that are used as sensors.

Figure 11: XRD behavior of the poly(Py-co-DDS 0.1 M SiO$_2$)-film on the ITO plate
Slika 11: XRD-spekter poly(Py-co-DDS 0,1 M SiO$_2$) plasti, ki pokriva ITO-ploščo

5 REFERENCES

[1] P. K. H. Ho, J. S. Kim, J. H. Burroughes, H. Becker, S. F. Y. Li, T. M. Brown, F. Cacialli, R. H. Friend, Nature, 404 (**2000**), 481–484

[2] S. Möller, C. Perlov, W. Jackson, C. Taussig, S. R. Forrest, Nature, 426 (**2003**), 166–169

[3] J. L. Boehme, D. S. K. Mudigonda, J. P. Ferraris, Chem. Materials, 13 (**2001**), 4469–4472

[4] A. A. Argun, P. H. Aubert, B. C. Thompson, I. Schwendeman, C. L. Gaupp, J. Hwang, N. J. Pinto, D. B. Tanner, A. G. MacDiarmid, J. R. Reynolds, Chem. Materials., 16 (**2004**), 4401–4412

[5] G. D. Stucky, Nature, 410 (**2001**), 885–886

[6] T. A. Skotheim, R. L. Elsenbaumer, J. R. Reynolds (Eds.), Handbook of Conducting Polymers, Marcel Dekker, New York 1998

[7] D. T. Mcquade, A. E. Pucllen, T. M. Swager, Chem. Rev., 100 (**2000**) 7, 2537–2574

[8] W. Lu, H. Zhao, G. G. Wallace, Anal. Chim. Acta, 315 (**1995**), 27–32

[9] J. Cha, J. I. Han, Y. Choi, D. S. Yoon, K. W. Oh, G. Lim, Biosens. Bioelectron., 18 (**2003**), 1241–1247

[10] N. F. Atta, A. Galal, H. B. Mark, T. Yu, P. Bishop, Talanta, 47 (**1998**), 987–999

[11] G. E. Wnek, In: T. A. Skotheim (ed.), Handbook of Conducting Polymers, Marcel Dekker, New York 1986, 205

[12] W. S. Wu, T. C. Wen, A. Gopalan, J. Electrochem. Soc., 148 (**2001**) 11, 10–16

[13] C. H. Yang, T. C. Wen, J. Electrochemi. Soc., 144 (**1997**), 2078–2085

[14] C. H. Yang, T. C. Wen, J. Appl. Electrochem., 24 (**1994**), 166–178

[15] C. H. Yang, T. C. Wen, J. Electrochemi. Soc., 141 (**1994**), 2624–2632

[16] H. Qiu, M. Wan, J. Poly. Sci., Part A: Polymer Chemistry, 39 (**2001**), 3485–3497

[17] J. W. Choi, M. G. Han, S. Y. Kim, S. G. Oh, S. S. Im, Syn. Metals., 141 (**2004**), 293–299

[18] Y. Lu, A. Pich, H. Adler, Syn. Metals., 37 (**2003**), 135–136

[19] S. M. Yang, K. H. Chen, Syn. Metals., 51 (**2003**), 135–142

[20] P. Manisankar, A. Sarpudeen, S. J. Viswanathan, Pharma. Biomedical. Anal., 26 (**2001**), 873–881

[21] K. I. Okamoto, K. Tanaka, H. Kita, A. Nakamura, Y. J. Kusuki, J. Poly. Sci., Part B: Polymer Physics, 27 (**1989**), 2621–2635

[22] G. M. Kim, H. Qin, X. Fang, F. C. Sun, P. T. J. Mather, J. Poly. Sci., Part B: Polymer Physics, 41 (**2003**), 3299–3313

[23] P. Manisankar, C. Vedhi, G. Selvanathan, R. M. Somasundaram, Chem. Materials., 17 (**2005**), 1722–1727

[24] P. Manisankar, D. Ilangeswaran, Electrochim. Acta, 55 (**2010**), 6546–6552

[25] S. H. Si, X. J. Xu, L. H. Nie, S. Z. Yao, Electrochim. Acta, 40 (**1995**), 2715–2721

[26] A. Dan, P. K. Sengupta, J. Appl. Poly. Sci., 90 (**2003**), 2337–2347

[27] R. S. Ferreira Jr., V. R. Oliveira, R. G. C. S. Reis, G. Maia, G. A. Camara, J. Power Sources., 185 (**2008**), 853–856

[28] P. Manisankar, C. Vedhi, G. Selvanathan, H. Gurumallesh Prabu, Electrochim. Acta, 52 (**2006**), 831–838

[29] J. Cai, Q. Yu, X. Zhang, J. Lin, L. Jiang, J. Poly. Sci., Part B: Polymer Physics, 43 (**2005**), 2885–2897

SEWAGE-SLUDGE STABILIZATION WITH BIOMASS ASH

STABILIZIRANJE KOMUNALNEGA MULJA S PEPELOM BIOMASE

Primož Pavšič[1], Danijel Oštir[2], Ana Mladenovič[3], Sabina Kramar[3,4], Matej Dolenec[4], Peter Bukovec[5]

[1]PMA d.o.o., Tbilisijska 61, 1000 Ljubljana, Slovenia
[2]VIPAP d.d., Tovarniška 18, 8270 Krško, Slovenia
[3]Zavod za gradbeništvo Slovenije, Dimičeva 12, 1000 Ljubljana, Slovenia
[4]Naravoslovnotehniška fakulteta, Aškerčeva 12, 1000 Ljubljana, Slovenia
[5]Fakulteta za kemijo in kemijsko tehnologijo, Aškerčeva 5, 1000 Ljubljana, Slovenia
primoz.pavsic@pma-lj.si

By mixing the sewage biodegradable sludge and biomass ash a stable composite is formed. A study showed that, in this way, a building material with a compressive strength of about 2 MPa is produced, which can be used mainly for landfill covers, road-shoulder management, road-base stabilization and rehabilitation of degraded areas. An analysis of the chemical composition of the water eluate from the composite showed that the new composite material is inert and, as such, does not pose a threat and does not burden the environment. From the sustainable-development point of view this kind of waste-residue management presents an optimum – a zero waste solution.

Keywords: biodegradable sewage sludge, stabilization, biomass ash, composite construction material

Z mešanjem komunalnega biomulja in pepela biomase se tvori stabilen kompozit. Raziskave so pokazale, da tako pridobljen gradbeni material s tlačno trdnostjo okoli 2 MPa lahko uporabimo na območju deponij komunalnih odpadkov za dnevne in končne prekrivke, za ureditev brežin in bankin, pa tudi kot podlago za gradnjo transportnih poti in sanacijo degradiranih območij. Tudi analiza kemične sestave izlužka iz kompozita je pokazala, da je novi kompozit inerten in kot takšen ne obremenjuje okolja. Z vidika trajnostnega razvoja je takšna rešitev optimalna, saj je rezultat predelave uporaben produkt (predelava "zero waste").

Ključne besede: komunalni biomulj, stabilizacija, pepel biomase, kompozitni gradbeni material

1 INTRODUCTION

In the waste-water treatment process large amounts of biodegradable sewage sludge are produced. Sewage sludge, due to its high organic content, a presence of pathogenic bacteria, heavy metals and organic pollutants,[1] poses a major environmental problem. Up-to-date biodegradable sewage sludge management mainly includes composting and reuse in agriculture, recycling with anaerobic digestion or thermal treatment for energy utilization and landfilling.[1] Unfortunately, the reuse of biodegradable sewage sludge in agriculture is often impossible due to the presence of bacteria and heavy metals, while energy utilization and landfilling still burden the environment. In addition, the management of different waste-ash residues is environmentally very demanding. However, some of these products were already successfully applied in the field of construction,[2–5] though this is not true of the ashes from biomass combustion. Alternatively, biodegradable sewage sludge and biomass ash can be treated in the same process.[6] By mixing waste-biomass ash and biodegradable sewage sludge, a composite construction material for specific purposes can be obtained.[7] From the sustainable-development point of view this presents an optimum – a zero waste solution.

2 EXPERIMENTAL WORK

For assessing the mechanical properties of the composite material, cube samples (150 mm × 150 mm × 150 mm) were prepared by mixing biodegradable sewage sludge with biomass ash cooled to ambient temperature in the 1 : 1 mass ratio.

The compressive strength of the composite was determined according to SIST EN 12390-3 after (7, 14, 28, 56 and 90) d of curing the specimens in moist (100 % air moisture) and for some specimens (after 7, 28 and 56 d) also in wet conditions (submerged in water). During the mixing process the changes in the temperature and pH level were monitored. The eluate was obtained from the composite after 28 days of curing the specimens in moist conditions according to SIST EN 1744-3:2002 at the liquid/solid (L/S) ratio of 10 : 1. Inorganic parameters of the composite eluate, biomass-ash eluate and biodegradable sewage sludge were determined by the inductively coupled plasma mass spectrometry (ICP MS) according to SIST EN ISO 17294-2:2005, ISO 16772:2004-modif. and SIST EN ISO 10304-1:2009, respectively. The effect of stabilization on microbiological quality of the material was assessed with the aerobic mesophilic bacteria count

before and after the stabilization according to the internal method of the Pulp and Paper Institute Laboratory. For this purpose samples were kept in aseptic conditions, diluted in a Ringer's solution and spread on a standard plate count agar. After a 2 d incubation period at 37 °C, a colony count was performed. To gather more information on the processes accompanying the stabilization, the mineral compositions of raw materials (sludge, ash) and composites were also determined with the X-ray powder diffraction (XRD) using a Philips PW 3710 diffractometer and Cu K(alfa) radiation. Powdered samples were scanned at a rate of 2°/min, over the range of 2–70° (2Θ). The results were stored on a PC and analysed by the X'Pert HighScore Plus diffraction software. In addition, selected samples were analysed with Fourier transform infrared spectroscopy (FTIR), using a Perkin Elmer Spectrum 100 spectrometer. Sixty-four signal-averaged scans of the samples were acquired. Powder pellets were pressed from the mixtures of the samples with KBr at a ratio of about 1 : 200. The FTIR spectra were recorded with a spectral resolution of 4 cm^{-1} in the range of 4000–400 cm^{-1}.

3 RESULTS AND DISCUSSION

Biodegradable sewage sludge used in this study originates from an aerobic, biological, waste-water-treatment plant at the company VIPAP d.d., where industrial and municipal waste waters are treated. It represents a fluid component with 0.84 % of dry matter with a pH of 7.1 and conductivity of 318 mS/m. As seen in **Table 1**, concentrations of inorganic substances in the biodegra-

Table 1: Inorganic parameters of biomass-ash and composite eluates, and of biodegradable sewage sludge
Tabela 1: Anorganski parametri izlužkov pepela biomase in kompozita, ter koncentracije preiskovanih parametrov v biomulju

Parameter	Biodegradable sewage sludge	Biomass ash	Composite after 28 days
pH	7.1	12.5	11.9
Conductivity (µS/cm)	3180	7370	18
Inorganic parameters	mg/L	mg/kg$_{s.s.}$	mg/kg$_{s.s.}$
As	0.010	<0.02	<0.02
Ba	1.2	59	2.7
Cd	<0.0005	<0.005	<0.005
Total Cr	0.0035	<0.01	0.016
Cu	0.19	<0.07	0.08
Hg	<0.01	<0.004	<0.01
Mo	0.0077	<0.05	<0.05
Ni	0.0050	0.048	<0.01
Pb	<0.005	<0.05	0.066
2102416 Sb	0.0026	<0.006	0.018
Se	<0.001	<0.01	<0.002
Zn	0.58	0.12	<0.1
Cl$^-$	44.7	25.3	15.6
F$^-$	<1.0	4.5	<2
SO$_4^{2-}$	50.6	<5	8.6

Note: mg/kg$_{s.s.}$ – milligram per kilogram of dry matter

dable sludge, when compared to the limit values concerning discharge of waste water,[8] are not environmentally problematic. The mineral composition, determined with XRD, showed that the sludge consists of calcite, quartz, dolomite and clinochlore (**Figure 1**).
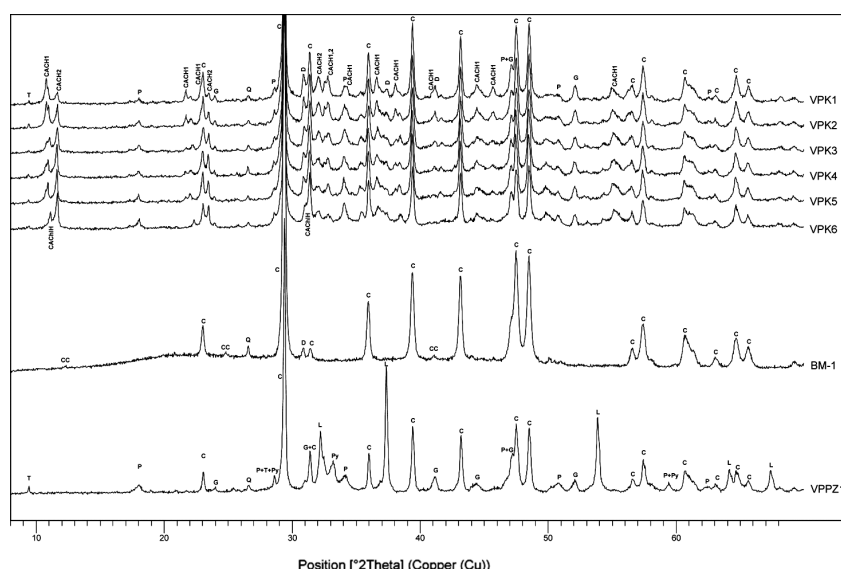
Figure 1: X-ray diffraction pattern of biodegradable sludge (BM), biomass ash (VPPZ1) and the composites after 3, 7, 14, 28, 56 and 90 days (VPK-1 to VPK-6, respectively)
Legend: C-calcite, T-talc, P-portlandite, Q-quartz, L-lime, G-gehlenite, CC-clinochlor, D-dolomite, Py-pyrite; CACH1: Ca$_8$Al$_4$O$_{14}$CO$_2$*24H$_2$O, CACH2: Ca$_4$Al$_2$O$_{14}$CO$_9$*11H$_2$O, CaCh1H: Ca$_4$Al$_2$O$_6$Cl$_2$ *10H$_2$O
Slika 1: Difraktogram komunalnega biomulja (BM), pepela biomase (VPPZ1) in kompozitov po 3, 7, 14, 28, 56 in 90 dneh (VPK-1 do VPK-6)
Legenda: C-kalcit, T-lojevec, P-portlandit, L-apno, G-gehlenit, CC-klinoklor, D-dolomit, Py-pirit, CACH1: Ca$_8$Al$_4$O$_{14}$CO$_2$*24H$_2$O, CACH2: Ca$_4$Al$_2$O$_{14}$CO$_9$*11H$_2$O, CaCh1H: Ca$_4$Al$_2$O$_6$Cl$_2$ *10H$_2$O
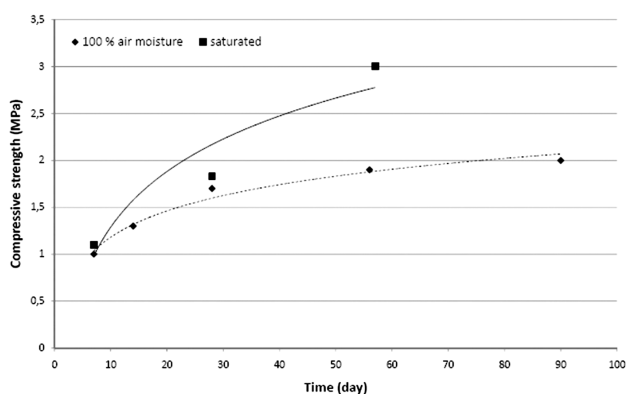
Figure 2: Compressive strength of the composite vs. the curing time
Slika 2: Odvisnost tlačne trdnosti kompozita od časa negovanja

Biomass ash is a residue from a steam boiler K5 at VIPAP d.d. According to the inorganic parameters of the eluate (**Table 1**) this material is classified as a non-hazardous waste.[9]

The ash consists of free lime (CaO), portlandite (Ca(OH)$_2$), gehlenite, calcite, quartz, pyrite, talc, and an amorphous phase.

In the process of mixing the biodegradable sludge and biomass ash a stable matrix is formed. As recognized experimentally, the optimum mass ratio of biodegradable sludge (liquid component) and biomass ash is 1 : 1. This ratio ensures an adequate hardening time (starting at 285 min, ending at 1140 min) and workability of the produced material. During mixing, the temperature is elevated up to about 45 °C and the pH value exceeds 12. This reduced the mesophilic bacteria count from 2.6×10^{11} CFU/g a. s. to 2.2×10^5 CFU/g a. s., thus, the microbial activity was effectively inhibited and the obtained composite product does not pose a

health threat[10] when used for the intended purpose. Furthermore, analyses of the eluate from a cube sample of the composite after 28 days of moist curing (**Table 1**) showed, that the new composite material is inert[9] and, as such, environmentally acceptable. Mechanical properties, assessed with the compressive-strength determination, are time dependent (**Figure 2**). The compressive strength after 28 d ranged from 1.7 MPa (moist curing) to 1.8 MPa (wet curing – saturated). As seen from the compressive-strength evolution, the process of hydration was not yet completed after 28 d. The compressive strength after 57 d increased up to about 2 MPa or even up to 3 MPa (saturated). Although the qualitative mineralogical composition of the composites (**Figure 1**) consisted of talc, dolomite, portlandite, calcite, gehlenite and quartz, and did not change with time, we can observe that the amounts of free lime and portlandite are reduced, but the amount of calcite is increased. During the curing period new hydration products were also observed, namely, calcium carboaluminate (chloride) hydrates $Ca_8Al_4O_{14}CO_2 \times 24H_2O$ (CACH1), $Ca_4Al_2O_{14}CO_9 \times 11H_2O$ (CACH2) and $Ca_4Al_2O_6Cl_2 \times 10H_2O$ (CAChlH), where the CACH1/CACH$_2$ ratio is changing with the curing time. The formation of new products during the curing was also confirmed with FTIR spectra (**Figure 3**) that show an obvious difference when comparing the initial materials and the composites. This is especially indicated by the shift of bands in the range of 1015–1075 cm^{-1} towards the lower wavenumbers after the stabilisation of the composite, and by the appearance of three additional bands at around (3675, 3621 and 3530) cm^{-1} ascribed to the newly formed hydrates.

4 CONCLUSIONS

The study showed that the stabilization process of biodegradable sewage sludge with biomass ash in a mass ratio of 1 : 1 effectively inhibits further microbial activity and the associated degradation. In the process a stable composite is formed with a 28 d compressive strength of about 1.7 MPa. In the process of hydration the amounts of free lime and portlandite were reduced, whereas the amount of calcite increased due to the carbonation of the composite. During this period, hydration products were generated – namely, the calcium carboaluminate hydrates. An analysis of the chemical composition of the water eluate from the composite showed that the new composite material is inert and, as such, does not pose a threat for the environment. This kind of composite can be used as a construction material mainly for landfill covers, road-shoulder management and road-base stabilization, as well as rehabilitation of degraded areas. In view of sustainable development the described waste-residue management presents an optimum – a zero waste solution.
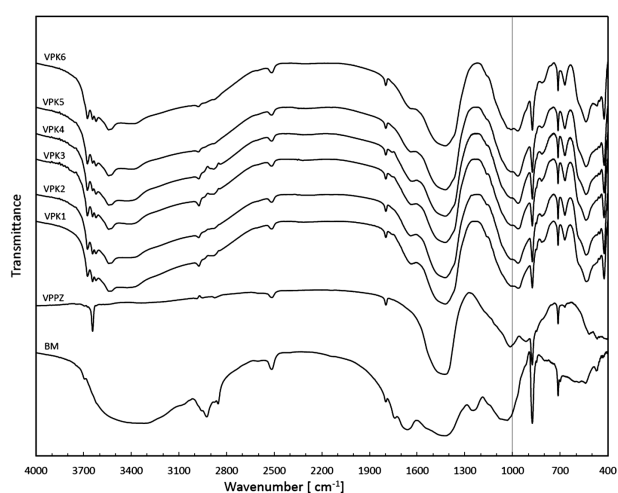

Figure 3: FTIR spectra of biodegradable sludge (BM), biomass ash (VPPZ) and the composites after 3, 7, 14, 28, 56 and 90 days (VPK-1 to VPK-6, respectively)
Slika 3: FTIR-spekter komunalnega biomulja (BM), pepela biomase (VPPZ) in kompozitov po 3, 7, 14, 28, 56 in 90 dneh (VPK-1 do VPK-6)

5 REFERENCES

[1] V. Grilc, G. D. Zupančič, M. Roš, Alternativni načini sodobnega ravnanja z odvečnim blatom iz bioloških čistilnih naprav, Zbornik referatov / [Simpozij z mednarodno udeležbo] Vodni dnevi, Portorož, 2006, 99–109

[2] H. K. Lam, J. P. Barford, G. McKay, Utilization of incineration waste ash residues as Portland cement clinker, Chemical Engineering Transactions, 21 (**2010**), 757–762

[3] M. A. Daous, Utilization of Cement Kiln Dust and Fly Ash in Cement Blends in Saudi Arabia, JKAU: Eng. Sci., 15 (**2004**) 1, 33–45

[4] M. M. Al Bakri, H. Mohammed, H. Kamarudin, I. Khairul Niza, Y. Zarina, Review on fly ash-based geopolymer concrete without Portland Cement, Journal of Engineering and Technology Research, 3 (**2011**) 1, 1–4

[5] D. J. White, Fly Ash Soil Stabilization for Non-Uniform Subgrade Soils, Volume I: Engineering Properties and Construction, Guidelines (IHRB Project TR-461, FHWA Project 4), Iowa Highway Research Board, Federal Highway Administration, 2005

[6] F. Černec, J. Zule, Stability properties of biosludge-wood ash composites, International Conference Waste Management, Environmental Geotechnology and Global Sustainable Development (ICWMEGGSD'07 - GzO'07), Ljubljana, 2007
Available from World Wide Web: http://www.srdit.si/gzo07/papers/97FCernec_FinalPaperGzO07.pdf

[7] P. Pavšič, Poročilo o rezultatih raziskav biomulja stabiliziranega z ostanki gorenja kotla K5 v družbi VIPAP, PMA d.o.o., 2011

[8] Uredba o emisiji snovi in toplote pri odvajanju odpadnih voda v vode in javno kanalizacijo, Uradni list RS, 2007, 45

[9] Uredba o odlaganju odpadkov na odlagališčih, Uradni list RS, 2011, 61

[10] T. Rupel, T. Pavlica, P. Planina, J. Vidrih, S. Glas, T. Car, L. Kobola, M. Lušicky, D. Bošnjak, D. Sabotin, Smernice za mikrobiološko varnost živil, ki so namenjena končnemu potrošniku, IVZ RS, 2005
Available from World Wide Web: http://www.mz.gov.si/fileadmin/mz.gov.si/pageuploads/mz_dokumenti/zakonodaja/varnost_hrane/pesticidi/smernice_za_mikrobiolo__ko_varnost___ivil.pdf

DREDGED MUD FROM THE PORT OF KOPER – CIVIL ENGINEERING APPLICATIONS

MULJ IZ LUKE KOPER – UPORABNOST V GRADBENIŠTVU

Ana Mladenović[1], Željko Pogačnik[2], Radmila Milačič[3], Anica Petkovšek[4], Franka Cepak[5]

[1]Slovenian National Building and Civil Engineering Institute, Dimičeva 12, 1000 Ljubljana, Slovenia
[2]Salonit Anhovo, Joint-Stock Co., Vojkova 1, 5210 Deskle, Slovenia
[3]Department of Environmental Sciences, Jožef Stefan Institute, Jamova 39, 1000 Ljubljana, Slovenia
[4]University of Ljubljana, Faculty of Civil Engineering and Geodesy, Jamova 2, 1000 Ljubljana, Slovenia
[5]Luka Koper, d. d., Vojkovo nabrežje 38, 6501 Koper, Slovenia
ana.mladenovic@zag.si

The Port of Koper, one of the biggest and the most important ports in the Northern Adriatic Sea, is constantly faced with the problems caused by the accumulation of marine sediments inside the port, disturbing some of the port's crucial operations. However, these sediments can be viewed as a potential raw material and, in order to define the best way of using them in the civil-engineering field, an extensive research project has been launched. The preliminary results of this project are presented and discussed in the paper. So far the project has given two main results: first, the concentration of heavy metals in the aqueous leachates is low and, secondly, in their present state, the sediments are too wet, so that there are only limited possibilities for drying them out naturally. For this reason additional technological treatment will be needed.

Keywords: dredged mud, civil-engineering applications

Luka Koper, kot eno najpomembnejših pristanišč v severnem delu Jadranskega morja, se nenehno spopada s težavo akumulacije sedimentov na plovnih poteh, kar povzroča težave pri najbolj kritičnih delovnih zmogljivostih pristanišča. Po drugi strani ta material lahko obravnavamo kot potencialno surovino v gradbeništvu. V prispevku so podani preliminarni rezultati interdisciplinarnih raziskav, ki kažejo naslednje: prvič, koncentracija težkih kovin v izlužkih je nizka in drugič, v stanju, kot je, je sediment preveč vlažen, da bi ga bilo mogoče osuševati z naravnimi postopki in je zato potrebna dodatna tehnološka obdelava.

Ključne besede: mulj, uporaba v nizkih gradnjah

1 INTRODUCTION

The Port of Koper is one of the biggest and the most important ports in the Northern Adriatic Sea, and it is primarily transit oriented. It is a multi-purpose port with two piers, 26 berths, and 12 specialized terminals. One of its main problems is related to a constant accumulation of marine sediments inside various parts of the port, resulting in disturbances to some of its most crucial

Figure 1: The mud in the temporary landfill at Koper Port
Slika 1: Mulj na začasni deponiji v Luki Koper

operational capacities. A total of 80000 m³ of sediments have to be removed annually. The sediment found in the Port of Koper is a mixture of clay and silt (henceforth referred to as mud) and represents the kind of waste, for which there is insufficient disposal space along the Slovenian coast (**Figure 1**). According to the slogan "No waste here, just resources!" this sediment can be viewed as a potential raw material. In order to define the best way of using it in civil-engineering applications, an extensive research project is under way. Some of the preliminary results are presented and discussed in the paper.

2 EXPERIMENTAL WORK

2.1 Materials and methods

In January 2012 several batches of mud were taken from the temporary deposits at the end of Pier I (the mud from Basin 1) and Pier II (the mud from Basin 2). All the material was homogenised and divided into subsamples for the targeted analyses – except for the chemical analyses, which were performed on the mud from each location separately and, additionally, on the sample from Basin 3. Quantitative mineralogical compositions were determined using X-ray diffraction (Phillips PANalytical

X'Pert PRO equipment with Cu Kα radiation). Powdered samples were scanned at a rate of 2 °/min, over the range of 2–70 ° (2θ). A particle-size analysis was performed using a Cilas 920 laser granulometer in the water as a suspension media. The samples for the thermal testing were heated in cylindrical pots, made of inert materials, by applying a temperature scan of 10 °C/min at room temperature, up to 1400 °C. A STD 2960 Simultaneous DTA-TGA analyser was used, complemented with the Universal Analysis for Windows 95/98/NT software tool, edition 2.5H.

Several geomechanical tests were performed in order to evaluate the basic properties and behaviour of the mud under loaded conditions. The most crucial test was the edometer test carried out according to SIST/ISO/TS 17892-5:2004.

In order to evaluate the environmental impact, the extent of pollution was estimated by determining the total metal concentrations, by identifying the most hazardous, highly mobile metal fractions and by partitioning the metals into easily, moderate soluble, and sparingly soluble fractions. For this purpose various sequential extraction procedures were applied.[1–3] Special attention was paid to the estimation of the content of the highly mobile, biologically available fractions of metals in the sediments. The total metal concentrations in the sediments and in various stages of the sequential-extraction procedure were determined using inductively coupled plasma mass spectrometry (ICP-MS) on an Agilent 7700x ICP-MS. A CEM Corporation CEM MARS 5 Microwave Acceleration Reaction System was used to digest the sediments. Mechanical shaking of the samples was performed with a Vibromix 40 elliptical, orbital shaker. The samples were centrifuged using a Hettich Universal 320 Centrifuge, and a WTW 330 pH meter was used to determine the pH values.

2.2 Reagents

Merck suprapur acids and Milli-Q water (Direct-Q 5 Merck suprapur acids and ultrapure water) were used for the preparation of the samples and standard solutions. All the other reagents were of the analytical reagent grade. A Stock IV CertiPUR ICP Multi Element Standard Solution containing (1000 ± 10) mg L^{-1} element concentrations in 1 mol L^{-1} HNO$_3$ was obtained from Merck. Sartorius 0.45 μm cellulose nitrate membrane filters with 25 mm diameters were used in the filtration procedure.

2.3 Determination of the total metal and aqueous leachate concentrations

0.2 g of a dry homogenised sediment was weighed in a Teflon tube, and microwave-assisted digestion using a mixture of HNO$_3$, HCl and HF was applied according to the procedure proposed by Ščančar et al.[3] All the analyses were performed in triplicates. In order to determine the element concentrations of the aqueous leachates, 10 g of each sample were shaken for 24 h with 100 mL of water, centrifuged and filtered through 45 μm membrane filters. The elements in the aqueous leachates were determined by ICP-MS.

3 RESULTS AND DISCUSION

3.1 Particle-size analysis

The results of the particle-size analysis showed that the majority of the grains had a dimension of less than 2 mm, and that the quantity of the grains with a size of 63 μm or less varied between 75 % and 97 % by mass. About 40 % by mass of the grains were under 5 μm, i.e., within the clay size range.

3.2 Mineralogical composition

The quantitative mineral composition of an average sample of the mud determined by XRD is presented in **Table 1**. The results show that clay minerals, i.e., illite, chlorite and Ca montmorillonite, made up more than 40 % of the investigated mud. These results are in good correlation with those obtained by Ogorelec[4].

Table 1: Quantitative mineral composition of the mean sample of mud
Tabela 1: Kvantitativna mineralna sestava povprečnega vzorca mulja

Mineral	% by mass
Illite/muscovite	25
Chlorite	20
Quartz	21
Calcite	19
Feldspar	9
Dolomite	3
Pyrite	2
Ca montmorillonite	1

3.3 Thermal analysis

Within the range between 200 °C and 450 °C a strong exothermic peak was observed. This peak represents an oxidation of organic matter and dewatering of clayey mineral assemblages and probably some amorphous Fe-Al oxide gels (**Figure 2**). Within the temperature interval between 400 °C and 500 °C the S + O$_2$ ⇔ SO$_2$ reaction takes place, which is due to the decomposition of pyrite into pyrrhotite and free oxygen, which reacts at the same time with H$_2$$^+$; H$_2$ + 1/2O$_2$ ⇔ H$_2$O within the temperature range of 530–580 °C, producing another exothermic peak.[5] At a temperature of about 580 °C the $\alpha \rightarrow \beta$ inversion of quartz and a likely dehydroxylation reaction of kaolinite[6] occur. In the same endothermic interval, illite loses its constitutive water, which is caused by dehydroxilation of the octahedral sheet, as the hydroxyl groups of the tetrahedral sheet are gradually removed up to a temperature of 850 °C.[7] The second endothermic peak at about 600 °C and another, smaller one, at around 700 °C can be attributed to chlorites.[3] The third and
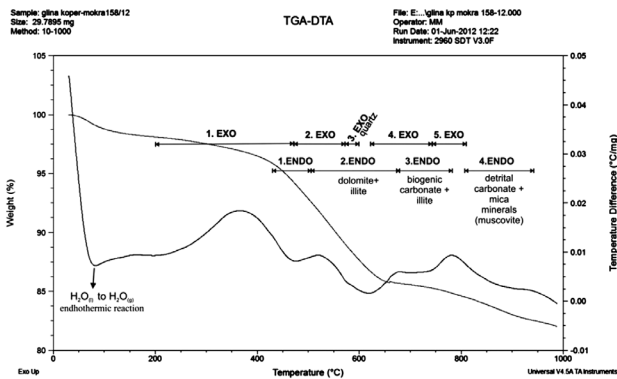
Figure 2: TGA-DTA analysis
Slika 2: TGA-DTA analiza

fourth endothermic peaks form a decarbonatization interval: (a) calcium carbonate derived from marine fauna skeletons, i.e., a biogenic carbonate; (b) dolomite; and (c) terrigenic carbonate.[8] The final exothermic peak, at approximately 800 °C, belongs to various phase transformations of amorphous Fe-Al minerals.[6]

3.4 Geomechanical parameters

The initial research was focused on determining the basic physical and mechanical parameters that are crucial for evaluating a possible stabilization of the mud. It was concluded that the content of the water in the mud is extremely variable (from 55 % to 95 % by mass) and that the density of the untreated material is very low so that it is not possible to stabilise it in its existing form. It can be seen, from the edometer curves, that, at an effective normal pressure of 200 kPa, it is possible to achieve a pore coefficient of between 0.9 and 1.1, which corresponds to the moisture content of between 33 % and 40.7 %. Only at such moisture contents (i.e., between 33 % and 40 %) the material is close to the state when a

chemical stabilization by means of inorganic binders, e.g., fly ash, lime, cement and their various combinations, is technically and technologically feasible.

3.5 Environmental analysis

In order to estimate the extent of pollution, the total element concentrations and the concentrations in the aqueous leachates were determined. From the results of these analyses and a comparison with the limiting values prescribed by the existing legislation for the inert and non-hazardous waste, it is clear that the highest total element concentrations were found in the sediment from Basin 3. The elevated total element concentrations were observed in the case of Cr (within the range from 200 mg/kg to 380 mg/kg), Ni (within the range from 140 mg/kg to 175 mg/kg) and As (within the range from 15 mg/kg to 40 mg/kg), i.e., the concentrations that are higher than those found in the sediments elsewhere in the Slovenian costal area.[3] In general, the concentrations in the aqueous leachates are also the highest for the sediment from Basin 3, but still lower than the limits set by the legislation for the inert waste leachates.[9] In order to estimate the partitioning of the elements between the easily and sparingly soluble sediment fractions, a 6-step sequential-extraction procedure was also performed. The data obtained indicated that the measured concentration of the elements in the easily soluble fractions was, in general, very low. The only exception was Mo. The partitioning of Mo is presented in **Figure 3.** It is clear that the easily soluble fraction (i.e., the water-soluble fraction and the exchangeable fraction) makes up about 25 % of the sediment from Basin 1 and about 10 % of the sediment from Basins 2 and 3. It can be concluded that, with regard to the total heavy-metal concentrations, the concentrations in the aqueous leachates and the partitioning of the elements between easily and sparingly soluble sediment fractions, the sediments from the basins of the Koper Port can be used as a secondary material in civil engineering.

4 CONCLUSIONS

Preliminary results show that the mud from the Port of Koper does not represent a threat to the environment with regard to heavy-metal pollution. However, due to its salt content it is not possible to plan the use of this mud in the areas outside the Port of Koper. It is planned to use an appropriate treatment to fix the chlorides within the building composite. Due to a high quantity of water in the mud, it will be more economical to stabilize it with a drying-out process, using suitable technology.

Acknowledgments

Figure 3: Partitioning of Mo between various phases (I: Water-soluble, II: Exchangeable, III: Bound to carbonates, IV: Bound to Fe and Mn oxides, V: Bound to organic matter, VI: Residual fraction) in sediments (B1, B2 and B3) from Luka Koper
Slika 3: Porazdelitev Mo med različne faze sedimenta (B1, B2 in B3) iz luke Koper: (I: vodotopni, II: izmenljivi, III: vezan na karbonate, IV: vezan na Fe in Mn okside, V: vezan na organsko snov, VI: težko topni ostanek)

5 REFERENCES

[1] A. Šömen Joksič, S. A. Katz, M. Horvat, R. Milačič, Comparison of single and sequential extraction procedures for assessing metal leaching from dredged costal sediments, Water, Air and Soil Pollution, 162 (**2005**), 265–283

[2] R. Milačič, J. Ščančar, S. Murko, D. Kocman, M. Horvat, A complex investigation of the extent of pollution in sediments of the Sava River, Part 1, Selected elements, Environmental Monitoring and Assessment, 163 (**2010**), 263–275

[3] J. Ščančar, T. Zuliani, T. Turk, R. Milačič, Organotin compounds and selected metals in the marine environment of Northern Adriatic Sea, Environmental Monitoring and Assessment, 127 (**2007**), 271–282

[4] B. Ogorelec, M. Mišič, J. Faganeli, P. Stegnar, B. Vrišer, A. Vukovič, The recent sediment of the Bay of Koper (Northern Adriatic), Geologija, 30 (**1987**), 87–121

[5] G. Locher, Mathematical models for the cement clinker burning process, ZKG International, 55 (**2002**), 29–50

[6] R. C. Mackenzie, The differential thermal investigation of clays, Mineralogical Society (Clay Minerals Group), London 1957, 456

[7] J. H. Araújo, N. F. da Silva, W. Acchar, U. U. Gomes, Thermal decomposition of illite, Material Research, 7 (**2004**), 359–361

[8] Ž. Pogačnik, J. Pavšič, A. Meden, Geological records as an indicator of the thermal characteristics of mudstones within the temperature range of decarbonatisation, Mater. Tehnol., 43 (**2009**) 3, 157–163

[9] Official Gazette of the Republic of Slovenia, No. 61/11, 2011

AUTOMATED DIAGNOSTICS OF DAMAGE TO AN ALUMINUM ALLOY UNDER THE CONDITIONS OF HIGH-CYCLE FATIGUE

AVTOMATIZIRANA DIAGNOSTIKA POŠKODBE ALUMINIJEVE ZLITINE PRI VISOKO-CIKLIČNEM UTRUJANJU

Pavlo Maruschak[1], Igor Konovalenko[1], Mykhailo Karuskevich[2], Vladimir Gliha[3], Tomaž Vuherer[3]

[1]Ternopil Ivan Pul'uj National Technical University, 46001 Ternopil, Ukraine
[2]National Aviation University, Aircraft Design Department, Komarova Ave. 1, 03058 Kyiv, Ukraine
[3]University of Maribor, Faculty of Mechanical Engineering, Smetanova 17, 2000 Maribor, Slovenia
maruschak.tu.edu@gmail.com

An identification and quantitative analysis of the deformation relief of the aluminium alloy for an aircraft construction based on a digital-image processing has been performed. The behaviour of defects has been assessed on the basis of diagnostics results for individual stages of the deformation process. It has been established that the individual stages of the damage-accumulation process are characterised by the values of integral-image parameters. Based on the consecutive processing of the data on the surface cyclic deformation, the main regularities of the propagation of defects have been found. Theoretical preconditions have been substantiated and experimental results obtained.

Keywords: fatigue, surface, digital image, diagnostics, accumulated damage, defect propagation, evaluation

Identificirali in kvantitativno analizirali smo relief deformirane površine aluminijeve zlitine za gradnjo letal. Temelj obojega je izdelava digitalne podobe površine vzorcev. Oceno vedenja defektov omogočajo rezultati diagnostike posameznih stopenj deformacijskega procesa. Ugotovili smo, da so te stopnje med akumulacijo poškodbe značilne po vrednostih integralnih parametrov slike. Na osnovi zaporedne obdelave podatkov ciklične deformacije na površini smo ugotovili glavne zakonitosti pri širjenju defektov. Tako smo dokazali teoretične predpostavke in pridobili eksperimentalne podatke.

Ključne besede: utrujanje, površina, digitalna podoba, diagnostika, akumulirana poškodba, širjenje defekta, vrednotenje

1 INTRODUCTION

An analysis of the loading conditions of modern civil aircrafts, the existing methods for evaluating the accumulated fatigue damage, the peculiarities of fatigue damage of aviation structural materials and the results of the previous fatigue investigations allowed formulating an approach to solving the problem of a quantitative evaluation of the accumulated fatigue damage of the aircraft structural elements[1]. However, the technological complexity of many of the existing instrumental methods for evaluating the accumulated fatigue damage as well as their insufficient accuracy and reliability limit the use of these methods for practical purposes.[2]

The initial diagnostics of the contemporary aircraft-skin condition involves the search and identification of the fatigue damage using the visual-control methods. It is known that the incubation period of the fatigue damage accumulation is, in many cases, reflected in the visual signs, which determine the possibility of both qualitative and quantitative evaluations of the accumulated fatigue damage.[3] The quantitative evaluation of the accumulated damage at the initial stage of fatigue allows predicting the place and the time of a fatigue-crack appearance. At the stage of designing aviation equipment such a prediction reduces the cost of a full-scale fatigue tests significantly due to shortening their duration, and, at the stage of operation, it allows increasing the reliability of aircrafts and safety of flights.[4]

A deformation relief is formed on the surface of the cladding layer of aluminium alloys under the stresses corresponding to the loading conditions of many structural elements during operation and testing. Stress concentration causes a prior formation of the relief in the vicinity of riveting holes, glue-cooking points, etc., which are the areas of potential failures. A surface deformation relief is observed at several scale levels. Using the optical microscopy the signs of a relief can be observed at the meso- and macro-levels.[5]

The need for substantiating and implementing the objective indicators of the deformation-relief intensity as the characteristics of the accumulated fatigue damage is obvious. The solution of this problem, by means of an analysis of damaged-surface images, will be shown below. The dependencies that allow predicting the residual life are of the most practical importance. Such dependences can be obtained on the basis of the data on deformation-relief-parameter evolution.[6]

It is proposed herein to use the integral parameters obtained by analysing the investigated surface images.

They allow evaluating the fatigue damage of the aluminium alloy for the aircraft construction.
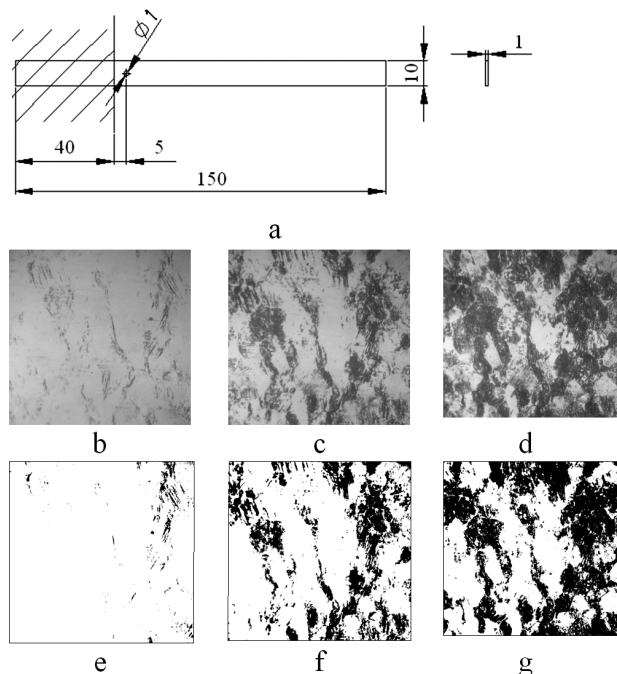
2 DEFORMATION-RELIEF-EVALUATION TECHNIQUE

The specimen geometry is shown in **Figure 1**; the specimen was tested with cantilever bending at $R = 0$, $\sigma_{max} = 147$ MPa. The analysis of the deformation relief was performed near the stress concentrator (a hole with a diameter of 1.0 mm).

In the process of testing we recorded the surface condition in the vicinity of the stress concentrator after an application of cyclic loading, the number of loading cycles necessary for the initiation of a fatigue crack with a length of 1.0 mm, and the number of loading cycles leading to a complete failure. The specimen surface condition was evaluated by analysing its photo images obtained in a series after a certain number of loading cycles. The images taken with a photo camera (**Figures 1b** to **d**) were transformed into grayscale images with the brightness function $I(x,y)$. The absolute values of horizontal and vertical gradients were calculated for every pixel of an image:

$$\nabla I_x(x,y) = \left|\frac{\partial I(x,y)}{\partial x}\right|, \quad \nabla I_y(x,y) = \left|\frac{\partial I(x,y)}{\partial y}\right| \quad (1)$$

where $x \in N_m$, $y \in N_n$ (m and n are the width and height of an image, respectively):

a

b   c   d

e   f   g

Figure 1: a) Scheme of the specimen investigated; examples of the deformation relief after 15, 100, 711 thousand loading cycles: b), c), d) initial image and e), f), g) binary image
Slika 1: a) Shema vzorca za preiskavo; primer reliefa deformirane površine po 15, 100, 711 tisoč obremenilnih ciklih: b), c), d) začetna slika in e), f), g) binarna slika

The mean values of horizontal and vertical gradients were used for a generalised evaluation of the condition of the surface investigated:

$$G_x = \overline{\nabla I_x} = \frac{1}{mn}\int_1^n\int_1^m \nabla I_x(x,y)\mathrm{d}x\mathrm{d}y$$

$$(2)$$

$$G_y = \overline{\nabla I_y} = \frac{1}{mn}\int_1^n\int_1^m \nabla I_y(x,y)\mathrm{d}x\mathrm{d}y$$

The gradient allows determining the predominant direction of the defect propagation and the nonuniformity degree of the surface investigated.[7] A low mean value of the gradient indicates an insignificant variation of intensities along the given axis of an image. In practice this shows a more uniform picture of the deformation relief in a certain direction[8] and indicates the coordinate axis that corresponds to the predominant direction of the defect propagation. In order to enhance the informative features corresponding to the elements of the damaged surface, binary transformation was applied to the obtained grayscale images.[9] This resulted in black-and-white images of the damaged surface with the intensity function IB, in which white pixels correspond to the background and black ones to the objects of the deformation relief (**Figures 1e** to **g**). The most general parameter that allows evaluating the degree of specimen damage using the obtained images, is the relative area of defects:

$$S_d = \frac{S}{m \cdot n} \cdot 100\% \quad (3)$$

where S is the number of deformation relief pixels in an IB image.

The distribution of deformation relief elements along the image axes is described with horizontal H_x and vertical H_y histograms:[8]

$$H_x(y) = \sum_{x=1}^m I(x,y), \quad H_y(x) = \sum_{y=1}^n I(x,y) \quad (4)$$

Each element of a histogram contains a number of pixels that correspond to the objects of the deformation relief, in columns and lines of the image analysed, respectively. Histogram functions (4) contain the basic information about the distribution of the deformation relief along the coordinate axes of an image.

For a generalised evaluation of the surface damage based on histograms it is proposed in[8] to use the mean values of histograms $\mu_x = S/n$ and $\mu_y = S/m$ (where S is the general number of black pixels). However, it is reasonable to use these parameters during multiple measurements under similar conditions with a permanent rectangular watch window. During laboratory testing of different specimens, especially under different conditions of the surface defect nucleation, the mean values of histograms contain little information. In addition, in the case of a rectangular watch window the values of μ_x and μ_y are scaled differently (relative to the image

dimensions) and are inconvenient for a comparison, while in the case of a square watch window they become similar.

For a quantitative evaluation of the histogram view (4) a spectral analysis of the functions was performed. Using the fast Fourier transformation the histogram functions were presented in the form of a row:

$$H_x(y) \approx \sum_{k=0}^{K_x} A_{xk} \cos(2\pi \frac{k}{n} y - \varphi_x)$$

$$H_y(x) \approx \sum_{k=0}^{K_y} A_{yk} \cos(2\pi \frac{k}{n} x - \varphi_y) \qquad (5)$$

The number of the harmonics of histograms K_x and K_y was chosen in such a way as to ensure that the accuracy of presenting a histogram function as a sum of harmonics is not lower than the limit value of ε:

$$\left| H_x(y) \approx \sum_{k=0}^{K_x} A_{xk} \cos(2\pi \frac{k}{n} y - \varphi_x) \right| \leq \varepsilon$$

$$\left| H_y(x) \approx \sum_{k=0}^{K_y} A_{yk} \cos(2\pi \frac{k}{n} x - \varphi_y) \right| \leq \varepsilon \qquad (6)$$

The mean amplitudes of the spectrum of the functions of the horizontal A_{ax} and vertical A_{ay} histograms were taken as the informative parameters:

$$A_{ax} = \frac{1}{K_x - 1} \sum_{k=1}^{K_x} A_{xk}, \quad A_{ay} = \frac{1}{K_y - 1} \sum_{k=1}^{K_y} A_{yk} \qquad (7)$$

The mean amplitude of the spectrum yields the quantitative evaluation of the damage propagation along the image axes. Its higher values correspond to a higher degree of damage along the given axis. Thus, while comparing the values of A_{ax} and A_{ay} it is possible to get information about the size and predominant direction of the surface-defect propagation.

The presence of the pairs of generalized characteristics – the mean gradients G_x, G_y and the mean amplitudes of the spectrum A_{ax}, A_{ay} – allows obtaining the complex integrated characteristics of the image analysed in two, mutually perpendicular, coordinate directions.

3 REGULARITIES IN DAMAGE ACCUMULATION

Cyclic loading forms a deformation relief on the surface of structural aluminium alloys, the intensity of which indicates the level of the accumulated fatigue damage.[10] The relief of this type was observed on both the standard specimens for the fatigue tests in a broad range of loading conditions and the specimens prepared from the skin of the An-24 aircraft; both were tested under stresses close to the operational ones.[1–3] The results of the investigations carried out using the methods of optical and electronic microscopy show the appropriateness of using the deformation-relief term and
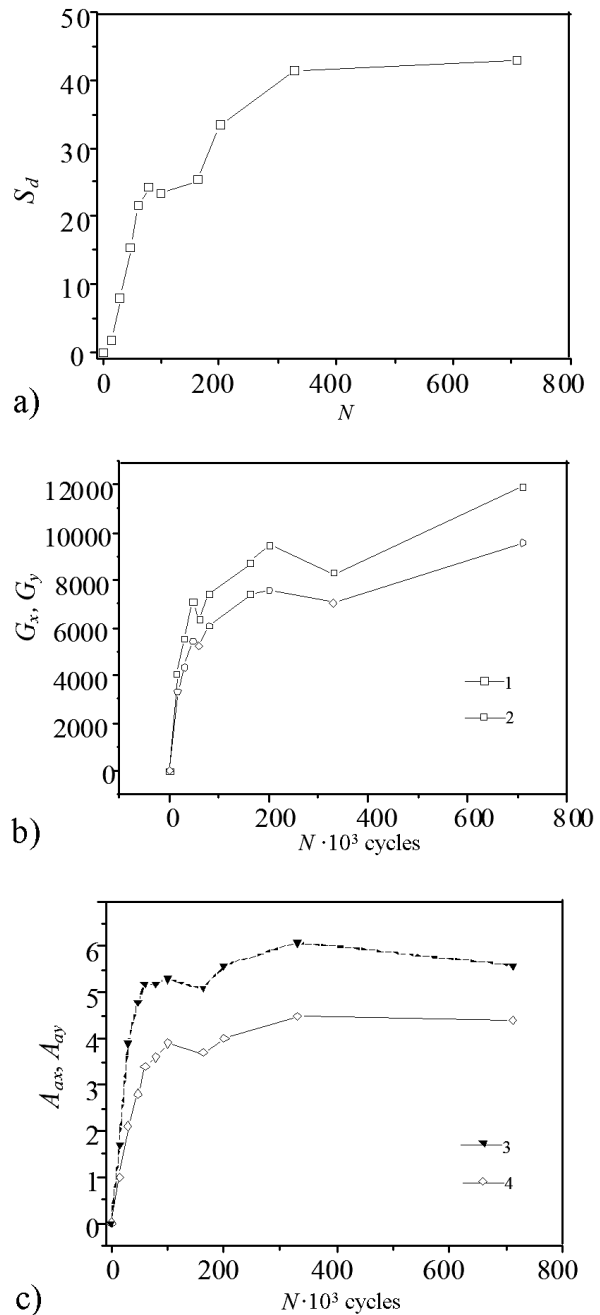
Figure 2: Dependence of integral parameters of deformation relief on: a) cyclic loading of a specimen, N: general area of defects S_d, b) mean horizontal and vertical gradients G_x and G_y, c) mean amplitudes of the spectrum, A_{ax} and A_{ay}

Slika 2: Odvisnost integralnih parametrov reliefa utrujenosti od: a) ciklične obremenitve vzorca N: skupna površina defektov S_d, b) povprečen horizontalni in vertikalni gradient G_x and G_y, c) srednja amplituda spektra A_{ax} and A_{ay}

applying it as a diagnostic parameter of fatigue damage.[1,2]

Figure 2 shows the dependence of the calculated integral image parameters on the number of loading cycles. An increase in the S_d parameter indicates an increase in the degree of damage to the surface investigated. According to the experimental data, in the

cases of up to 100,000 loading cycles, fast growing surface defects take place (**Figure 2a**). At the same time, after 100,000 loading cycles the deformation relief changes insignificantly.

The quantitative analysis of the kinetics of the changes in the deformation-relief orientation during cyclic loading of the aluminium alloy is performed. It is found that cyclic loading of 80,000 cycles causes a formation of a complex system of shears on the specimen surface. At this stage, an intense saturation of the surface with deformation shears takes place. Individual crystal blocks and their conglomerates sometimes ascend and sometimes descend above the surface, while their formations coalesce in groups and the sizes of defects increase gradually. This dynamic chaos is a depiction of the dynamic, cooperative dislocation processes at the micro- and meso-levels.[1,5] Nearly identical values of the gradients during the first phase of the investigation reflect the chaotic disorderly process of defect nucleation.

Later on the relief acquires an orderly orientation. Lower values of the vertical gradient (as compared to the horizontal one) show that along the vertical axis the picture of the deformation relief is more uniform, while along the horizontal axis sharper changes in the image intensity are observed. Thus, lower values of the gradient correspond to the direction, along which the areas of the surface damage stretch. A monotonous increase in the G_x

and G_y parameters confirms the results obtained earlier,[11] indicating self-similarity and scaling of the formed deformation structures. The mean amplitudes of the spectrum of histogram functions A_{ax} and A_{ay} (**Figure 2c**) duplicate, to a certain extent, the dependence presented in **Figure 2a**; however, they allow characterising the surface failure process in two coordinate directions. Higher values of the vertical amplitude indicate a more significant damage in this particular direction.

The quantitative parameter of fatigue failure is found and it allows assessing the surface condition and the defect propagation direction within the section analysed based on the analysis of the surface saturation with visual signs of the deformation relief (**Figure 3**).

The chosen diagnostic parameter of damage and the technique of its quantitative evaluation allow considering the developed method as the express diagnostic of fatigue failure.

4 GRADED NATURE OF THE DEFORMATION-RELIEF DEVELOPMENT

The first stage is the fast accumulation of defects on the surface analysed. The structural non-uniformity causes a formation of residual stress fields, which relax partly by means of forming sliding bands, extrusions and intrusions in the individual grains of the material[12]. Characteristic structural traces of the localisation are observed in macro extrusions in the form of the aggregates of "ridges" ("hills"). An intense formation of the deformation relief takes place. This stage accounts for approximately 15–20 % of the general number of cycles to the onset of crack formation.

The second stage is the slowing down of microplastic shears of the grains of the material, coalescence of individual sections of the deformation relief and saturation of the system. Although the damage accumulation process (deformation relief) is slowed down at this stage as compared to the previous one, its course is quasistationary. It is this that allows using it for technical diagnostics of a damaged-surface condition with a view to predicting the limit state. The limit state refers to the nucleation of a fatigue crack with the length of 1.0 mm that can be identified by means of optical control. The limiting value of damage parameters was considered as the last one in the row of values that were obtained before the moment of the fatigue-crack formation.

5 CONCLUSIONS

A technique has been developed for evaluating the aluminium-alloy surface condition by analysing its image and calculating its integral parameters, including the general area of damage, the mean gradients along the coordinate axes, and the mean amplitude of the spectrum of histogram functions along the coordinate axes. The basic factor that allows using the proposed technique is
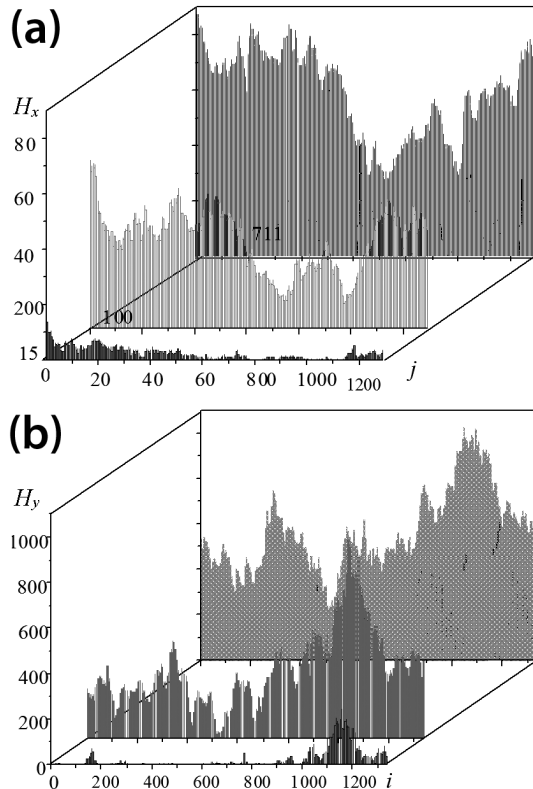
Figure 3: a) Horizontal and b) vertical histograms for depicting the deformed surface after 15, 100, 711 thousand loading cycles
Slika 3: a) Horizontalni in b) vertikalni histogram za opisovanje deformirane površine po 15, 100, 711 tisoč obremenilnih ciklih

the saturation of the material surface with the visual signs of the relief that are detected with the methods of optical microscopy. For the quantitative characteristic of the relief, the damage parameters can be used and they allow analysing the variation of spatial orientation of the defects caused by a deformation within the surface, on which the signs of localised strain are absent.

The main regularities in the accumulation of fatigue damage on the surface of an aluminium alloy have been established. The possibility of using the developed technique for determining the accumulated fatigue damage under high-cycle fatigue is substantiated.

6 REFERENCES

[1] M. Karuskevich, O. Karuskevich, T. Maslak, S. Schepak, Int. J. of Fatigue, 39 (**2012**), 116

[2] S. R. Ignatovich, Materials Science, 47 (**2011**), 636

[3] Y. G. Gordienko, R. G. Gontareva, J. S. Schreiber, E. E. Zasimchuk, I. K. Zasimchuk, Adv. Eng. Mater., 8 (**2006**), 957

[4] M. V. Karuskevich, E. Yu. Korchuk, A. S. Yakushenko, T. P. Maslak, Strength of Mat., 40 (**2008**), 693

[5] L. S. Derevyagina, V. E. Panin, A. I. Gordienko, Physical Mesomechanics, 11 (**2008**), 51

[6] E. E. Zasimchuk, M. V. Karuskevich, A. I. Radchenko, Strength of Materials, 22 (**1990**), 1855

[7] P. V. Yasnii, I. V. Konovalenko, P. O. Marushchak, Materials Science, 45 (**2009**), 291

[8] A. Hassani, H. Ghasemzadeh Tehrani, Crack detection and classification in asphalt pavement using image processing, in Pavement Cracking: Mechanisms, Modelling, Detection, Testing and Case Histories, CRC Press, Chicago 2008, 891–896

[9] I. V. Konovalenko, P. O. Marushchak, Optoelectronics, Instrumentation and Data Processing, 47 (**2011**), 360

[10] P. Yasniy, P. Maruschak, I. Konovalenko, Strain, 47, (**2011**), 238

[11] M. V. Karuskevych, I. M. Zhuravel', T. P. Maslak, Materials Science, 47 (**2011**), 621

[12] Yu. G. Kabaldin, S. N. Murav'yev, Russian Engineering Research, 27 (**2007**), 513

WELDED ALUMINIUM AND MAGNESIUM ALLOYS – CORROSION AND MECHANICAL PROPERTIES FOR REFRIGERATION COMPRESSORS IN COMPARISON WITH DEEP-DRAWING STEEL

VARJENE ALUMINIJEVE IN MAGNEZIJEVE ZLITINE – KOROZIJSKE IN MEHANSKE LASTNOSTI ZA KOMPRESORJE HLADILNIKOV V PRIMERJAVI Z JEKLOM ZA GLOBOKO VLEČENJE

Klaus Günther Kerschbaumer, Rudolf Vallant, Norbert Enzinger, Christof Sommitsch

Institute for Materials Science and Welding, Kopernikusgasse 24, 8010 Graz, Austria
rudolf.vallant@tugraz.at

Increasing the energy efficiency of household refrigeration appliances as a result of legal requirements is more and more important (2010/30/EUEG2010 Directive). This means that the equipment with the energy efficiency lower than D can no longer find its place in the European trading. In this investigation aluminium alloys (AW5083-O, AW6181-T4) and a magnesium alloy (AZ31) were selected via a material selection. They are compared to the currently used deep-drawing steels (DD11, DD13) with respect to the corrosion and strength properties of similar overlap-welded joints.
To verify the corrosion properties the neutral salt spray test (NSS) and the fruit acid spray test were performed with an overall test duration of 480 h. The type of corrosion, its influence on the corrosion rate and the strength of the welded joints were evaluated. Magnesium shows a very high corrosion and therefore cannot be used uncoated, like deep-drawing steel. The aluminium alloys show only slight selective corrosion phenomena and are, from the welding and corrosion point of view, an attractive alternative to steel. Due to a higher thermal conductivity of aluminium, in comparison with steel, a higher energy efficiency of the cooling compressor is expected.

Keywords: MIG/CMT-P welding, aluminium, magnesium, corrosion, deep-drawing steel, fruit acid, neutral salt spray test, tensile test, AW5083-O, AW6181-T4, AZ31, DD11, DD13, DIN 8985, DIN ISO 6227

Vedno bolj postaja pomembno povečanje energijske učinkovitosti gospodinjskih hladilnih naprav kot posledica legalnih zahtev (2010/30/EUEG2010 Directive). To pomeni, da oprema z energijsko učinkovitostjo, manjšo od D nima več mesta v evropski trgovini. V tej raziskavi sta bili pri izbiri materiala izbrani aluminijevi zlitini (AW5083-O, AW6181-T4) in magnezijeva zlitina (AZ31). Primerjane so s sedaj uporabljanima jekloma za globoko vlečenje (DD11, DD13) glede na korozijo in trdnostne lastnosti podobnih zvarov s prekrivanjem.
Za preverjanje korozijskih lastnosti sta bila izvršena preizkusa v nevtralni slani komori (NSS) in preizkus s škropljenjem sadne kisline v povprečnem trajanju 480 h. Na zvarjenih spojih je bila ocenjena vrsta korozije, vpliv na hitrost korozije in na trdnost zvarjenih spojev. Magnezij izkazuje veliko korozivnost in ga zato ni mogoče uporabljati brez površinske zaščite tako kot jeklo za globoki vlek. Aluminijevi zlitini izkazujeta samo rahle selektivne korozijske pojave in sta s stališča varjenja in korozije zanimivi kot alternativa za jeklo. Zaradi večje toplotne prevodnosti aluminija v primerjavi z jeklom se pričakuje tudi večja energijska učinkovitost kompresorja za hlajenje.

Ključne besede: MIG/CMT-P-varjenje, aluminij, magnezij, korozija, jeklo za globoki vlek, sadna kislina, nevtralni preizkus škropljenja s slanico, natezni preizkus, AW5083-O, AW6181-T4, AZ31, DD11, DD13, DIN 8985, DIN ISO 6227

1 INTRODUCTION

The main focus of the technological development of household cooling compressors is on an "energy-efficiency improvement" stimulated by the increased competition, cost pressures and a stricter EU legislation[1,2] for cooling compressors. Furthermore, the noise reduction in service and an improvement of the corrosion properties are important aims for a long-term system improvement of household cooling compressors. These future requirements can be met, in part, by finding a new, innovative housing material.

Currently, the steel materials DD11 and DD13 are used for deep-drawn, almost spherical housings.[3] The main problem is, however, that the material corrosion

resistance in the above mentioned application is not satisfactory. Preliminary studies have shown that aluminum and magnesium alloys have a potential to replace the steel materials. For a material-selection process, according to Reuter[4], the following housing requirements have been defined:

- the minimum static strength of 85 MPa for the maximum internal pressure of 40 bar
- MIG or equivalent weldability
- the materials should be industrially formable (cold or hot forming)
- hermetic-gas proofness

The Al-alloys AW5083-O (annealed) and AW6181-T4 (naturally aged) and the magnesium alloy AZ31 were selected as suitable candidates for further investigations.

Corrosion investigations of these base materials and their similar welded joints in the neutral salt spray (NSS) and fruit acid spray tests (FS) have been performed.

2 EXPERIMENTAL WORK

2.1 Base materials and weld filler metals

MIG pulsed-arc welding was used for the annealed, AlMgMn, wrought alloy AW5083-0 and the naturally aged, AlMgSi, wrought alloy AW6181-T4. For the deep-drawing steels DD11 and DD13, MAG pulsed-arc welding was applied. The CMT+P welding procedure

Figure 1: Welding-torch positions for similar overlap welded joints
Slika 1: Pozicija varilnika pri enako debelih prekrivnih varjenih spojih

was applied for magnesium AZ31. The sheet thickness of the materials was 3 mm, except for the 2.5 mm AW6181-T4.
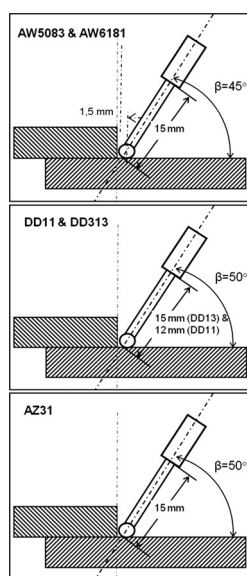
The filler metals were selected according to the recommendations of DVS 0913[5] and Davis.[6] The AlMg5 filler was selected for AW5083-O, and AlSi5 for AW6181-T4. Considering the Böhler Welding Guide for DD11 and DD13, the G3Si1 (EMK6) filler was used[7]. For the AZ31 sheet, Kammer[8] recommends AZ61. AM50[9] was used as it easily meets the strength requirements of 85 MPa.

It is notable that the AlSi5 filler metal has only about 50 % of the strength of the AW6181-T4 sheet. Nevertheless, it was used as the hot-cracking susceptibility of 6000 alloys can be significantly reduced according to Davis.[6] The 440 MPa yield strength of the G3Si1 weld metal is much higher than the 170 MPa yield strength of deep-drawing steels, as there is no even matching filler available. The chemical compositions and mechanical properties of the examined sheet alloys and filler metals are summarized in **Table 1**.[3,7,9–12]

2.2 Experimental set-up and investigations

2.2.1 Welding experiments

In **Figure 1** the joint geometry and welding torch position are shown schematically for different material combinations. The top and bottom sheets were positioned with an overlap of 20 mm and clamped on the welding table. The welding experiments were carried out with a Fronius TPS4000+CMT welding machine. The torch was conducted with an ABB robot IRB140. The torch angle β varied between 45° and 50° depending on the material combinations. The contact tip distance

Table 1: Chemical analyses and mechanical properties of sheet alloys (GW) and weld-filler metals (FM)
Tabela 1: Kemijska analiza in mehanske lastnosti pločevin (GW) ter varilnega dodajnega materiala (FM)

material BM / FM element	AW5083-O (BM)[10]	AlMg5 (FM)[11]	6181-T4 (BM)[10]	AlSi5 (FM)[11]	DD11 (BM)[3]	DD13 (BM)[3]	EMK 6 (FM)[7]	AZ31 (BM)[12]	AM50A (FM)[9]
Si	0.4	<0.25	0.7–1.1	4.5–6.0			0.9		≤0.1
Fe	0.4	<0.4	0.15–0.5	<0.6	balance	balance	balance		≤0.008
Cu	0.1	<0.1	0.25	<0.3					≤0.01
Mn	0.4–1.0	0.05–0.2	0.4	<0.15	≤0.6	≤0.40	1.49	≤0.2	0.26–0.60
Mg	4.0–4.9	4.5–5.5	0.6–1.0	<0.2				balance	balance
Cr	0.05–0.25	0.05–0.2	0.15	-					
Zn	0.25	<0.1	0.3	<0.1				1.0	≤0.22
Ti	0.15	0.06–0.2	0.15	<0.15					
Be	-	<0.0003	0.1	<0.0003					
others	0.15	<0.05	0.15	<0.05					
Al	balance							3	4.4-5.4
C					≤0.12	≤0.08	0.08		
P					≤0.045	≤0.03			
S					≤0.045	≤0.03			
$R_{p0.2}$/MPa	145	110	125	40	170	170	440	170	125
R_m/MPa	300	240	235	120	<440	<400	530	240	230
A_5/%	22	17	23	8	28	33	30	17	10

covers from 12 mm to 15 mm. The contact point of the welding wire at the lower sheet for all the material combinations is about 1.5 mm away from the fillet weld root.

For all the welding experiments optimised parameters were used to get good wetting at the weld flank. For AW5083-O and AW6181-T4 the welding parameters refer to Kerschbaumer[13]. The fillet welds of deep-drawing steels were welded utilising the optimised parameter sets of the company ACC Austria for the 30 mm/s weld speed. For the Al und Mg experiments the welding speed of 15 mm/s was selected. The forehand angle α varied between 0° (AW5083-O, AZ31) and 5° (AW6181-T4, DD11 and DD13). The shielding gases of 50 : 50 Ar and He and Corgon 18 (which is 18 : 82 CO_2 and Ar) were used for Al, Mg and steel welding. The energy input varied between 0.9 kJ/cm (AZ31) and 3.4 kJ/cm (DD13). Aluminium and DD11 were welded with a similar energy input. All the welding parameters are listed in **Table 2**.

2.2.2 Tensile and corrosion tests

From the welded overlap joints the 50 mm × 180 mm samples for corrosion and shear tests as well as metallographic investigations were prepared and the 50 mm × 100 mm ones were prepared from the base materials, **Figure 2**. The shear strength of the joints was tested according to EN ISO 9018:2006[14] utilizing a Zwick RMC100 tensile-testing machine. The free clamping length was adjusted to 120 mm. The strain rate (traverse speed) was 2 mm/min at room temperature. For comparability, the measured fracture forces were converted to the tensile strength (50 mm sample width, 3 mm or 2.5 mm sheet thickness). The arithmetic mean and the standard deviation have been calculated for each sample.
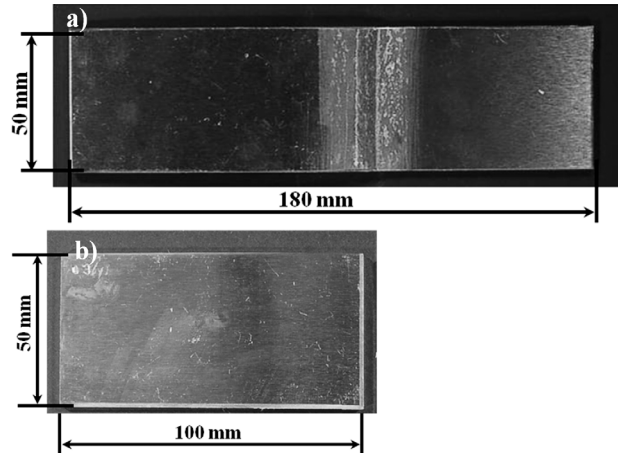
Figure 2: Corrosion samples; a) welding joint for tensile-shear test and metallography; b) base material
Slika 2: Vzorci za korozijo; a) varjeni spoj za natezni strižni preizkus in metalografijo; b) osnovni material

The corrosion resistance of the welded joints and base materials was investigated using the neutral salt spray test (NSS) according to EN ISO 9227:2006[15] as well as the fruit acid spray test (FS) according to DIN 8985.[16] Corrosion testing was performed using a Köhler corrosion chamber HKT500. The samples were taken out after (2, 6, 24, 48, 96, 168, 240 and 480) h, documented macroscopically with a digital reflex camera Nikon D50 and the mass gain was determined with a scale of the company Denver Instrument MXX-612 with an accuracy of 0.01 g, according to DIN 50905-1.[17] Due to a limited number of the samples the determination of the mass loss after removing the corrosion product was not carried out. After 240 h and 480 h metallographic investigations with LOM (Zeiss Z1m) and REM (Zeiss 1415VP) and the tensile-shear tests were performed to detect the impact of corrosion on the weld strength.

Table 2: Welding parameters for the selected material combinations/TPS 4000/CMT
Tabela 2: Parametri varjenja za izbrane kombinacije materialov /TPS 4000/CMT

Base material	AW5083-O	AW6181-T4	DD11	DD13	AZ31
Filler metal	AlMg5	AlSi5	EMK6	EMK6	AM50
Current type	Pulse	Pulse	Pulse	Standard	CMT+P
Sheet thickness (mm)	3	2.5	3	3	3
Shielding gas/quantity (L/min)	50 : 50 Ar:He 17	50 : 50 Ar:He 17	Corgon 18 18	Corgon 18 18	50 : 50 Ar:He 17
rapdefaultWire feed drive (m/min)	7.1	5.8	7.5	11.5	11
Voltage U/V	19	24.6	23.3	29.4	12.3
Current I/A	123	113	244	344	113
Welding speed v/(mm/s)	15	15	30	30	15
Energy input E/(kJ/cm)	1.55	1.85	1.90	3.37	0.93
Comments	α = 0° β = 50°	LBK -2 α = 5° forehand β = 50°	α = 5° forehand β = 50°	α = 5° forehand β = 50°	LBK-1 α = 0° β = 50°

3 RESULTS

3.1 Theoretical background

3.1.1 Deep-drawing steel

In saline solutions or brines, uniform- or shallow-pitting corrosion occurs, and occasionally there is also pitting corrosion, if chloride is deposited locally.[18–20] In the seawater with a salt concentration of about 29.2 g/l shallow pitting or pitting corrosion appears on deep-drawing steel. In the hydrochloric acid the corrosion rate increases linearly with the temperature and acid concentration.[18,20] In organic acids iron is corrosion resistant as long as the access to oxygen is prohibited. Generally, the uniform corrosion attack increases with an increase in the organic-acid concentration.[18,20]

3.1.2 Aluminium

In the atmosphere the less noble aluminium (with an electrochemical potential of –1.66 V) forms an Al_2O_3 dense oxide layer. This oxide layer causes a chemical resistance in the pH range of 4.5 to 8.8. For lower and higher pH values, i.e., for acidic or alkaline attacks the passive layer is dissolved and a uniform corrosion takes place. In chloride media aluminium shows pitting, intergranular corrosion and stress-corrosion cracking. In drinking water aluminium and Al_2O_3 are resistant unless the Al_2O_3 layer is mechanically damaged, e.g., due to grinding.[18,19,21–25] In milk aluminium forms an oxide layer with a good resistance. It is attacked by salt, hydrofluoric acid and alkali.[18]

Aballe has found in his work that precipitates [Al(Mn, Fe, Cr) and Al(Si, Mg)] cause the pitting in AW5083-O. The precipitates Al(Mn, Fe, Cr) are more noble than the base material matrix and the corrosion takes place in the Al matrix.[26,27]

An intergranular corrosion attack is formed along the Mg_2Si precipitates at the grain boundaries in AW61814-T4. The following precipitates stimulate an intergranular corrosion attack: $CuAl_2$ in 2xxx[28], Mg_2Al_3 in 5xxx[25], $MgZn_2$ in 7xxx[25] and Mg_2Si[29] or $CuAl_2$[28] in 6xxx. There are two types of intergranular corrosion, dependent on the nobility of the grain boundaries. The less noble Al_8Mg_5 precipitates in the 5xxx alloys[30,31] and the $MgZn_2$ precipitates in the 7xxx alloys are dissolved anodically. With the more noble grain-boundary precipitates like Mg_2Si or $CuAl_2$, the surrounding matrix material is dissolved.[18,19,22,24,32–35]

3.1.3 Magnesium

In the chloride-containing atmospheres and in salt solutions magnesium is not resident, as the protective oxide layer MgO is dissolved. In natural brines magnesium-salt crystals are formed that dissolve easily in water. Therefore, no further protective oxide layer is formed because in an aqueous chloride solution the passive layer is dissolved and no other corrosion protection is in place. In neutral media like humid air, MgO is transformed into a protective $Mg(OH)_2$ layer[2].

Manganese and zinc have a positive effect on the corrosion resistance of magnesium, where the Zn content must be below 3 %. When alloying aluminium and magnesium, the corrosion resistance in salt water increases[18,20,21,30,33,36–38].

3.2 Corrosion behaviour in the salt spray and fruit acid tests

Macroscopically a distinct difference in corrosion behaviour between the welded and base-material sheets is visible if the NSS and FS tests are compared. The steel sheets show a relatively thick rust layer after a 480 h NSS test, whereas after a FS test only a slight rust layer can be seen. It is noticeable that during the FS test rust layers are formed only on the welded steel joints, not on their base sheets. In the case of magnesium pitting can be seen macroscopically after the NSS and FS tests. In the case of aluminium both AW5083-O and AW6181-T4 show formations of white corrosion products (aluminum hydroxide) during the NSS and FS tests and they are more distinctive for the latter (**Figures 3a** and **b**).

#### 3.2.1 Salt spray test (NSS) – metallographic investigations

3.2.1.1 Base materials

After 480 h, on the AW5083-O surface, a few small pitting sites could be detected with a stereo microscope (**Figure 4a**), while AW6181-T4 showed no pitting. Both alloys were covered with white corrosion products that were more pronounced on AW6181-T4, **Figure 4b**. The steel and magnesium sheets showed strong corrosion
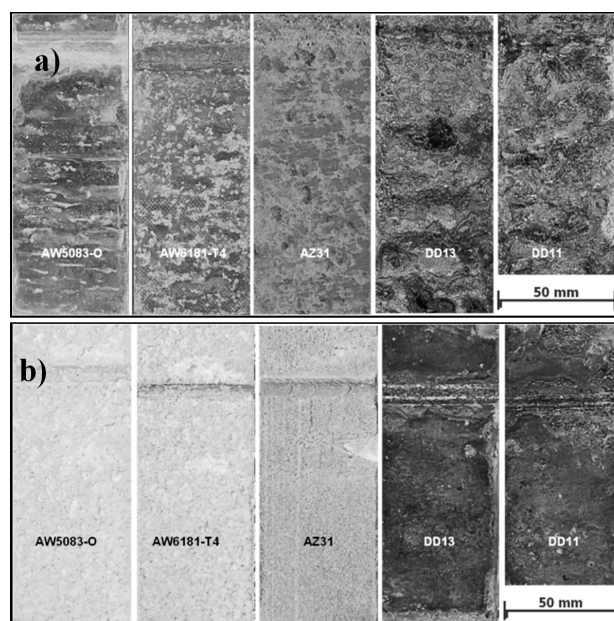

Figure 3: Corrosion samples after 480 h: NSS test (left), FS test (right)
Slika 3: Vzorci s korozijo po 480 h: NSS-preizkus (levo), FS-preizkus (desno)
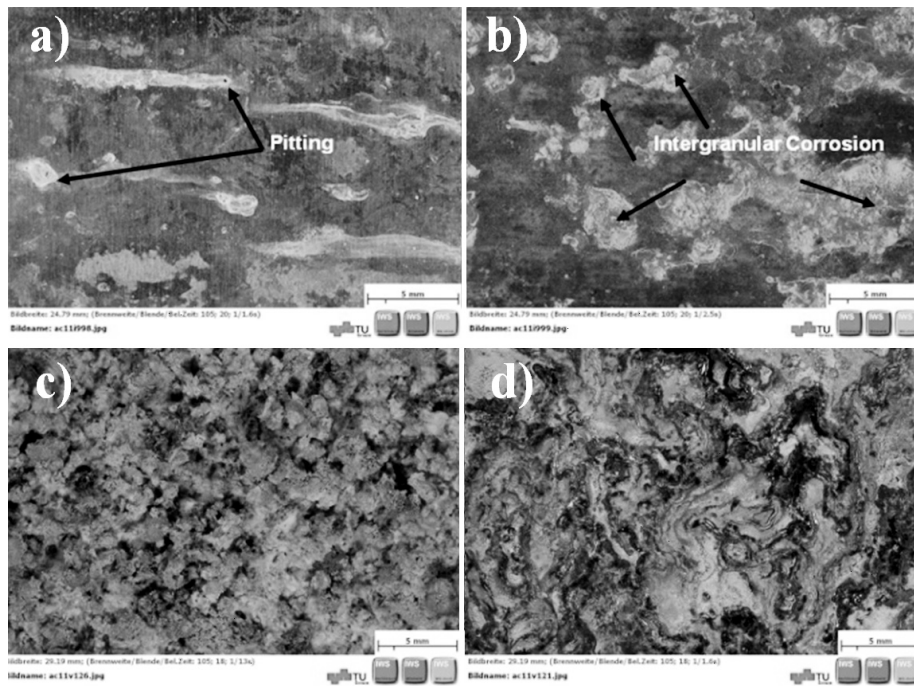
Figure 4: Corrosion after the NSS test/surfaces shown with a stereo microscope: a) AW5083-O, 480 h, b) AW6181-T4, 480 h; c) AZ31, 240 h; d) DD11, 240 h
Slika 4: Korozija po NSS-preizkusu; površine, prikazane s stereomikroskopom: a) AW5083-O, 480 h, b) AW6181-T4, 480 h; c) AZ31, 240 h; d) DD11, 240 h
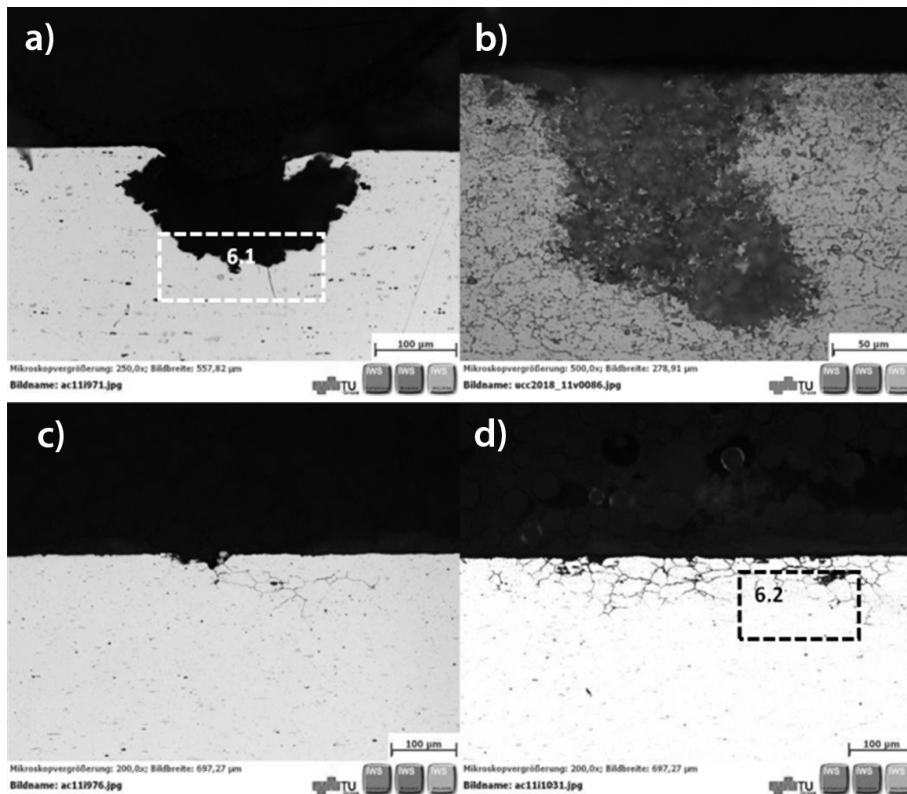
Figure 5: Corrosion after the NSS test/cross-section details in LOM: a) AW5083-O, 240 h; b) AW5083-O, 480 h; c) AW6181-T4, 240 h; d) AW6181-T4, 480 h
Slika 5: Korozija po NSS-preizkusu; detajli prereza, svetlobna mikroskopija (LOM): a) AW5083-O, 240 h; b) AW5083-O, 480 h; c)AW6181-T4, 240 h; d) Aw6181-T4 po 480 h
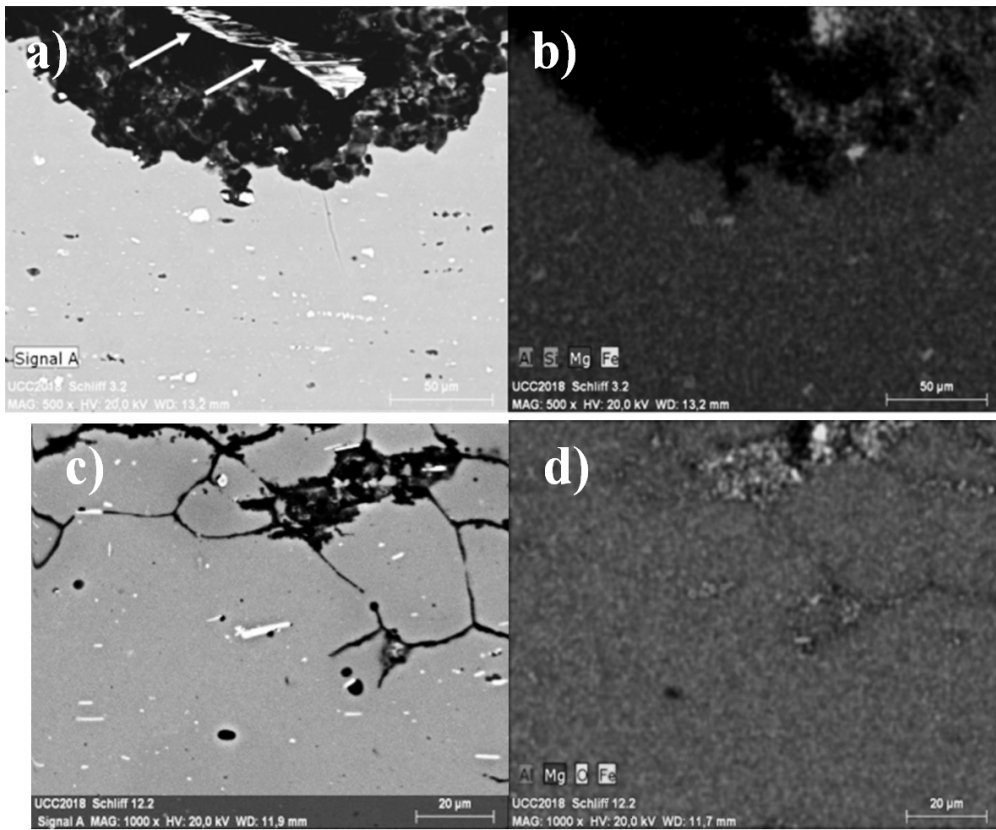
Figure 6: SEM and EDX of **Figure 5:** a) and b) AW5083-O, detail 6.1; c) and d) AW6181-T4, detail 6.2
Slika 6: SEM- in EDX-posnetka področij na **sliki 5**: a) in b) AW5083-O, detajl 6.1; c) in d) AW6181-T4, detajl 6.2

already after 240 h. On the AZ31 sheet, a porous white corrosion product was formed, **Figure 4c**. The steels show abundant red rust, whereat the first signs of corrosion occurred already after a few hours, **Figure 4d**.

The cross sections confirm the pitting corrosion for the AW5083-O alloy observed after 168 h with the stereo microscope. Significant pits were found after 240 h. **Figure 5a** shows a pit depth of about 0.16 mm observed with a light optical microscope (LOM). Primary precipitates and impurities containing Fe, Si and Mg were detected at the bottom of the pit with an energy-disper-

sive X-ray analysis (EDX) using a scanning electron microscope (SEM), **Figures 6a** and **b**. These precipitates behave electrochemically nobler and get exposed to the corrosion. The pitting progress into the depth from 240 h to 480 h is marginal (**Figure 5b**). The AW6181-T4 alloy shows intergranular corrosion (IG) starting in the small pitting areas and reaching a depth of about 0.1 mm (**Figures 5c** and **d**). The corrosion progress from 240 h to 480 h shows no further increase in the depth but spreading. The first superficial corrosion attack was visible already after 2 h. On closer examination, primary
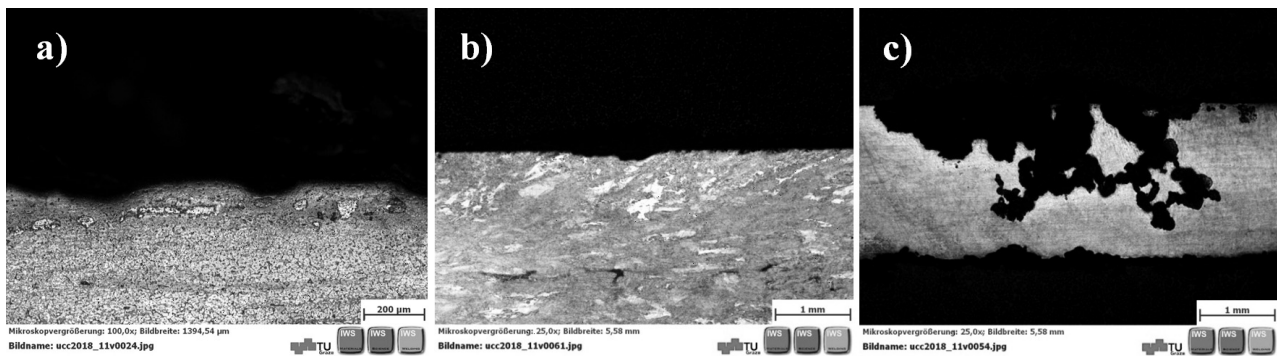
Figure 7: Corrosion after 480-h NSS/base-material cross sections in LOM: a) DD11 – uniform corrosion and shallow pitting; b) AZ31 grinded sample – uniform corrosion; c) AZ31 non-grinded sample – severe corrosion attack
Slika 7: Korozija po 480 h NSS; prerez osnovnega materiala, svetlobna mikroskopija (LOM): a) DD11 – enakomerna korozija in plitve jamice; b) AZ31 brušeno – enakomerna korozija; c) AZ31 nebrušeno – resen pojav korozije
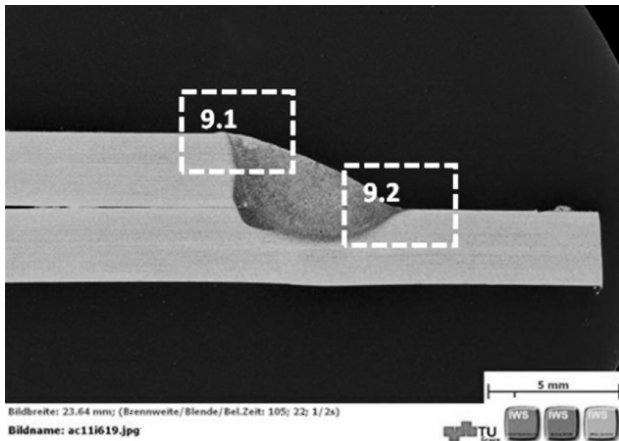
Figure 8: AW5083-O welded joint/fillet-weld cross section in LOM prior to the NSS test; hydrofluoric acid/alcoholic etchant
Slika 8: AW5083-O varjeni spoj; prerez zvara, svetlobna mikroskopija LOM pred NSS-preizkusom; kislina HF in alkoholno jedkalo

precipitates could be detected. In the SEM investigations no secondary phases (T4 aged) could be found, **Figures 6c** and **d**.

The cross section of the DD11 steel shows uniform corrosion and shallow pitting. It can be expected that DD13 has a similar corrosion behaviour, **Figure 7a**.

The magnesium alloy AZ31 exhibits a strong dependence on the initial surface roughness. Generally, the grinded samples have uniform corrosion and shallow pits, which are then fortified in depth. But the non-grin-ded AZ31 samples show a very strong local-corrosion attack combined with uniform corrosion. After 480 h almost the entire 3-mm sheet was dissolved, i.e., corroded as seen in **Figures 7b** and **c**. This significant difference can be attributed to the effect that a corrosive medium adheres less on the surfaces with low roughness.

3.2.1.2 Welded joints

In general, no effect of the used welding parameters on the corrosion behaviour was detected, compare[13]. The corrosion attack after 480 h was analyzed in the cross sections of the fillet welds, **Figure 8**.

Pitting corrosion occurred at the heat affected zone (HAZ) of alloy AW5083-O and in the AlMg5 weld metal. At the weld edges and the fusion line, local corrosion was detected, too. Furthermore, the surface pores in the AlMg5 weld metal were found to be the starting points for pitting and crevice corrosion as seen on **Figure 9**, compare.[13]

Sanchez-Amaya[39] also found this corrosion beha-viour with the corrosion tests involving a mixture of NaCl and H_2O_2. In the investigations of Mutombo in 2011[40], AW5083-O was MIG-welded with both filler metals, AlMg5 and AlSi5, to a Y-joint and tested in 3 % NaCl. He traced the corrosion start back to the existing surface pores. The tough AlMg5 weld and HAZ showed pitting.

The AW6181-T4 welded joints showed no corrosion at the fusion line or on the AlSi5 weld metal.
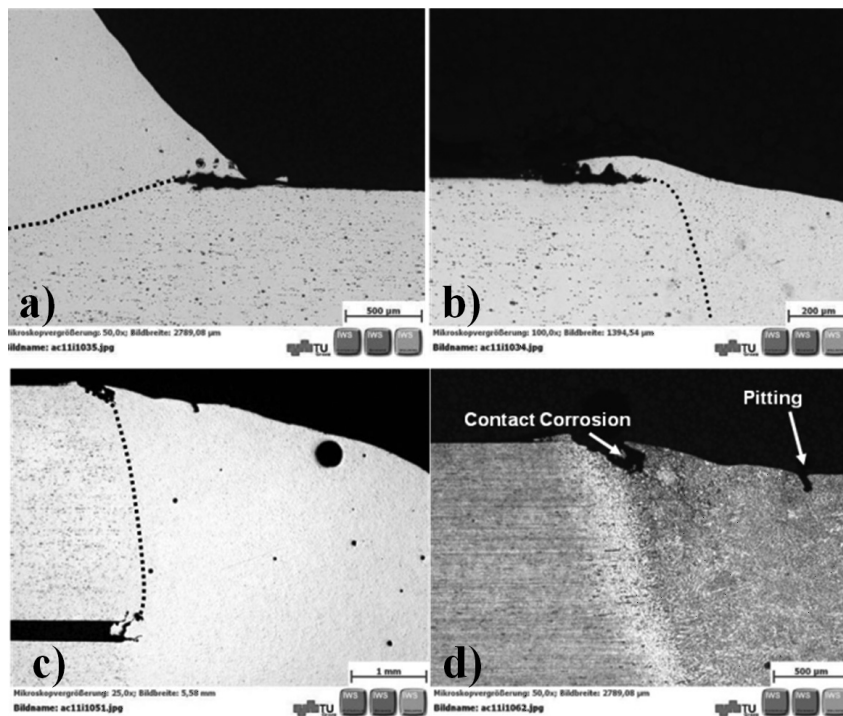
**Figure 9:** Welded AW5083-O joint cross sections in LOM/corrosion after the 480 h NSS test/local corrosion at the fusion line and weld-metal surface pores: a)–d) details 9.1 and 9.2 from **Figure 8**
Slika 9: Svetlobna mikroskopija (LOM) prečnega prereza zvara AW5083-O; korozija po 480 h NSS-preizkusa; lokalna korozija na liniji taljenja in pore na površini materiala zvara: a)–d) detajli 9.1 in 9.2 s **slike 8**
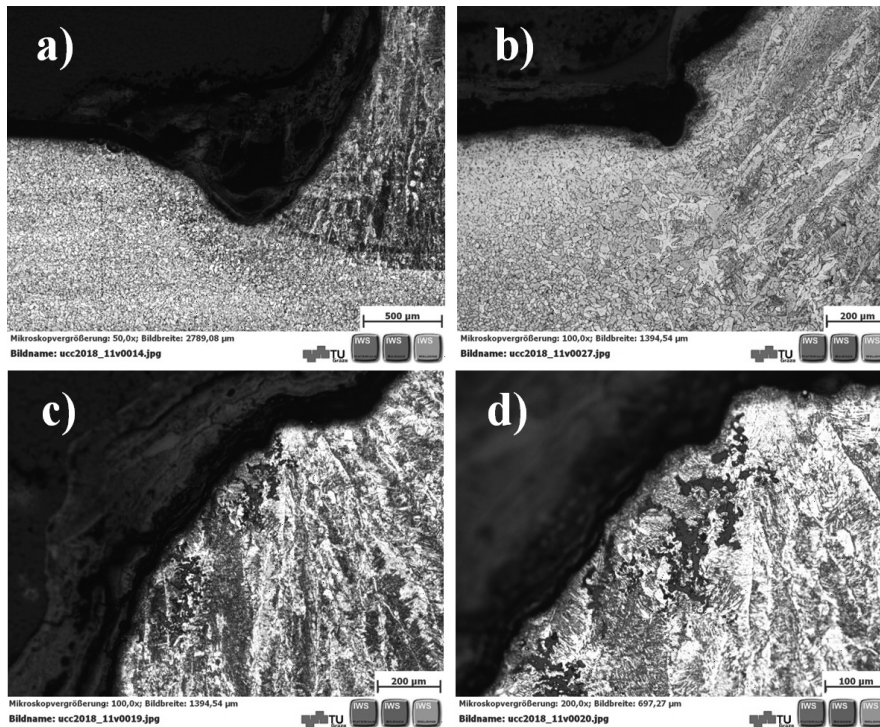
Figure 10: Welded steel-joint details – cross sections in LOM/corrosion after the 480 h NSS test/local corrosion at the fusion line: a) DD11; b) DD13; c and d) G3Si1 weld metal
Slika 10: Detajli zvarjenega spoja jekla – prečni prerez s svetlobno mikroskopijo (LOM); korozija po 480 h NSS-preizkusa; lokalna korozija na liniji taljenja: A) DD11; b) DD13; c) in d) G3Si zvarjena kovina
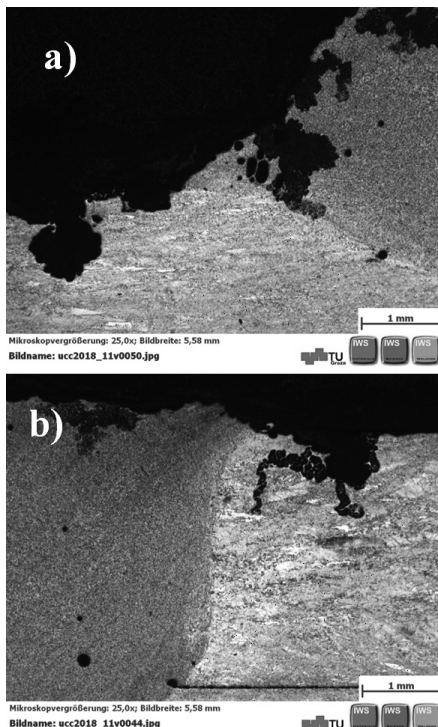
Figure 11: Welded AZ31 joint, grinded – cross sections in LOM/ corrosion after the 480 h NSS test: a) lower weld edge; b) upper weld edge – strong corrosion of the AM50 weld metals and the base metal
Slika 11: Zvarjen AZ31 spoj, brušeno – prečni prerez, svetlobna mikroskopija LOM; korozija po 480 h NSS-preizkusa: a) spodnji rob zvara, b) zgornji rob zvara – močna korozija AM50 zvarjene kovine in osnovnega materiala

The welded steel joints showed an intense corrosion attack along the fusion line and selective corrosion of the G3Si1weld metal, **Figures 10a** to **d**.

The AZ31 welded joints were manufactured only from the grinded magnesium alloy and were NSS tested. **Figures 11a** and **b** shows strong and partially localized corrosion on the AM50 weld metal as well as on the base material. Obviously, the bottoms of the formed cavities (large pits) act as starters for more pitting corrosion progressing into the depth.

3.2.2 Fruit acid test (FS) – metallographic investigations

3.2.2.1 Base materials

For AW5083-O, pitting corrosion of about 0.1 mm in depth occurred after the 240 h FS test. Continuing the corrosion test to 480 h, the pits did not progress in depth but grew wider, to about 0.6 mm, **Figures 12a** and **b**. This was caused by an electrolytic dissolution of metal in an acidic medium, compare.[10] In contrast, AW6181-T4 shows intergranular corrosion after 240 h (0.15 mm deep), just slightly progressing in depth (0.18 mm) during the 480 h FS test. However, the IG corrosion spread by about 2–3 mm in width after 480 h, **Figures 12c** and **d**.

The DD11-steel base material exhibits pitting corrosion after the 240 h and 480 h FS tests. In the etched cross section, partial IG corrosion could be found, too, **Figures 13a** to **c**. The results of the corrosion
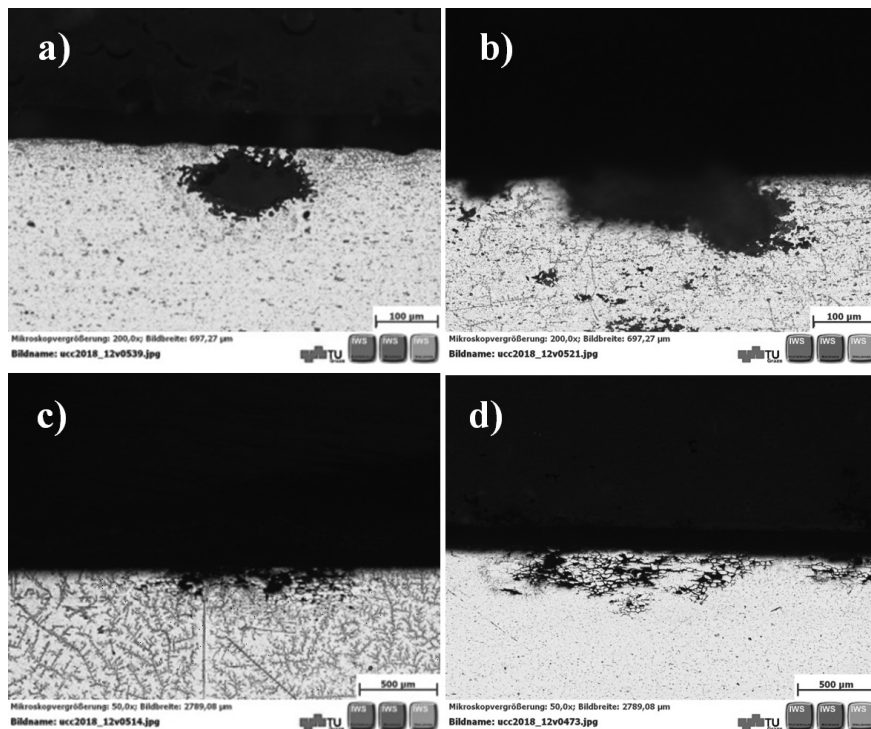
Figure 12: Corrosion after the FS test/cross-section details in LOM: a) AW5083-O, 240 h; b) AW5083-O, 480 h; c) AW6181-T4, 240 h; d) AW6181-T4, 480 h

Slika 12: Korozija po FS-preizkusu; detajli prečnega prereza s svetlobno mikroskopijo (LOM): a) AW5083-O, 240 h; b) AW5083-O, 480 h; c) AW6181-T4, 240 h; d) AW6181-T4, 480 h
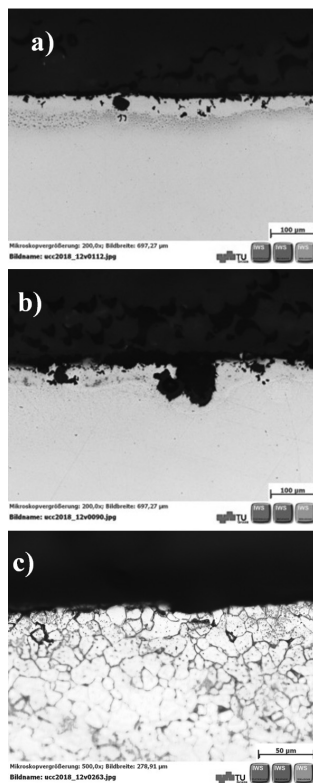

Figure 13: Corrosion of DD11 steel after the FS test/cross-section details in LOM: a) 240 h; b) 480 h; c) 480 h, etched with Nital

Slika 13: Korozija DD11 jekla po FS-preizkusu; detajli prečnega prereza, svetlobna mikroskopija (LOM): a) 240 h; b) 480 h; c) 480 h, jedkano z nitalom

behaviour of the DD13-steel base material are quite similar to the DD11 results.

The grinded AZ31 magnesium base material shows shallow pitting after the 240 h FS. Contrary to the NSS, during the 480 h test the corrosion progresses strongly, whereat localized corrosion and pitting arise, especially at the backside of the sample, **Figures 14a** and **b**.
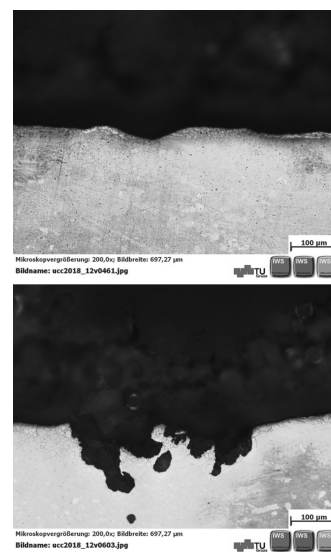
Figure 14: Corrosion of AZ31 after the FS test/cross-section details in LOM: a) 240 h; b) 480 h

Slika 14: Korozija AZ31 po FS-preizkusu; detajli prečnega prereza, svetlobna mikroskopija (LOM): a) 240 h; b) 480 h

3.2.2.2 Welded joints

After the 240 h FS test, alloy AW5083-O exhibits pitting corrosion at the fusion line and on the base material. After 480 h distinct pitting is found in the AlMg5 weld metal, too. At the weld edges a strong localized corrosion attack is found along the marked fusion line, whereat the corrosion depth remained to be about 0.8 mm between 240 h and 480 h, **Figures 15a** to **c**.

The welding joint AW6181-T4 does not lead to the corrosion of the weld edges or the AlSi5 weld metal. Here the IG corrosion is found on the base material as shown in **Figures 12c** and **d**.

After the 240 h FS test, the welded DD11-steel joint shows local corrosion at the weld edges. The shallow-pitting corrosion in the G3Si1 weld metal can be seen after 480 h, **Figures 16a** and **b**. These results are similar to the ones for the NSS test, **Figure 10a**.

In the AM50 weld metal of the AZ31 magnesium joint, a notable amount of pores appeared. They had no significant influence on the corrosion behaviour during the FS test. **Figures 17a** and **b** shows shallow pitting corrosion as well as crevice corrosion at the cold weld edge after 240 h. These results are less critical than those related to the strong localized corrosion in the NSS test.
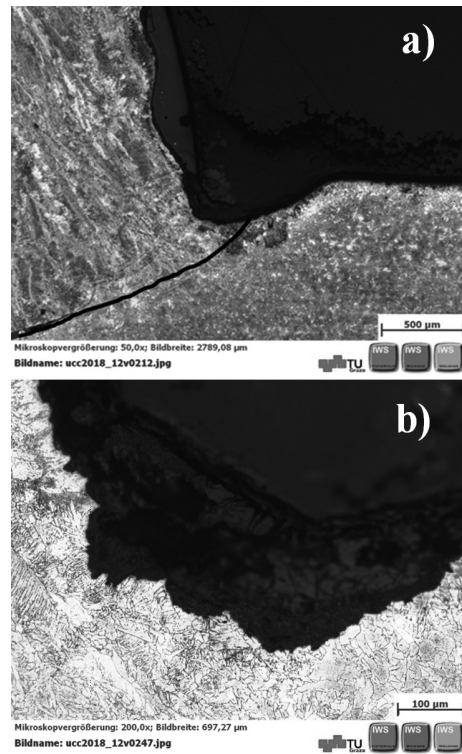
Figure 16: Welded DD11-steel joint details – corrosion after the FS test: a) 240 h; b) 480 h, G3Si1 weld metal
Slika 16: Detajli zvarjenega spoja DD11-jekla; korozija po FS-preizkusu; a) 240 h; b) 480 h G3Si1 zvar
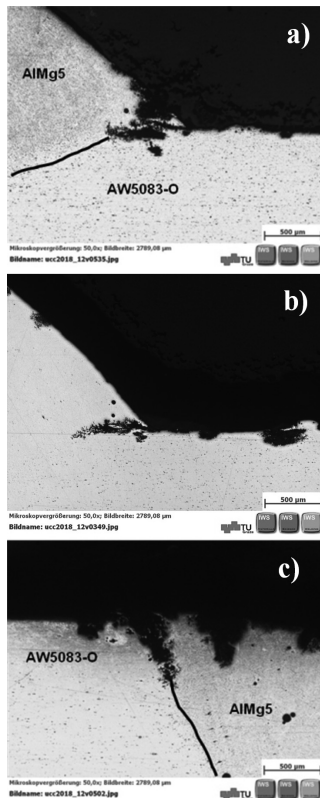
Figure 15: Welded AW5083-O joint cross sections in LOM/corrosion after the FS test: a) 240 h; b) 480 h, lower weld edge; c) 480 h, upper weld edge (see **Figure 8**)
Slika 15: Prečni prerez zvarjenega spoja AW5083-O, svetlobna mikroskopija (LOM); korozija po FS-preizkusu: a) 240 h; b) 480 h, spodnji rob zvara; c) 480 h, zgornji rob zvara (glej **sliko 8**)
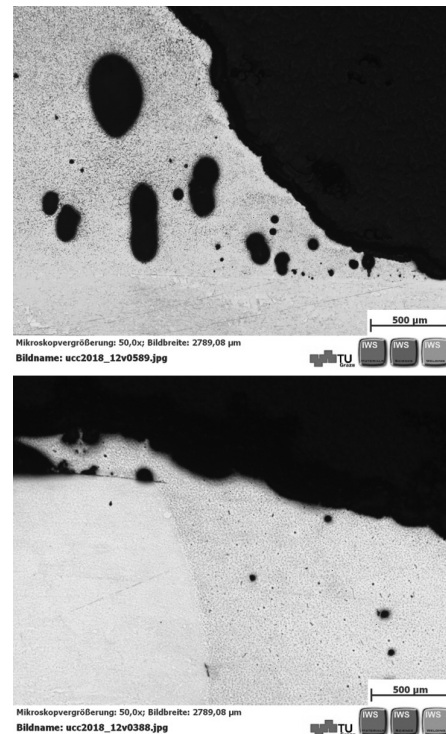
Figure 17: Welded AZ31 joint, grinded – AM50 weld metal details/ corrosion after the 240 h NSS test: a) lower weld seam; b) upper weld seam
Slika 17: Spoj zvarjenega AZ31, brušeno – detajl AM50 zvara; korozija po 240 h NSS-preizkusa: a) spodnji šiv zvara; b) zgornji šiv zvara

3.3 Corrosion influence on the welded-joint strength

The tensile-shear test results before and after the corrosion testing are shown in **Figures 18a** and **b**. The fracture forces were recorded and standardized with the initial cross-sectional area (50 mm × 3 mm and 50 mm × 2.5 mm for AW6181-T4). The fracture location for all the welded shear- test samples runs along the fusion line. In the as-welded condition, the DD11 and DD13 steels had the highest weld strength (352 MPa and 298 MPa). The difference is due to the lower carbon content of DD13. AW5083-O samples show a weld strength of 274 MPa and AW6181-T4 a strength of 113 MPa. Magnesium AZ31 has the lowest weld strength that is 104 MPa. Considering the influence of the corrosion time and corrosive medium, the following can be observed:

NSS test

The DD13-steel weld showed a 12 % drop in the strength, to 309 MPa, and the DD11 weld strength depletes even by 26 %, to 222 MPa, after the 480 h NSS test. In contrast, no loss in the strength was found for both aluminium alloys. Due to the severe corrosion attack, the strength of the magnesium AZ31/AM50 weld joint decreased significantly, by 78 %, down to 23 MPa, **Figure 18a**.
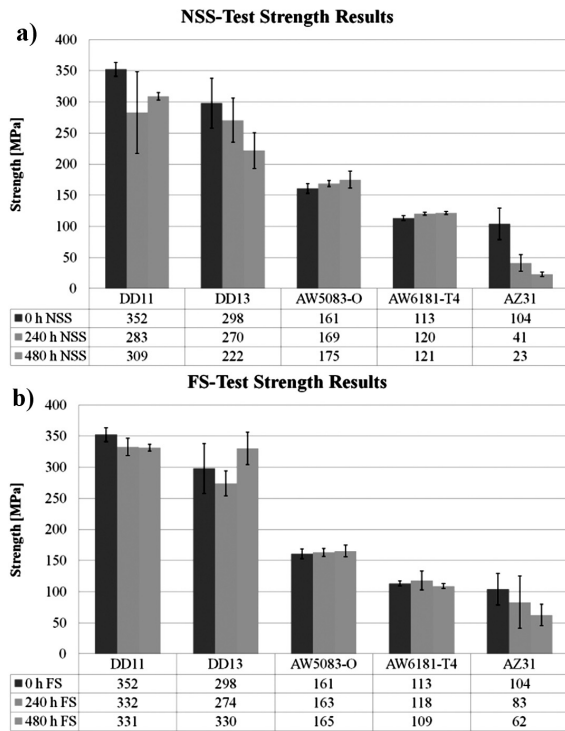
FS test

The DD11-steel weld strength decreased to a value of 331 MPa (–6 %). However, for DD13 no loss of strength

was detected. Also, for the AW5083-O/AlMg5 and AW6181-T4/AlSi5 weld joints no effect of corrosion occurred after 480 h. The weld strength of AZ31 decreased sharply to 62 MPa (–40 %), **Figure 18b**.

3.4 Approximation of the base-material-corrosion mass losses and rates

Weight measurements were performed on the 50 mm × 100 mm base-material samples, see results in **Figure 19**. To calculate the mass loss per unit area (g/m^2) Formula 1 was used. Therefore, the chemical composition of the resulting corrosion products (Me$_n$X$_m$) on the sample surfaces must be known. Their respective compositions from the literature are Fe$_2$O$_3$ for iron[41], Al$_2$O$_3$ for aluminum[10,42] and Mg(OH)$_2$ for magnesium[8]. According to DIN 50905, part 2[43], the mass loss per unit area and the corrosion rate can be calculated for the supposed uniform surface corrosion. It must be noted that the aluminum samples showed irregular or localized corrosion. For pitting corrosion, selective corrosion and intergranular corrosion, DIN 50905, Part 3[44] describes the evaluation of the corrosion samples by determining the thinning. But in order to obtain comparability for all the tested materials, a simplified uniform surface corrosion was presumed. Applying Formula 2 and Formula 3, the material-loss rates can be calculated[43]. The mass-loss rate per unit area was calculated with difference m_a from mass loss m_a at time t_n reduced by the mass loss of the previous evaluation time $t_{(n-1)}$.

$$m_a = \frac{-\Delta m}{A} = \frac{+\Delta m}{A} \cdot \frac{n \cdot A_{r,Me}}{m \cdot A_{r,X}}$$

Formula 1: Mass loss per unit area [17]

$$v_{diff} = \frac{dm_a}{dt}$$

Formula 2: Mass-loss rate per unit area (g/m^{2}h) [43]

$$w_{diff} = 8.76 \cdot \frac{v_{diff}}{\rho}$$

Formula 3: Corrosion rate (mm/a) [43]

Legend:

m_a… Mass loss per unit area (g/m^2)

$-\Delta m$… Mass loss (g)

$+\Delta m$… Mass increase (g)

A… Surface (m^2)

$n*A_{r,Me}$… $n \cdot$ relative atomic mass of corrosion product Me$_n$X$_m$

$m \cdot A_{r,X}$… $m \cdot$ relative atomic mass of non-metal X (oxygen) in composition Me$_n$X$_m$

v_{diff}… Mass loss rate per unit area (g/m^{2}h)

dm_a… Differential mass loss per unit area (g/m^2)

dt… Differential time between single tests (h)

ρ… Base material density (g/cm^3)

The calculation results are the following:

NSS-Test Strength Results

a)

	DD11	DD13	AW5083-O	AW6181-T4	AZ31
0 h NSS	352	298	161	113	104
240 h NSS	283	270	169	120	41
480 h NSS	309	222	175	121	23

FS-Test Strength Results

b)

	DD11	DD13	AW5083-O	AW6181-T4	AZ31
0 h FS	352	298	161	113	104
240 h FS	332	274	163	118	83
480 h FS	331	330	165	109	62

Figure 18: Welded-joint strength over the corrosion testing time; a) NSS; b) FS test

Slika 18: Trdnost zvarjenega spoja v odvisnosti od časa korozijskega preizkušanja; a) NSS-; b) FS-preizkus

3.4.1 NSS test

In **Figure 19a** the mass gains of all the examined materials during the period of 480 h are shown. Four samples were evaluated for each base material. Non-grinded magnesium AZ31 (line 6) initially shows the highest mass increase. After 240 h the mass decreases due to the loss in the corrosion product. The mass increase in the grinded AZ31 samples (line 5) is much lower and even below the steel mass increase. The DD11 (line 3) and DD13 (line 4) steels show the same mass gain up to 96 h. Thereafter, DD13 corrodes more significantly. Aluminium AW5083-O (line 1) and AW6181-T4 (line 2) tend towards pitting and intergranular corrosion, causing very low mass gains.

3.4.2 FS test

In **Figure 19b** the mass loss over the testing time for all the tested materials is exhibited. It can be seen that AZ31 (line 5) and DD13 (line 4) are forming adherent corrosion layers up to 2 h. All the other materials (AW6181-T4, AW5083-O and DD11) show neither an increase nor a decrease. Up to 24 h all the samples gain weight due to the formation of corrosion products. Afterwards, until the test end, a steady weight loss for all the samples is observed (except for the AW5083-O increase up to 48 h). After 48 h steels DD11 (line 3) and DD13 (line 4) sustain a strong weight loss, i.e., approxi-

mately 1.25 g. By comparison, the 0.3 g weight losses in the aluminium alloys are quite low. The weight loss in AZ31 after 480 h amounts to 0.45 g. While drying the AZ31 samples, flaky corrosion products fall off the samples that cannot be included in the mass loss.

3.4.3 Mass loss per unit area – the NSS test

The standardized mass losses after 240 h for steels DD13 ($1250 \ g/m^2$ – line 4), DD11 ($1000 \ g/m^2$ – line 3) and non-grinded magnesium AZ31 ($800 \ g/m^2$ – line 6) progress relatively linear, **Figure 20a**. At 480 h the corrosion for DD11 decreases stronger than for DD13. Non-grinded AZ31 shows a negative mass loss after 480 h due to the corrosion product falling off. The grinded AZ31 (line 5) shows a constant and much lower mass loss of just corrosion until the test end, whereat the corrosion product adheres on the sample due to the low surface roughness. AW5083-O (line 1) and AW6181-T4 (line 2) show a very low mass loss as expected.
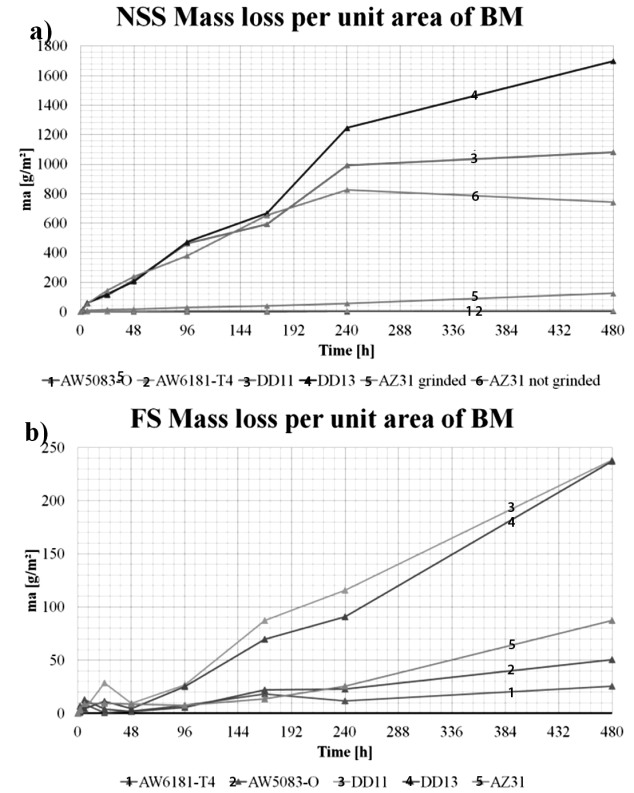
3.4.4 Mass loss per unit area – the FS test

Figure 20b shows that steels DD11 (line 3) and DD13 (line 4) have the highest mass loss. From 96 h onwards the loss increases quite linearly up to approximately $240 \ g/m^2$ after 480 h. For the materials AW6181-T4 ($25 \ g/m^2$), AW5083-O ($50 \ g/m^2$) and AZ31 ($87 \ g/m^2$) the mass loss is considerably lower.
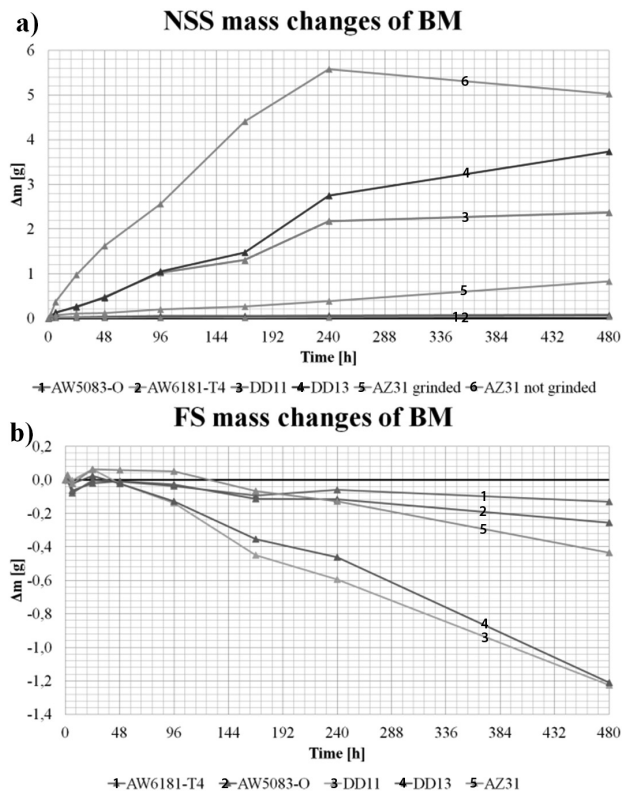
Figure 19: Base-material mass changes over the 480 h test period, a) NSS test b) FS test

Slika 19: Spreminjanje mase osnovnega materiala med preizkusom 480 h, a) NSS-preizkus b) FS-preizkus

Figure 20: Mass loss per unit area over the 480 h test period: a) NSS test, b) FS test

Slika 20: Zmanjšanje mase na enoto površine med preizkusom 480 h; a) NSS-preizkus, b) FS-preizkus

3.4.5 Corrosion rate – the NSS test

For the steels at the beginning of the NSS test, the corrosion rates are quite high, i.e., around 12 mm per year at instant 6 h. The non-grinded magnesium AZ31 exhibits a tremendous corrosion rate of 52 mm per year, but the grinded AZ31 shows just 8.4 mm per year. To the contrary, the aluminium alloys show low or immeasurable corrosion rates (AW6181-T4: 2.2 mm per year; AW5083-O: 0.0 mm per year) at instant 6 h. By continuing the test, the corrosion rates decrease more or less to 240 h and fall down further at instant 480 h for all the materials, **Figure 21a**. The reason for these materials' passivation is probably the adherent corrosion products on the sample surfaces acting as corrosion barriers. At the end of the NSS test, the steels (0.6 and 2 mm per year for DD11 and DD13) have the highest and the aluminium alloys (AW5083-O and AW6181-T4, each having 0.04 mm per year) the lowest corrosion rate, see **Table 3**.

3.4.6 Corrosion rate – the NSS test

The maximum corrosion rates were found at instant 6 h for AW6181-T4 (13 mm per year), AW5083-O (10 mm per year), AZ31 (5.6 mm per year) and DD13 (0.9 mm per year). Steel DD11 (1.5 mm per year) shows its maximum at instant 24 h. Thereafter, the corrosion rates of the Al and Mg alloys fall significantly and only slightly

Figure 21: Corrosion-rate behaviour over the 480 h test period: a) NSS test b) FS test
Slika 21: Spreminjanje hitrosti korozije med preizkusom 480 h: a) NSS-preizkus, b) FS-preizkus

for the steels. At the end of the FS test AW6181-T4 (0.2 mm per year) and AW5083-O (0.3 mm per year) show the lowest corrosion rate. On the other hand, DD11 (0.5 mm per year) and DD13 (0.7 mm per year) have a significantly higher rate and AZ31 (1.4 mm per year) has the highest rate, **Figure 21b** and **Table 3**.

4 DISCUSSION

The type of corrosion in the salt spray test (NSS test) and fruit acid test (FS test) is as follows:

Aluminium alloys exhibit localized corrosion. It is notable that the progress in pitting for AW5083-O and intergranular corrosion for AW6181-T4 is reduced during the testing time.

The grinded magnesium alloy AZ31 shows a stronger tendency for localized corrosion in the FS test than in the NSS test. The non-grinded AZ31 is not applicable as a very heavy corrosion attack appears.

The corrosion behaviours of deep-drawing steels DD11 and DD13 are quite similar. In the NSS test mainly uniform corrosion or shallow pitting arises and in the FS test a partial pitting corrosion is observed.

Note that the mass changes due to the corrosion in the NSS test for the steels and magnesium alloy are two to three times higher than in the FS test. Because of the localized-corrosion behaviour of aluminium alloys their mass change is marginal. Similarly, the corrosion rates at certain testing times in the NSS test are multiple compared to the FS test for the steels, **Table 3**.

It is remarkable that in the NSS test adherent corrosion layers are formed on all the materials and the samples gain in weight. In contrast, the corrosion products drain off in the FS test making the samples lose weight.

The corrosion behaviour of the welded joint AW5083-O in the NSS and FS tests is similar. Here the pitting and localized corrosion was found at the fusion line and also at the weld edges on the AlMg5 weld metal. Amazingly, the AW6181-T4 welded joints showed no corrosion at the fusion line or on the AlSi5 weld metal, but just the IG corrosion on the base material.

The corrosion attack on the AZ31 magnesium welded joint was stronger in the NSS test than in the FS. In the former a strong and partially localized corrosion on the AM50 weld metal and on the base material occurred. In the latter only shallow pitting corrosion was found.

The welded steel joints showed an intense corrosion attack at the fusion line in the NSS and FS tests. The corrosion of the G3Si1 weld metal was selective in NSS and took the form of shallow pitting corrosion in the FS test.

The degradation of the tensile-shear strength of the steel welding joints is stronger in the NSS (up to 25 %) than in the FS test. Due to a very high strength loss of the AZ31 magnesium this joint is not applicable. It is a
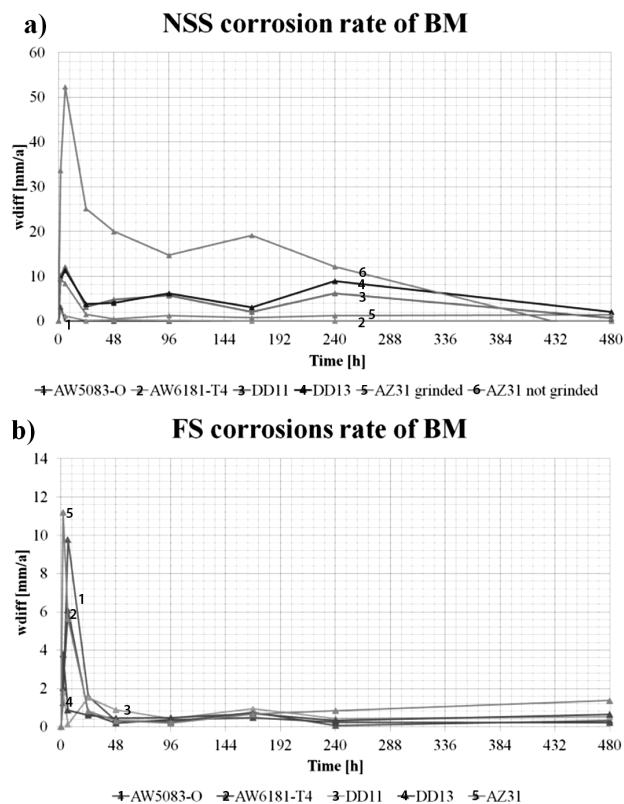
Table 3: Comparison of the mass-loss rates v/(g/(m^2 h)) and corrosion rates w/mm per year in the NSS and FS test intervals
Tabela 3: Primerjava hitrosti izgube mase v/(g/(m^2 h)) in korozijska hitrost w/mm na leto pri NSS- in FS-intervalih preizkušanja

Material	Neutral salt spray test (NSS test)						Fruit acid spray test (FS test)					
	96–168		168–240		240–480		96–168		168–240		240–480	
	v g/(m^2 h)	w (mm/y)	v g/(m^2 h)	w (mm/y)	v g/(m^2 h)	w (mm/y)	v g/(m^2 h)	w (mm/y)	v g/(m^2 h)	w (mm/y)	v g/(m^2 h)	w (mm/y)
DD11	1.80	2.01	5.53	6.16	0.54	0.60	0.84	0.94	0.39	0.44	0.47	0.52
DD13	2.71	3.02	8.01	8.91	1.85	2.06	0.62	0.69	0.29	0.33	0.58	0.65
AW5083-O	0	0	0.02	0.05	0.01	0.04	0.23	0.76	0.02	0.07	0.1	0.33
AW6181-T4	0.01	0.02	0.02	0.07	0.01	0.04	0.15	0.48	0.07	0.24	0.07	0.22
AZ31	0.14	0.73	0.24	1.22	0.27	1.35	0.13	0.66	0.17	0.84	0.27	1.37

benefit of aluminium alloys that they show no influence of corrosion on the welding-joint strength.

5 CONCLUSIONS

Basically, the results of this investigation program allow a technical comparison between the influences of the two relevant corrosion media on the household cooling compressor shells.

The currently used deep-drawing steels cannot be used without an anti-corrosion coating (KTL). Due to a low strength and even a poor corrosion resistance, it is not advisable to use AZ31 as a housing material for household cooling compressors.

The overall result regarding weldability, corrosion resistance and joint strength proves that aluminium alloys can bring improvements to the future compressor shells.

6 REFERENCES

[1] ceced. New EU Energy Labelling and Ecodesign Measures, Brüssel ceced, 2009

[2] Amtsblatt der Europäischen Union, Richtlinie 2010/30/EU des Europäischen Parlaments und des Rates, Brüssel s.n., 2010

[3] Voestalpine, Technische Lieferbedingungen: Weiche, unlegierte Stähle zum Kaltumformen, 2011, www.voestalpine.com/stahl

[4] M. Reuter, Methodik der Werkstoffauswahl- Der systematische Weg zum richtigen Material, Carl Hanser Verlag, München 2007

[5] DVS 0913, DVS Merkblatt 0913, Deutscher Verband der Schweißtechnik, Düsseldorf 1994

[6] J. R. Davis, Aluminum and aluminium alloys, ASM International, vol. 3, Materials Park, Ohio 1994

[7] Böhler welding, Wissenswertes für den Schweißer, Böhler welding, Kapfenberg 09/2010, 2–28

[8] C. Kammer, Magnesium Taschenbuch; 1. Auflage, Aluminium-Verlag, Düsseldorf 2000, 289, 558

[9] Elisental, 10 Juli 2012. [Cited: 10 Juli 2012.] http://www.elisental.de.

[10] F. Ostermann, Anwendungstechnologie Aluminium: 2. neu bearbeitete und aktualisierte Auflage, Springer, Berlin, Heidelberg, New York 2007, 246

[11] Safra, aluminium-copper welding alloys wires & rods, 2012

[12] S. Häuselmann, Magnesium-Halbzeug, 25 Juni 2012, [Cited: 12 Juni 2012.] http://www.haeuselmann.ch.

[13] K. Kerschbaumer et al., (ed.), Das Korrosionsverhalten von MIG-geschweißten Aluminium-Blechen Al5083 und Al6181 im Neutral-Salzsprühnebeltest und die Auswirkung auf die Verbindungsfestigkeit, DVS Congess 2012, Saarbrücken, 2012

[14] EN ISO 9018:2006, Zerstörende Prüfung von Schweißverbindungen an metallischen Werkstoffen – Zugversuch am Doppel-T-Stoß und Überlappstoß, Österreichisches Normungsintitut, Wien 2006

[15] ÖNORM EN ISO 9227, Korrosionsprüfungen in künstlichen Atmosphären – Salzsprühnebelprüfungen, Österreichisches Normungsinstitut, Wien 2006

[16] DIN 8985, Oberflächenprüfung an anschlussfertigen Kühl- und Gefriergeräten, Österreichisches Normungsinsitut, Wien 1983

[17] DIN 50905 Teil 1, Korrosion der Metalle – Korrosionsuntersuchungen-Teil 1, Beuth Verlag GmbH, Berlin 2009, 8

[18] F. Tödt, Korrosion und Korrosionsschutz, 2. Auflage, Walter de Gruyter & Co, Berlin 1961, 143–148, 416–418, 443, 1087

[19] E. Wendler-Kalsch, H. Gräfen, Korrosionsschadenkunde, Springer Verlag, Erlangen 1998, 63, 91–95

[20] K. H. Tostmann, Korrosion – Ursachen und Vermeidung, Wiley – VCH Verlag GmbH, Weinheim 2000, 34, 68–77

[21] G. Schulze, Die Metallurgie des Schweißens, 3., neubearbeitete und erweiterte Auflage, Springer, Berlin 2003, 118, 541

[22] F. Ostermann, Anwendungstechnologie Aluminium: 2. neu bearbeitete Auflage, Meckenheim, Springer, Berlin Deidelberg New York, 2007, 232–248

[23] H. J. Bargel, Werkstoffkunde, 10. bearbeitete Auflage, Springer Verlag, Berlin Heidelberg 2008, 292

[24] C. Kammer, Aluminium Taschenbuch Bd. 1, 16. Auflage, Aluminium Verlag, Düsseldorf 2002, 423

[25] G. E. Totten, D. S. MacKenzie, Handbook of Aluminium, Volume 1, Physical Metallurgy and Processes, Marcel Dekker, Basel 2003, 429

[26] A. Aballe, M. Bethencourt, F. J. Botana, M. J. Cano, M. Marcos, Localized alkaline corrosion of alloy AA5083 in neutral 3.5% NaCl solution, Corrosion Science, 43 (**2001**) 9, 1657–1674

[27] A. Aballe, M. Bethencourt, F. J. Botana, M. Marcos, J. M. Sanchez-Amaya, Influence of the degree of polishing of alloy AA 5083 on its behaviour against localised alkaline corrosion, Corrosion Science, 46 (**2004**) 6, 1909–1920

[28] G. E. Totten, D. S. MacKenzie, Handbook of Aluminium, Volume 2, Alloy Production and Materials Manufacturing, Marcel Dekker Inc., New York, Basel 2003, 435–437

[29] J. R. Davis, Aluminum and aluminium alloys, ASM International, Materials Park, Ohio 1994, Bd. 3., 582

[30] E. Ghali, Corrosion Resistance of Aluminium and Magnesium Alloys, John Wiley & Sons Inc., Hoboken, New Jersey 2010, 171

[31] J. R. Davis et al., ASM Handbook Vol. 2: Poperties and Selection: Nonferrous Alloys and Special-purpose Materials, ASM, USA 2007, 582

[32] W. Hufnagel, Aluminium Taschenbuch, 14. Auflage, Aluminium Verlag, Düsseldorf 1983, 137, 177

[33] R. A. Cottis et al., Shreir's Corrosion forth Edition, Volume 3, Corrosion and degradation of engineering materials, Elsevier, Manchester 2010, 1992, 2025

[34] G. Svenningsen et al., Effect of high temperature heat treatment on intergranular corrosion of AlMgSi(Cu) modell alloy, Corrosion Science, 48 (**2006**), 258–272

[35] G. Svenningsen et al., Effect of low copper content and heat treatment on intergranular corrosion of model AlMgSi alloys, Corrosion Science, 46 (**2006**), 226–242

[36] C. Kammer, Magnesium Taschenbuch; 1. Auflage, Aluminium-Verlag, Düsseldorf 2000, 289

[37] H. Schumann, H. Oettel, Metallografie, 14. Auflage, Wiley-VCH Verlag, Weinheim 2005, 338

[38] K. U. Kainer, Magnesium – Eigenschaften, Anwendungen, Potentiale, Wiley-VCH-Verlag, Weinheim 2000, 238

[39] J. M. Sanchez-Amaya, T. Delgado, L. Gonzalez-Rovira, F. J. Botana, Laser welding of aluminium alloys 5083 and 6082 under conduction regime, Applied Surface Science, 255 (**2009**) 23, 9512-9521

[40] K. Mutombo et al., Corrosion Fatigue Behaviour of Aluminium 5083-H111 Welded Using Gas Metal Arc Welding Method, South Africa, CSIR / University of Pretoria South Africa, 2011

[41] M. Pourbaix, Atlas of Electrochemical Equilibria in Aqueous Solutions, Second English Edition. s.l., Cebelcor Verlag, 1974, 314

[42] H. Göner, S. Marx, Aluminium Handbuch. s.l., VEB Verlag Technik, Berlin 1969

[43] DIN 50905 Teil 2, Korrosion der Metalle-Korrosionsuntersuchungen-Teil 2, Beuth Verlag GmbH, Berlin 1987

[44] DIN 50905 Teil 3, Korrosion der Metalle-Korrosionsuntersuchungen – Teil 3, Beuth Verlag GmbH, Berlin 1987

WATER-VAPOUR PLASMA TREATMENT OF COTTON AND POLYESTER FIBRES

OBDELAVA BOMBAŽNIH IN POLIESTRSKIH VLAKEN S PLAZMO VODNE PARE

Jelena Vasiljević[1], Marija Gorjanc[1], Rok Zaplotnik[2], Alenka Vesel[2], Miran Mozetič[2], Barbara Simončič[1]

[1]Department of Textiles, Faculty of Natural Sciences and Engineering, University of Ljubljana, Aškerčeva 12, 1000 Ljubljana, Slovenia
[2]Department of Surface Engineering and Optoelectronics, Jožef Stefan Institute, Jamova cesta 39, 1000 Ljubljana, Slovenia
marija.gorjanc@ntf.uni-lj.si, barbara.simoncic@ntf.uni-lj.si

This study deals with the treatment of cotton and polyester fibres with a low-pressure, inductively coupled RF plasma, in which the water vapour from the fibres was used as a plasma-forming gas. Cotton, which is a hydrophilic, natural, cellulose fibre and polyester, which is a hydrophobic, synthetic, polyethylene terephthalate fibre, were used. Plasma characteristics during the treatment were investigated using optical emission spectroscopy (OES). The morphological and chemical changes in the fibre surfaces induced by plasma treatment were analysed using atomic force microscopy (AFM), scanning electron microscopy (SEM) and X-ray photoelectron spectroscopy (XPS). The optical emission spectra showed the presence of OH and H radicals at the beginning of the plasma treatment, whereas a CO Angstrom band appeared in the spectra recorded during the plasma treatment of both fibres. The cotton fibre roughness showed a three-fold increase after the plasma treatment that increased the surface area by approximately 8 %. The changes in the polyester fibre roughness were much less distinct and the surface area increased by approximately 3 %. The plasma treatment induced an increase in the O/C atomic ratio by approximately 43 % for cotton and 56 % for polyester fibres. The etching action of the water-vapour plasma was thus found to be more effective on the surface of cotton fibres than on polyester fibres. However, the water content of polyester fibres was sufficiently high to cause an oxidation of the fibre surface that was even higher than the oxidation of cotton.

Keywords: water-vapour plasma, effectiveness of treatment, cotton, polyester, water content, morphological and chemical changes

Raziskava vključuje obdelavo bombažnih in poliestrskih vlaken z nizkotlačno induktivno sklopljeno RF-plazmo vodne pare. Izvir vodne pare kot delovnega plina so bila vlakna bombaža, predstavnika hidrofilnih naravnih celuloznih vlaken, in vlakna poliestra, predstavnika hidrofobnih sintetičnih polietilenteraftalnih vlaken. Lastnosti plazme med obdelavo tekstilnih vzorcev so bile preiskane z optično emisijsko spektroskopijo (OES). Morfološke in kemijske spremembe površin plazemsko obdelanih vlaken so bile analizirane z mikroskopijo na atomsko silo (AFM), z vrstično elektronsko mikroskopijo (SEM) in rentgensko fotoelektronsko spektroskopijo (XPS). Optični emisijski spektri so na začetku obdelave s plazmo pokazali prisotnost OH in H radikalov. Med plazemsko obdelavo obeh vrst vlaken so bili v optičnih emisijskih spektrih opazni tudi trakovi, ki izvirajo iz prehodov radikalov CO. Po obdelavi s plazmo se je hrapavost površine bombažnega vlakna trikrat povečala, kar je vplivalo na povečanje specifične površine za približno 8 %. Spremembe v hrapavosti so bile pri poliestrskem vlaknu manj izrazite, specifična površina vlaken se je povečala za približno 3 %. Po obdelavi s plazmo se je na površini obeh vrst vlaken povečalo razmerje O/C, in sicer za 43 % pri bombažu in za 56 % pri poliestru. Glede na vsebnost vode v tekstilnih vzorcih je imela obdelava s plazmo vodne pare večji učinek jedkanja na bombažnih kot na poliestrskih vlaknih. Kljub temu je poliester vseboval dovolj vodne pare, da se je površina vlaken v plazmi oksidirala. Oksidacija na poliestru je bila celo večja kot na bombažu.

Ključne besede: plazma vodne pare, učinkovitost obdelave, bombaž, poliester, vsebnost vode, morfološke in kemijske spremembe

1 INTRODUCTION

Non-equilibrium gaseous plasma is a unique technology for treating the surfaces of fibrous polymers without affecting their bulk properties.[1–9] Accordingly, plasma systems using different power sources, pressures, electrode configurations and gasses have been used to generate plasma discharges and treat polymers.[10–20] Oxygen-containing plasma increases the specific surface area and surface energy of polymers, which results in an incorporation of oxygen-containing groups, such as C–O, O–C=O and C=O.[21–26] Plasma discharges in water vapour can potentially be used in a wide range of applications.[27–32] Water-vapour plasma is superior to the other plasma-forming gasses because of its unique properties, i.e., an extremely high enthalpy, environmentally

safe conditions, a relatively low cost and an endless amount of plasma-forming gas.[33] Water-vapour plasma generates a high concentration of OH radicals that can further dissociate to H and O radicals,[34–36] although the probability of a dissociation of OH radicals is lower than that of a dissociation of water molecules (some of the OH radicals remain undissociated).[36] The first effect of a plasma treatment is the functionalization of the polymer surface, which is followed by etching reactions. These reactions are initiated by an H-atom abstraction and formation of a free radical.[35,37–40]

Cotton and polyester are the two most important and widely used polymers in the textile industry. They differ from each other in their chemical and morphological structures, and the amounts of water content. There are several publications dealing with the influence of diffe-

rent plasma discharges on the surface properties of cotton or polyester, but these two polymers were rarely investigated together under the same plasma parameters. The aim of this study was to investigate the surface changes of cotton and polyester after a treatment with water-vapour plasma under the same plasma parameters. The water vapour from the fibres was used as a plasma-forming gas. The low-pressure plasma was chosen as an environmentally friendly (pre)treatment of the textiles, water vapour was chosen as an environmentally safe and cheap plasma-forming gas that is already present in the fibres, and the same plasma parameters were chosen to investigate the surface changes occurring on the two different yet most commonly used polymers. Additionally, plasma treatment was observed using OES, where the optical spectra were recorded during the treatment of textiles. The changes to the fibre surfaces were investigated using SEM, AFM and XPS analyses.

2 EXPERIMENTAL WORK

2.1 Materials and methods

Scoured, bleached and mercerised cotton woven fabric (119 g/m^2) made by Tekstina, d. d., Ajdovščina, and washed polyester woven fabric (67 g/m^2) made by Velana, d. d., Ljubljana, were used in the study.

Low-pressure, inductively coupled, radiofrequency (RF) plasma was used for the treatment. Our RF reactor scheme was previously presented in detail.[27] The plasma was created using a fixed frequency of 27.12 MHz, an output power of approximately 5 kW, a pressure of 20 Pa and a current of 0.4 A. Water vapour was used as a working gas. The fabric was the source of the water vapour. The fabric samples were treated for 30 s.

2.2 Analyses and measurements

The water content of the fabric samples was determined according to the standard SIST ISO 6741-1:1996.

The plasma treatments were observed using optical emission spectrometry. An Avantes AvaSpec-3648 optical spectrometer with a 3648-pixel CCD detector array and a 75 cm focal length was used. This spectrometer records the optical emission spectra in the wavelength range of 200–1100 nm with a resolution of 0.5 nm.

The sample morphology was evaluated using a JEOL JSM 6060 LV scanning electron microscope. The samples were coated with a thin layer of gold before observation.

The sample surface topography was evaluated using an atomic force microscope (AFM/MFM – Veeco Dimension 3100) in the contact mode. Surface scans of 1 μm^2 square areas were performed at 22 °C in atmosphere for different sample positions using a scanning rate of 1.51 Hz. Images with a resolution of 256 × 256 lines were obtained using the Nanoscope software with a Flatten filter. From the AFM analyses, the mean rough-

ness (R_a; the arithmetic average of the deviation from the centre plane), root-mean-square roughness (R_{ms}; the standard deviation of the Z-value within a given area) and surface area (SA; a three-dimensional given region) were calculated as the mean values of 10 AFM scans of different sample regions. The standard error of the mean was calculated to perform statistical analyses.

The sample-surface chemical compositions were analysed with X-ray photoelectron spectroscopy using a PHI-TFA XPS spectrometer (Physical Electronics Inc). The analysed areas had a diameter of 0.4 mm and a depth of approximately 3–5 nm. The sample surfaces were excited with the X-ray radiation from a monochromatic Al K_{α} source at a photon energy of 1486.7 eV. The sample-surface chemical compositions were quantified on the basis of the XPS peak intensities measured for two different spots on the sample using the MultiPak v7.3.1 software from Physical Electronics that was supplied with the spectrophotometer.

3 RESULTS AND DISCUSSION

Inductively coupled RF plasma excited at the ultimate pressure emitted the spectra shown in **Figure 1**. As water remained in the samples, the residual atmosphere was mostly water vapour. Therefore, hydrogen emission lines were the main lines that were visible in the optical emission spectra recorded at the beginning of the treatment (**Figure 1**).

Hydrogen is a good emitter of radiation, which is why the intensities of the Balmer series emission lines are so high. Water molecules dissociate into the hydrogen and oxygen atoms, but in the OES spectra of the inductively coupled plasma at the ultimate pressure, the oxygen lines are not present, whereas the excitation energy of oxygen atoms is much higher than the excitation energy of hydrogen atoms. Nitrogen emission bands are
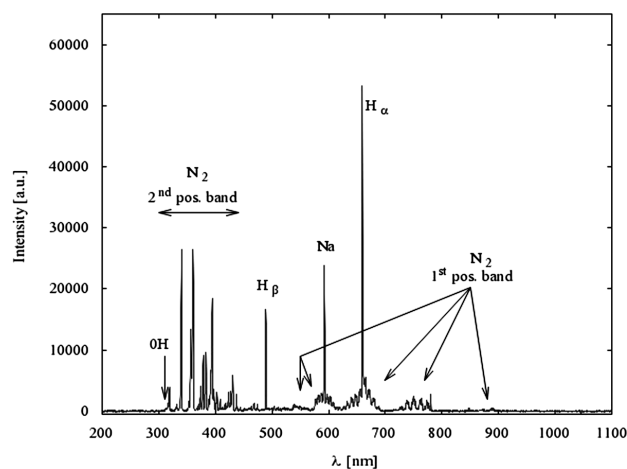
Figure 1: OES spectra of the plasma, generated at the ultimate pressure before etching
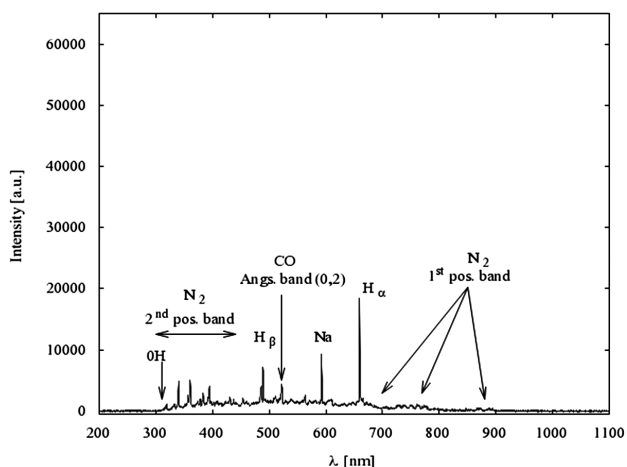**Slika 1:** OES-spektri plazme, ustvarjene pri končnem tlaku pred jedkanjem
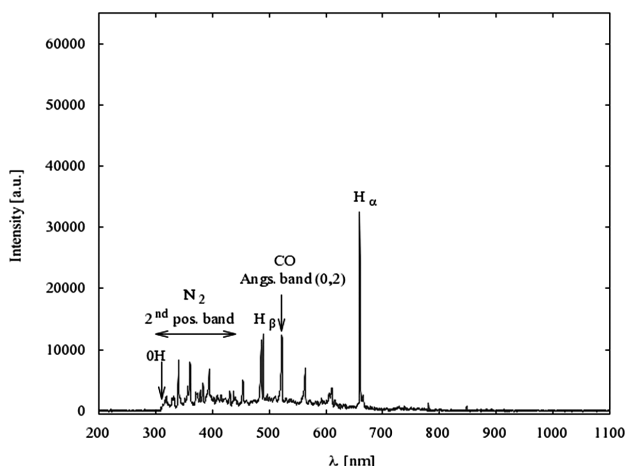
Figure 2: OES spectra of the plasma during the etching of cotton
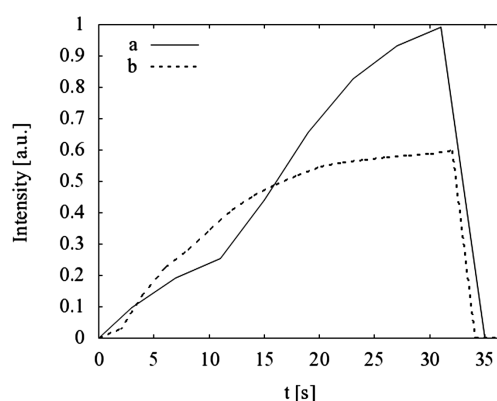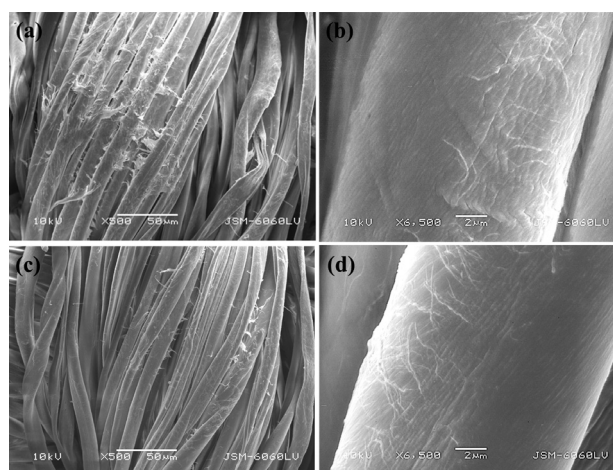**Slika 2:** OES-spektri plazme med jedkanjem bombažnega vzorca

Figure 4: Time evolution of the CO emission peak (519 nm), normalised with the H_β line during the treatment of: a) cotton and b) polyester
Slika 4: Časovni razvoj emisije vrha CO (519 nm), normaliziranega s H_β-črto, med obdelavo vzorca: a) bombaž, b) poliester

present in the spectra because of the small leakages in the system.

The optical spectra recorded during the treatment of the samples (**Figures 2** and **3**) revealed several CO Angstrom-band emission lines as well as a broad continuum between 400 nm and 700 nm that most likely resulted from a partial overlapping of the radiative transitions within CO molecules. The CO emission lines are attributed to the etching of the cotton and polyester samples. OES is a qualitative technique and, therefore, the density of particles cannot be determined from these measurements. However, CO is a poor emitter and from the high CO emission lines, we can conclude that the etching was efficient.

The time evolution of the etching was recorded after the CO Angstrom band (0, 2) emission peak was observed. To eliminate the effects of different spectrometer optical-fibre positions, the CO emission line (519 nm) was normalised with the H_β line. The time evolution of

the normalised CO emission line during the sample treatment is presented in **Figure 4**.

Better etching was achieved for the cotton samples when compared with the polyester samples. The etching rate for both samples increased monotonically with time. This etching increase was attributed to the thermal effects: the samples underwent heating during the treatment that increased the etching rate.

The etching effects of the water-vapour plasma treatment were further examined using SEM and AFM analyses. The SEM images of cotton and polyester fibres before and after the plasma treatment are presented in **Figure 5**. Under the used plasma parameters, the impurities on the cotton surface were cleaned and removed (**Figures 5a** and **c**). The same plasma parameters did not induce such changes to the polyester surface (**Figures 6a** and **c**). The plasma treatment did not cause any visible

Figure 3: OES spectra of the plasma during the etching of polyester
Slika 3: OES-spektri plazme med jedkanjem poliestrskega vzorca

Figure 5: SEM images of: a), b) untreated cotton and c), d) plasma-treated cotton fibres; 500-times magnification was used for a) and c), 6500-times magnification for b) and d)
Slika 5: SEM-posnetki vlaken: a), b) neobdelanega bombaža ter c), d) s plazmo obdelanega bombaža; a) in c) 500-kratna povečava in b) in d) 6500-kratna povečava
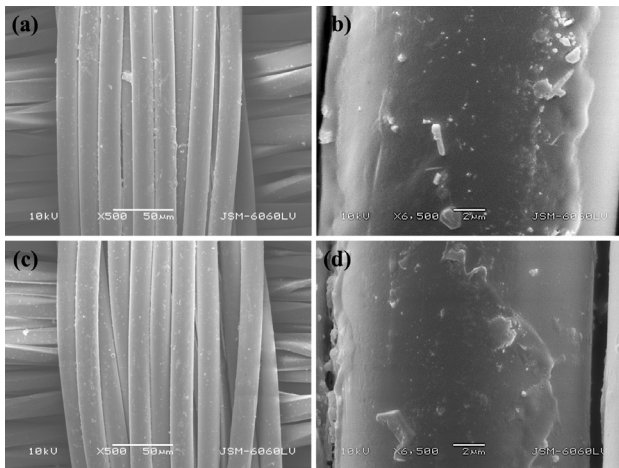
Figure 6: SEM images of: a), b) untreated polyester and c), d) plasma-treated polyester fibres; 500-times magnification was used for a) and c), 6500-times magnification for b) and d)
Slika 6: SEM-posnetki vlaken: a), b) neobdelanega poliestra ter c), d) s plazmo obdelanega poliestra; a) in c) 500-kratna povečava in b) in d) 6500-kratna povečava

morphological surface changes on cotton (**Figures 5b** and **d**) or on polyester fibres (**Figures 6b** and **d**), indicating that the bulk properties of both types of fibres remained unchanged.

AFM analyses showed the changes in the nanotopography that were induced by the water-vapour plasma treatment of both samples (**Figure 7**).

The quantitative evaluation of the nanotopography changes is presented in **Figure 8** in terms of R_a and SA. As the calculated R_{ms} values had the same trend as the R_a values, they are not presented in the paper. The plasma treatment produced a three-fold R_a increase in the cotton fibres, but did not cause significant changes in the polyester fibres (**Figure 8a**). The calculated SA values ob-
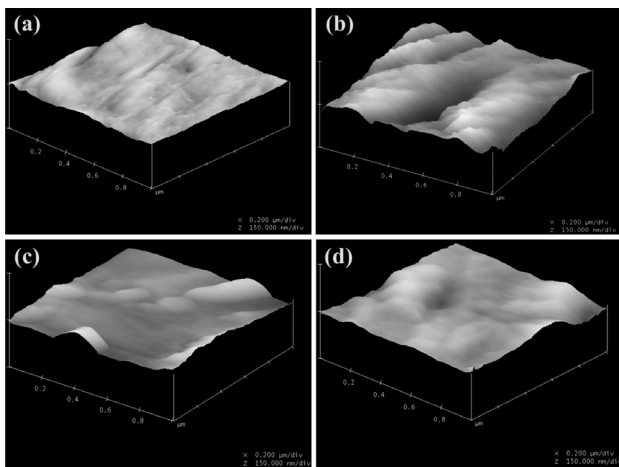
Figure 7: AFM scans of: a) untreated cotton, b) plasma-treated cotton, c) untreated polyester and d) plasma-treated polyester fibres
Slika 7: AFM-posnetki vlaken: a) neobdelanega bombaža, b) s plazmo obdelanega bombaža, c) neobdelanega poliestra in d) s plazmo obdelanega poliestra
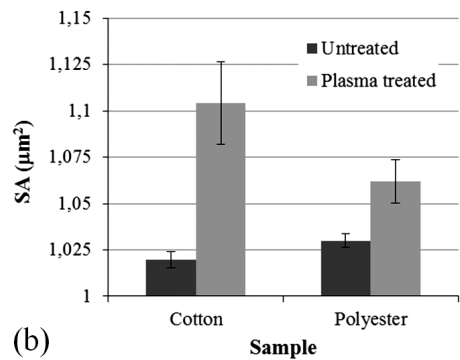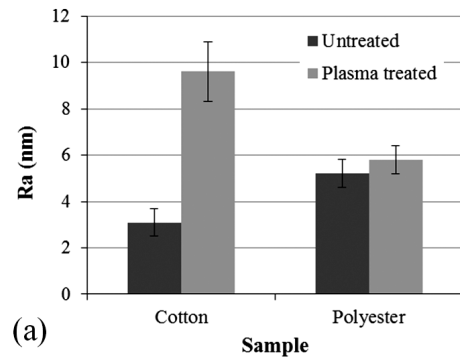
Figure 8: a) Mean roughness, R_a, and b) surface area, SA, of cotton and polyester samples
Slika 8: a) Srednja vrednost hrapavosti, R_a, in b) specifična površina, SA, bombažnih in poliestrskih vzorcev

Table 1: Elemental compositions of the fabric-sample surfaces determined with a XPS analysis
Tabela 1: Elementarna sestava površine vzorcev tkanin, dobljena z XPS-analizo

Sample	Elemental composition in mole fractions (%)		Atomic ratio O/C
	x(C)	x(O)	
Untreated cotton	69.4	30.6	0.44
Plasma treated cotton	61.3	38.7	0.63
Untreated polyester	72.0	28.0	0.39
Plasma treated polyester	62.2	37.8	0.61

tained after the plasma treatment were also higher for cotton than for polyester fibres (**Figure 8b**). For cotton and polyester, the SA values increased by approximately 8 % and 3 %, respectively. These results are in agreement with the obtained OES results. A higher etching effectiveness of the water-vapour plasma during the cotton treatment was caused by a different water content of the sample, i.e., 6.9 % for cotton and 0.5 % for polyester. A higher fibre water content leads to a higher level of reactive plasma species in the discharge, which contributes to an enhanced etching effect.

The XPS analyses (**Table 1**) suggest that the oxidation of plasma-treated cotton and polyester is not dependant on their water contents. After a plasma treatment, the atomic concentration of carbon (C1s, 285 eV) decreased and the atomic concentration of oxygen (O1s, 533 eV) increased in both cases. The calculated

increases of the O/C atomic ratios were 43 % for cotton and 56 % for polyester. Despite a low water content of the polyester sample, the fibre oxidation during the plasma treatment was successful.

4 CONCLUSIONS

A low-pressure water-vapour plasma was used for treating cotton and polyester fabrics. The source of the water vapour was the fabric itself. The basis of this research was to investigate the surface changes in the two chemically and morphologically different textiles when the same plasma parameters were used. Before and after the plasma treatment the surface properties of cotton and polyester fibres were evaluated and compared using the XPS, SEM and AFM analyses. The plasma treatment of the textiles was observed using an OES analysis. The results showed that the etching rate increases with the treatment time for both types of polymers due to the sample heating during the plasma treatment. The etching effect of the low-pressure water-vapour plasma was more pronounced for the hydrophilic cotton fibres than for hydrophobic polyester fibres. The cleaning effect on the surface of the cotton fabric was observed, when the surface impurities were removed. Under the used plasma parameters, surface morphology of the fibres remained unchanged for both types of polymers, indicating that the bulk properties of the fibres remained undamaged. The water content of both types of polymers was sufficiently high to achieve a good oxidation of the fibre surfaces.

This preliminary research is very important for understanding what is happening during plasma treatment of cotton and polyester and how the same plasma parameters influence the surface changes made to these two most important and widely used polymers. Since cotton and polyester are also used together as a cotton/polyester blend, the results will help us with our further research focusing on the water-vapour plasma (pre)treatment of blends.

5 REFERENCES

[1] G. Borcia, C. A. Anderson, N. M. D. Brown, Surf. Coat. Technol., 201 (**2006**) 6, 3074–3081

[2] C. Canal, P. Erra, R. Molina, E. Bertran, Text. Res. J., 77 (**2007**) 8, 559–564

[3] N. Ristić, P. Jovančić, C. Canal, D. Jocić, J. Appl. Polym. Sci., 117 (**2010**) 5, 2487–2496

[4] M. Devetak, N. Skoporc, M. Rigler, Z. Peršin, I. Drevenšek Olenik, M. Čopič, K. Stana - Kleinschek, Mater. Tehnol., 46 (**2012**) 1, 69–73

[5] L. Fras Zemljič, Z. Peršin, P. Stenius, Biomacromolecules, 10 (**2009**) 5, 1181–1187

[6] Z. Peršin, P. Stenius, K. Stana - Kleinschek, Tex. Res. J., 18 (**2011**) 16, 1673–1685

[7] K. Stana - Kleinschek, Z. Peršin, T. Maver, Mater. Tehnol., 45 (**2011**) 3, 253–257

[8] K. Navaneetha Pandiyaraj, V. Selvarajan, J. Mater. Process. Technol., 199 (**2008**) 1–3, 130–139

[9] H. U. Poll, U. Schladitz, S. Schreiter, Surf. Coat. Technol., 142–144 (**2001**), 489–493

[10] R. Morent, N. De Geyter, J. Verschuren, K. De Clerck, P. Kiekens, C. Leys, Surf. Coat. Technol., 202 (**2008**) 14, 3427–3449

[11] K. H. Kale, A. N. Desai, Indian J. Fibre Text. Res., 36 (**2011**) 3, 289–299

[12] M. Gorenšek, M. Gorjanc, V. Bukošek, J. Kovač, Z. Petrović, N. Puač, Tex. Res. J., 80 (**2010**) 16, 1633–1642

[13] V. Hody, T. Belmonte, C. D. Pintassilgo, F. Poncin-Epaillard, T. Czerwiec, G. Henrion, Y. Segui, J. Loureiro, Plasma Chem. Plasma Process., 26 (**2006**), 251–266

[14] T. Belmonte, C. D. Pintassilgo, T. Czerwiec, G. Henrion, V. Hody, J. M. Thiebaut, J. Loureiro, Surf. Coat. Technol., 200 (**2005**) 1–4, 26–30

[15] V. Hody, T. Belmonte, T. Czerwiec, G. Henrion, J. M. Thiebaut, Thin Solid Films, 506–507 (**2006**), 212–216

[16] M. Sowe, I. Novak, A. Vesel, I. Junkar, M. Lehocky, P. Saha, I. Chodak, Int. J. Polym. Anal. Ch., 14 (**2009**) 7, 641–651

[17] A. Asadinezhad, I. Novak, M. Lehocky, V. Sedlarik, A. Vesel, P. Saha, I. Chodak, Colloids Surf. B Biointerfaces, 77 (**2010**) 2, 246–256

[18] N. Puač, Z. Lj. Petrović, M. Radetić, A. Đorđević, Mat. Sci. Forum, 494 (**2005**), 291–296

[19] L. Chvatalova, R. Cermak, A. Mracek, O. Grulich, A. Vesel, P. Ponizil, A. Minarik, U. Cvelbar, L. Benicek, P. Sajdl, Eur. Polym. J., 48 (**2012**) 4, 866–874

[20] A. Popelka, A. Vesel, I. Junkar, Molecules, 17 (**2012**) 1, 762–785

[21] T. Vrlinic, D. Debarnot, M. Mozetic, A. Vesel, J. Kovac, A. Coudreuse, G. Legeay, F. Poncin-Epaillarda, J. Colloid. Interface Sci., 362 (**2011**) 2, 300–310

[22] Z. Persin, P. Stenius, K. Stana-Kleinschek, Text. Res. J., (**2011**) doi:10.1177/0040517511410110

[23] M. Gorenšek, M. Gorjanc, V. Bukošek, J. Kovač, P. Jovančić, D. Mihailović, Tex. Res. J., 80 (**2010**) 3, 253–262

[24] F. Leroux, C. Campagne, A. Perwuelz, L. Gengembre, Surf. Coat. Technol., 203 (**2009**) 20–21, 3178–3183

[25] G. Poletti, F. Orsini, A. Raffaele-Addamo, C. Riccardi, E. Selli, App. Surf. Sci., 219 (**2003**) 3–4, 311–316

[26] K. K. Samanta, M. Jassal, A. K. Agrawal, Surf. Coat. Technol., 203 (**2009**) 10–11, 1336–1342

[27] M. Gorjanc, V. Bukošek, M. Gorenšek, A. Vesel, Text. Res. J., 80 (**2010**) 6, 557–567

[28] M. Gorjanc, J. Vasiljević, A. Vesel, M. Mozetič, B. Simončič, Plasma and Sol-Gel Technology for Creating Nanostructured Surfaces of Fibrous Polymers, Proceedings of the International Conference Nanomaterials: Application and Properties, the Crimea, Ukraine, 2012, 04PITSE03-p1 - 04PITSE03-p4

[29] L. L. Pranevicius, D. Milcius, S. Tuckute, K. Gedvilas, Appl. Surf. Sci., 258 (**2012**) 22, 8619–8622

[30] S. J. Zheng, Y. C. Zhang, B. Ke, F. Ding, Z. L. Tang, K. Yang, X. D. Zhu, Phys. Plasmas, 19 (**2012**) 6, 063507-1 – 063507-4

[31] L. Liu, D. Xie, M. Wu, X. Yang, Z. Xu, W. Wang, X. Bai, E. Wang, Carbon, 50 (**2012**) 8, 3039–3044

[32] S. V. T. Nguyen1, J. E. Foster, A. D. Gallimore, Rev. Sci. Instrum., 80 (**2009**) 8, 083503-1 – 083503-8

[33] A. Tamošiunas, V. Grigaitiene, P. Valatkevičius, Nukleonika, 56 (**2011**) 2, 131–135

[34] M. Gorjanc, V. Bukosek, M. Gorensek, A. Vesel, Text. Res. J., 80 (**2010**) 6, 557–567

[35] N. Médard, J. C. Soutif, F. Poncin-Epaillard, Langmuir, 18 (**2002**) 6, 2246–2253

[36] N. Glavan, N. Krstulović, N. Čutić, S. Milošević, U. Cvelbar, A. Vesel, A. Drenik, M. Mozetič, Vakuumist, 25 (**2005**) 4, 23–27

[37] C. M. Weikart, H. K. Yasuda, J. Polym. Sci., Part A: Polym. Chem., 38 (**2000**) 17, 3028–3042

[38] T. Belmonte, C. D. Pintassilgo, T. Czerwiec, G. Henrion, V. Hody, J. M. Thiebaut, J. Loureiro, Surf. Coat. Techn., 200 (**2005**) 1–4, 26–30

[39] E. A. Bernardelli, T. Belmonte, D. Duday, G. Frache, F. Poncin-Epaillard, C. Noël, P. Choquet, H. N. Migeon, A. Maliska, Plasma Chem. Plasma Process., 31 (**2011**) 1, 189–203

[40] W. Dal'Maz Silva, T. Belmonte, D. Duday, G. Frache, C. Noël, P. Choquet, H. N. Migeon, A. M. Maliska, Plasma Processes Polym., 92 (**2012**), 207–216

INFLUENCE OF SAMPLE DIRECTION ON THE IMPACT TOUGHNESS OF THE API-X42 MICROALLOYED STEEL WITH A BANDED STRUCTURE

VPLIV USMERJENOSTI VZORCEV NA UDARNO ŽILAVOST MIKROLEGIRANEGA JEKLA API-X42 S TRAKAVO MIKROSTRUKTURO

Ahmadreza Salimi[1], Hossein Monajati Zadeh[1], Mohammad Reza Toroghinejad[2], Davod Asefi[1], Amir Ansaripour[1]

[1]Department of Materials Engineering, Najafabad Branch, Islamic Azad University, P.O. Box 517, Isfahan, Iran
[2]Department of Materials Engineering, Isfahan University of Technology, Isfahan, Iran
salimy.ahmadreza@gmail.com

The layering of a microstructure parallel to the direction of the material flow during the hot working process is called banding. In the present paper, the severity of ferrite-pearlite banding in the API-X42 microalloyed steel and its effects on the impact energy are studied. Specifically, the impact toughness is examined in the cases of banded and non-banded samples along two directions, perpendicular and parallel to the rolling, and the obtained results are compared. Metallographic examinations, together with the Charpy impact tests at 0 °C and –18 °C, were done for both directions, parallel and perpendicular to the rolling. The results showed a dependence of the impact energy on the sample direction relative to the rolling to be larger with the banded than the non-banded sample. The difference between the impact energies for the directions parallel and perpendicular to the rolling was also noticed to be caused by the increasing anisotropy index.

Keywords: API-X42 steel, pearlite-ferrite banding, impact energy

Usmerjanje mikrostrukture vzporedno s smerjo vročega preoblikovanja se imenuje trakavost. V članku je predstavljena študija preprostosti feritno-perlitnih pasov v mikrolegiranem jeklu API-X42 in njihov vpliv na udarno energijo. Specifično je primerjana udarna žilavost med vzorci s trakavo in netrakavo mikrostrukturo vzdolž dveh smeri, pravokotno in vzporedno s smerjo valjanja. Opravljene so bile metalografske preiskave in udarni preskusi Charpy pri 0 °C in –18 °C vzporedno in pravokotno na smer valjanja. Rezultati so pokazali odvisnost udarne energije glede na usmerjenost vzorca pri valjanju, relativno bolj v trakavih kot v netrakavih vzorcih. Pri naraščajočem indeksu anizotropije je bila opažena razlika med energijo udarca pri vzporedni in pravokotni smeri valjanja.

Ključne besede: jeklo API-X42, perlitno-feritni trakovi, udarna energija

1 INTRODUCTION

The layering of a microstructure parallel to the direction of the material flow during the hot working process is called banding. Generally, banding is classified into two major categories. The microscopic bands include deformation bands, transformation bands and shear bands, and the macroscopic bands include carbide banding in tool steels, layered ferrite-pearlite structure of rolling in low-carbon alloy steels and martensite banding in heat-treated alloy steels.[1–4] Because of these various micro and macro features, there is no universally accepted definition of banding. Moreover, there are clearly various mechanisms that can cause these structures.

Ferrite-pearlite banding may occur due to a segregation of some alloying elements during solidification after casting and hot-working processes.[5] When steel is slowly cooled from the austenite region, the pro-eutectoid ferrite is formed initially in the areas with a relatively low number of austenite-stabilizing elements, whereas pearlite is formed in the areas with more austenite-stabilizing elements after being cooled down to the temperatures below the eutectoid line, creating a banded microstructure containing successive pearlite and ferrite areas.[6]

There have been several studies on the effect of banding on mechanical properties[7–9]. Working on heavily banded 0.3 % carbon steel, Jatczak et al.[10] found little or no effect on the anisotropy of tensile properties, while a significant anisotropy of the reduction in area and impact properties was discovered. They also observed a very small change in mechanical properties in longitudinal direction as well as in impact properties and ductility in transverse direction due to homogenization.

Grange[11] found that both banding microstructure and longitudinally directed inclusions cause anisotropy in the mechanical properties of 0.025 % C and 1.5 % Mn steel, eliminating the decrease in anisotropy caused by banding; however, this decrease is trivial if numerous inclusions are elongated in longitudinal direction. In some studies, the effect of banding and specimen orientations on the fracture toughness has been investigated and it has been shown that banding has a significant

effect on the rolling-plane anisotropy.[12–14] However, little has been done to examine the differences between banded and non-banded samples in different directions.

In the previous researches, the samples with a banded structure were selected, and after the study of structural and mechanical properties, the same steel was heat treated, by normalizing or annealing it, to remove micro-structural banding.[2–15] The potential problem of this method is that this treatment makes it possible to prepare samples of the same steel in a virtually non-banded versus severely banded conditions; however, the differences in the chemical-composition distribution, grain size and inclusion morphology during heat treatment are inevitable. So, they can affect the accuracy of the results. In this study, the impact properties of several API-X42 steel samples with different bandy degrees of the ferritic-pearlite structure after hot rolling have been investigated. No heat treatment was done on the samples to reduce the banding phenomenon.

2 EXPERIMENTAL PROCEDURE

In this study, the initial production data of 50 samples of the API-X42 steel were obtained. Among them, 16 samples with the same chemical composition were selected. The chemical composition in mass fractions (%) is 0.12 C, 0.905 Mn, 0.21 Si, 0.007 P, 0.003 S and 25 N (µg/g). The samples were investigated with optical metallography.

Metallographic specimens were prepared in accordance with the guidelines and recommended practices given by ASTM-E3 Methods. Their images provided by an optical microscope at the magnification of 100 and 500 were also taken.

To investigate just the banding effects and remove the other effects of metallurgical variables, samples with the same grain size and chemical composition and with very low amounts of inclusions have been selected.

The banding in API-X42 is the ferrite-pearlite banding. Hence, the banded samples and non-banded ones were separated from each other by using the
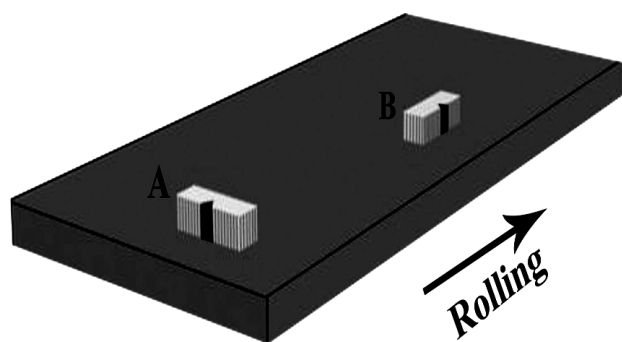
Assessing the Degree of Banding or Orientation of Microstructures standard (ASTM-E1268). The aniso-tropy index (AI) was estimated from the following equation:

$$AI = N_{L\perp}/N_{L\parallel} \qquad (1)$$

where $N_{L\perp}$ and $N_{L\parallel}$ are the mean numbers of the feature interceptions with the test lines respectively perpendicular and parallel to the deformation direction per length unit of the test lines. For a randomly oriented, non-banded microstructure, AI has a value of one. As the degree of orientation or banding increases, AI increases, too.

For the impact testing (according to the ASTM-E23 standard), three samples from each plate in a direction perpendicular to rolling and three samples in parallel with the rolling direction were prepared as shown in **Figure 1**. (At the state A, the test piece is perpendicular to the rolling direction and the notch is parallel to rolling. At the state B, the test piece is parallel to the rolling direction and the notch is perpendicular to rolling and the pendulum strikes the test piece in the direction parallel to rolling).

The Charpy impact tests at 0 and –18 °C were done. The amount of the absorbed energy was determined for each test piece. Finally, the mean of the three results for each temperature was reported as the final result. The fracture surface was coated with nickel to be prepared for examining the crack-propagation path in normal view of the fractured face. Nickel prevents damaging the studied fracture surface. Then the back of the broken test-piece notch was investigated with SEM microscopy.
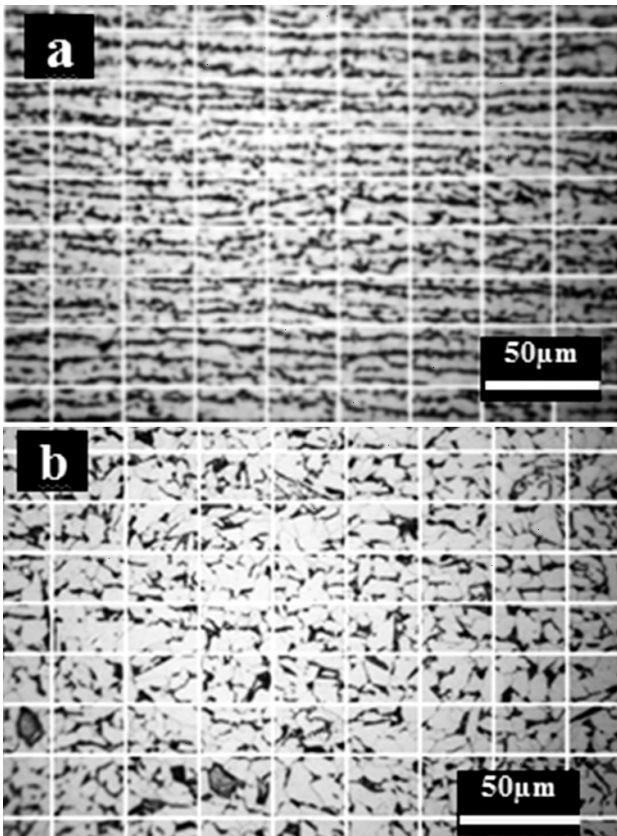
3 RESULTS AND DISCUSSION

Figure 2 shows two metallographic images used for determining AI for the two cases of highly and poorly banded microstructures. The results for the classified specimens after the metallography, the anisotropy index and the impact energy, are shown in **Table 1**.

Table 1: Relationship between the impact energy and the anisotropy index for the two temperatures of 0 °C and –18 °C
Tabela 1: Odvisnost med udarno energijo in indeksom anizotropije za dve temperaturi, 0 °C in –18 °C

No. of piece	AI	Impact energy, J	
		(–18°C)	(0°C)
1A	2.07	46.4	63.0
2A	2.18	55.4	67.5
3A	1.57	67.9	72.3
4A	1.55	67.4	74.0
1B	2.07	84.0	87.9
2B	2.18	88.8	89.7
3B	1.57	78.6	83.0
4B	1.55	79.6	85.0

In accordance with the banding standard, the optimal state is achieved when AI is equal to 1. It means that the

Figure 1: Schematic representation of the sample direction relative to the plate rolling direction
Slika 1: Shematski prikaz smeri vzorčenja in usmerjenost plošče glede na smer valjanja

Figure 2: Two examples of a: a) banded structure and b) non-banded structure, for which the anisotropy index was determined
Slika 2: Primer: a) trakave mikrostrukture in b) mikrostrukture brez trakavosti, za katero je bil določen indeks anizotropije
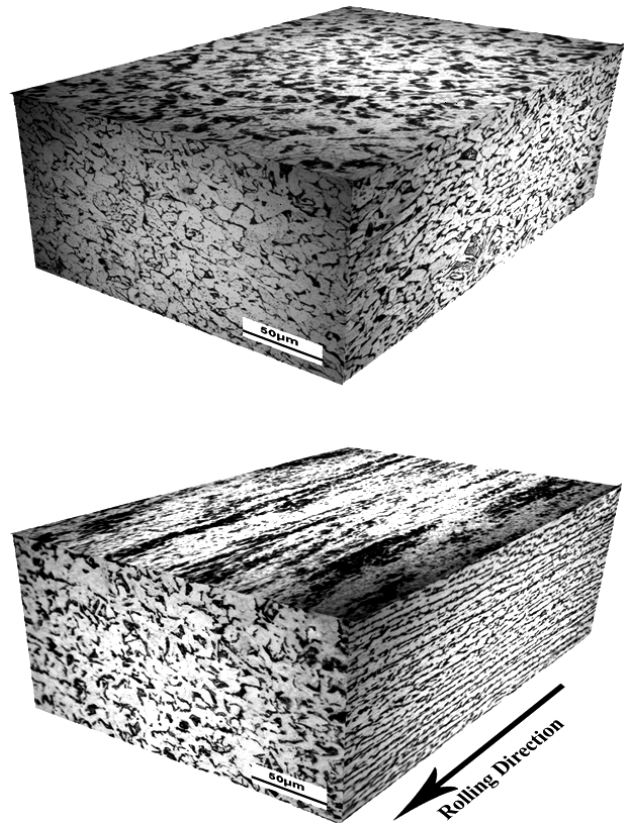
Figure 3: Three-dimensional images of metallographic samples 4A and 2B as the two samples with a low and a high *AI*
Slika 3: Tridimenzionalna slika metalografskega vzorca 4A in 2B kot dva vzorca z nizkim in visokim indeksom anizotropije *AI*

number of $N_{\text{L}\perp}$ must be equal to the number of $N_{\text{L}\parallel}$. By increasing it to a number higher than 1, $N_{\text{L}\perp}$ is higher than $N_{\text{L}\parallel}$, and the microstructure becomes more banded.

According to **Table 1,** all the measured values of *AI* are greater than 1. This indicates that all the samples are banded. But two series of more banded specimens containing the test pieces *1A, 2A, 1B, 2B* and two series of less banded specimens containing the test pieces *3A, 4A, 3B, 4B* can be singled out.

Three-dimensional metallographic microstructure images of samples 4A and 2B are shown in **Figures 3a** and **3b,** respectively, as the samples with a poorly and a highly banded microstructures.

As can be seen, the banding phenomenon is more visible in the direction parallel to the rolling cross-section. The relationship between the impact energy and *AI* for the eight test pieces examined in the directions of *A* and *B*, is shown in **Figure 4**.

According to **Figure 4**, in the samples of series *A*, the impact energy is reduced with an increase in *AI*. As the samples of series *B* behave differently, an increase in *AI* causes an increase in the impact energy. About a 40 % increase in *AI* results in about a 10 % increase in the impact energy of *B* samples and about a 25 % decrease in *A* samples.

This increasing and decreasing of the impact energy caused by the increasing banding can be attributed to the crack-growth path in the banding layers of the impact sample. Schematic representations of the crack-growth paths from samples *A* and *B* are shown in **Figure 5**. According to this figure, in the *A* sample the crack
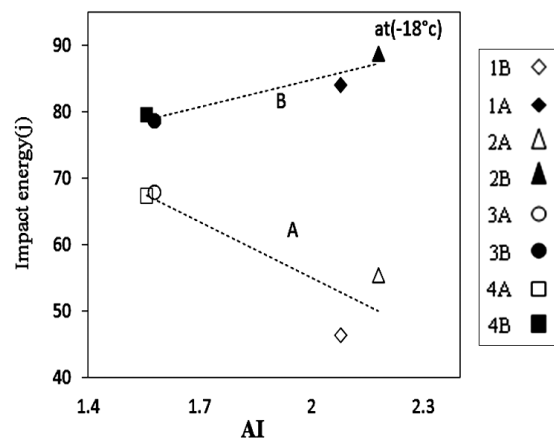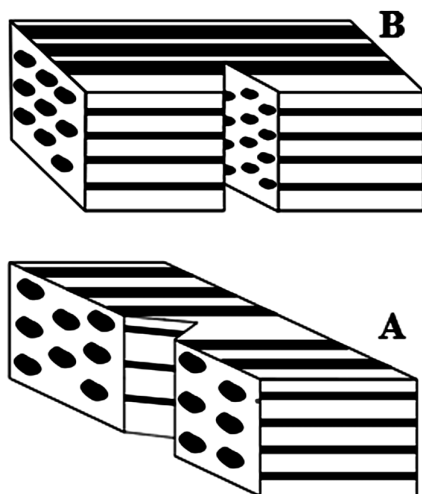

Figure 4: Dependence of the impact energy on the sample direction (A and B according to **Figure 1**) and *AI* at –18 °C
Slika 4: Odvisnost udarne energije od usmerjenosti vzorca (A in B na **sliki 1**) in indeksa anizotropije *AI* pri –18 °C

moves along the path of the layers placed on each other, while in the *B* sample the crack movement is perpendicular to the layers and is encountered by different layers on its path. So, a stronger banding is more harmful for the *A* sample and more useful for the *B* sample. This is because more layers on the crack-growth path can absorb more energy.
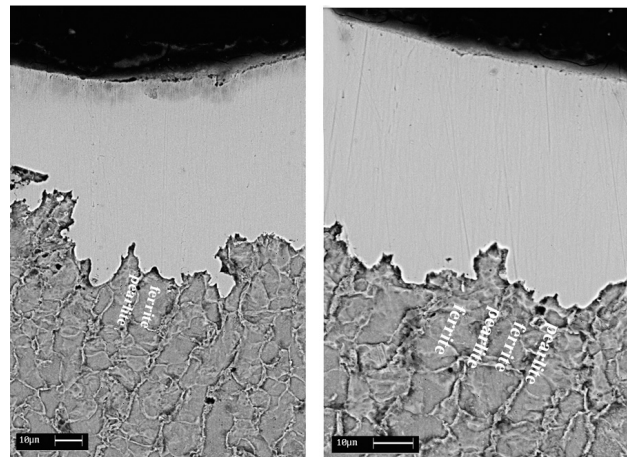
According to **Table 1** and **Figure 3**, the *1B* and *2B* test pieces that have a high AI, absorbing more energy before the fracture, while the 3B and *4B* test pieces that have a low *AI* absorbing less energy and allowing the fracture to occur. In addition, the minimum value is related to the *3B* sample having the lowest *AI*. It means that banding can be useful to impact properties if the pendulum impact on the test piece is in the direction perpendicular to the rolling. A crack can deviate from its main path due to grain boundaries, flow lines, inclusions and banding. It can be seen in **Figure 2** that in the banded samples the distance between the ferrite and pearlite is smaller than in the non-banded samples and the crack is forced to encounter many more phases on its path. Also, the phase continuity is a more important factor in the case of highly banded samples than in the case of poorly banded samples. The reason for this is the fact that when phases are continuous, a crack is forced to encounter many more phases on its path. On the other hand, due to the discontinuity of the phases in the poorly banded samples, a crack may follow a longer path before encountering another phase. This can be better seen in **Figure 6**, which shows a SEM image of the section perpendicular to the fracture surface of sample 2. This figure implies that the crack path has been serrated while crossing the ferrite-pearlite banded structure.

The crack path on this figure is perpendicular to the plate. So, during the crossing, it has been involved with the structures of ferrite and pearlite. This caused a change in the path and can be the reason for an increase


Figure 6: SEM image of a crack-growth path in the cross-section perpendicular to the fracture surface of sample 2B
Slika 6: SEM-posnetek poti rasti razpoke na preseku pravokotno na površino preloma vzorca 2B

in the absorbed impact energy in *B* similar to the banded samples.

The *A* banding structure can also be compared to a fiber composite or a composite with constant reinforcing particles, in which the reinforcing phase is located in the field phase. The fracture in the direction perpendicular to
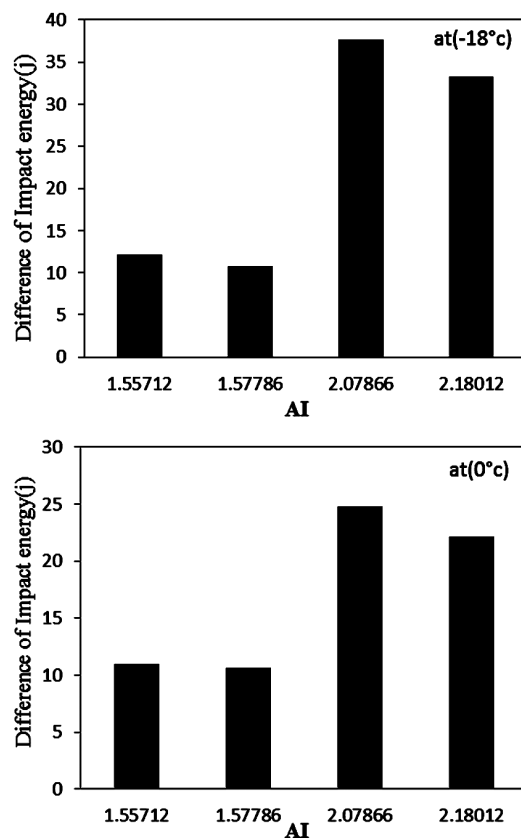
Figure 7: Difference in the impact energies for the A and B samples at –18 °C and 0 °C
Slika 7: Razlika v udarni energiji pri dveh vzorcih A in B pri –18 °C in 0 °C

Figure 5: Schematic image representing the crack-growth path in the A and B banded samples
Slika 5: Shematski prikaz poti rasti razpoke v trakavih vzorcih A in B

the fibers is more serious than the one in the parallel direction. **Figure 7** shows the differences in the impact energies for the two directions, perpendicular and parallel, of the rolling.

In a study on an aluminum composite, in which the SiC reinforcing particles are used in two forms, an elongated and a random orientation in the aluminum matrix, the sample with a random distribution showed no difference in the fatigue crack growth in the two directions, the perpendicular and parallel, while the sample with an elongated reinforcement showed an obvious difference.[16]

Also, the repeated impact tests at the zero temperature indicated a similar behavior shown in this diagram, and the diagram in **Figure 4** shows that with the increasing *AI* the differences in the impact energies for the two directions, the perpendicular and parallel, increase from 11 J to 37 J. Therefore, the direction of the samples has a significant effect on the banded samples, reflected in the impact-test results. Due to a more homogeneous microstructure of the non-banded samples or the samples with a lower *AI*, the mechanical properties are not very dissimilar for different directions and are close to the homogeneous state.

However, at the temperature of –18 °C the amount of the impact energy in the banded samples was slightly smaller than at the temperature of 0 °C. This shows that banding has a larger effect on the impact properties at lower temperatures.

4 CONCLUSION

1. Impact energy shows an obvious dependence on the sample direction. As *AI* increases (which is an index of banding), the impact energy decreases in the rolling direction, while it increases in the direction perpendicular to rolling.
2. With the increasing *AI* the differences in the impact energies for the two directions, perpendicular and parallel, increase.

3. At lower temperatures banding has a greater influence on impact properties.

Acknowledgments

5 REFERENCES

[1] ASTM International, Metals-Mechanical Testing, Annual Book of ASTM Standards, 2009
[2] J. D. Verhoeven, Journal of Materials Engineering and Performance, 9 (**2000**), 286–296
[3] X. P. Liang, H. Z. Li, L. Huang, T. Hongc, B. Ma, Y. Liu, Transactions Of Nonferrous Metals Society Of China, 22 (**2012**) 6, 1270–1279
[4] S. W. Hwang, J. H. Ji, K. T. Park, Materials Science and Engineering: A, 528 (**2011**), 7267–7275
[5] L. E. Samuels, Light Microscopy of Carbon Steels, ASM International, 1999, 81–124
[6] H. Chandler, Heat Treater's Guide, Practices And Procedures For Irons And Steels, 2nd ed., ASM International, 1995
[7] L. Hellner, T. O. Norrman, Jernkont. Ann., 152 (**1968**), 269–86
[8] W. A. Spitzig, Metallurgical Transactions A, 14 (**1983**), 271
[9] A. S. Bor, Iron Steel Inst. Jpn. Int., 31 (**1991**), 1445–46
[10] E. F. Jatczak, D. J. Girardi, E. S. Rowland, Transactions of American Society of Metals, 48 (**1952**), 279–303
[11] R. A. Grange, Metall Transactions, 2 (**1971**), 417–426
[12] L. Tau, S. Chan, C. Shin, Journal of Marine Science and Technology, 1 (**1993**), 19–22
[13] M. Z. Shah Khan, S. J. Alkemade, G. M. Weston, D. G. Wiese, Int Journal Fatigue, 20 (**1998**), 233–239
[14] P. Shanmugam, S. D. Pathak, Engineering Fracture Mechanics, 53 (**1996**), 991–1005
[15] M. Mazinani, W. J. Poole, Metallurgical and Materials Transactions A, 38 (**2007**), 432
[16] J. J. Mason, R. O. Ritchie, Materials Science and Engineering A, 231 (**1997**) 1–2, 170–182

EXPERIMENTAL AND NUMERICAL INVESTIGATION OF AN AIR-PCM HEAT-STORAGE UNIT

EKSPERIMENTALNA IN NUMERIČNA PREISKAVA ENOTE ZRAK – PCM ZA SHRANJEVANJE TOPLOTE

Tomas Mauder, Pavel Charvat, Milan Ostry

Brno University of Technology, Faculty of Mechanical Engineering, Technicka 2896/2, Brno, Czech Republic
ymaude00@stud.fme.vutbr.cz

The phase-change materials (PCMs) are quite promising heat-storage media for applications that require a high heat-storage capacity in a relatively narrow temperature interval. One of the areas of the latent-heat-storage application is thermal-energy storage in solar air systems, where a lower heat-storage temperature leads to an increase in the overall efficiency of the system. The paper deals with numerical and experimental investigations of the thermal performance of an air-PCM heat-storage unit. The studied unit contained 100 aluminum containers filled with a paraffin-based PCM. Both experimental and numerical investigations were done for a constant air temperature at the inlet of the heat-storage unit.

Keywords: heat exchanger, PCM, simulation

Materiali s fazno premeno (PCM) so obetavni mediji za shranjevanje toplote za uporabo, ki zahteva veliko kapaciteto shranjevanja toplote v relativno ozkem temperaturnem intervalu. Eno od področij uporabe shranjevanja latentne toplote je shranjevanje toplotne energije v solarnih sistemih, kjer nizka temperatura shranjevanja toplote povečuje splošno učinkovitost sistema. Članek obravnava numerične in eksperimentalne preiskave toplotne zmogljivosti enote zrak – PCM za shranjevanje toplote. Preiskovana enota je sestavljena iz 100 aluminijevih vsebnikov, napolnjenih s parafinskim PCM. Eksperimentalne in numerične preiskave so bile izvršene za konstantno temperaturo zraka, pri vhodu v napravo za shranjevanje toplote.

Ključne besede: izmenjevalnik toplote, PCM, simulacija

1 INTRODUCTION

Most of the solar thermal systems cannot effectively operate without thermal storage.[1] Water is generally used as a heat-storage medium in water-based solar systems, but it is less practical for air-based systems. The rock beds, where solid materials (usually pebbles) are used for heat storage,[2] can be used in air-based solar thermal systems, but they have certain disadvantages. The rock beds use a lot of space, they are difficult to clean, the air-flow distribution in the beds is usually non-uniform causing highly non-uniform temperature distribution in the heat-storage medium and thus decreasing the energy efficiency of the system. In order to achieve a higher heat-storage density, the rock beds need to be heated up to high temperatures leading to a decrease in the overall energy efficiency. Promising media for thermal storage in these applications are phase-change materials.[3]
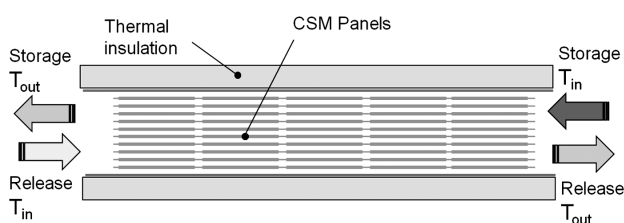
Figure 1: Schematic view of the heat-storage unit
Slika 1: Shematski prikaz enote za shranjevanje toplote

The phase change of a material provides a rather high thermal-storage capacity (and also energy-storage density) in a narrow temperature interval around the melting point of the material.[4] Latent heat is absorbed or released when the material changes phase from solid to liquid or from liquid to solid. The most commonly used PCMs are paraffins, fatty acids and esters, and various salt hydrates.[5]

2 HEAT-STORAGE UNIT

PCM-based heat-storage units can be of various designs. The studied heat-storage unit had a rather simple design (**Figure 1**). It was a thermally insulated box that contained 100 aluminum panels filled with the PCM (arranged in 5 rows). The Rubitherm CSM panels were used in the unit. The panels have the dimensions of 450 mm × 300 mm × 10 mm and each of them can accommodate approximately 700 ml of PCM. The panels were filled with the Rubitherm RT42 paraffin-based PCM. The RT42 has a melting range from 38 °C to 43 °C, heat-storage capacity of 174 kJ/kg (in the temperature range between 35 °C and 50 °C) and a thermal conductivity of 0.2 W/(m K). The overall heat-storage capacity of the unit was 12.3 kJ (3.4 kW h) in the temperature interval between 25 °C and 55 °C.

In the situations when the unit is not fully charged it can make sense to reverse the air-flow direction in the

discharging mode (in comparison to the charging mode – as indicated in **Figure 1**) in order to increase the outlet air temperature and, thus, to increase the efficiency. Another issue is the position of the PCM panels in the unit. When the panels are positioned horizontally the PCM in the fully melted state collects at the lower part of the panel and there will be an air gap between the PCM and the upper surface of the container. That gap can significantly influence the heat transfer between the PCM and the air passing through the heat-storage unit. The volume change between the solid and liquid state is rather significant for many PCMs (it can be larger than 15 %) and thus some empty space needs to be kept in the containers to allow for that volume change. An experimental set-up was prepared in order to investigate the thermal performance of the unit. The experimental set-up consisted of the unit, a fan, an electric air heater, and the temperature and air-velocity probes connected to a data logger (**Figure 2**).

The experiments were carried out at a constant air-flow rate throughout the unit and a constant inlet air temperature.
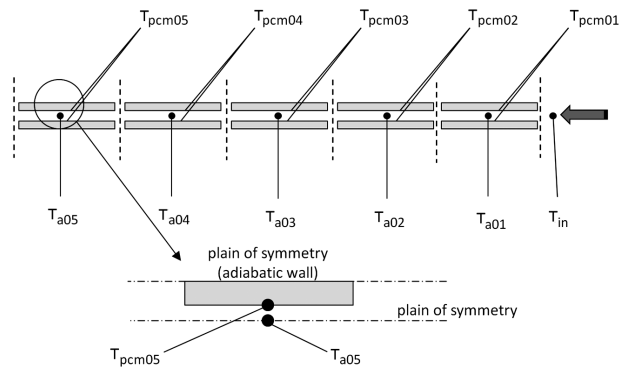
3 NUMERICAL MODEL OF THE UNIT

The simulation tool TRNSYS 17 was used for numerical investigations. TRNSYS 17 is a 1D simulation tool that can be used for energy-performance simulations of systems and buildings. A schematic of the numerical model of the heat-storage unit is shown in **Figure 3**. Simulations were done for 5 rows of the CSM panels with 20 panels in each row as was the case in the experimental investigations. Since there are 19 geometrically equal air channels between the CSM panels, only one channel was modeled. Actually, assuming the planar symmetry, only a half of a channel with a half of the CSM panel thickness was modeled. The numerical model of the heat transfer including a phase change in the PCM unit was implemented in MATLAB and connected to TRNSYS.[6]

The numerical model for the heat transfer in the PCM created in MATLAB is based on the implementation of the 1D heat-transfer equation that includes the source of the latent heat of the phase change:[6]

$$\frac{\partial}{\partial t}(\rho c T) = k \frac{\partial^2 T}{\partial x^2} + \dot{Q} \qquad (1)$$
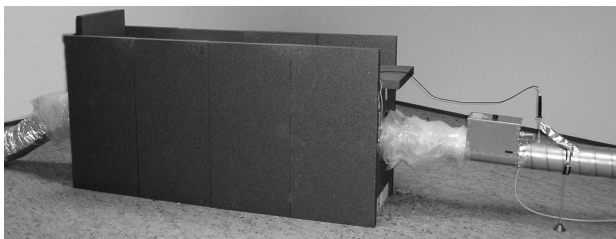
Figure 2: Experimental set-up
Slika 2: Eksperimentalni sestav

Figure 3: Simplification of the storage unit for the numerical model
Slika 3: Poenostavitev naprave za shranjevanje za numerični model

where ρ represents the density, c denotes the heat capacity, k stands for the thermal conductivity, t is the time, T represents the temperature and x is the spatial coordinate. The term $\dot{Q}$ in equation (1) can be expressed as follows:

$$\dot{Q} = \rho \Delta H \frac{\partial f_s}{\partial t} \qquad (2)$$

where ΔH denotes the latent heat and f_s is the solid fraction that represents the ratio between the solid and liquid phases. If $f_s = 0$, the material is in the liquid state and, therefore, only thermo-physical properties related to the liquid state are considered. Conversely, if $1 f_s = 0$, the material is in the solid state. The theoretical analysis of solidification is based on the equilibrium with the assumption that a complete diffusion occurs between the solid and liquid phases. A simple premise is to assume that the latent heat increases linearly with the temperature:

$$f_s = \frac{T_L - T}{T_L - T_S} \qquad (3)$$

In equation (3) T_S and T_L represent the solidus and liquidus temperatures, respectively. The solution of equation (1) strictly depends on the initial and boundary conditions. The initial condition describes the temperature distribution for $t = 0$:

$$T(x, t = 0) = T_0(x) \qquad (4)$$
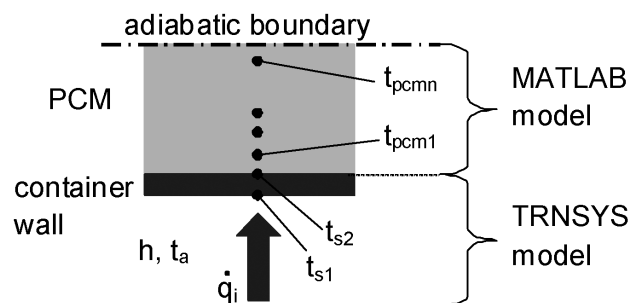
Figure 4: Detail of the computational domain
Slika 4: Detajl računske domene

The numerical model takes into account the Neumann type of boundary conditions determined by the heat fluxes $\dot{q}$ on the surface:

$$-\lambda \frac{\partial T}{\partial x}(x=0, f) = \dot{q} \qquad (5)$$

The adiabatic boundary condition ($\dot{q}=0$) is used at the plain of symmetry in the middle of the container.

A detail of the computational domain is shown in **Figure 4**. The communication between the TRNSYS model and the MATLAB model is described below.

The computations started from a given initial temperature profile in the PCM layer (temperatures t_{pcm1} to t_{pcmn}). A constant temperature across the layer was assumed in the simulations.

The heat flux $\dot{q}_i$ at the surface of the aluminum wall of the container was obtained from the TRNSYS model. No thermal resistance between the PCM and the container wall was assumed and the wall temperature t_{s2} was considered to be equal to the temperature t_{pcm1}. The heat flux obtained from the TRNSYS model was then used as an input for the MATLAB model for the PCM layer. The MATLAB model provided a new value of the t_{pcm1} that was used for calculating the heat flux in the next time step in the TRNSYS model. A time step of 60 s was used in the TRNSYS model while the MATLAB model used a much shorter time step of 1 s in line with the stability condition. The stability condition for explicit formula was used according to[7].

4 RESULTS AND DISCUSSION

Figure 5 shows the comparison of experimental and numerical results for the heat-storage rate in the unit. The heat-storage rate was obtained from the air-mass-flow rate and the air temperatures at the inlet and the outlet of the storage unit. The air temperature at the inlet of the unit in the heat-storage period was 58 °C and the air-flow rate was 230 m³/h. Though a constant air temperature at the inlet of the unit is of rare occurrence under real operating conditions, it is very illustrative for the
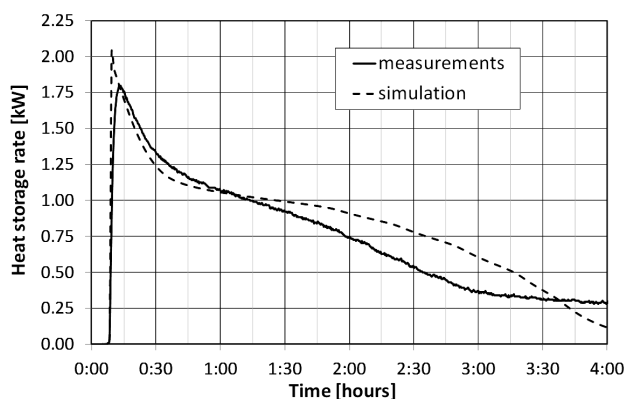
theoretical analyses. There are certain discrepancies between the predicted and measured heat-storage rates. The electric air heater used in the experiments had an output of 2 kW, but since the heater needed some time to reach that output the measured heat-storage peak is not as sharp as in the case of numerical simulations. The current version of the simulation model neglects the heat loss to the surroundings. This is one of the reasons for the increasing discrepancies over longer periods of time. At a certain point the air-temperature difference between the inlet and the outlet of the unit is not due to the storage rate but due to the thermal loss of the unit. Another reason for discrepancies is associated with the air flow inside the unit.

Though the heat transfer in the case of the air flow between two parallel planes is well described in the literature, the uncertainty remains about the air-flow rates in particular air channels. The melting of the PCM is yet another source of uncertainties. A proper simulation of the melting and solidification requires a complex 3D numerical model that takes into account the convection in the liquid PCM as well as the PCM volume change (to address the void formation during solidification).

The heat-release rates can be seen in **Figure 6**. The air temperature at the inlet of the unit was 25 °C during the heat-discharge period. The air-flow rate was the same as in the heat-storage period. Again, there is a relatively good match between the numerical and experimental results at the beginning of the heat-release period, but the discrepancies increase with the elapsed time. The heat-release rate peaks at more than 2 kW at the beginning of the heat-release period, but it very quickly drops to around 1 kW when the sensible heat above the melting range is released. The differences between the numerical and experimental results can be explained with the non-uniform air-flow rates in the air channels between the panels. The numerical model assumes that the air-flow rates in all the air channels are the same and, therefore, the heat fluxes stored to, or released from, all the panels in one row are the same.

Figure 5: Heat-storage rates
Slika 5: Hitrost shranjevanja toplote
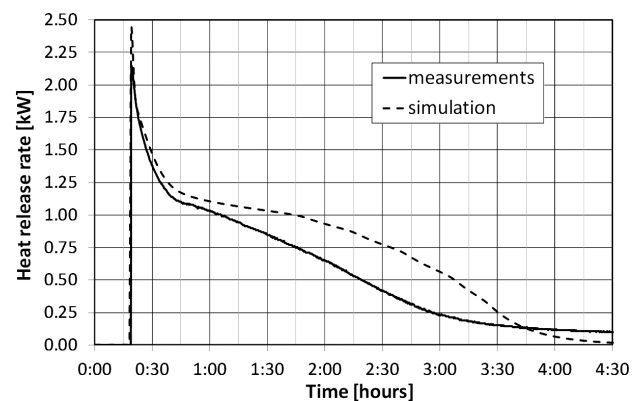
Figure 6: Heat-release rates
Slika 6: Hitrost sproščanja toplote

5 CONCLUSION

A 1D simulation model of a heat-storage unit with a PCM for thermal-energy systems using air as a heat carrier was developed. The model of the unit was created with the use of coupling between the TRNSYS 17 simulation tool and the in-house MATLAB model for PCMs. An experimental setup with a test heat-storage unit was put together in order to validate the developed numerical model experimentally. The comparison of experimental and numerical results revealed certain discrepancies in the predicted and measured temperatures and energies. The simulation model neglected the heat loss to the ambient environment, the uncertainties associated with the air-flow inside the unit and it used a rather simple approach to the model phase change of the PCM. The necessary communication between TRNSYS and MATLAB also significantly slowed down the simulations. To address all these issues a more advanced model of a heat-storage unit implemented as a TRNSYS type (programmed in C++) is under development.

Acknowledgement

6 REFERENCES

[1] M. Muhieddine, É. Canot, R. March, Various approaches for solving problems in heat conduction with phase change, International Journal on Finite Volumes, 6 (**2009**), 20

[2] S. Jaber, S. Ajib, Optimum design of Trombe wall system in Mediterranean region, Solar Energy, 85 (**2011**), 1891–1898

[3] D. L. Zhao, Y. Li, Y. J. Dai, R. Z. Wang, Optimal study of a solar air heating system with pebble bed energy storage, Energy Conversion and Management, 52 (**2011**), 2392–2400

[4] P. Pinel, C. A. Cruickshank, I. Beausoleil-Morrison, A. Wills, A review of available methods for seasonal storage of solar thermal energy in residential applications, Renewable and Sustainable Energy Reviews, 15 (**2011**), 334–3359

[5] Y. Dutil, D. R. Rousse, N. Ben Salah, S. Lassue, L. Zalewski, A review on phase-change materials: Mathematical modeling and simulations, Renewable and Sustainable Energy Reviews, 15 (**2011**), 112–130

[6] L. Klimeš, P. Popela, An Implementation of Progressive Hedging Algorithm for Engineering Problems, In: Mendel 2010, Proceedings of the 16th International Conference on Soft Computing, Brno, BUT, 2010, 459–464

[7] R. Tavakoli, P. Davami, Unconditionally stable fully explicit finite difference solution of solidification problems, Metallurgical and Materials Transactions B, 38 (**2007**) 1, 121–142

EXPERIMENTAL INVESTIGATION OF A HEAT-TRANSFER COEFFICIENT

PREISKAVE KOEFICIENTA PRENOSA TOPLOTE

Martin Chabičovský, Miroslav Raudenský

Heat Transfer and Fluid Flow Laboratory, Faculty of Mechanical Engineering, Brno University of Technology, Technická 2, 616 69 Brno, Czech Republic
chabicovsky@LPTaP.fme.vutbr.cz

A special piece of apparatus was developed to study the cooling of hot steel surfaces using full-cone nozzles. This apparatus allowed the movement of the test sheet in a vertical direction, up and down. Experiments with different water pressures and flow rate**s** were conducted. It was observed that the value of the average heat-transfer coefficient increased with an increase in the water pressure for all the surface-temperature range and the dependence of the heat-transfer coefficient on the water-impingement density is linear in the region of stable film boiling. A mathematical model based on a regression analysis for predicting the heat-transfer coefficient in the region of stable film boiling was developed.

Keywords: cooling, impingement density, full cone nozzles, heat-transfer coefficient

Razvita je bila posebna naprava za preučevanje ohlajanja vroče površine jekla s področjem s šobami. Ta naprava omogoča vertikalno pomikanje preizkusne pločevine dol in gor. Izvršeni so bili preizkusi z različnimi tlaki vode in hitrostmi pretokov. Opaženo je bilo, da narašča srednja vrednost koeficienta prenosa toplote z naraščanjem tlaka vode za vsa območja temperature površine in da je linearna odvisnost med koeficientom prenosa toplote in zmanjševanjem gostote vode v območju stabilne tanke plasti pri vrenju. Na osnovi regresijske analize je bil razvit matematični model za napovedovanje koeficienta prenosa toplote v območju stabilne tanke plasti pri vretju.

Ključne besede: ohlajanje, zmanjševanje gostote, področje s šobami, koeficient prenosa toplote

1 INTRODUCTION

The spray cooling of vertically moving, hot, stainless-steel sheet was studied in the Heat Transfer and Fluid Flow Laboratory. The temperature range from 900 °C to 200 °C was covered by these experiments. The experiments with different water-impingement densities were conducted. The dependence of the heat-transfer coefficient (*HTC*) on different water-impingement densities (mL) has been studied by many authors, but it is known that different nozzles and test conditions provide different results. It is also known that in the range of stable film boiling, the heat-transfer coefficient is independent of the surface temperature and that it is mostly influenced by the water-impingement density. It was shown in[1] (**Figure 1**), that the dependence of the heat-transfer coefficient on the impingement density is linear for water temperatures under 20 °C and water-impingement densities of 100–2000 kg /(m² min).

2 EXPERIMENTAL PROCESS

An experimental apparatus developed for the vertical moving of a hot-test, stainless-steel sheet was used in the experiments (**Figure 2**). The hot-test sheet with a thickness of 1 mm moved vertically up and down, and it was cooled by three rows of collectors with full-cone nozzles. The collectors were connected through a pump to a water tank with an adjustable water temperature. Each collec-

tor was directly connected to a manometer. The heater, which heated the test sheet to 900 °C, was on the top of the experimental apparatus. Four thermocouples of type
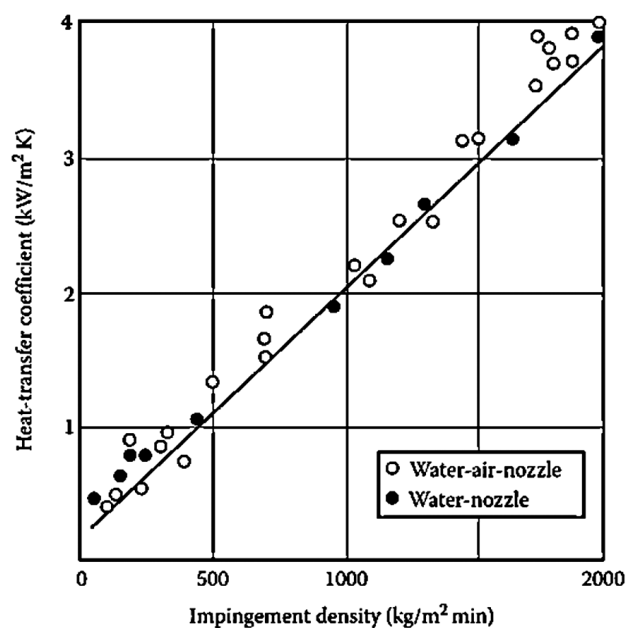

Figure 1: Heat-transfer coefficient as a function of the impingement density[1]
Slika 1: Koeficient prenosa toplote v odvisnosti od zmanjševanja gostote[1]
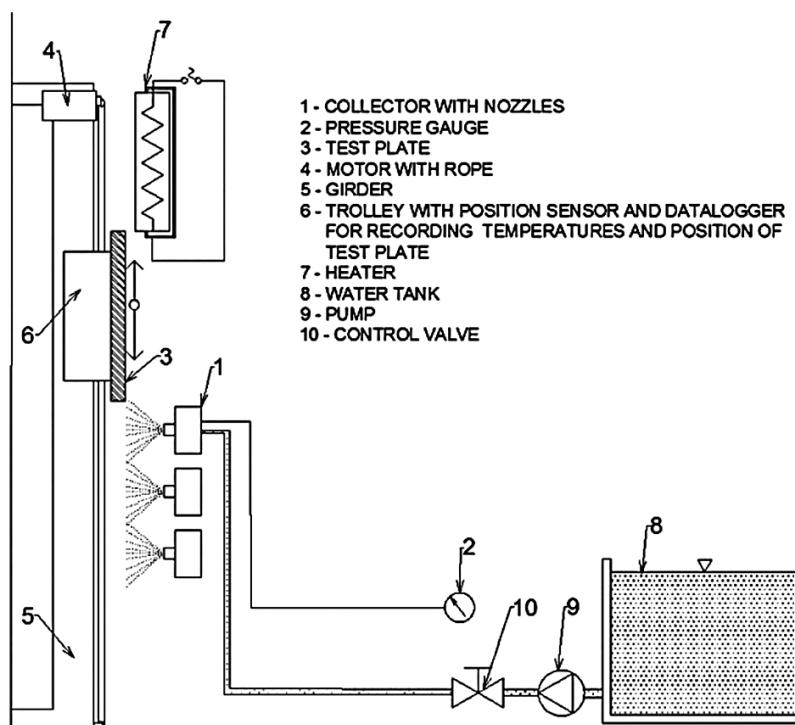
Figure 2: Experimental apparatus
Slika 2: Preizkusna naprava

K were welded on the rear side of the test sheet. The distance between the thermocouples was 20 mm (**Figure 3**). The holder of the test sheet was equipped with a position sensor and data logger, which recorded the information about the test-sheet temperature and the position. The test sheet was heated in a furnace at a temperature of 900 °C and then moved up/down under spraying nozzles until it was cooled to a temperature of 200 °C. The movement of the test sheet was conducted with a velocity of 3 m s^{-1}. The distance between the
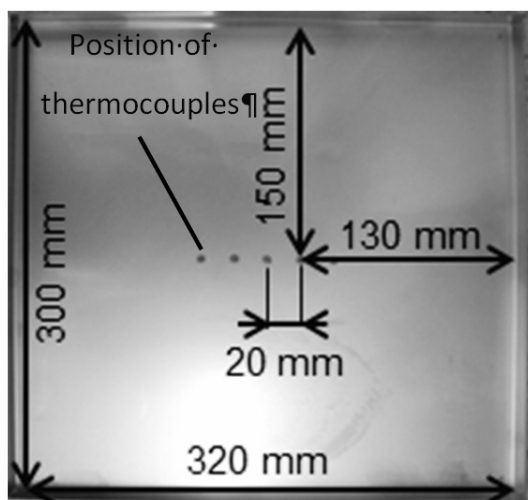

Figure 3: Rear side of the test sheet with marked positions of the thermocouples
Slika 3: Zadnja stran preizkusne pločevine z označenimi položaji termoelementov

nozzles was 40 mm, while the distance between the collectors was 330 mm, and the distance from the nozzle orifice to the test sheet was 250 mm. An example of the nozzle configuration and photographs of the experiment are shown on the **Figure 4**. The experiments were made with a water temperature of 40 °C and differed only in terms of the pressures. The pressures and water-impingement densities used in experiments are shown in **Table 1**.

Table 1: Measured experiments
Tabela 1: Rezultati meritev preizkusov

Experiment	Water pressure p/bar	Water impingement density (kg m^{-2} s^{-1})
1	0.2	3.3
2	1.3	9.7
3	4.3	18.8
4	6	22.6

3 RESULTS

The measured temperatures were recomputed to the surface temperatures (sprayed/cooled side) for the location of the temperature sensors by the inverse task.[2] An example of the four computed surface temperatures is shown in the **Figure 5**. The heat-transfer coefficient was then computed using the inverse conduction algorithm.[3] The average heat-transfer coefficient (average value over the length of the cooling section, i.e., 660 mm) was computed for all the measured experiments. Their comparison is shown in the **Figure 6**. It is evident
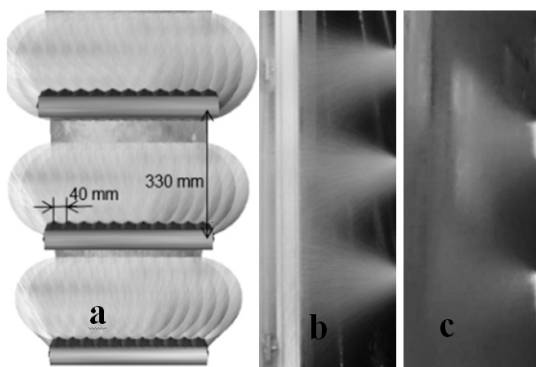
Figure 4: a) Nozzles configuration, b) spraying nozzles, c) nozzles spraying the hot test sheet
Slika 4: a) Razporeditev šob, b) razpršilne šobe, c) šobe, ki škropijo vročo preizkusno pločevino

Figure 6: Comparison of experiments
Slika 6: Primerjava preizkusov

that the average heat-transfer coefficient is increasing with the increasing water pressure (impingement density) and the Leidenfrost point increases with the increasing water-impingement density. The average heat-transfer coefficient is increasing with the decreasing of the surface temperature in the region of the film boiling. It is caused by thinning of the vapor layer. Lowering the surface temperature under the Leidenfrost temperature is connected with a change in the type of boiling. Film boiling is changed into transition boiling and this change in the type of boiling leads to a sharp increase in the heat-transfer coefficient. It was also observed that the dependence of the heat-transfer coefficient on the water-impingement density is linear in the region of stable film boiling (**Figure 7**). The first derivative of the regression functions is increasing with the lowering of the surface temperature (**Table 2**). The constant in the regression functions represents the measured natural convection and radiation. The result for a surface temperature of 900 °C is in good agreement with the result presented in[1] (**Figure 7**). The regression functions presented in the **Table 2** can be used to
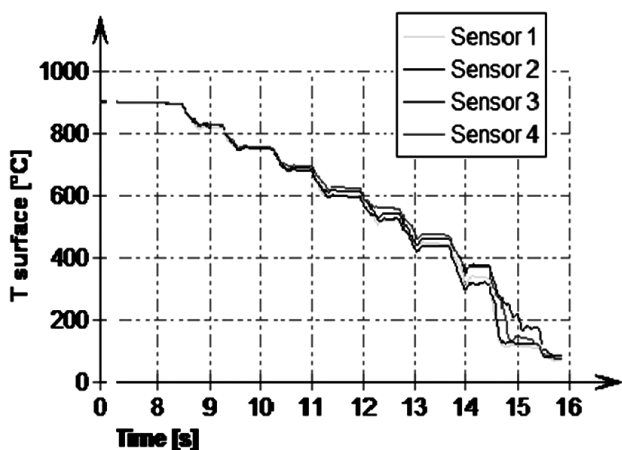

Figure 7: Regression functions for predicting *HTC*
Slika 7: Regresijske odvisnosti za napovedovanje *HTC*

extrapolate or interpolate the average heat-transfer coefficient for different water-impingement densities in the region of stable film boiling. This model can only be used for predicting the heat-transfer coefficient for parameters (type of nozzles, water temperature, configuration of nozzles, etc.) that were used in the experiments from which the regression analysis was made.

Table 2: Regression functions
Tabela 2: Regresijske funkcije

Surface temperature, T/°C	Regression function
600	$HTC = 212 \text{ mL} + 128$
700	$HTC = 166 \text{ mL} + 138$
800	$HTC = 123 \text{ mL} + 149$
900	$HTC = 113 \text{ mL} + 159$

4 CONCLUSION

Experiments with horizontally oriented nozzles and vertically moving hot sheet were conducted. Different water-impingement densities were tested. It was observed that the heat-transfer coefficient increases with an increasing water-impingement density at all the

Figure 5: Example of computed surface temperature
Slika 5: Primer izračunane temperature površine

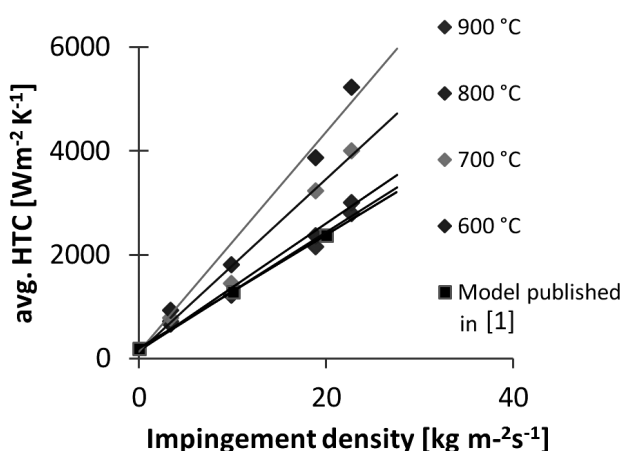surface temperatures and the Leidenfrost point increases with an increasing water-impingement density. The dependence of the heat-transfer coefficient on the water-impingement density is linear in the film boiling regime. The functions for predicting the average heat-transfer coefficient in the surface temperature range from 600 °C to 900 °C were determined.

Acknowledgement

5 REFERENCES

[1] R. Jeschar, U. Reiners, R. Scholz, Heat transfer during water and water-air spray cooling in the secondary cooling zone of continuous casting plants, Proceeding of the 69th Steelmaking Conference, Washington, 69 (**1986**), 551–521

[2] M. Pohanka, K. A. Woodbury, A Downhill, Simplex method for computation of interfacial heat transfer coefficients in alloy casting, Inverse Problems in Engineering, 11 (**2003**), 409–424

[3] M. Raudensky, Heat Transfer Coefficient Estimation by Inverse Conduction Algorithm, International Journal of Numerical Methods for Heat and Fluid Flow, 3 (**1993**) 3, 257–266

IN MEMORIAM
PROF. DR. JOŽE RODIČ (26. 5. 1931–3. 3. 2013)

Odšel je prof. dr. Jože Rodič. Odšel je metalurg, ki je bil eden izmed inženirjev, zaslužnih za to, da je metalurgija prerasla iz dobro razvite obrti v inženirsko stroko. Slovenska metalurgija se je razvila v pomembno tehniško vedo v Sloveniji in postala prepoznavna v vsem evropskem prostoru. Odšel je inženir praktik, vodja razvoja, ki se je hitro zavedel, da napredek tehnologije in proizvodov ni več mogoč samo na podlagi izkušenj, marveč je postalo znanje temelj poznavanja metalurških in tehnoloških procesov ter zgradbe trdnih kovin. Zaposlovali so ga tekoči in razvojni problemi proizvodnje in proizvodov železarne na Ravnah, podpiral je tudi raziskovanje in sofinanciranje nove raziskovalne opreme, ki je presegalo interes podjetja. Zavedal se je razlike med znanostjo in znanjem. Znanost nastaja v strogo nadzorovanih razmerah dela laboratorijev, znanje pa je le tisti njen del, ki ga je mogoče vgraditi v tehnološke procese, kot jih omogočajo proizvodna oprema in dosegljive surovine za izdelavo jekla. Delo dr. Jožeta Rodiča je še danes eden od temeljev proizvodnje orodnih jekel in elektropretaljevanja pod žlindro, dveh danes vitalnih delov podjetja Metal Ravne.

Poleg strokovnega delovanja je bil tudi odličen pedagog, ki je znal izbrati številne mlade sodelavce. Ti so se razvili v vrhunske inženirje in strokovnjake na svojem področju. Bil je izrazit zagovornik timskega dela in uvajanja računalnikov ter procesnega vodenja izdelave jekla. Zaradi svoje komunikativnosti je bil poznan v številnih državah in pridobil si je številne prijatelje široko po svetu. Bil je med ustanovitelji in dolgo leta tudi član uredniškega odbora revije Materiali in tehnologije ter zagovornik vsakoletne konference Materiali in tehnologije v Portorožu. Kot avtor ali soavtor je objavil številna znanstvena in strokovna dela pri nas in v tujini ter na konferencah.

Leta 1987 se je tedanji direktor Metalurškega inštituta v Ljubljani upokojil in dr. Rodič je prevzel vodenje inštituta. V svojem mandatu je poskrbel tudi za novo investicijo v pilotno proizvodnjo inštituta, to je v sistem horizontalnega kontinuirnega ulivanja tanke žice iz materialov, ki se uporabljajo za navarjanje trdih plasti in drugih specialnih zlitin. Žal pa je ta tehnologija, kljub svoji naprednosti, zaradi hitrega nižanja cen teh mate-

rialov, torej iz ekonomskih razlogov, postala nekonku-renčna in se je nehala uporabljati.

V mladih letih je bil aktiven smučar, zagovornik športa pa je ostal vse življenje. Njegova zasluga je razvoj plavalnega športa na Ravnah na Koroškem. Sin in hči sta bila prvaka v smučanju in plavanju ter bila člana državne reprezentance.

Prof. dr. Jože Rodič je bil ves čas aktiven tudi na področju zbiranja podatkov s področja lastnosti orodnih jekel in obdelave podatkov ter njihovega sistematičnega urejanja. Želel si je izdelati katalog o orodnih jeklih ter te podatkovne zbirke povezati v učinkovit računalniški program za izbiro orodnih jekel. S tem se je aktivno ukvarjal tudi še po upokojitvi. Žal pa mu je načrte pre-križala prehitra smrt, ki ga je ustavila sredi izvajanja svojih idej in načrtov.

Prof. dr. Jožeta Rodiča se bomo spominjali kot veli-kega strokovnjaka s področja orodnih jekel, kot odprtega in za novosti dovzetnega človeka ter velikega ljubitelja svojih vnukov.

doc. dr. Matjaž Torkar
Glavni in odgovorni urednik
Materiali in Tehnologije